

Zhou, Liangchen (2013). The aerodynamic and structural study of flapping wing vehicles.  
(Unpublished Doctoral thesis, City University London)



**CITY UNIVERSITY  
LONDON**

[City Research Online](#)

**Original citation:** Zhou, Liangchen (2013). The aerodynamic and structural study of flapping wing vehicles. (Unpublished Doctoral thesis, City University London)

**Permanent City Research Online URL:** <http://openaccess.city.ac.uk/3164/>

#### **Copyright & reuse**

City University London has developed City Research Online so that its users may access the research outputs of City University London's staff. Copyright © and Moral Rights for this paper are retained by the individual author(s) and/ or other copyright holders. All material in City Research Online is checked for eligibility for copyright before being made available in the live archive. URLs from City Research Online may be freely distributed and linked to from other web pages.

#### **Versions of research**

The version in City Research Online may differ from the final published version. Users are advised to check the Permanent City Research Online URL above for the status of the paper.

#### **Enquiries**

If you have any enquiries about any aspect of City Research Online, or if you wish to make contact with the author(s) of this paper, please email the team at [publications@city.ac.uk](mailto:publications@city.ac.uk).



**CITY UNIVERSITY  
LONDON**

**School of Engineering and Mathematical Sciences**

# **The Aerodynamic and Structural Study of Flapping Wing Vehicles**

Liangchen Zhou BSc, MSc

**A thesis submitted in partial fulfilment of the requirements for the  
degree of Doctor of Philosophy**

**Centre for Aeronautics  
Department of Mechanical Engineering and Aeronautics**

**July 2013**

## ACKNOWLEDGEMENTS

First and foremost, I would like to thank my parents for their uncountable moral and financial support.

I would also like to express my appreciation to Dr. Chak W. Cheung, my project supervisor, for his valuable advices, guidance and suggestions throughout my PhD research project.

In addition, I would like to give my personal and greatest gratitude to Mr. Tim Barnes and Mr. Jim Hooker for their willingness to help during the experimental work of my research.

Last but not least, I also wish to convey a thousand thanks to those who have directly or indirectly provided me with encouragement and useful information throughout my PhD research project.

Thank you.

## DECLARATION

I declare that the work presented in this thesis is my own and has been produced under the supervision of Dr Chak W. Cheung.

I grant powers of discretion to City University London Librarian to allow single copies of this thesis for study purposes subject to normal conditions of acknowledgement.

City University London

周良辰

---

(Zhou Liangchen)

## ABSTRACT

This thesis reports on the aerodynamic and structural study carried out on flapping wings and flapping vehicles. Theoretical and experimental investigation of aerodynamic forces acting on flapping wings in simple harmonic oscillations is undertaken in order to help conduct and optimize the aerodynamic and structural design of flapping wing vehicles. The research is focused on the large scale ornithopter design of similar size and configuration to a hang glider.

By means of Theodorsen's theory the aerodynamic forces on a thin aerofoil subject to heaving, pitching, and combined heaving and pitching motions are carefully studied. The analytical method is then employed to calculate the lift acting on the rigid flat plate undergoing small simple harmonic oscillations at different airspeeds and frequencies. The theoretical calculations are compared with experimental results which show reasonably good agreement. However experimental study shows that the wing frame deformation induces extra aerodynamic forces which can change the overall wing performance. Hence an experimental investigation focusing on wing flexibility effect on aerodynamic forces is also carried out. Three wings of similar planform geometry but slightly different degree of flexibility are manufactured for wind tunnel testing. Test results show that the wing deformation not only affects the aerodynamic forces but also the required power for various wing flapping motions.

By understanding the aerodynamic performance of flapping wings from both theoretical and experimental studies the preliminary design of large scale ornithopter is carried out based on a hang glider prototype. Theoretical and experimental studies are carried out to validate aerodynamically the loading acting on the wing and finite element analysis is carried out to evaluate the structural strength. In addition, DeLaurier's method is employed to calculate the aerodynamic forces of flapping wings by taking into account of the wing aspect ratio. The test results show good agreement with the theoretical calculation by DeLaurier's method. However the FEA results indicate structural failure based on the original calculation by assuming the wing is completely rigid. Modification

## ABSTRACT

---

of aerodynamic modelling is carried out to reassess the structural strength by taking into account of the wing deformation and possible effect due to large angle of attack which shows a much more reasonable stress distribution on the entire wing structure without failure. Furthermore three wing planform and structural modifications are carried out to improve the aerodynamic performance of the flapping wing. Finally the folding wing design case is selected as the optimal design which produces the highest overall positive lift and a variable geometric system is employed to control the folding motion of the wing.

# TABLE OF CONTENTS

<b>ACKNOWLEDGEMENTS .....</b>	<b>i</b>
<b>DECLARATION.....</b>	<b>ii</b>
<b>ABSTRACT.....</b>	<b>iii</b>
<b>TABLE OF CONTENTS .....</b>	<b>v</b>
<b>LIST OF FIGURES.....</b>	<b>x</b>
<b>LIST OF TABLES .....</b>	<b>xvii</b>
<b>NOMENCLATURE .....</b>	<b>xix</b>
<b>ACRONYM.....</b>	<b>xxi</b>
<b>1 Introduction.....</b>	<b>1</b>
1.1 Research Motives and Objectives.....	1
1.2 Flying Species in the Natural World.....	5
1.3 Man-made Aircraft.....	7
1.3.1 Micro Air Vehicles.....	8
1.3.2 Large Scale Ornithopters.....	9
1.4 Thesis Outline.....	10
<b>2 Literature Review .....</b>	<b>12</b>
2.1 Literature Review .....	12
2.1.1 Analytical Studies on Flapping Wing .....	12
2.1.2 Numerical Studies on Flapping Wing .....	13
2.1.3 Flapping Wing Investigation from Nature.....	14
2.1.4 Flapping Wing Structural Modelling .....	17
2.1.5 Aeroelastic Effect on Flapping Wing.....	17
2.1.6 Experimental Studies on Flapping Wings .....	18
2.2 Summary .....	19
<b>3 Methodology .....</b>	<b>20</b>

## TABLE OF CONTENTS

---

3.1	Parametric Study of Flying Species .....	21
3.2	How Birds Fly .....	24
3.3	Prototype Selection .....	27
3.3.1	Case Study of Ornithopter .....	28
3.3.2	Structural Configuration Investigation.....	29
3.4	Theoretical Study and Validation of Flapping Wing Designs .....	31
3.5	Ornithopter Design and Optimization.....	31
<b>4</b>	<b>Modelling of Oscillatory Aerodynamics using Theodorsen’s Function.....</b>	<b>33</b>
4.1	Two-dimensional Aerodynamic Forces on Flapping Aerofoil.....	36
4.1.1	Study of Theodorsen’s Lift Function .....	36
4.1.1.1	Pure Heaving Case .....	36
4.1.1.2	Pure Pitching Case.....	38
4.1.2	Study of Theodorsen’s Lift Function in Time History.....	39
4.1.2.1	Study of Heaving Motion in Time History.....	40
4.1.2.2	Study of Pitching Motion in Time History .....	40
4.1.2.3	Study of Heaving and Pitching Combined Motion in Time History.....	41
4.1.3	Inertia Study of Flapping Wing .....	42
4.1.4	Propulsive Force and Efficiency of Flapping Aerofoil .....	42
4.2	3-D Aerodynamic Force Study of Flapping Wing .....	45
4.2.1	Strip Theory of 3-D Aerodynamic Force .....	45
4.2.2	DeLaurier’s Method on Flapping Wing Study .....	48
4.3	Theoretical Calculation of Flapping Wing Aerodynamics .....	51
4.3.1	Aerodynamic Force on Rigid Wing in Simple Harmonic Motions .....	53
4.3.1.1	3-D Aerodynamic Force Calculation in Whole-wing Motion .....	54
4.3.1.2	3-D Aerodynamic Force Calculation in Root Flapping .....	55
4.3.1.3	3-D Aerodynamic Force Calculation by DeLaurier’s Method .....	57
4.3.2	Aerodynamic Force on Flapping Wing in Time History .....	59
4.3.2.1	Forces on the Wing in Heaving Motion .....	60
4.3.2.2	Forces on the Wing in Pitching Motion.....	62
4.3.2.3	Forces on the Wing in Combined Heave and Pitch Motion .....	64



## TABLE OF CONTENTS

---

4.3.2.4	Wing Propulsion and Propulsive Efficiency.....	68
<b>5</b>	<b>Experimental Investigation .....</b>	<b>72</b>
5.1	Wind Tunnel Test of Rigid Wings.....	72
5.1.1	Wing and Test Rig Design.....	72
5.1.2	Construction of Test Rig for Different Motions .....	76
5.1.2.1	Pure Heaving Motion .....	76
5.1.2.2	Pure Pitching Motion.....	76
5.1.2.3	Heaving and Pitching Combined Motion .....	77
5.1.3	Wind Tunnel Test Equipment.....	78
5.1.4	Wind Tunnel Test.....	81
5.1.4.1	Force Calibration.....	81
5.1.4.2	Inertia Force Measurement .....	85
5.1.4.3	Force Measurement in Heaving Motion.....	87
5.1.4.4	Force Measurement in Pitching Motion .....	88
5.1.4.5	Force Measurement in Heaving and Pitching Combined Motion.....	89
5.1.5	Test Results Comparison.....	91
5.1.5.1	Inertia Force Comparison .....	91
5.1.5.2	Aerodynamic Force Comparison .....	93
5.2	Wind Tunnel Test of Flexible Wings.....	100
5.2.1	Experimental Study of Flexible Wing.....	100
5.2.1.1	Wing Configuration.....	100
5.2.1.2	Experimental Arrangement.....	101
5.2.1.3	Load Cell Calibration .....	103
5.2.1.4	Sting and Fuselage Calibration .....	107
5.2.1.5	Wing Flexibility Evaluation.....	108
5.2.1.6	Steady Aerodynamic Force Test.....	109
5.2.1.7	Inertia Test .....	110
5.2.1.8	Experiment of Flapping Wing.....	111
5.2.2	Wing Flexibility Effect.....	117

<b>6</b>	<b>Preliminary Ornithopter Wing Design and Finite Element Modelling .....</b>	<b>126</b>
6.1	Hang Glider Prototype Design .....	126
6.1.1	Hang Glider Study.....	126
6.1.1.1	Product of Wills Wing Class.....	127
6.1.1.2	Definition of Technical Terms for Hang Gliders.....	128
6.1.1.3	Structural Components of Hang Gliders .....	129
6.1.1.4	Flight Mechanics of Hang Gliders .....	130
6.1.1.5	The HGMA Airworthiness Program .....	131
6.1.2	Design Specifications .....	134
6.1.3	n-V Diagram and Loading Action.....	135
6.1.3.1	Calculation of the Lift Curve Slope .....	136
6.1.3.2	n-V Diagram .....	139
6.1.3.3	Spanwise Lift Distribution.....	141
6.1.3.4	Shear Force and Bending Moment.....	144
6.1.4	Dimension of Wing Component .....	147
6.1.5	CATIA Model of Hang Glider.....	148
6.2	Ornithopter Design.....	151
6.2.1	Design Specification .....	151
6.2.2	Flapping Motion Control.....	154
6.2.3	CATIA Model of Ornithopter.....	155
6.2.4	Spanwise Lift Distribution of Ornithopter.....	158
6.3	Experimental Study.....	159
6.3.1	Scale Down Model.....	160
6.3.2	Test Rig Setup.....	160
6.3.3	Balance Calibration.....	161
6.3.4	Wind Tunnel Test.....	163
6.4	Finite Element Modelling.....	167
6.4.1	FE Modelling of Hang Glider .....	167
6.4.2	FE Modelling of Ornithopter .....	177
6.4.2.1	FE Modelling of Ornithopter in Gliding.....	178
6.4.2.2	FE Modelling of Ornithopter in Flapping.....	180

TABLE OF CONTENTS

---

**7 Ornithopter Design and Optimisation ..... 187**

7.1 Optimisation of Wing Design..... 187

7.1.1 Wing Design Cases ..... 187

7.1.2 Wind Tunnel Tests of the Wing Design Cases ..... 190

7.1.2.1 Aerodynamic Force Comparison of Case 1 and Case 2 ..... 194

7.1.2.2 Aerodynamic Force Comparison of Case 1 and Case 3 ..... 195

7.1.2.3 Aerodynamic Force Comparison of Case 1 and Case 4 ..... 196

7.1.2.4 Horizontal Aerodynamic Force Comparison ..... 197

7.1.2.5 Test Result in Time History ..... 200

7.1.3 Summary of Wing Design Cases ..... 202

7.2 Modification of FE Modelling..... 203

7.2.1 Frequency Modification of FE Modelling..... 203

7.2.2 Aerodynamic Force Modification for FE Modelling ..... 204

7.3 Optimisation of Ornithopter Structure ..... 211

**8 Conclusions and Recommendations for Future Work ..... 217**

8.1 Conclusions ..... 217

8.2 Recommendations for Future Work..... 219

**REFERENCES ..... 221**

**APPENDIX A ..... 228**

**APPENDIX B ..... 262**

**APPENDIX C ..... 269**

## LIST OF FIGURES

Figure 1.1 Research flowchart .....	4
Figure 1.2 The relationship between weight, wing loading and cruising speed .....	6
Figure 1.3 Several successful fixed-wing MAVs .....	8
Figure 1.4 Several ornithoptic MAV concepts .....	9
Figure 1.5 Large scale ornithopters UTIAS 1 and Snowbird .....	10
Figure 2.1 Flight regime of steady-state and unsteady-state of natural flyers .....	16
Figure 2.2 Wing span versus body mass .....	16
Figure 3.1 Research plan of ornithopter design .....	20
Figure 3.2 The relation between weight and wing loading .....	22
Figure 3.3 Wing beat frequency in birds .....	24
Figure 3.4 Wing twist over a stroke .....	26
Figure 3.5 Force vector on the take-off mode and cruising mode .....	27
Figure 4.1 Mean line of chord of a rigid aerofoil .....	33
Figure 4.2 Value of $G(k)$ and $F(k)$ vs $k$ .....	35
Figure 4.3 Aerofoil displacement .....	42
Figure 4.4 Thrust generation .....	43
Figure 4.5 Whole-wing heaving .....	46
Figure 4.6 Root flapping .....	47
Figure 4.7 Lift coefficient amplitude variation against $1/k$ per unit heave and pitch angle .....	53
Figure 4.8 Spanwise lift distribution calculated by Theodorsen for whole-wing motion .....	55
Figure 4.9 Spanwise lift distribution calculated by Theodorsen for root flapping .....	56
Figure 4.10 Spanwise lift distribution comparisons for whole-wing motion .....	58
Figure 4.11 Spanwise lift distribution comparisons for root flapping .....	59
Figure 4.12 Forces due to heaving motion in time history .....	61
Figure 4.13 Simple harmonic motion of heaving .....	61
Figure 4.14 Forces due to pitching motion in time history .....	63
Figure 4.15 Simple harmonic motion of pitching .....	63

## LIST OF FIGURES

---

Figure 4.16 Heaving and pitching combined motion.....	65
Figure 4.17 Combined motion of mode 1.....	66
Figure 4.18 Combined motion of mode 2.....	67
Figure 4.19 Combined motion of mode 3.....	67
Figure 4.20 Combined motion of mode 4.....	68
Figure 4.21 Propulsive efficiency of heaving motion.....	69
Figure 4.22 Energy dissipated in the wake of pitching.....	70
Figure 5.1 Wing frame with strain gauge attached at the root.....	73
Figure 5.2 Gear box design.....	73
Figure 5.3 Side panel with gear box.....	74
Figure 5.4 Floor.....	74
Figure 5.5 Assembled test rig.....	75
Figure 5.6 Position sensor.....	75
Figure 5.7 Beam for displacement test.....	75
Figure 5.8 Test rig design for pure heaving motion.....	76
Figure 5.9 Test rig for pure pitching motion.....	77
Figure 5.10 Test rig for heaving and pitching combined motion.....	78
Figure 5.11 Test section of the T3 wind tunnel.....	78
Figure 5.12 Pitot tube.....	79
Figure 5.13 Micro-manometer.....	80
Figure 5.14 Test data logging set up.....	80
Figure 5.15 Spanwise inertia distribution.....	81
Figure 5.16 Spanwise aerodynamic force.....	83
Figure 5.17 Relationship between tip load $W_c$ and strain gauge signal in heaving motion .....	84
Figure 5.18 Relationship between tip load $W_c$ and strain gauge signal in pitching motion .....	84
Figure 5.19 Relationship between tip load $W_c$ and strain gauge signal in combined motion.....	85
Figure 5.20 Inertia force test.....	86
Figure 5.21 Inertia test results.....	87

## LIST OF FIGURES

---

Figure 5.22 Heaving motion in wind tunnel test.....	88
Figure 5.23 Moment due to lift in heaving motion .....	88
Figure 5.24 Pitching motion in wind tunnel test.....	89
Figure 5.25 Moment due to lift in pitching motion.....	89
Figure 5.26 Combined motion in wind tunnel test.....	90
Figure 5.27 Moment due to lift in combined motion .....	90
Figure 5.28 Inertia force comparison of heaving motion .....	91
Figure 5.29 Inertia force of pitching motion.....	92
Figure 5.30 Inertia force comparison of combined motion .....	93
Figure 5.31 Aerodynamic force comparison for heaving motion.....	94
Figure 5.32 Test result of heaving motion in time history for 4m/s, 4Hz .....	95
Figure 5.33 Computed result of heaving motion in time history for 4m/s, 4Hz.....	95
Figure 5.34 Aerodynamic force comparison for pitching motion .....	96
Figure 5.35 Test result of pitching motion in time history for 4m/s, 4Hz.....	97
Figure 5.36 Computed result of pitching motion in time history for 4m/s, 4Hz .....	97
Figure 5.37 Aerodynamic force comparison for combined motion.....	98
Figure 5.38 Test result of combined motion in time history for 4m/s, 4Hz .....	99
Figure 5.39 Computed result of combined motion in time history for 4m/s, 4Hz.....	99
Figure 5.40 Wing configuration.....	101
Figure 5.41 Test rig setup .....	102
Figure 5.42 Electrical equipment setup.....	103
Figure 5.43 Data log setup.....	103
Figure 5.44 Arrangement of balance calibration .....	104
Figure 5.45 Lift force calibration .....	105
Figure 5.46 Drag force calibration.....	105
Figure 5.47 Lift and drag coefficients of sting with fuselage.....	107
Figure 5.48 Wing frame stiffness calibration .....	108
Figure 5.49 Steady lift coefficient at 0° angle of attack.....	109
Figure 5.50 Steady drag coefficient at 0° angle of attack.....	110
Figure 5.51 Inertia test comparison.....	111
Figure 5.52 Test results measurement .....	112

## LIST OF FIGURES

---

Figure 5.53 Lift amplitude of flapping wings at 3Hz and 0° angle of attack .....	113
Figure 5.54 Mean horizontal force of flapping wings at 3Hz and 0° angle of attack .....	113
Figure 5.55 Input power of flapping wings at 3Hz and 0° angle of attack.....	114
Figure 5.56 Theoretical calculation of flapping motion at 2m/s, 3Hz .....	115
Figure 5.57 Test result of flapping motion of Wing 1 at 2m/s, 3Hz.....	115
Figure 5.58 Test result of flapping motion of Wing 1A at 2m/s, 3Hz .....	116
Figure 5.59 Test result of flapping motion of Wing 1B at 2m/s, 3Hz .....	116
Figure 5.60 Steady loading acting on the flexible wing .....	117
Figure 5.61 Total lift comparison in 0° angle of attack.....	118
Figure 5.62 Image of flapping wing upstroke motion.....	119
Figure 5.63 Image of flapping wing downstroke motion .....	119
Figure 5.64 Flexible wing performance in flapping motion.....	121
Figure 5.65 Theoretical and proposed lift distribution on half span.....	121
Figure 5.66 Flapping flight with wing twist .....	122
Figure 5.67 Combined heaving and pitching flapping wing motion .....	123
Figure 5.68 Twist angle effect .....	125
Figure 6.1 Hang glider comparisons .....	127
Figure 6.2 Hang glider structure .....	130
Figure 6.3 Force and velocity vectors for gliding flight.....	131
Figure 6.4 Wills Wing Sport 2-155 hang glider .....	134
Figure 6.5 Wing geometry .....	134
Figure 6.6 Comparison of L/D estimates with manufacturer's data.....	136
Figure 6.7 Lift coefficient versus angle of attack .....	137
Figure 6.8 Drag coefficient versus angle of attack .....	137
Figure 6.9 Lift-to-drag ratio versus angle of attack .....	138
Figure 6.10 Weight effect on minimum sink rate .....	138
Figure 6.11 Sink rate vs angle of attack .....	139
Figure 6.12 n-V diagram .....	141
Figure 6.13 Spanwise lift coefficient distribution.....	143
Figure 6.14 Spanwise lift distribution .....	143
Figure 6.15 Loading action on cantilever .....	144

## LIST OF FIGURES

---

Figure 6.16 Shear force diagram at $n = 1$ .....	146
Figure 6.17 Bending moment diagram at $n = 1$ .....	146
Figure 6.18 Wing frame construction.....	147
Figure 6.19 Schematic drawing of the Wills Wing Sport 2-155 hang glider .....	148
Figure 6.20 Top view of hang glider.....	149
Figure 6.21 Bottom view of hang glider .....	149
Figure 6.22 Front view of hang glider.....	150
Figure 6.23 Side view of hang glider .....	150
Figure 6.24 Ornithopter wing frame .....	152
Figure 6.25 Wing frame dimension.....	153
Figure 6.26 Location of the hang point and control bar point .....	153
Figure 6.27 Dimension of each section of wing .....	154
Figure 6.28 Isometric view of ornithopter.....	155
Figure 6.29 Isometric view of flapping mechanism.....	156
Figure 6.30 Motor support frames .....	157
Figure 6.31 Comparison of spanwise lift distribution on semi-span .....	159
Figure 6.32 1:20 scale wing configuration .....	160
Figure 6.33 Test rig setup .....	161
Figure 6.34 Lift force calibration .....	162
Figure 6.35 Drag force calibration .....	163
Figure 6.36 Inertia force comparison .....	164
Figure 6.37 Aerodynamic force comparison .....	165
Figure 6.38 Test result of flapping motion of design case 1 for 4m/s, 2Hz .....	166
Figure 6.39 Theoretical calculation of flapping motion for 4m/s, 2Hz.....	166
Figure 6.40 Geometry modelling of hang glider.....	167
Figure 6.41 Geometry modelling of hang glider wire.....	168
Figure 6.42 Mesh elements of wing surface .....	169
Figure 6.43 Mesh and bar elements of wing frame and boundary condition .....	169
Figure 6.44 Loading case with factor of $n = 1$ .....	170
Figure 6.45 Stress on the wing skin .....	172
Figure 6.46 Stress on the wing frame.....	172



## LIST OF FIGURES

---

Figure 6.47 Axial stress on the wing frame .....	173
Figure 6.48 Wing deformation.....	173
Figure 6.49 Stress on the wing skin (n=7).....	174
Figure 6.50 Stress on the wing frame (n=7) .....	175
Figure 6.51 Axial stress on the wing frame (n=7) .....	175
Figure 6.52 Wing deformation (n=7) .....	176
Figure 6.53 FE modelling of ornithopter.....	178
Figure 6.54 Stress on the wing skin in gliding.....	179
Figure 6.55 Stress on the wing frame in gliding.....	179
Figure 6.56 Axial stress on the wing frame in gliding .....	180
Figure 6.57 Wing deformation in gliding .....	180
Figure 6.58 Spanwise lift comparison of flapping and gliding.....	181
Figure 6.59 Spanwise lift and inertia distribution.....	182
Figure 6.60 Stress on the wing skin in flapping.....	183
Figure 6.61 Stress on the wing frame in flapping.....	183
Figure 6.62 Axial stress on the wing frame in flapping .....	184
Figure 6.63 Wing deformation in flapping .....	184
Figure 7.1 Design case 1.....	189
Figure 7.2 Design case 2.....	189
Figure 7.3 Design case 3.....	190
Figure 7.4 Design case 4.....	190
Figure 7.5 Inertia force comparison .....	191
Figure 7.6 Measured lift amplitudes in downstroke at 0° angle of attack.....	192
Figure 7.7 Measured lift amplitudes in upstroke .....	193
Figure 7.8 Drag force comparison of flapping wing.....	194
Figure 7.9 Lift amplitude comparison over a cycle (Case 1 & 2).....	195
Figure 7.10 Lift amplitude comparison over a cycle (Case 1 & 3).....	196
Figure 7.11 Lift amplitude comparison over a cycle (Case 1 & 4).....	197
Figure 7.12 Drag comparison of case 1 .....	198
Figure 7.13 Drag comparison of case 2.....	198
Figure 7.14 Drag comparison of case 3.....	199

## LIST OF FIGURES

---

Figure 7.15 Drag comparison of case 4.....	200
Figure 7.16 Test result of flapping motion of design case 2 for 4m/s, 2Hz .....	201
Figure 7.17 Test result of flapping motion of design case 3 for 4m/s, 2Hz .....	201
Figure 7.18 Test result of flapping motion of design case 4 for 4m/s, 2Hz .....	202
Figure 7.19 Angle of attack of spanwise strip .....	205
Figure 7.20 Wing tip deformation at 2Hz.....	205
Figure 7.21 Comparison of modified spanwise lift.....	207
Figure 7.22 Stress on the wing skin with modified flapping aerodynamic load .....	208
Figure 7.23 Stress on the wing frame with modified flapping aerodynamic load .....	208
Figure 7.24 Axial stress on the wing frame with modified flapping aerodynamic load .	209
Figure 7.25 Wing deformation subject to modified flapping aerodynamic load.....	209
Figure 7.26 Modified ornithopter wing frame .....	212
Figure 7.27 CATIA model of optimal design of ornithopter.....	212
Figure 7.28 CATIA model of fold axis .....	213
Figure 7.29 Outer wing fold control.....	214
Figure 7.30 VG system.....	215

## LIST OF TABLES

Table 3.1 Power functions of wing dimensions and flight parameters against body mass .....	23
Table 3.2 Design specification comparisons of two ornithopters.....	28
Table 3.3 Preliminary design specifications .....	31
Table 4.1 Parameters for whole-wing motion .....	54
Table 4.2 Parameters used for heaving motion.....	60
Table 5.1 Specifications of wing sample.....	101
Table 5.2 Calibration coefficients .....	106
Table 5.3 Lift and drag forces of sting and fuselage.....	108
Table 5.4 Input and output data .....	112
Table 6.1 Hang glider design specifications.....	128
Table 6.2 Speed in different conditions.....	133
Table 6.3 Wing design specification.....	135
Table 6.4 Hang glider performance.....	139
Table 6.5 Flight speed definition .....	141
Table 6.6 Wing frame dimension.....	147
Table 6.7 Estimated weight of ornithopter parts.....	151
Table 6.8 Design specification of ornithopter .....	151
Table 6.9 Radne Racket engine.....	154
Table 6.10 Tip amplitude and arm length.....	155
Table 6.11 Ornithopter wing design specification .....	158
Table 6.12 Calibration coefficients .....	163
Table 6.13 Material properties of 7075-T6 aluminum alloy .....	170
Table 6.14 Material properties of glass fiber .....	171
Table 6.15 Material properties of steel alloy .....	171
Table 6.16 Stress on each layer of the skin .....	171
Table 6.17 FEA results with load factor $n = 1$ and $n = 7$ .....	176
Table 7.1 Wing design cases.....	188

## LIST OF TABLES

---

Table 7.2 FEA results comparison .....	203
Table 7.3 Comparison of FEA results in different loading case.....	210
Table 7.4 FEA results comparison in different speed .....	210
Table 7.5 FEA results comparison in different speed .....	211
Table 7.6 Extra weight of mechanical component.....	216

## NOMENCLATURE

$c$ :	Wing chord
$b$ :	Half of wing chord
$s$ :	Wing span
$l$ :	Geometric length
$S$ :	Wing area
$AR$ :	Wing aspect ratio
$h$ :	Displacement
$\alpha$ :	Pitch angle
$a$ :	Pitch axis normalized by half chord
$V$ :	Velocity
$\rho$ :	Air density
$\omega$ :	Frequency
$f$ :	Flapping frequency
$k$ :	Reduced frequency
$C(k)$ :	Complex Theodorsen's circulatory function
$L$ :	Lift
$D$ :	Drag
$T$ :	Thrust
$I$ :	Inertia
$W$ :	Weight
$Q$ :	Shear force
$M$ :	Bending moment
$P$ :	Power
$\varphi$ :	Phase shift
$t$ :	Time
$\eta$ :	Propulsive efficiency
$\overline{W}$ :	Average work done per unit time

## NOMENCLATURE

---

$\bar{E}$ :	Average kinetic energy increase in unit time
$N_c$ :	Section's circulatory normal force
$N_a$ :	Apparent mass
$C_l$ :	Lift coefficient
$C_d$ :	Drag coefficient
$\phi$ :	Angle
$\Lambda$ :	Wing sweep angle
$n$ :	Load factor
$\bar{c}$ :	Geometric mean chord
$\lambda$ :	Taper ratio
$\bar{y}$ :	Semi-spanwise pressure centre

## ACRONYM

MAV: Micro Air Vehicle

VLA: Very Light Aircraft

CSF: Calibration Scale Factor

AF: Aerodynamic Force

Dis: Displacement

AoA: Angle of Attack

CFC: Carbon Fiber Composite

FEA: Finite Element Analysis

FEM: Finite Element Method

CFD: Computational Fluid Dynamics

VG: Variable Geometry

# 1 Introduction

## 1.1 Research Motives and Objectives

The simultaneous production of aerodynamic lift and propulsion by means of flapping wings is hardly a new idea. Humans have been intrigued and fascinated by observations of bird and insect flights for hundreds of years and many of them were inspired to invent machines that can sustain them in flights. However, it wasn't until the beginning of the last century when other forms of propulsion were invented, such as propellers followed by jet engines that human flights had become a reality.

Conventional aerodynamic theory development is mostly based upon studies of fixed wings in a steady airflow, while the airflow around flapping wings is anything but steady and challenges our understanding. The success of a man-made flapping-wing flight vehicle depends greatly upon a full understanding and application of unsteady aerodynamics, structural stability, vibration and aeroelasticity. In these fields, some classical theory such as Theodorsen's theory and more advanced numerical methods such as Computational Fluid Dynamics (CFD) and Finite Element Method (FEM) have been well developed and employed for flapping-wing study. However there is a lack of an efficient and yet accurate approach not just for understanding but also for designing a successful large scale flapping-wing aircraft. The aim of this project is to develop an aerodynamic and structural model for a flapping wing ornithopter design and analysis based on extended use of a classical aerodynamic theory and FEM structural modelling.

The ornithopter is an aircraft heavier than air which flies like a bird by flapping its wings. The special feature lies in the wings that do not only generate lift but also thrust. Compared with fixed-wing aircraft, ornithopters have some practical benefits for flight vehicles design:



- Improved Efficiency

An aeroplane propeller is only about 70% efficient. Energy is wasted because some of the aerodynamic force produced on the blades acts to resist the motion of the propeller. In an ornithopter, the downstroke wing resistance provides lift, and during the upstroke the wing can be feathered so resistance is minimized. Therefore the ornithopter has potentially higher efficiency than an aircraft with rotating propeller. The jet-engined aircraft has yet to match piston-engined aircraft in fuel efficiency and due to the complexity of the propulsive system the weight of the jet engine is dramatically increased with high fuel consumption.

- More Lift

Flapping wings have some additional ways of producing lift and thrust that are not available with fixed wings or rotating blades. The rotating blades have to be designed with a fixed angle in order to generate lift and thrust but the flapping wing can work effectively at different angles relative to the direction of airstream with unique flexibility to adapt to the flow while flapping. One example of this adaptability is the clap-fling technique, first discovered in insects. By bringing together the wings and then abruptly flinging them apart, a powerful burst of thrust can be produced. Another technique is delayed stall. Flapping wings do not stall as easily as fixed wings because the cyclical motion does not allow much time for a stall to develop. In some situations, it might actually be useful to stall the wing, because the downstroke air resistance is actually a strong lifting force. These techniques can be used to improve the slow flight and hovering capabilities of some ornithopter designs.

- High Manoeuvrability

Whereas an aeroplane relies on its forward speed to produce manoeuvring forces, the flapping wing with suitably adaptable flapping cycle and wing geometry can produce large manoeuvring forces at any time. The incredible manoeuvrability of birds is partly due to their small size and partly due to their use of flapping wings which can be adapted geometrically to suit different manoeuvres.

- Reduced Noise

Aeroplane and helicopters make a lot of noise. Much of the noise is produced by the high velocity jet flow emitting from the engine casing or the helicopter blades rotating at high speed. The environmental impact of high noise levels is one of the many factors preventing the wider use of helicopters.

As demonstrated by birds, flapping wings offer potential advantage in manoeuvrability and energy saving compared with fixed-wing aircraft, as well as potentially vertical take-off and landing capabilities. With further development, ornithopters could offer great fuel economy combined with the manoeuvrability of a helicopter achievable at greatly reduced or minimal noise impact to the environment. By exploring these advantages of flapping wing aircraft a great deal of work has been done recently in studying and experimenting small scale ornithopter flight which is so called insect flight. However the imitation nature's flapping-wing flight has been humanity's oldest aeronautical dream. History provides numerous examples of human efforts and attempts trying to achieve that dream by him strapping on wings and falling from high places. Due to the limitation of knowledge and understanding of aerodynamic, structures and control techniques required for the design of flapping flight vehicles people have been trying for a hundred years but not much success has been achieved.

The objective of this research is to carry out aerodynamic and structural investigation of flapping wings in simple harmonic oscillations. The aim is to carry out extensive study of the performance of flapping wings of various configurations and man-made models in order to gain a thorough understanding to help optimise the wing and configuration design for a human-controlled ornithopter. The key research scopes are summarized as follows:

- Flapping wing species investigation
- Theoretical study of unsteady aerodynamics for simple harmonic oscillatory motions

- Experimental investigation of flapping wings in different oscillatory motions
- Preliminary design of manned ornithopter
- Optimal design of ornithopter

A research flow-chart, giving an overview of the approach used in the present investigation, is given below.

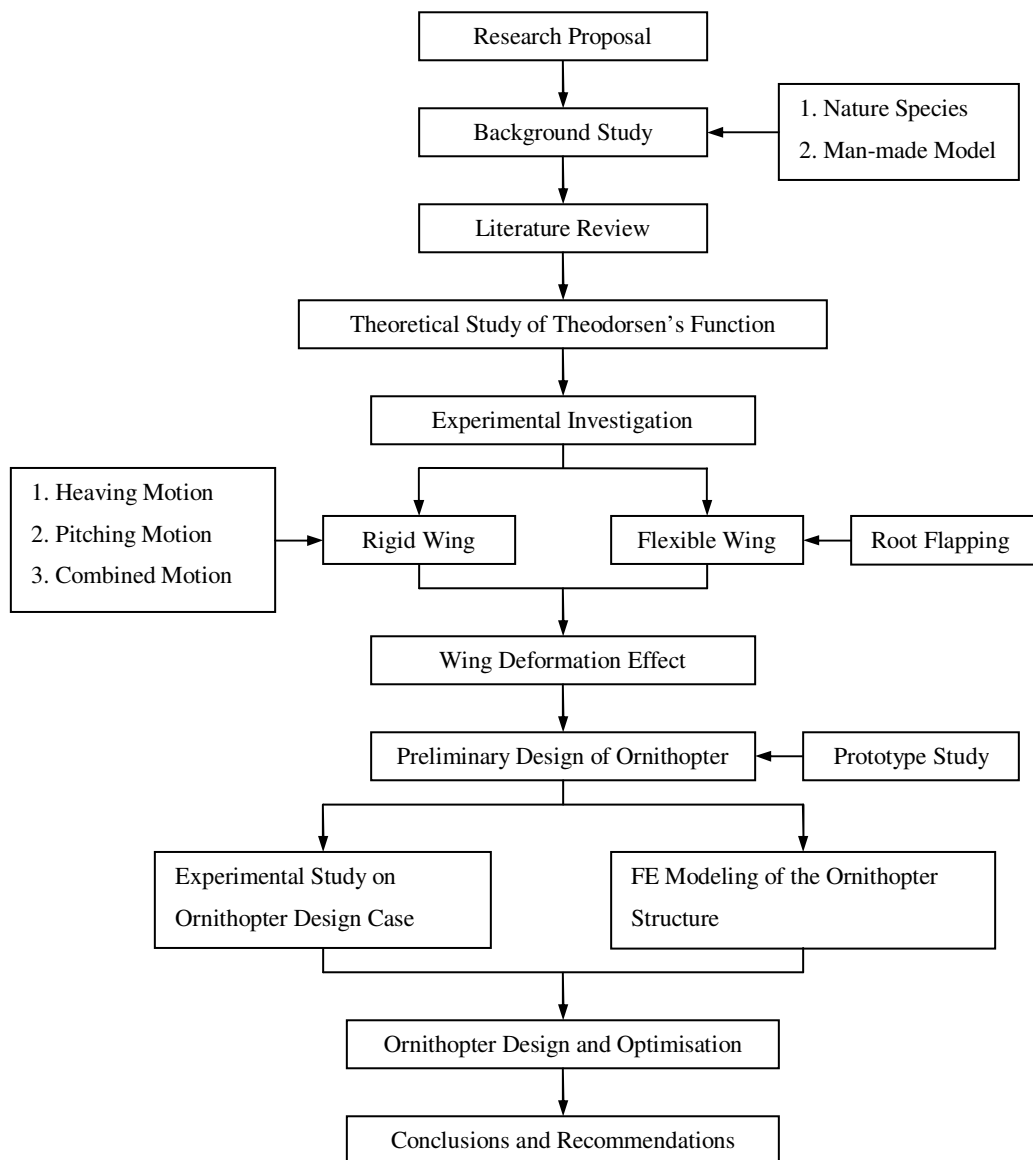


Figure 1.1 Research flowchart

## 1.2 Flying Species in the Natural World

Studies on flapping wing flight have always been done as an attempt to simulate the flight of flying animal species, birds in particular. In nature 10,000 types of birds and bats have been found and attracted scientific attention. The kinematic descriptions of the flapping motions have been made according to their flapping frequency, weight, wing span and power requirement.

Birds range in size from 5cm (Bee hummingbird) to 2.75m (Ostrich) and insects are even smaller and lighter. The flapping frequency of the above species that fly varies from 10Hz to 100Hz and the total weight varies from a few grams to 100kg. In Henk Tennekes' book [1] a trend line of weight against cruising speed for most known flying objects is illustrated in Fig. 1.2. In the left bottom region it indicates the insects with low weight and speed. In the right top area it shows the man-made aeroplanes with high weight and speed. The region relating to birds is in the centre of the graph. The objects above this trend line indicate that in spite of their significantly greater weight, flight can be sustained by higher cruising speeds. The fliers below this line indicate very low speed flights can only be sustained with very low body weights. Following the diagram most of natural flying species with low cruising speed can support even higher body weight relative to its size by adopting flapping wing motion instead of other forms of propulsion. Hence the flapping wing motion plays a remarkable role in low speed flights.

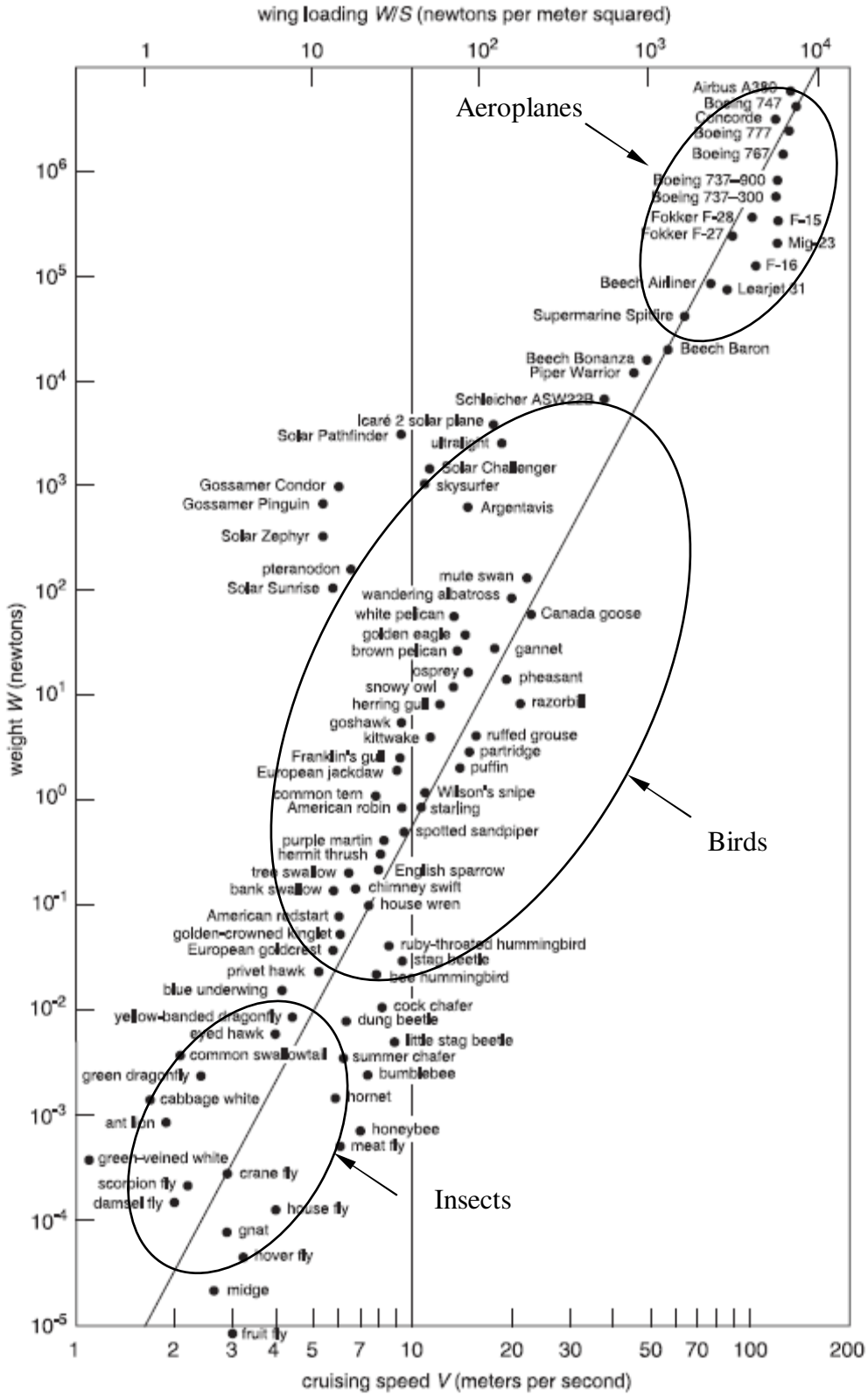


Figure 1.2 The relationship between weight, wing loading and cruising speed [1]

### **1.3 Man-made Aircraft**

Man's urge to fly has been around for as long as he has become an intelligent being and developed curiosity and fascination about how all things work in nature. The idea comes from seeing the beauty, grace and freedom of soaring birds. The early concept of flying machine is to imitate birds by the use of flapping wing which is so called an ornithopter. Leonardo da Vinci created dozens of sketches of flying machine based on the flapping wing concept. However all the attempts failed because the flying capabilities of birds have never been fully understood and replicated by humans. Then another early idea of aviation attempt is by putting hot air or gas lighter than air in a closed container which is so called lighter-than-air craft. The most famous airship was built by Zeppelin in 1900. However the gas used in early days was flammable and the airship was economically inefficient and operationally unreliable. By copying soaring birds without flapping the glider was developed in latter part of the nineteenth century which was the first so called heavier-than-air craft. In 1903 Wright brothers built the first powered aeroplane and launched flight successfully. After the Wright brothers aeronautical activities took place in civilizations. During World War I & II aircraft were rapidly developed and evolved driven by military needs. After World War II fantastic technological advances have been realised in both military and civil aircraft. The jet engine was rapidly improved to increase thrust and reduce fuel consumption. Wing sweepback was employed to achieve supersonic flight.

Following the recent rapid development of aircraft and other unmanned flight vehicles the early concept of flapping flight is beginning to draw people's attention again. The question is as follows: with rapid advances in both knowledge and technologies available for aircraft design and manufacturing nowadays, can we achieve our original dream of human-designed and powered flapping flight, mimicking what nature has mastered for millions of years? To this end, many works have been carried out to investigate and design flapping flight aircraft which are described below.

### 1.3.1 Micro Air Vehicles

Since the Wright brothers built their biplane in the early twentieth century powered by man-made engines and propellers, no serious attention has been dedicated to the flapping wing problem as an alternative way of propulsion. However, the advent of new technologies and development of Micro Air Vehicles (MAV) capable of flying at low Reynolds number have given researchers in the last decade impetus to reconsider flapping wing vehicles as alternative design possibilities. In practice, a lot of effort has been concentrated in recent years in developing analytical models of a flapping wing to explain the high lift coefficients that steady state aerodynamics cannot explain. Although complicate in general, the motion of bird wings can be decomposed in three main components: plunging, pitching and sweeping. Simplification of this motion should enable us to investigate forces acting on a wing performing vertical and rotational displacements. Micro air vehicle is generally defined as a class of aircraft with a maximum dimension of 6 inches that is capable of operation at flight speeds of approximately 25mph or less, with mission duration of 20 to 30 minutes.

A number of successful fixed-wing MAV designs have been produced by several universities, commercial and institutions. As shown in Fig. 1.3 from left to right, they are Aerovironment's Black Widow, NLB's Trochoid, and the University of Florida's flexible wing design. The potential application of current fixed-wing MAV designs is limited due to manoeuvre constraints.



Figure 1.3 Several successful fixed-wing MAVs [2-4]

Numerous MAVs have been proposed for civil and military applications and of which examples are shown in Fig. 1.4 from left to right. They are Aerovironment's Microbat,

Vanderbilt's Elastodynamic Ornithoptic Insect, and UC Berkeley's Micromechanical Flapping Insect. These models have been designed and made for both the biological and engineering studies of natural insect fliers. Microelectronic system is employed to achieve the flight control and smart material is used in the manufacturing of wing membrane and driving mechanism.



Figure 1.4 Several ornithoptic MAV concepts [5]

### **1.3.2 Large Scale Ornithopters**

To design, build and fly a large scale ornithopter has been of interests among some keen aviators and aeronautical engineers for centuries. Ornithopters are mechanical, powered, flapping-wing aircraft designed and built to imitate the flapping wings and flights of birds. Some notable developments in flapping wing flight vehicles included the gliding human-powered ornithopter of Alexander Lippisch in 1929, Percival Spencer's series of engine-powered, free-flight models in the 1960s. The most recent major advancement in flapping wing flight was spawned from the ingenuity and ambition of Jeremy Harris and James DeLaurier. In 1999, the Harris/DaLaurier engine-powered piloted aircraft was able to self-accelerate, by flapping wings alone, to lift-off speed, however it has yet to maintain steady flight. The major problem was the wing could barely provide enough thrust for unassisted liftoff. In 2006, Yves Pousseau succeeded in flying a human-muscle-powered ornithopter on his 212<sup>th</sup> attempt. DeLaurier also had success with an engine-powered ornithopter in 2004. The UTIAS Ornithopter No. 1 made a jet-assisted takeoff and 14 seconds flight. Later on Delaurier's Snowbird flight managed to sustain both altitude and airspeed for 19.3 seconds, covering a distance of 145 meters.



The latest two successful ornithopter design cases worthy of detailed studies are the engine-powered (UTIAS No.1) and human-powered ornithopters (Snowbird) both developed by DeLaurier as shown in Fig. 1.5. These two existing big scale ornithopters will be studied in details in Chapter 3 as design case reference.



Figure 1.5 Large scale ornithopters UTIAS 1 and Snowbird [6]

## 1.4 Thesis Outline

The present thesis consists of eight chapters including the introduction Chapter 1, where the motivation, research background and main focus and contribution of this research are outlined.

In Chapter 2 recent research works are reviewed both in the theoretical methods and practical design cases. Relevant literature publications are studied on analytical and numerical methods developed for unsteady simple harmonic oscillatory wing motions and successful design cases of MAVs and large scale ornithopters.

Chapter 3 introduces the methodologies of this research. By investigating natural fliers and man-made aircraft it is shown that scale effect is one of the key issues which affect ornithopter design. The design concept of large scale ornithopter is presented in terms of weight, aerodynamic and structural considerations.

Chapter 4 reports on the study of unsteady aerodynamics by Theodorsen's function and other analytical methods extended from Theodorsen's theory. Aerodynamic forces in terms of reduced frequency are investigated for wings undergoing different simple harmonic oscillations. Theoretical calculations are carried out of aerodynamic forces acting on the flapping wing with specific parameters to compare with experimental measurements. Theodorsen's function is employed for the calculations of rigid and flexible wings undergoing different simple harmonic motions. Different wing configurations are also studied in this chapter.

Chapter 5 describes the experimental study of flapping wings of different configurations, flexibility and flapping motions. Wind tunnel tests are carried out to validate the theoretical calculations and the wing flexibility effect is studied in detail. The wing deformation is discussed in relation to the flapping motion and flight orientation.

In Chapter 6 the preliminary ornithopter design is carried out. Hang glider is employed as a prototype to conduct the wing design. Aerodynamic forces are measured and validated by theoretical calculations. Finite element modelling is carried out to assess the structural strength and stiffness of the ornithopter.

Based on the previous investigation the modification and optimisation of the ornithopter is carried out in Chapter 7. The modified wing structure and control system is described.

Chapter 8 concludes the thesis with a summary of major findings of the research. Recommendations for further work in this area are also presented in this chapter.

## 2 Literature Review

The following literature survey provides an overview of recent research work and a summary of their most important findings relevant to the present investigation. The overview focuses on a number of areas: the theoretical methods in the study of flapping wing aerodynamics, the study of natural flyers, structural design of flapping wing aircraft, experimental study of flapping wings.

### 2.1 Literature Review

#### *2.1.1 Analytical Studies on Flapping Wing*

Theodorsen [7] first brought to general attention the problem of flutter in 1934. In his paper a mathematical model was given subject to the unsteady forces acting on a flat wing section performing infinitely small oscillations in pitch and plunge in an inviscid fluid with an undisturbed uniform flow. Expressions for lift and moment were derived which have been used extensively for the study of unsteady aerodynamics and aeroelasticity for many years.

However Theodorsen's function is not able to predict any horizontal force acting on the aerofoil in the streamwise direction because of the assumptions of inviscid flow underlying the theory. In 1936 Garrick [8] derived an expression for the horizontal force of an aerofoil undergoing small oscillations based on Theodorsen's theory. By considering the wake's energy gain during a complete cycle of oscillation he found that thrust can be generated and it depended upon the frequency and the amplitude of oscillation of the aerofoil motion. Garrick's results, which will be described in detail in Chapter 4 shows that for a pitching aerofoil thrust is obtained only beyond a threshold frequency, while below this frequency drag is obtained. For a wing undergoing plunge oscillations a thrust is created regardless of the frequency and in particular the efficiency is 100% for infinitely small oscillations.

The theories from Theodorsen and Garrick are based on the rigid thin aerofoil. In 1953 Spielberg [9] provided a method for studying two-dimensional, incompressible aerodynamic coefficients associated with harmonic changes in camber. In his study the flexibility of a thin aerofoil is first taken into account. The derivation makes use of linearized aerodynamic equations relating the pressure on the profile to the downwash distribution. From this theory the flexibility of chordwise has a positive effect in the high lift generation for small oscillations of thin aerofoil.

A design-oriented model for the unsteady aerodynamics of a flapping wing has been developed using a modified strip theory approach by DeLaurier [10]. In contrast to Theodorsen's approach the finite wing planform is taken into account. In particular, an alternative expression to account for circulatory flow effect due to wing aspect ratio  $AR$  has been proposed (see 4.2.2, Chapter 4).

The analytical method is user friendly in the initial design as a guide. The theory is based on the thin rigid aerofoil under small simple harmonic oscillation with air flow fully attached on the wing.

### ***2.1.2 Numerical Studies on Flapping Wing***

The limitation of Theodorsen's theory is that it is valid only for thin aerofoil with small plunge amplitude and is not suitable for describing the phenomena of large oscillation due to the large angle of attack.

Numerical method is also widely used to solve aerodynamic force problems in unsteady flow conditions. When the flow is incompressible, the velocity potential satisfies Laplace's equation. For flow over a thin aerofoil, Laplace's equation is solved subject to the boundary condition on the aerofoil section with respect to which the flow field is antisymmetrical. These flow conditions are fulfilled by placing a sheet of continuous vorticity on the aerofoil surface and its wake. The problem then becomes one of evaluating the strengths of the vortices by satisfying the known vertical velocity

distribution along the aerofoil surface. S. Guo [11] developed a numerical modelling tool for predicting the aerodynamic forces on an oscillating aerofoil and the aeroelastic response of a flexible flapping wing. In his paper comparisons are carried out of results obtained by using Theodorsen method, deformable wavy wake method, unsteady panel method and by experimental work.

A group of researchers, in particular K.D. Jones and M.F. Platzer [12-17] employ an unsteady panel method code for the computation of flapping wing flowfield based on potential flow theory. In their papers aerodynamic forces in vertical and horizontal directions are investigated and validated with experimental work. The effect of aerofoil thickness is also investigated and compared with linear theory. Some important results are found in particular, the thrust increases with the frequency of oscillation, but the efficiency decreases because of the unsteady effects of the wake which appears to confirm Garrick's findings earlier.

CFD is well developed in recent years for investigation of aerodynamic phenomena. Although CFD approach should be capable of providing more accurate simulation of the vorticity and flow unsteadiness for flapping wings, it is usually discarded in the early design phase of the wing due to its high complexity involving grid generation and huge computational time.

### ***2.1.3 Flapping Wing Investigation from Nature***

Unlike fixed-wing aerodynamics, there have not been any available design rules for flapping-wing aerodynamics. Two approaches are adopted for this project. One is to learn from natural flyers and try to understand and replicate their flight performance characteristics. The other is to study flapping-wing aerodynamics both theoretically and experimentally in order to improve our understanding and provide data for flapping-wing vehicle design. A lot of research has been done in the study of flying animals. In T. Nick Pornsin-sirak's report [18] the flying animals are investigated in terms of wing span, flying speed and body mass. The relationship of speed and body mass is shown in Fig.

2.1. From this plot the flight of flyers can be separated into two regimes: quasi-steady and unsteady states. For larger flyers, their flights can be approximated by quasi-steady-state assumptions because their wings flap at lower frequency during cruising and behave closely to fixed-wings. On the other hand, smaller birds and insects fly in an unsteady-state flow regime in which their wingtip speed is faster than their flight speed. For small flyers the research is focused on the high lift coefficient and high efficiency generation. In Ellington's research [19] the insect flapping flight is investigated. Some insects use the fling mechanism: the wings are clapped together and then flung open before the start of the downstroke, creating a lift-enhancing vortex around each wing. Most insects, however, rely on a leading-edge vortex (LEV) created by dynamic stall during flapping; a strong spanwise flow is also generated by the pressure gradients on the flapping wing, causing the LEV to spiral out to the wingtip. In Okamoto's work [20] the aerodynamic characteristics of the wings and body of a dragonfly and of artificial wing models were studied by conducting two types of wind tunnel tests and a number of free flight tests of gliders made using dragonfly wings. The results were consistent between these different tests. In M. Sato's research [21] the images of damselflies in free flight in a transparent container is video-taped and kinematic data used in the calculations obtained by analyzing the images. In Taylor's report [22] the propulsive efficiency of animals is investigated and was found to be related to the Strouhal number  $St$  which is normally defined in terms of the characteristic length of the object  $L$  and its wing frequency  $f$  of the oscillation and the speed of the airstream  $V_\infty$  as  $St = fL/V_\infty$ . It indicated that propulsive efficiency is high over a narrow range of  $St$  and usually peaks within the interval  $0.2 < St < 0.4$ . Experiments have been done within the interval  $0.2 < St < 0.4$  and high peak propulsive efficiency is obtained as high as 70% or even 80%.

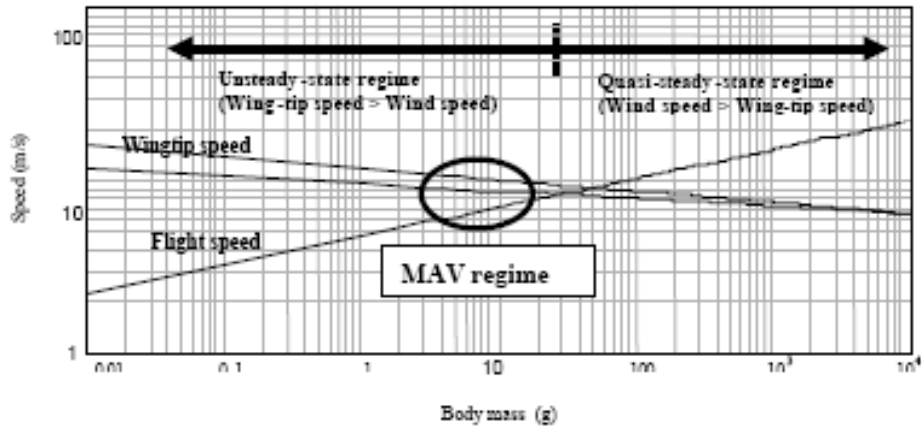


Figure 2.1 Flight regime of steady-state and unsteady-state of natural flyers

In Wei Shyy's report [23] a large amount of work has been done by studying the structure of birds in order to conduct the MAV wing design. In his study a scale factor of wing span with body mass is given in Fig. 2.2. Relations between characteristic geometry and flapping motion are obtained by summarizing the performance data of fliers. The aerodynamic forces and power required under different flapping motions are also investigated.

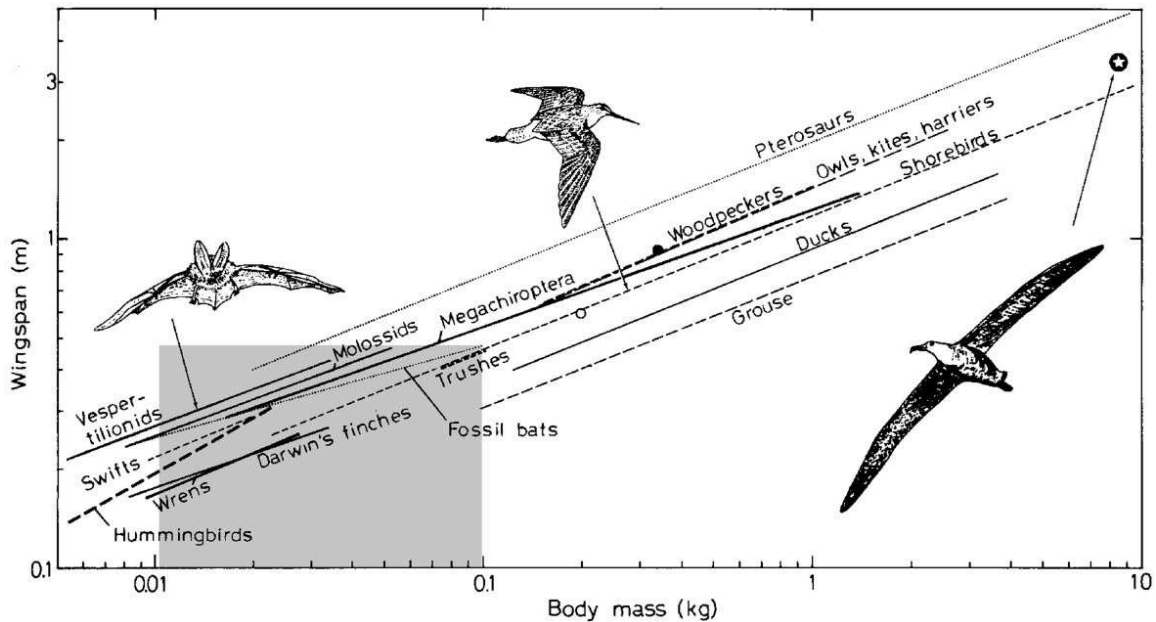


Figure 2.2 Wing span versus body mass

### ***2.1.4 Flapping Wing Structural Modelling***

By simulating insect flight several flapping wing design cases have been done in recent years [17], [24-28]. By employing new techniques and advanced materials the wing mass can be kept rather low and at the same time strong enough. The flapping wing models are mostly micro air vehicles by simulating insect flyers with limited wing span of 150mm. In the current design of MAV the system is composed of an electric motor, a transmission system, and two wings. Powered by the electric battery plunging motion is achieved to generate lift and propelling force in low speed. In the last several years micro air vehicles have been well developed in flying performance and power transmission. However there had been no successful large flapping wing ornithopter available until 2003 when Sandra Mau [29] first built a large ornithopter with one pilot in Canada. For the large scale wing the major problem is that the wing can not provide enough lift and thrust even with large plunging amplitude and steady sustainable flight has never been achieved. In his work a unique wing was designed for the tests. From the tests, some interesting results were found. Increasing the spar torsional stiffness would increase both lift and thrust. The effect of structural stiffness is rather significant for large flapping wing aircraft.

### ***2.1.5 Aeroelastic Effect on Flapping Wing***

Subject to the unsteady aerodynamic forces acting on the flapping wing the deformation of the wing leads to another phenomenon of aeroelasticity. In S.A. Combe's paper [30] the aeroelastic effect of the insect wings was investigated. It indicated that the dynamic, three-dimensional shape of flapping insect wings may influence many aspects of flight performance. Finite element model was developed to compare with the measured displacement along the wing in response to a point force. The results suggest that the sharply declining flexural stiffness measured in real wings helps maintain rigidity near the wing base, while localizing bending to the tip and trailing edge, which are regions of particular importance in controlling aerodynamic force production. Experimental work was carried out by Pin Wu [31] to study the aeroelasticity of flapping wing MAVs. Six pairs of wings with varying elastic properties are tested for thrust measurement. The aim of the investigation was to obtain useful guidelines for future flapping wing designs.



### **2.1.6 Experimental Studies on Flapping Wings**

To validate computational results experimental work needs to be carried out in the wind tunnel or water tunnel. New techniques are employed in the test measurement such as high speed camera and balance. In recent years the experimental work has mainly focused on the testing of vortex passing by the wing [11] [32], lift and thrust due to the wing plunging motion [28] [33], and propulsive efficiency of flapping wing [34]. In Ebrahimi's [35] research a flexible membrane wing was developed with 0.8m wing span. Wind tunnel test were conducted between 6m/s and 12m/s at frequency of 0 to 9Hz. Averaged thrust and lift were measured at 10° angle of attack. The results were used to find optimum performance of the flapping wing vehicle. Two wings with 25cm and 74cm were constructed by Sergey [36] to carry out the study of features of flexible flapping wings used in micro air vehicles. Lift and thrust generated by the flapping motion were measured to conduct the study of the required power and propulsive efficiency. Optimisation of flapping wing kinematics was carried out by Thomson [37] based on experimental results. Vertical force was measured using a load cell subject to a scaled-up hawkmoth wing. The test result was used to optimize the trajectory of a flapping wing mechanism. Jonathan Warkentin [38] designed a tandem wing flapping wing model with span of 0.72m. Lift and thrust were measured through various angles of attack and compared with the results from studies of dragonflies. Many experiments [39-41] have been done to conduct the design and construction of a flapping wing model. Unlike the test of fixed-wing the output results of flapping wing shows a sinusoidal manner due to the simple harmonic wing motion. Therefore the accuracy of the test results requires rather high sensitivity of the test equipment. Most of the experimental work has focused on the aerodynamic force measurement in terms of total force. The inertia force is normally ignored which compromises the accuracy of test results. Not many works have shown the aerodynamic forces in time history with the variation of the wing position. Furthermore, there appears neither serious attempt nor a proper method has been developed to filter the raw data. Noise due to vibration is the main problem in affecting the measured aerodynamic forces. In the wind tunnel test the wing is designed as light as possible with rigid frame covered with flexible film which is considered as flexible wing. However the wing frame is rigid and the skin is fully in tension helped by the

membranes. By using this kind of design it is not feasible to carry out the test for flexible effect because the wing frame is rigid and there is not obvious deformation.

## **2.2 Summary**

From the large amount of literature, the current state-of-the-art of flapping wings in unsteady conditions is studied. By studying and mimicking flyers in nature several ornithoptic concepts have been attempted. Theoretical solutions are developed to predict the aerodynamic forces for flapping wing motions. Based on the theory many prototypes are designed by applying new techniques and advanced materials to optimise the flight performance. Many works are focused on the aerodynamic forces investigation of flapping wing micro air vehicles (MAV), in particular with the investigation of different wing motions. In most recent works that have been done the main method used is simulating wake vorticities to predict aerodynamic forces in low speed and high oscillatory frequencies. The method requires large amount of numerical calculations and complicated test condition to validate.

The objective of this project is to investigate the aerodynamic and structural effects of flapping wings and develop a plausible large scale ornithopter design. However the main thrust of this project is not to focus on the aerodynamic forces prediction. Analytical method is employed in the initial stage of the force calculations such as Theodorsen's theory. Wing planform is designed by studying the existing design cases and natural flyers. Experiment will be carried out in the wind tunnel subject to low air flow speeds and low frequencies as a means of validating the computed results.

### 3 Methodology

The research plan and its scientific approaches are represented in this chapter. The aim of this thesis is to develop a practical design of human-controlled ornithopter. The design method is shown in Fig. 3.1

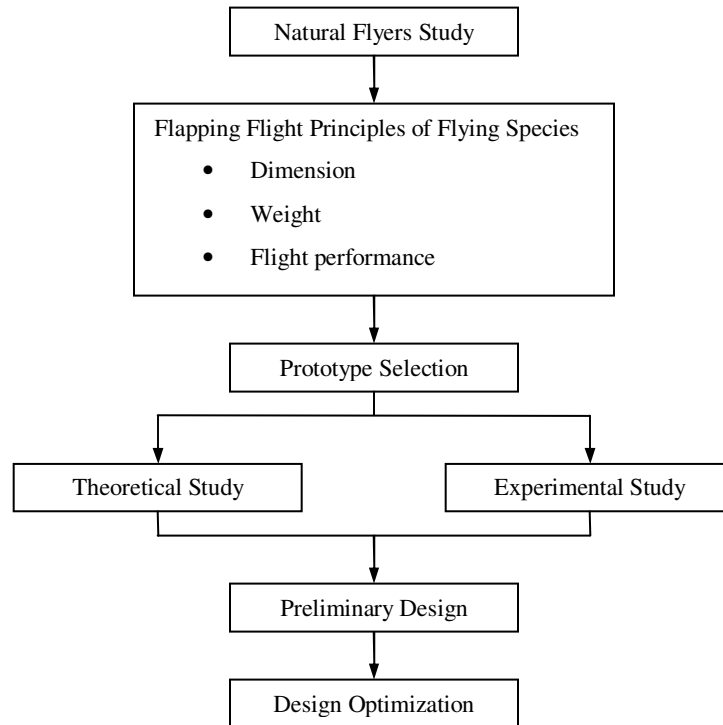


Figure 3.1 Research plan of ornithopter design

In order to design such an aircraft that flies by flapping its wing the fundamental principles of flapping flight need to be studied first aerodynamically and biologically. By studying the aerodynamic flights of natural flyers trends can be found of the flapping performance in terms of characteristic dimensions of the flying species. By comparing existing man-made aircraft the design profile is decided in terms of weight, scale, and flight conditions. Several types of aircraft are assessed in order to find a suitable baseline ornithopter design prototype. Detailed studies of flapping wing aerodynamic are carried out by means of theoretical methods and wind tunnel measurements in order to provide useful data for ornithopter design and optimisation. The preliminary design is carried out

based on the prototype specifications. Validations and modifications of the design are based on theoretical and experimental investigations.

### 3.1 Parametric Study of Flying Species

An ornithopter is defined as a heavier-than-air craft designed to be propelled through the air by flapping its wings. An effective ornithopter must have wings capable of generating both thrust, the force that propels the craft forward, and lift, the force perpendicular to the direction of flight that keeps the craft airborne. These forces must be strong enough to counter the effects of drag and the weight of the craft. A good understanding of how these aerodynamic lift and propulsive forces can be achieved simultaneously by flapping wings is essential for the design and construction of such an aircraft. To this end flying species of the natural world will be carefully studied.

In studying of birds, it is very helpful to assess the effect of different parameters, such as wing area, wing span, cruising speed, body weight, and wing loading. Tennekes [1] presents a diagram of the relationship between weight and wing loading of several birds as illustrated in Fig. 3.1. A proportional scale relationship between weight and wing loading of most seabirds is given by

$$\frac{W}{S} = c \times (W)^{1/3} \quad (3.1)$$

where  $W$  is the body weight,  $S$  is wing area and  $c$  is a constant.

For the seabirds in Fig. 3.2  $c$  has a value of about  $25\text{N}^{2/3}/\text{m}^2$  so at a weight of 1N, the wing loading  $W/S$  is  $25\text{N}/\text{m}^2$ . A smaller wing loading means the bird can fly more slowly and be more maneuverable.

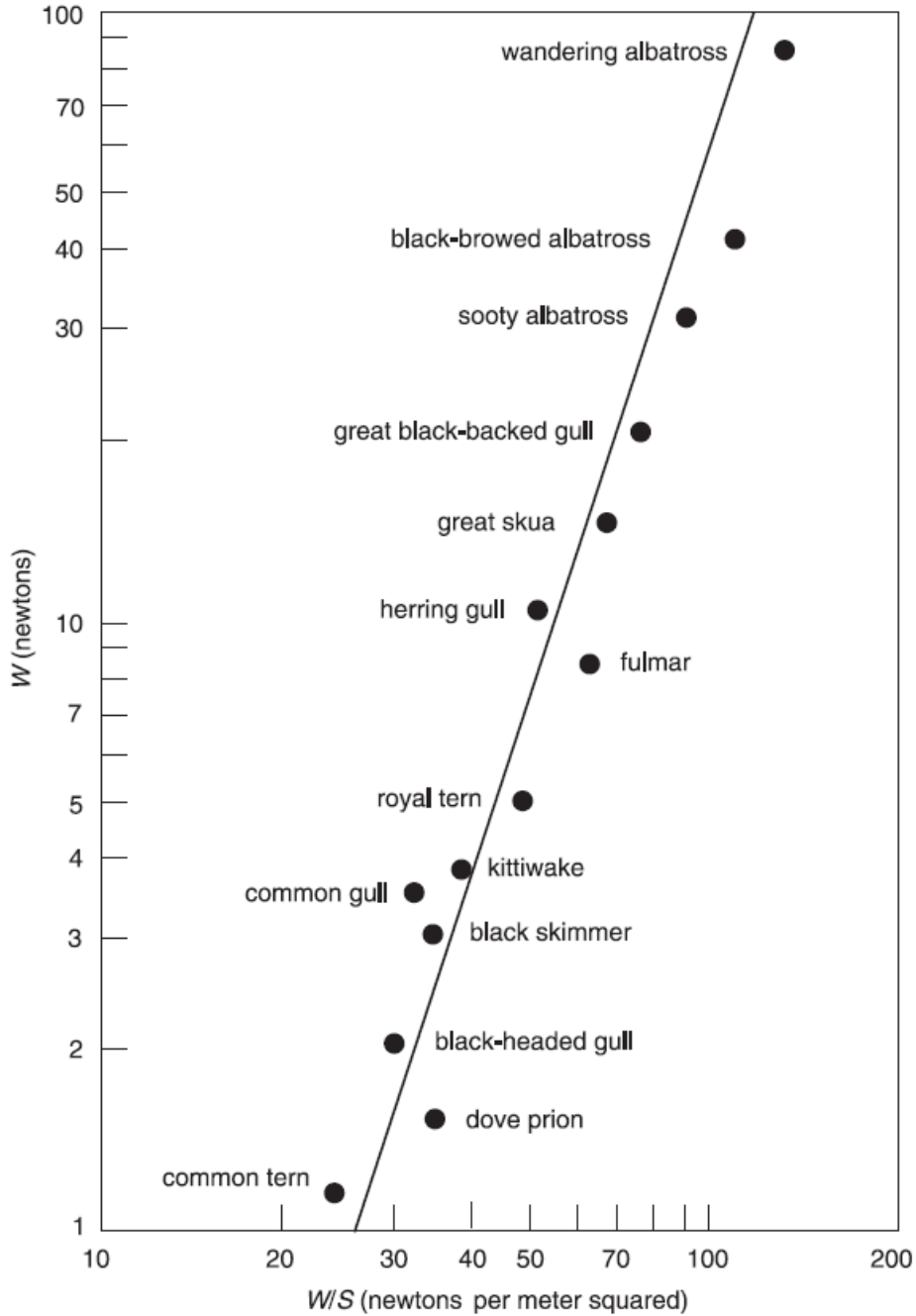


Figure 3.2 The relation between weight and wing loading for some seabirds[1]

Due to the geometrical similarity of birds recent studies have been attempted to find relations between parameters connected to bird flight and some of these are given in Table 3.1. However the equations do not always give correct predictions as stated in Greenewalt's report [42] because birds differ widely in body shapes and size. In

particular it has been found that in many cases the relation between wing loading and mass increases slower than that indicated in Table 3.1.

Animal group	Wing span (m)	Wing area (m <sup>2</sup> )	Wing loading (N/m <sup>2</sup> )	Aspect ratio
All birds except humming-birds	$1.17M^{0.39}$	$0.16M^{0.72}$	$62.2M^{0.28}$	$8.56M^{0.06}$
Humming-birds	$2.24M^{0.53}$	$0.69M^{1.04}$	$14.3M^{0.04}$	$7.28M^{0.02}$

Table 3.1 Power functions of wing dimensions and flight parameters against body mass  $M$

By flapping their wings the flying species are able to maintain airborne in low speed because of their low weight and therefore low wing loading. The main function of the wing is to transmit a force to external environment during flight. For flapping wings flyers, the flapping frequency turns out to be an important parameter in both lift and thrust generation and therefore against body mass. Norberg [43] summarized the various trends of wing beat frequency against body mass of a wide range of natural flyers as shown in Fig. 3.3. For hummingbirds the trend clearly locates in a region of high flapping frequency and light weight. With an increasing body mass the wing beat frequency is reducing significantly. The trends exposed by these researches are that larger animals tend to oscillate their wings at lower frequencies than smaller ones. For all birds an estimation of wing beat frequency related to body mass is given by

$$f = 3.87M^{-0.33} \quad (3.2)$$

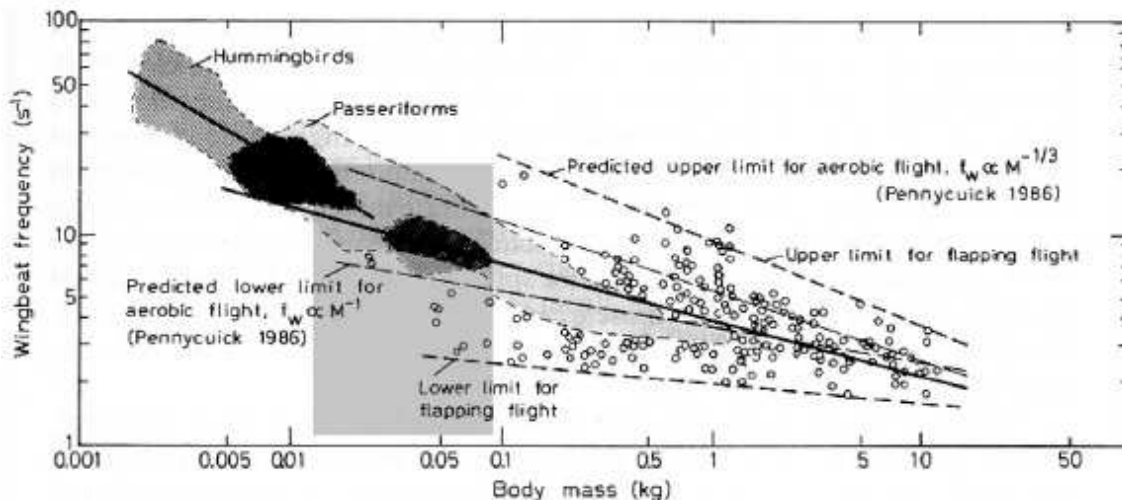


Figure 3.3 Wing beat frequency in birds [43]

### 3.2 How Birds Fly

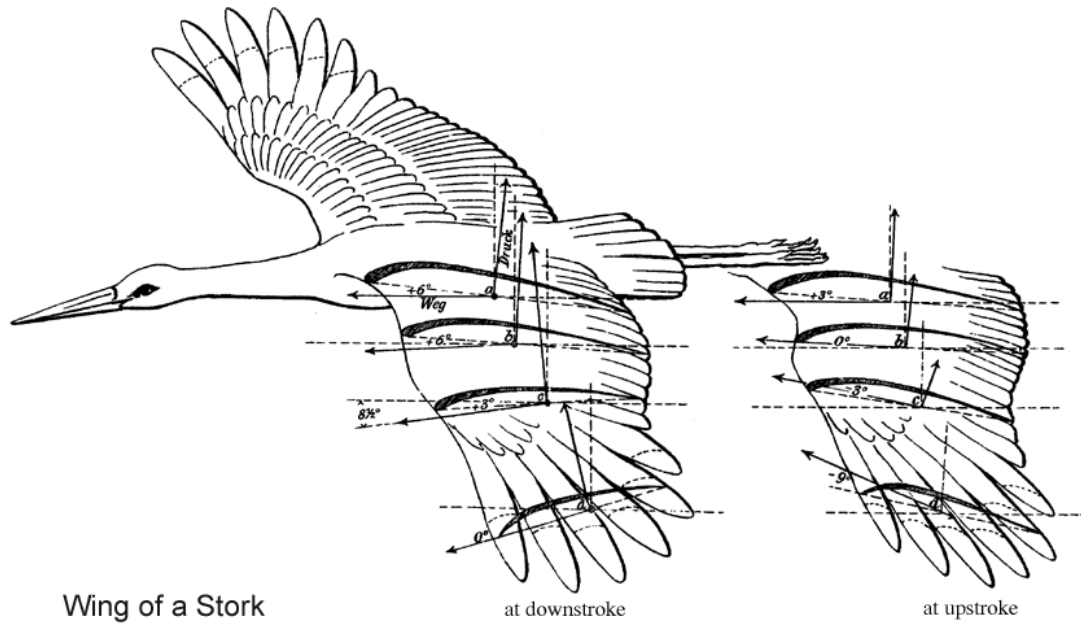
The mechanics and aerodynamics of bird flight have intrigued people for many centuries. Birds have many physical features that work together to enable them to fly efficiently such as light weight, smooth feathers, enlarged breastbone, light bones, rigid skeleton, and a streamline body. Above all these advantages the bird possesses the most important of its body's component is the wing. The shape of a bird's wing is critical for producing lift and its curvature allows the air to move faster over the top surface relative to the lower. Also the angle of the wing deflects air downwards, causing a reaction force in the opposite direction and therefore creating lift.

The performance of bird flight is studied in gliding, soaring and flapping. When a bird is gliding, it doesn't have to do any work. The wings are spread out to the side of the body but do not flap, maintaining at a slight angle to generate lift. The bird has to dive slightly to maintain forward speed. Soaring flight is a special kind of glide in which the bird flies in a rising column of air which is so called a thermal. Due to this rising air the bird can maintain or even gain height without flapping its wings. Therefore the gliding and soaring can be seen as steady flight without any movement of wings. In flapping the bird's wing flaps with an up-and-down motion. The entire wing span has to flap at the root with a right stroke angle in order to generate sufficient lift and thrust. The flapping

flight is seen as one of unsteady aerodynamic case studies and will be discussed in the following section.

In cruising condition of the level flight birds are able to control the speed by twisting their wings. During flapping a cycle of the wing oscillation consists of upstroke and downstroke. At the wing upstroke the air flow hits the wing from above and at downstroke from bottom. The majority of the overall positive lift is generated in downstroke motion and negative lift is produced in upstroke motion. However, the negative lift generated in upstroke can be minimized by adapting the chordwise curvature and spanwise twist of the wing so that the bird can still maintain flight efficiently and effortlessly. By properly varying the angle of attack of the wing along its span the bird can produce thrust or drag which is the component of the total force in horizontal direction in order to control the cruising speed. As shown in Fig. 3.4 the wing is twisted anticlockwise in downstroke to generate forward force which comes from horizontal component of the total force. In upstroke the overall lift is still positive due to the camber of the wing which allows the bird to sustain cruising flight. By studying the wing motion along spanwise the outboard of the wing contributes to the lift most in flapping. On the other hand, steady lift generation comes from the wing camber more effectively formed inboard of the wing.





Otto Lilienthal: Der Vogelflug als Grundlage der Fliegekunst,  
Publishing house R. Gärtnner, Berlin 1889, reprinting, publishing company Oldenbourg Munich 1943

Figure 3.4 Wing twist over a stroke [44]

For birds, there are mainly two ways of flying: ‘flying with thrust’ and ‘flying with lift’. When flying purely with thrust as shown in Fig. 3.5 (a) in take-off mode, the weight of the bird will only be balanced by the upward directed thrust force. Let's assume the bird has already taken off from the ground and the angle between the stroke plane of the wing and the perpendicular of the flight path line is roughly less than  $60^\circ$ . Flapping frequency and wing twisting are very high while the horizontal motion of the bird has started. Initially the weight is balanced very much like that of a helicopter by its lift but here the thrust is largely used to counteract the weight instead. As shown in Fig. 3.5 (b) in cruising flight the bird's body is now streamlined in the direction of flight and the lift alone generated by the wing is sufficient to carry the weight. The whole thrust is now directed straight forward and is substantially decreased together with minimum wing twisting. The bird is now flying completely with the lift which is very energy-efficient.

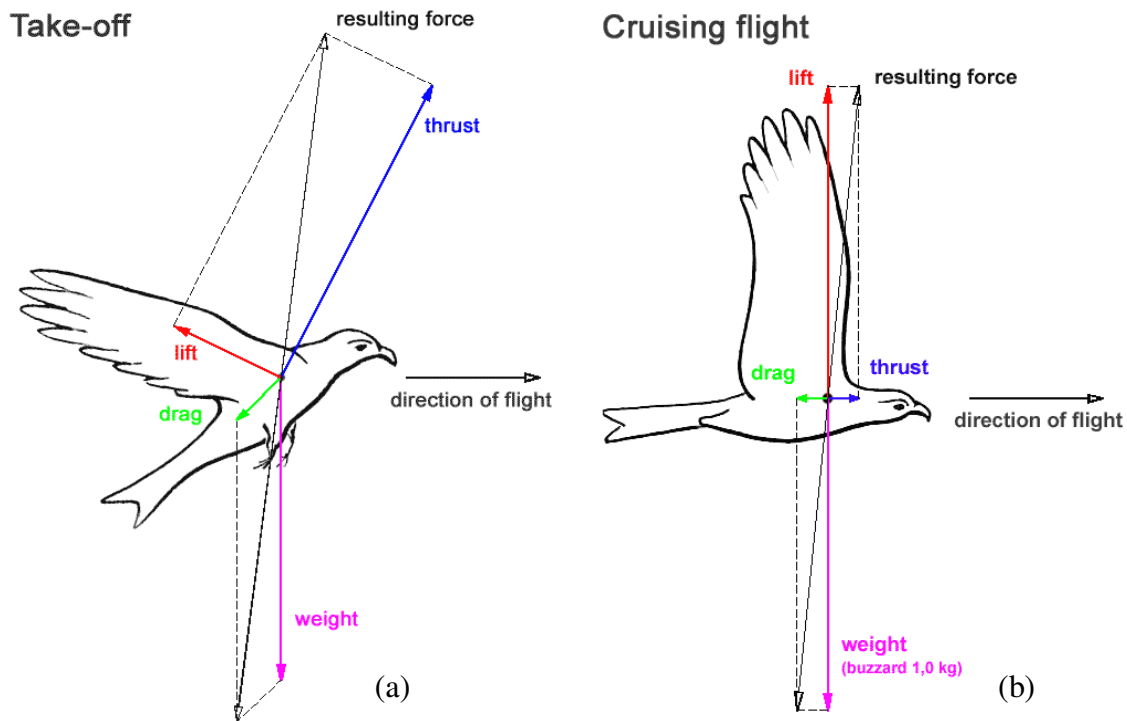


Figure 3.5 Force vector on the take-off mode and cruising mode [44]

But in practice, the transition to flying with lift is not as easy as it appears at first. At first, lift and thrust must have achieved relatively high values at the same time in spite of a small flight velocity. However, changing the way of flying is possible for birds with the complicated wing muscle system which allows bird to achieve different combined motions with very light weight.

### 3.3 Prototype Selection

By understanding the performance of bird flights, the knowledge and understanding of many of the physical features associated with accomplished flying birds can be used to conduct the ornithopter design. One of the requirements for heavier-than-air aircraft is a structure that combines strength with light weight. Different flight abilities are achieved by birds which are made possible by a system of complicated bones and joints forming the wing structure, including the wing trailing edge flap, rotation of the wing chord, large

stroke angle, wing sweep, and asymmetrical stroke over a cycle. By imitating the bird flight two ornithopter design cases are studied which are both built by DeLaurier [6].

### 3.3.1 Case Study of Ornithopter

The UTIAS Ornithopter No.1 was an ornithopter built in Canada in 1990s. It took off under its own power, assisted by a turbine jet engine. The wing span is 12.56m and the aircraft's gross weight is 322kg. With one pilot the aircraft was able to achieve 82km/h cruising speed. The model is constructed based on traditional concept of very light aircraft (VLA) with a tapered wing, slim fuselage, tails and landing gear. In the runway test the ornithopter was able to achieve the cruising speed with 1Hz flapping frequency. The aircraft lifted off and stayed off of the runway for a sustained flight of 14 seconds. The height was above one metre and the distance covered was about a third of a kilometre.

The Snowbird is a human-powered ornithopter built by DeLaurier's team. The aircraft has a wingspan of 32m and weights 43kg. Assisted by a tow vehicle for take-off from the ground the aircraft was able to sustain both altitude and airspeed for 19.3 seconds, covering a distance of 145m at an average speed of 25.6km/h. As shown in Fig. 1.5 the aircraft is designed as a glider. Wires are linked to the wing tip and driven by the pilot. The main design specifications of these two aircraft are tabulated below.

	UTIAS No.1	UTIAS Snowbird
Weight	322kg	43kg
Span	12.56m	32m
Speed	82km/h	25.6km/h
Pilot	1	1
Power	Gas engine powered	Human muscle powered
Wing Flapping Frequency	1Hz	1Hz
Force translation	Flapping mechanism	Cables

Table 3.2 Design specification comparison of two ornithopters

The design principles of these two models are different from each other. UTIAS ornithopter No.1 employed VLA configuration. With a gasoline engine and a great deal of control system the total weight is rather high (322kg). At 1.0Hz flapping frequency the power is not sufficient to maintain the flight. Another problem of the vehicle is its high wing loading which induced structural failure on the wing trailing edge. The experimental vehicle demonstrates the tremendous challenge to achieve take-off by wing flapping despite assisted by engine power.

The Snowbird is constructed as a glider with a long straight wing and very light weight. The design is only focused on the cruising flight and take-off phase is assisted by a tow vehicle. The aircraft is able to keep a good straight level flight by wing tip flapping. The wing tip is pulled by human power through cables. Obviously the lift generated by wing tip flapping is not sufficient compared with whole-wing flapping. And in cruising the human power is not suitable for long duration flight and flapping frequency is also limited. From this case study it can be concluded that the human controlled ornithopter requires light weight, flapping motion of larger wing area to contribute to lift and thrust generation, and power efficient flight.

### ***3.3.2 Structural Configuration Investigation***

Summarizing the advantages of these two design cases a new design concept can be explored. The design principles of the large scale ornithopter are shown below:

- Light weight
- Root flapping
- Engine powered
- Easy take-off
- Long duration cruising

In the existing man-made aircraft the weight of sailplanes is in rather low compared with other flight vehicles. However due to its long span wing and rigid body the weight is not as light as hang glider. With light frame and flexible wing surface the weight of hang glider can be kept to roughly 20kg which is an ideal prototype for use as possible

ornithopter configuration. The study of bird flight has shown that root flapping gives considerably more lift than tip flapping. Unfortunately the increase in lift can only be achieved at the expense of more drag due to large flapping amplitude at the tip. Therefore an engine is required to generate more power to balance the resistant force at a given speed during the flight. The total weight is increased by adding an engine on the aircraft therefore an even lighter air vehicle is required as a prototype for the ornithopter design. The hang glider is an ideal model to match the weight consideration. The simplicity of the hang glider frame provides more space to locate additional objects and structures such as the engine and driving linkages. In addition the foot-launch action of the hang glider allows easy take-off of the ornithopter. The tapered wing configuration is employed in most of hang glider designs.

By obtaining the knowledge of the bird flight and the existing air vehicle case study a few fundamental parameters are estimated by using the equations in Table 3.1.

$$\text{Wing Span} = 1.17M^{0.39} \quad (3.2)$$

$$\text{Wing Area} = 0.16M^{0.72} \quad (3.3)$$

$$\text{Wing Loading} = 62.2M^{0.28} \quad (3.4)$$

$$\text{Aspect Ratio} = 8.56M^{0.06} \quad (3.5)$$

By assuming the total mass  $M=100$  kg the preliminary design specification of the prototype is given as below:

Wing span	7 m
Wing area	4.4 m <sup>2</sup>
Wing loading	225 N/m <sup>2</sup>
Aspect Ratio	11
Beat frequency	0.8 Hz

Table 3.3 Preliminary design specifications

These design parameters are obtained based on the estimated trends of bird flight and will be used as a guideline for basic ornithopter design study.

### **3.4 Theoretical Study and Validation of Flapping Wing Designs**

To understand the aerodynamic loading action on the flapping wing analytical method will be employed in the early stage of the design. Several methods have been used to predict theoretical unsteady aerodynamic forces such as Theodorsen's theory [45] and Garrick's report [8]. In Theodorsen's theory mathematical equations are developed to compute the unsteady aerodynamic force and moment for the rigid thin flatplate undergoing small simple harmonic oscillations. The method of Garrick, which is an extension of Theodorsen's method, is used to compute the horizontal forces. Based on the forces calculated for two dimensional aerofoil section, the method of DeLaurier is then employed, which takes the wing aspect ratio into account, to calculate overall lift of the flapping wing. Experimental work will be carried out to validate the theoretical force prediction in the low speed wind tunnel T3 located in the Hadley Page Lab at City University. The study is mainly focused on the effect of frequency and speed for both rigid and flexible wings in different oscillatory motions.

### **3.5 Ornithopter Design and Optimization**

The ornithopter design is based on the prototype vehicle. By employing the original frame of the prototype additional parts will be added in order to achieve the flapping motion. Theoretical calculations and experimental validations are carried out the main

design guide to evaluate the aerodynamic performance and structure strength. Finite element method is employed to conduct the structure strength analysis and the aerodynamic load estimation is validated based on the wind tunnel test results. Modifications and optimizations are carried out to improve the structural design and aerodynamic performance.

## 4 Modelling of Oscillatory Aerodynamics using Theodorsen's Function

In this chapter a theoretical calculation of aerodynamic forces for flapping wing motions is provided based on Theodorsen's equation.

Theodorsen's theory [45] gives a mathematical model for calculating the unsteady aerodynamic forces acting on a flat wing section performing infinitely small simple harmonic oscillations in pitch and plunge in an inviscid and incompressible fluid of density  $\rho$  with an undisturbed mean stream velocity  $V_\infty$  as depicted in Fig. 4.1.

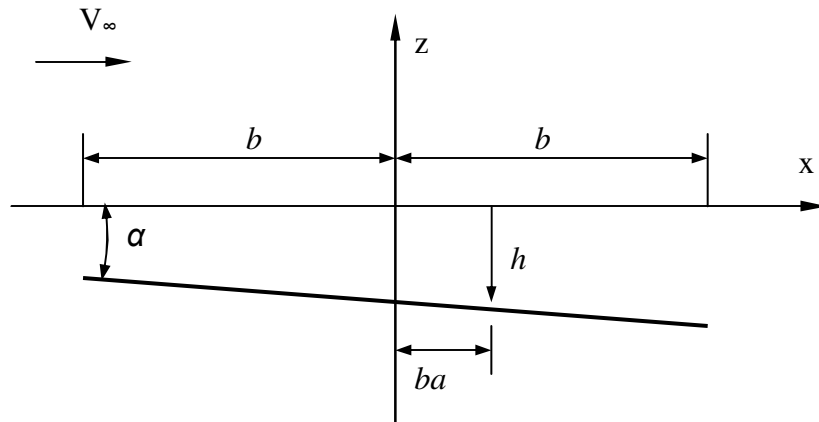


Figure 4.1 Mean line of chord of a rigid aerofoil

where  $h$  is the positive downward displacement and  $\alpha$  is the rotational displacement about the pitch axis  $x = ba$  ( $-1 < a < 1$ ) measured from the mid-chord of the aerofoil. The lift is given by the expression [1]:

$$L = \pi \rho b^2 \left[ \ddot{h} + V_\infty \dot{\alpha} - ba \ddot{\alpha} \right] + 2\pi \rho V_\infty b C(k) \left[ \dot{h} + V_\infty \alpha + b \left( \frac{1}{2} - a \right) \dot{\alpha} \right] \quad (4.1)$$

where for simple harmonic motions of small amplitudes  $h_0$  and  $\alpha_0$  and of frequency  $\omega$



$$\left. \begin{aligned} h &= h_0 e^{i\alpha} \\ \dot{h} &= i\omega h_0 e^{i\alpha} \\ \ddot{h} &= -\omega^2 h_0 e^{i\alpha} \end{aligned} \right\} \begin{aligned} \alpha &= \alpha_0 e^{i\alpha} \\ \dot{\alpha} &= i\omega \alpha_0 e^{i\alpha} \\ \ddot{\alpha} &= -\omega^2 \alpha_0 e^{i\alpha} \end{aligned} \quad (4.2)$$

where the dot indicates the derivative with respect to physical time  $t$  and  $C(k)$  is the complex Theodorsen's circulatory function

$$C(k) = F(k) + iG(k) \quad (4.3)$$

and  $k$  is the reduced frequency

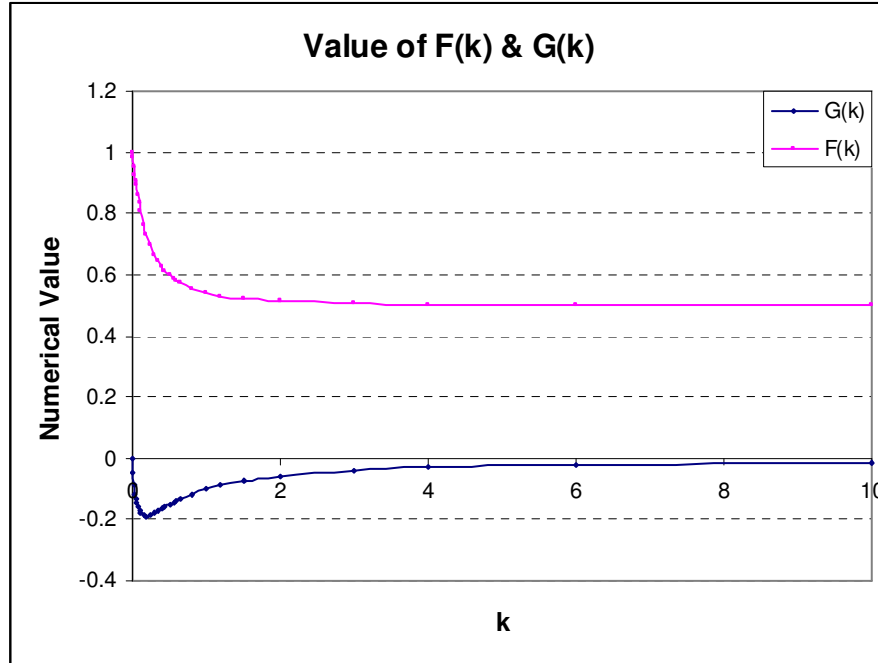
$$k = \frac{\omega b}{V_\infty} \quad (4.4)$$

A good approximation for  $C(k) = F(k) + iG(k)$  is given by [46]

$$C(k) = 1 - \frac{0.165}{1 - \frac{0.0455}{k}i} - \frac{0.335}{1 - \frac{0.3}{k}i} \quad \text{when } k < 0.5 \quad (4.5)$$

$$C(k) = 1 - \frac{0.165}{1 - \frac{0.041}{k}i} - \frac{0.335}{1 - \frac{0.32}{k}i} \quad \text{when } k > 0.5 \quad (4.6)$$

and its real and imaginary parts against  $k$  are shown graphically in Fig. 4.2.


 Figure 4.2 Value of  $G(k)$  and  $F(k)$  vs  $k$ 

The plunging or heaving motion can be considered as having an equivalent angle of attack for  $\dot{h}(t)$  as

$$\alpha = \frac{\dot{h}}{V_\infty} \quad (4.7)$$

A simplified approximation to Eq. (4.1) is the so-called quasi-steady-state assumption, which neglects the influence of the wake vortices on the flow. This is equivalent to replacing  $C(k)$  with the value 1 when  $k$  approaches to zero.

$$L_{QS} = \pi\rho b^2 \left[ \ddot{h} + V_\infty \dot{\alpha} - ba\ddot{\alpha} \right] + 2\pi\rho V_\infty b \left[ \dot{h} + V_\infty \alpha + b \left( \frac{1}{2} - a \right) \dot{\alpha} \right] \quad (4.8)$$

Another simplification is in common use for the approximation of very slow oscillatory motions where the frequency  $\omega$  is approaching zero. In the case of the  $h$  and  $\alpha$  motions described in Fig. 4.1, this procedure would lead to a steady assumption which is written

$$L \cong 2\pi\rho V_\infty b[\dot{h} + V_\infty \alpha] \quad (4.9)$$

This approximation assumes that all aerodynamic loads can be calculated from steady-state formula and the angle of attack  $\alpha$  is replaced by the instantaneous inclination between the resultant velocity vector and the chordline.

## 4.1 Two-dimensional Aerodynamic Forces on Flapping Aerofoil

Based on Theodorsen's theory, two-dimensional aerodynamic forces on a rigid thin aerofoil are calculated subject to several flapping motions: heaving, pitching and heaving with pitching combined motions. Inertia forces due to the aerofoil motions are also investigated.

### 4.1.1 Study of Theodorsen's Lift Function

In this section equations are derived from Theodorsen's function subject to pure heaving, pure pitching, and heaving and pitching combined simple harmonic oscillations. According to Theodorsen's notation used as depicted in Fig. 4.1 the aerofoil begins its motion from the minimum position in heave and maximum pitch angle leading edge up.

#### 4.1.1.1 Pure Heaving Case

From Eq. (4.1) a simplified equation of sectional lift per unit span for the pure heaving case can be written as

$$L = \pi\rho b^2 \ddot{h} + 2\pi\rho V_\infty bC(k)\dot{h} \quad (4.10)$$

Substituting Eq. (4.2) into Eq. (4.10) for simple harmonic heaving motion

$$\begin{aligned} L &= [-\pi\rho b^2 \omega^2 h_0 + i \cdot 2\pi\rho V_\infty bC(k)\omega h_0] \cdot e^{i\omega t} \\ &= (L_R + i \cdot L_I) e^{i\omega t} = L_0 e^{i(\omega t + \varphi)} \end{aligned} \quad (4.11)$$

where  $L_0 = \sqrt{L_R^2 + L_I^2}$  and  $\varphi$  is the phase shift between displacements  $h$  and lift  $L$ , given by

$$\varphi = \tan^{-1}\left(\frac{L_I}{L_R}\right) \quad (4.12)$$

Substituting Eq.(4.3) into Eq.(4.11) the real part  $L_R$  and imaginary part  $L_I$  of the oscillatory lift can be written as

$$L_R = -\pi\rho b^2 \omega^2 h_0 - G(k) \cdot [2\pi\rho V_\infty b \omega h_0] \quad (4.13)$$

$$L_I = 2\pi\rho V_\infty b \omega h_0 \cdot F(k) \quad (4.14)$$

Eq. (4.13) and Eq. (4.14) can be written in terms of  $k$  only as

$$L_R = -\pi\rho V_\infty^2 h_0 [k^2 + 2k \cdot G(k)] \quad (4.15)$$

$$L_I = 2\pi\rho V_\infty^2 h_0 [k \cdot F(k)] \quad (4.16)$$

The sectional lift amplitude and phase shift are given by

$$L_0 = \pi\rho V_\infty^2 h_0 k \sqrt{\{k + 2G(k)\}^2 + \{2F(k)\}^2} \quad (4.17)$$

$$\varphi = \tan^{-1}\left(-\frac{2F(k)}{k + 2G(k)}\right) \quad (4.18)$$

Therefore at a given value of  $k$  the sectional lift amplitude per unit span of a rigid aerofoil in heaving depends on the flight speed  $V_\infty$  and heaving amplitude  $h_0$ .

#### 4.1.1.2 Pure Pitching Case

Consider the aerofoil pitches about the mid-chord when  $a = 0$  the sectional lift expression is given by

$$L = \pi\rho b^2 \cdot V_\infty \dot{\alpha} + 2\pi\rho V_\infty b \cdot C(k) \left[ V_\infty \alpha + \frac{1}{2} b \dot{\alpha} \right] \quad (4.19)$$

$$= (L_R + i \cdot L_I) e^{i\omega t} = L_0 e^{i(\omega t + \varphi)}$$

where  $\varphi$  is now the phase shift between the pitch angle  $\alpha$  and lift  $L$ , given by

$$\varphi = \tan^{-1} \left( \frac{L_I}{L_R} \right) \quad (4.20)$$

Substituting Eq. (4.2) and Eq. (4.3) into Eq. (4.18) the real part  $L_R$  and imaginary part  $L_I$  of the oscillatory lift are

$$L_R = -\pi\rho V_\infty^2 b^2 \omega \alpha_0 \cdot G(k) + 2\pi\rho V_\infty^2 b \alpha_0 \cdot F(k) \quad (4.21)$$

$$L_I = \pi\rho b^2 V_\infty \omega \alpha_0 + \pi\rho V_\infty^2 b^2 \omega \alpha_0 \cdot F(k) + 2\pi\rho V_\infty^2 b \alpha_0 \cdot G(k) \quad (4.22)$$

The sectional lift amplitude is given by

$$L_0 = \sqrt{L_R^2 + L_I^2} \quad (4.23)$$

As a function of reduced frequency Eq. (4.21) and Eq. (4.22) can be expressed as

$$L_R = -\pi\rho V_\infty^2 b \alpha_0 [k \cdot G(k) - 2F(k)] \quad (4.24)$$

$$L_I = \pi\rho V_\infty^2 b \alpha_0 [k + k \cdot F(k) + 2G(k)] \quad (4.25)$$

The sectional lift amplitude and phase shift are given by

$$L_0 = \pi \rho V_\infty^2 b \alpha_0 \sqrt{\{k \cdot G(k) - 2F(k)\}^2 + \{k + k \cdot F(k) + 2G(k)\}^2} \quad (4.26)$$

$$\varphi = \tan^{-1} \left( -\frac{k + k \cdot F(k) + 2G(k)}{k \cdot G(k) - 2F(k)} \right) \quad (4.27)$$

Therefore at a given value of  $k$  the sectional lift amplitude per unit span of a rigid aerofoil in pitching depends on the flight speed  $V_\infty$  and pitching angle  $\alpha_0$ .

#### 4.1.2 Study of Theodorsen's Lift Function in Time History

According to Theodorsen's function in Eq. (4.1) the sectional lift of thin aerofoil under simple harmonic oscillation in time history are studied. By considering only real part of the aerofoil motion as given in Eq. (4.2), namely

$$\left. \begin{aligned} h &= h_0 \cos \omega t \\ \dot{h} &= -\omega h_0 \sin \omega t \\ \ddot{h} &= -\omega^2 h_0 \cos \omega t \end{aligned} \right\} \quad \left. \begin{aligned} \alpha &= \alpha_0 \cos \omega t \\ \dot{\alpha} &= -\omega \alpha_0 \sin \omega t \\ \ddot{\alpha} &= -\omega^2 \alpha_0 \cos \omega t \end{aligned} \right\} \quad (4.28)$$

Hence the sectional lift is given by

$$L = L_0 \cos(\omega t + \varphi) \quad (4.29)$$

where  $L_0$  is the lift amplitude under simple harmonic oscillation and  $\varphi$  is phase shift between the aerofoil motion and the sinusoidal lift  $L$ .

#### 4.1.2.1 Study of Heaving Motion in Time History

The sectional lift of pure heaving as a function of time can be represented by the lift amplitude  $L_0$  and the phase shift  $\varphi$  between the lift and displacement, according to Eq. (4.29).

$$L_H = L_0 \cos(\omega t + \varphi) \quad (4.30)$$

Refer to Eq. (4.17) and Eq. (4.18) the lift amplitude  $L_0$  and the phase shift  $\varphi$  are given by

$$\left. \begin{aligned} L_0 &= \pi \rho V_\infty^2 h_0 k \sqrt{\{k + 2G(k)\}^2 + \{2F(k)\}^2} \\ \varphi &= \tan^{-1} \left( -\frac{2F(k)}{k + 2G(k)} \right) \end{aligned} \right\} \quad (4.31)$$

The aerofoil displacement  $z$  in time history is given by

$$z = -h = -h_0 \cos \omega t \quad (4.32)$$

#### 4.1.2.2 Study of Pitching Motion in Time History

In pure pitching assuming the aerofoil rotates about mid-chord the sinusoidal sectional lift in time history is obtained by considering real part refer to Eq. (4.19) is given by

$$L_p = L_0 \cos(\omega t + \varphi) \quad (4.33)$$

Refer to Eq. (4.26) and Eq. (4.27) the lift amplitude  $L_0$  and the phase shift  $\varphi$  are given by

$$\left. \begin{aligned} L_0 &= \pi \rho V_\infty^2 b \alpha_0 \sqrt{\{kG(k) - 2F(k)\}^2 + \{k + kF(k) + 2G(k)\}^2} \\ \varphi &= \tan^{-1} \left( -\frac{k + kF(k) + 2G(k)}{kG(k) - 2F(k)} \right) \end{aligned} \right\} \quad (4.34)$$

The angle displacement is represented as

$$\alpha = \alpha_0 \cos \omega t \quad (4.35)$$

#### 4.1.2.3 Study of Heaving and Pitching Combined Motion in Time History

The lift amplitude of combined motion depends on the single motion of heaving and pitching and the phase shift between two individual motions in the same time history. Define  $\varphi_C$  as the phase shift between heaving and pitching the aerofoil oscillation in combined motion is given by

$$\left. \begin{aligned} h &= h_0 \cos \omega t \\ \alpha &= \alpha_0 \cos(\omega t + \varphi_C) \end{aligned} \right\} \quad (4.36)$$

The sectional lift of combined motion  $L_C$  is the combination of the lift due to heaving  $L_H$  and pitching  $L_P$  in the same time history

$$L_C = L_H + L_P \quad (4.37)$$

The total lift time history of the combined motion varies with variation of the phase shift  $\varphi_C$  between the heave and pitch motions. In the same time history different combination of the heaving and pitching results in different amount of the total lift.



### 4.1.3 Inertia Study of Flapping Wing

The inertia due to the mass and acceleration is given by

$$I = -m\ddot{z} \quad (4.38)$$

where  $z$  is the wing displacement and positive upward

Refer to Eq. (4.2)  $h$  is defined as vertical displacement and positive down as shown in Fig. 4.3. Therefore the relationship between  $h$  and  $z$  is given by

$$z = -h \quad (4.39)$$

Hence the inertia can be written as

$$I = m\ddot{h} = -m\omega^2 h_0 \cdot e^{i\alpha} \quad (4.40)$$

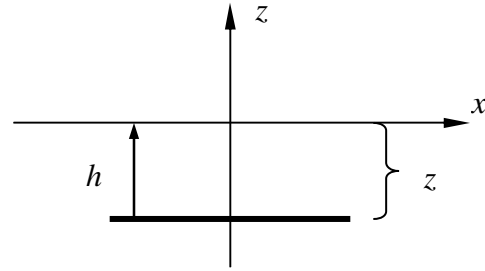


Figure 4.3 Aerofoil displacement

where  $h_0$  is heaving amplitude

By taking the real part of Eq. (4.40) the inertia force of the sectional aerofoil in time history is given by

$$I = -m\omega^2 h_0 \cdot \cos \alpha \quad (4.41)$$

### 4.1.4 Propulsive Force and Efficiency of Flapping Aerofoil

In this section the propulsive force of flapping aerofoil is studied. As shown in Fig. 4.4 the thrust is generated due to the total force projection in horizontal direction in both downstroke and upstroke.

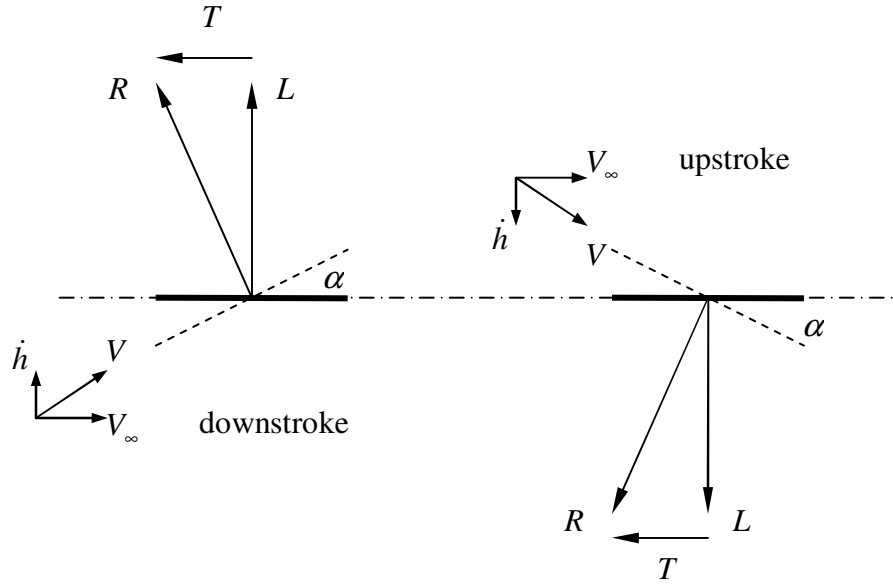


Figure 4.4 Thrust generation

The wing flapping motion can be split into two distinct phases within a cycle of its oscillation which are downstroke and upstroke. Due to the flapping movement  $h$  of the aerofoil vertical velocity  $\dot{h}$  is induced. Combined with the incoming flow  $V_\infty$  the resultant velocity  $V$  is generated with an angle of attack  $\alpha$  to the wing chord. And this angle is given by

$$\alpha = \frac{\dot{h}}{V_\infty} = \frac{i\omega h}{V_\infty} \cdot e^{i\alpha t} \quad (4.42)$$

Hence the thrust is given by

$$T = L \cdot \alpha \quad (4.43)$$

Based on Theodorsen's theory Garrick [8] provided a method for computing the lift, thrust and power efficiency due to unsteady thin aerofoil flapping motion. Formulas are given for the propelling or drag force experienced in a uniform airstream by an aerofoil or an aerofoil-aileron combination, oscillating in any of the following three degrees of

freedom: vertical flapping, torsional oscillations about a fixed axis parallel to the span, and angular oscillations of the aileron about a hinge. Simplifying Garrick's equation by considering heaving and pitching at mid-chord the sectional thrust  $T$  per unit span of a rigid thin aerofoil is given by

$$T = \pi\rho S^2 + \alpha L \quad (4.44)$$

where  $\rho$  is the density of the fluid and  $S$  is given by

$$S = \frac{\sqrt{2}}{2} [2C(k)(\dot{h} + V_\infty\alpha) - b\dot{\alpha}] \quad (4.45)$$

where  $S$  is related to the leading edge vorticity referred to in Garrick's report [3]

The propulsive efficiency  $\eta$  is given by

$$\eta = \frac{TV_\infty}{\overline{W}} \quad (4.46)$$

where  $TV_\infty$  is the energy of propulsion and  $\overline{W}$  is the average work done per unit time

By considering a special case of pure heaving the thrust  $T$  and propulsive efficiency are given by

$$T = \pi\rho b\omega^2 h_0^2 [F(k)^2 + G(k)^2] \quad (4.47)$$

$$\eta = \frac{TV_\infty}{\overline{W}} = \frac{F(k)^2 + G(k)^2}{F(k)^2} \quad (4.48)$$

For pitching oscillations about pitch axis  $a$  refer to Fig. 4.1 the thrust is given by

$$T = \pi \rho b \omega^2 b^2 \alpha_0^2 \left\{ (F(k)^2 + G(k)^2) \left[ \frac{1}{k^2} + \left( \frac{1}{2} - a \right)^2 \right] + \frac{1}{2} \left( \frac{1}{2} - a \right) - \frac{F(k)}{k^2} - \left( \frac{1}{2} - a \right) \frac{G(k)}{k} \right\} \quad (4.49)$$

and the energy formula is given by

$$\bar{W} = \bar{E} + TV_\infty \quad (4.50)$$

where  $\bar{E}$  represents the average increase in kinetic energy in unit time in the vortex wake

Eq. (4.50) can be rearranged as

$$\frac{\bar{E}}{\bar{W}} = 1 - \frac{TV_\infty}{\bar{W}} \quad (4.51)$$

Therefore  $\bar{E}/\bar{W}$  represents some measure of the propulsive inefficiency of the aerofoil pitching about pitch axis  $a$  where the value decreases as propulsive efficiency increases.

## 4.2 3-D Aerodynamic Force Study of Flapping Wing

In the study of three dimensional aerodynamic forces of flapping wings, the wing behaves as either whole-wing heaving or root flapping. In whole-wing heaving motion, each of the strips along wing span moves identically through the same heaving amplitude. And in root flapping the wing rotates at the root with maximum flapping amplitude at the tip and zero or minimum amplitude at root.

### 4.2.1 Strip Theory of 3-D Aerodynamic Force

In this section theoretical study of aerodynamic force acting on the wing is studied subject to two different wing motions which are the whole-wing heaving motion and root

flapping motion. In the whole-wing heaving the wing moves with constant amplitude through wing span. As shown in Fig. 4.5 the strip with uniform width  $dy$  heaves with amplitude of  $h_0$ .

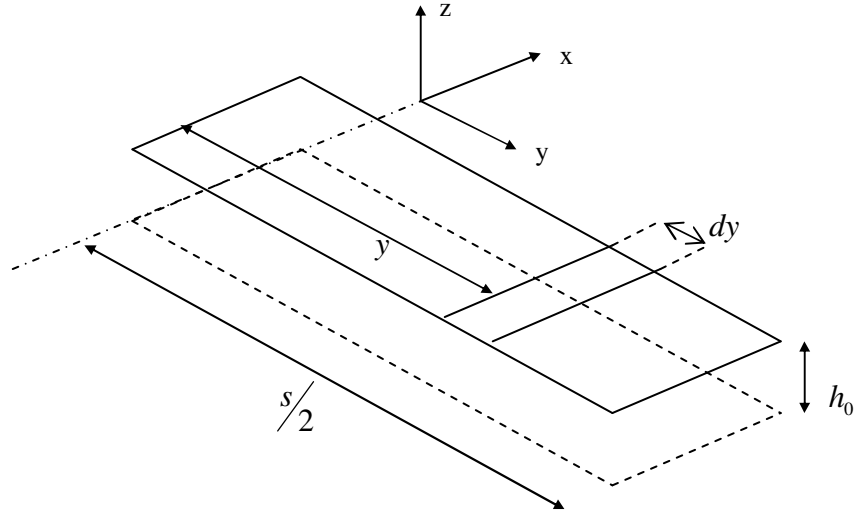


Figure 4.5 Whole-wing heaving

Following the strip theory [47] with elliptic lift distribution the lift per unit span  $L(y)$  at the spanwise position  $y$  measured from root is given by

$$L(y) = L_0 \sqrt{1 - \left(\frac{y}{s/2}\right)^2} \quad (4.52)$$

where  $L_0$  is the amplitude of sectional lift given in Eq. (4.10)

The total lift  $AF$  acting on the semi-wing of uniform chord is thus given by

$$AF = \int_0^{s/2} L(y) \cdot dy = L_0 \cdot \left(\frac{\pi}{8} s\right) \quad (4.53)$$

where  $s$  is wing span

The inertia due to semi-wing mass is given by

$$I = \frac{1}{2} m \ddot{h} \quad (4.54)$$

In root flapping the sectional lift of strip is linear proportional to heaving amplitude  $h_s$ . As shown in Fig. 4.6 the strip with width of  $dy$  heaves with amplitude of  $h_s$ . The tip heaving amplitude is  $h_0$ .

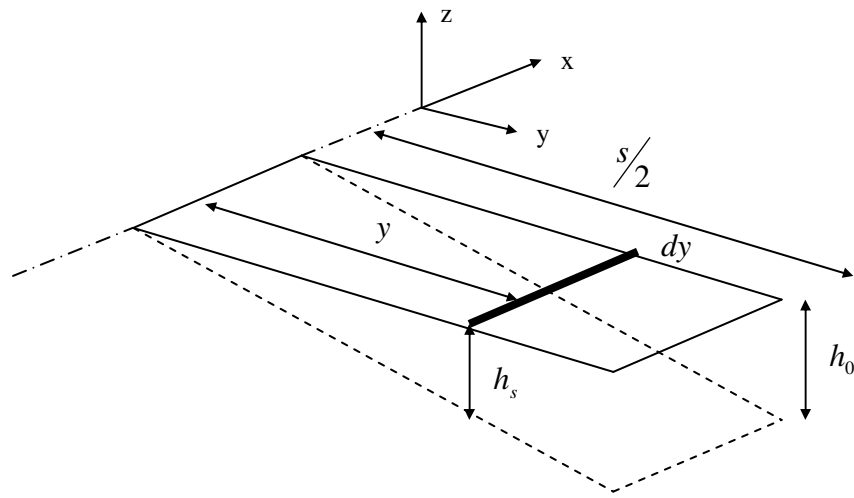


Figure 4.6 Root flapping

The heaving amplitude of strip is given by

$$h_s(y) = h_0 \frac{y}{s/2} \quad (4.55)$$

The strip at wing tip with maximum heaving amplitude is  $L_m$  given in Eq. (4.10) the sectional lift of strip of semi-span in root flapping motion is given by

$$L(y) = L_m \cdot \frac{y}{s/2} \quad (4.56)$$

The total lift  $AF$  acting on the semi-wing of uniform chord is given by

$$AF = \int_0^{s/2} L(y) \cdot dy = L_m \cdot \left( \frac{1}{4} s \right) \quad (4.57)$$

The acceleration and hence the inertia force of the strip is linearly proportional to heaving acceleration  $\ddot{h}$  at the tip. Upon integration over the whole semi-span, the total inertia force of the half wing is given by

$$I = \frac{1}{4} m \ddot{h} \quad (4.58)$$

### ***4.2.2 DeLaurier's Method on Flapping Wing Study***

In DeLaurier's report [10] a design-oriented model for the unsteady aerodynamics of a flapping wing has been developed using a modified strip theory approach which takes into account of the aspect ratio of the wing planform. Simplified equations are employed by considering flapping only based on DeLaurier's method.

The wing's aspect ratio is assumed to be large enough that the flow over each section is essentially chordwise. Therefore the section's circulatory normal force is given by

$$dN_c = \frac{1}{2} \rho V_\infty^2 C_n(y) c dy \quad (4.59)$$

where  $c$  is wing chord and

$$C_n(y) = 2\pi(\alpha' + \alpha_0) \quad (4.60)$$

where  $\alpha_0$  is a fixed value for aerofoil and  $\alpha'$  is given by

$$\alpha' = \left[ \frac{AR \cdot C'(k)}{2 + AR} \right] \alpha - \frac{w_0}{V_\infty} \quad (4.61)$$

where  $\alpha$  is the relative angle of attack at the  $3/4$  chord location due to the wing's motion, and  $AR$  is the wing aspect ratio, considering flapping only without chordwise twist  $\alpha$  is given by

$$\alpha = \frac{\dot{h}}{V_\infty} \quad (4.62)$$

The coefficient of  $\alpha$  accounts for the wing's finite span unsteady vortex wake by means of a strip theory model. Each chordwise strip on the wing is assumed to act as if it were part of an elliptical planform wing, of the same aspect ratio, executing simple harmonic whole wing motions identical to that of the strip. For such a wing, Jones [48] derived that the unsteady normal-force coefficient  $\delta C_n$  is given by

$$\delta C_n = 2\pi C(k)_{Jones} \alpha \quad (4.63)$$

where  $C(k)_{Jones}$  is a modified Theodorsen function for finite wings with aspect ratio  $AR$  and  $k$  is the reduced frequency subject to the straight wing with uniform wing chord  $c$  given by

$$k = \frac{c\omega}{2V_\infty} \quad (4.64)$$

and  $C(k)_{Jones}$  is given by

$$C(k)_{Jones} = \frac{AR \cdot C'(k)}{2 + AR} \quad (4.65)$$



where for complex term  $C'(k)$  is given by

$$C'(k) = F'(k) + iG'(k) \quad (4.66)$$

Scherer [49] presents the approximate equation:

$$\left. \begin{aligned} F'(k) &= 1 - \frac{C_1 k^2}{k^2 + C_2^2} \\ G'(k) &= -\frac{C_1 C_2 k}{k^2 + C_2^2} \end{aligned} \right\} \quad (4.67)$$

and

$$\left. \begin{aligned} C_1 &= \frac{0.5AR}{2.32 + AR} \\ C_2 &= 0.181 + \frac{0.772}{AR} \end{aligned} \right\} \quad (4.68)$$

Substitute Eq. (4.66) into Eq. (4.61)  $\alpha'$  is given by

$$\alpha' = \frac{AR}{2 + AR} \left[ F'(k)\alpha + \frac{c}{2V_\infty} \frac{G'(k)}{k} \dot{\alpha} \right] - \frac{w_0}{V_\infty} \quad (4.69)$$

The downwash term  $w_0/V_\infty$  is due to the mean lift produced by  $\alpha_0$  if no chordwise twist is considered, and is given by

$$\frac{w_0}{V_\infty} = \frac{2\alpha_0}{2 + AR} \quad (4.70)$$

An additional normal force contribution comes from the apparent mass effect, which acts the mid-chord and is given by

$$dN_a = \frac{1}{4} \pi \rho c^2 \dot{v}_2 dy \quad (4.71)$$

where  $\dot{v}_2$  is the time rate of change of the mid-chord normal velocity component due to the wing's motion

$$\dot{v}_2 = V_\infty \dot{\alpha} \quad (4.72)$$

Therefore the section's normal force for total attached flow is

$$dN = dN_c + dN_a \quad (4.73)$$

From DeLaurier the chordwise force due to camber is given by

$$dD_{camber} = -2\pi\alpha_0 \cdot \alpha' \frac{\rho V_\infty^2}{2} c dy \quad (4.74)$$

Garrick's expression for the leading edge suction of a two dimensional aerofoil may be applied to the present strip theory model given by

$$dT = 2\pi\alpha' \frac{\rho V_\infty^2}{2} c dy \quad (4.75)$$

### 4.3 Theoretical Calculation of Flapping Wing Aerodynamics

In this section theoretical calculations are carried out based on the theory of Theodorsen's function. A flat rigid wing of specifically defined geometry and parameters will be used to study the unsteady aerodynamic forces acting on it and to conduct the further experimental study. According to Theodorsen's Eq. (4.1) the lift coefficient acting on a rigid thin airfoil per unit span undergoing small amplitude simple harmonic motion can be expressed as

$$C_l = \frac{L}{\frac{1}{2}\rho V_\infty^2(2b)} = \frac{L}{\rho V_\infty^2 b} = (C_{lR} + iC_{lI})e^{i\omega t} = C_{l0}e^{i(\omega t + \phi)} \quad (4.76)$$

Refer to Eq. (4.15) and Eq. (4.16) lift coefficient for heaving can be split in terms of its real and imaginary parts.

$$C_{lR} = -\pi\left(\frac{h_0}{b}\right)\left[k^2 + 2k \cdot G(k)\right] \quad (4.77)$$

$$C_{lI} = 2\pi\left(\frac{h_0}{b}\right)\left[k \cdot F(k)\right] \quad (4.78)$$

Similarly, following Eq. (4.21) and Eq. (4.22) the lift coefficient pitching in terms of its real and imaginary parts are given by

$$C_{lR} = -\pi\alpha_0\left[k \cdot G(k) - 2 \cdot F(k)\right] \quad (4.79)$$

$$C_{lI} = \pi\alpha_0\left[k + k \cdot F(k) + 2 \cdot G(k)\right] \quad (4.80)$$

According to Theodorsen's equation  $k$  is the reduced frequency given in Eq. (4.4) and thus

$$\frac{1}{k} = \frac{V_\infty}{\omega b} \quad (4.81)$$

With a fixed wing chord  $2b$ , the performance of the flapping flight in terms of flight speed and flapping frequency can be studied against  $1/k$ .

The amplitude of the lift coefficient of flapping wing under simple harmonic oscillation is given by

$$C_{l0} = \sqrt{C_{lR}^2 + C_{lI}^2} \quad (4.82)$$

In order to understand the effects of heaving and pitching of flapping wing on the amplitude of lift coefficient theoretical calculation is carried out in the range of  $1/k$  from 0 to 8. Define heaving amplitude and pitching angle as unit 1, the amplitude of the lift coefficient of pure heaving and pure pitching are calculated as a function of  $1/k$  as shown in Fig. 4.7.

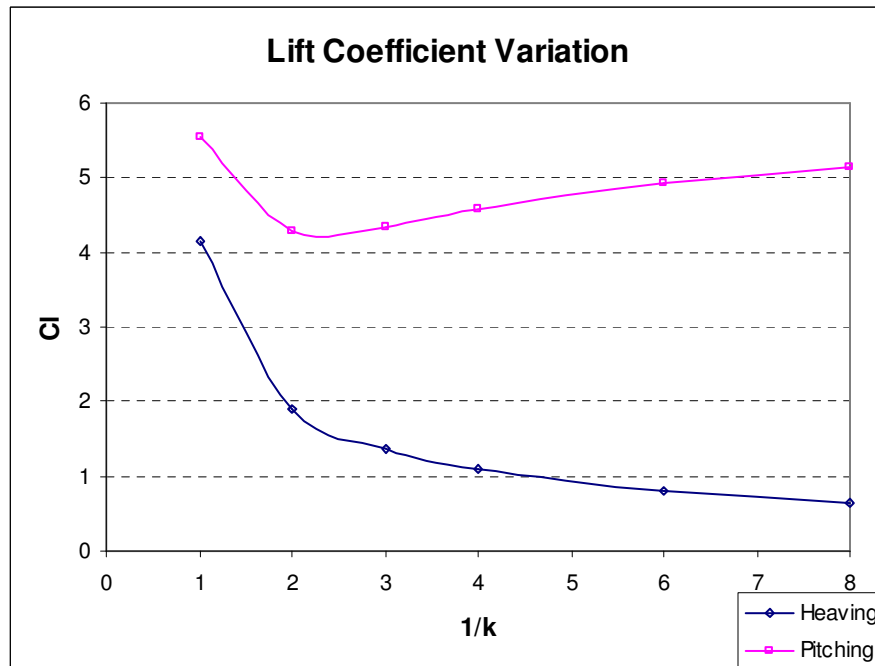


Figure 4.7 Lift coefficient amplitude variation against  $1/k$  per unit heave and pitch angle

The amplitude of the lift coefficients for heaving decreases as  $1/k$  increases either by an increase of speed and/or decrease of frequency.

### 4.3.1 Aerodynamic Force on Rigid Wing in Simple Harmonic Motions

In this section the three-dimensional aerodynamic forces on flapping wing are calculated under different rigid wing motions. The lift distribution along the wing span is studied by extending the sectional lift obtained from Theodorsen's function. Two rigid wing flapping motions are investigated which are whole-wing heaving motion and root flapping motion as shown in Fig. 4.5 and Fig. 4.6. Strip theory and DeLaurier's method

are employed to compute the spanwise lift distribution and the flow over each wing section is essentially assumed chordwise. The calculation is carried out by assuming the wing is rigid during a continuous sinusoidal motion with equal time between upstroke and downstroke.

### 4.3.1.1 3-D Aerodynamic Force Calculation in Whole-wing Motion

In the whole-wing motion the wing heaves vertically with uniform amplitude along span. Geometric parameters of a wing which will later be used for experimental validation purpose are given in Table 4.1 in order to carry out the spanwise lift calculation.

Wing span	$s$	150mm
Wing chord	$2b$	30 mm
Speed	$V_\infty$	4 m/s
Frequency	$f$	4 Hz
Heaving amplitude	$h_0$	10 mm

Table 4.1 Parameters for whole-wing motion

As given in Eq. (4.52) the local lift on a section of the wing at spanwise station  $y$  is related to the maximum lift at the centreline of the wing. Refer to Eq. (4.53) and after integrating the lift on each strip along spanwise direction the total lift acting on the wing is given by

$$AF = \frac{\pi}{4} L_0 s \tag{4.83}$$

where  $L_0$  is the sectional lift under heaving given in Eq. (4.10)

By assuming no flow separation at the wing tips the lift acting on each strip is proportional to the heaving amplitude. Hence the total lift with no flow loss at the wing tip is given by

$$AF = L_0 s \tag{4.84}$$

The lift obtained in Eq. (4.83) is based on elliptical lift distribution. On the other hand, in Eq. (4.84) the lift is obtained based on rectangular distribution. The computed results of the amplitude of spanwise lift  $L$  by these two types of distribution are shown below using the wing geometric parameters in Table 4.1.

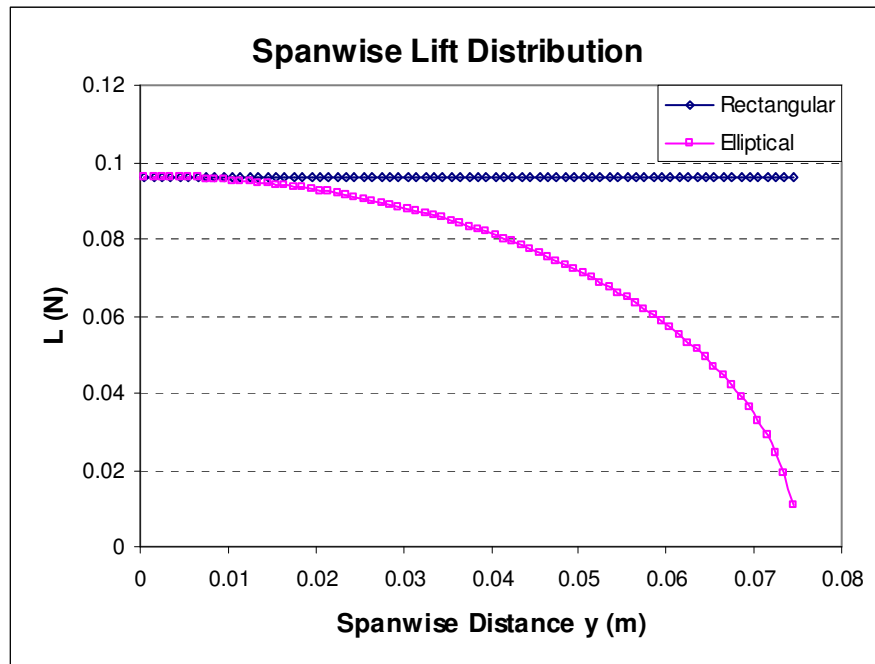


Figure 4.8 Spanwise lift distribution calculated by Theodorsen for whole-wing motion

### 4.3.1.2 3-D Aerodynamic Force Calculation in Root Flapping

In root flapping the wing rotates about stroke axis at its root. The flapping amplitude of each section on the wing is assumed linearly proportional to the distance away from stroke axis. Refer to Eq. (4.57) assume no flow loss at wing tip the total aerodynamic force acting on the root-flapping wing is given by

$$AF = \frac{1}{2} L_m s \quad (4.85)$$

By considering the lift loss at the wing tip the sectional lift is not only governed by the flapping amplitude but related to the wing span position. Refer to Eq. (4.52) the total lift of the wing in root-flapping is given by

$$AF = \frac{1}{3} L_m s \quad (4.86)$$

With the same specific parameters shown in Table 4.1 the calculation of amplitude of spanwise lift  $L$  is carried out with the wing tip experiencing maximum heaving amplitude which is 10 mm with and without considering the wing tip lift loss at  $0^\circ$  angle of attack.

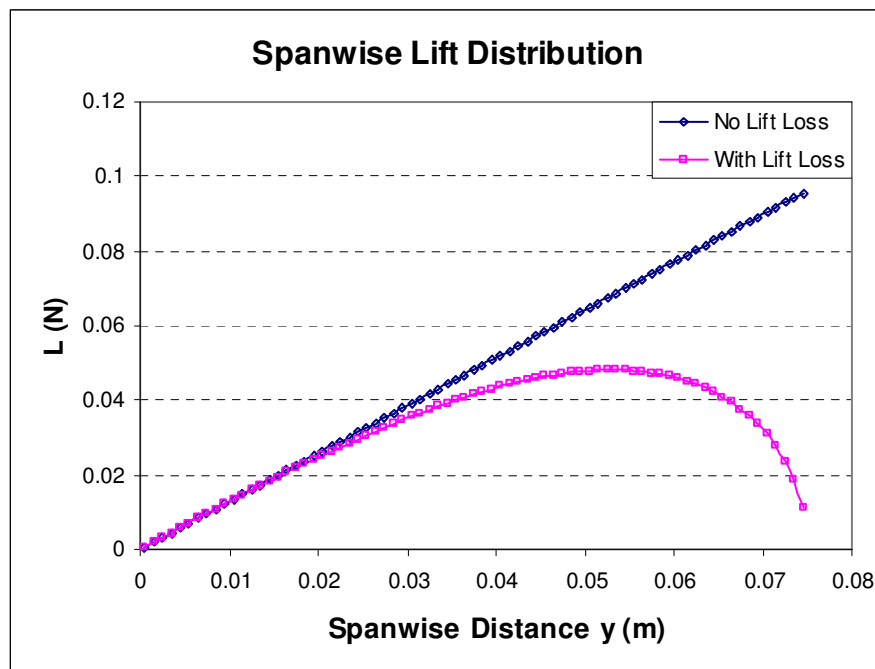


Figure 4.9 Spanwise lift distribution calculated by Theodorsen's method for root flapping

### 4.3.1.3 3-D Aerodynamic Force Calculation by DeLaurier's Method

DeLaurier's method induced the effect of wing aspect ratio  $AR$ . Refer to Eq. (4.59) and Eq. (4.71) the aerodynamic force of flapping wing consists of two components which are terms  $N_c$  and  $N_a$ . Term  $N_c$  is mainly due to the effect of wing flapping action and term  $N_a$  indicates the inertia of fluid. Subject to a thin flat plate with uniform chord under simple harmonic flapping oscillation the simplified equations of aerodynamic force are derived in terms of real part  $L_R$  and imaginary part  $L_I$ .

For term  $N_c$

$$L_R = -\frac{1}{2}\rho V_\infty^2 \left\{ 2\pi \frac{AR}{2+AR} G'(k) \frac{\omega h_0}{V_\infty} \right\} c \quad (4.87)$$

$$L_I = \frac{1}{2}\rho V_\infty^2 \left\{ 2\pi \frac{AR}{2+AR} F'(k) \frac{\omega h_0}{V_\infty} \right\} c \quad (4.88)$$

For term  $N_a$

$$L_I = -\frac{1}{4}\pi \rho c^2 \omega^2 h_0 \quad (4.89)$$

Theoretical calculation of the amplitude of the aerodynamic force has been carried out for a rectangular wing subject to whole-wing heaving and root flapping using the wing geometric parameters given in Table 4.1. The spanwise lift distributions by Theodorsen's and DeLaurier's method are plotted below. In Fig. 4.10 the blue curve presents the spanwise lift distribution obtained with rectangular distribution assumption for whole-wing heaving. Pink curve indicates that obtained based on elliptical lift distribution and the red curve is obtained by using DeLaurier's method. By integrating the lift along wing span the total force obtained from the pink curve is 79% and the red curve is 83% of that obtained from the blue curve. In Fig. 4.11 the same calculation has been carried out based on the root flapping motion. The blue curve describes the spanwise lift distribution with no lift loss at wing tip. The pink curve presents the wing tip lift loss compared with the



blue curve. And the red curve comes from DeLaurier's method. By integrating the spanwise lift the total lift of the pink curve is 67% of the blue curve and red curve is 83% of blue one. Obviously the no lift loss assumption at the wing tip shows the highest total lift by considering the wing with an infinite span. And the assumption of wing tip lift loss gives the minimum total lift based on a finite wing span. The DeLaurier's method takes the wing configuration into account as a finite wing and the total lift computed by this method is in between values obtained from the former two methods.

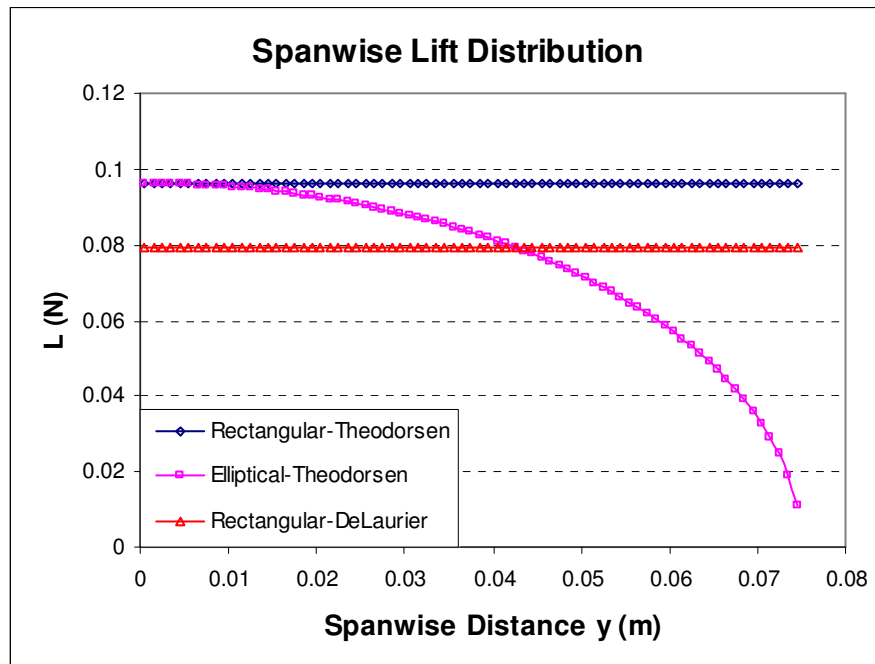


Figure 4.10 Spanwise lift distribution comparison for whole-wing motion

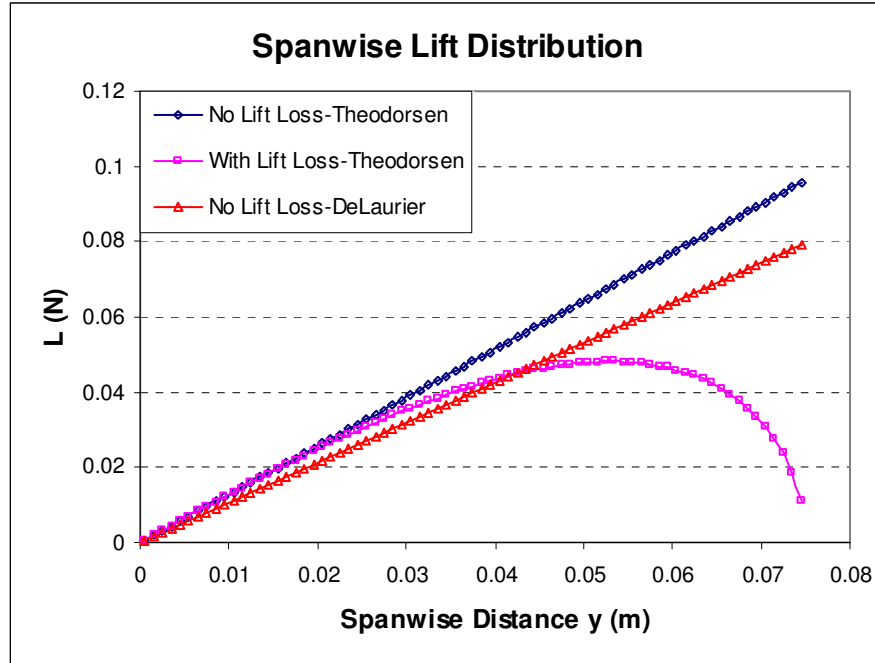


Figure 4.11 Spanwise lift distribution comparison for root flapping

### 4.3.2 Aerodynamic Force on Flapping Wing in Time History

In this section geometric parameters of a small uniform wing are used to compute the aerodynamic forces acting on its surface under simple harmonic motion which will later be compared with results from experimental measurements for pure heaving motions. The calculation is carried out based on Theodorsen's equation of lift in time history. The behavior of different forces acting on the oscillatory flatplate is studied in terms of force amplitude and phase shift.

Subject to the pure heaving and pitching the total aerodynamic force acting on the wing under whole-wing motion is given in Eq. (4.83)

$$AF = \frac{\pi}{4} Ls = \frac{\pi}{4} L_0 s \cdot \cos(\omega t + \varphi) \quad (4.90)$$

where  $L_0$  and  $\varphi$  are lift amplitude and phase shift given in Eq. (4.31) for heaving and Eq. (4.34) for pitching

The expressions of displacement, pitch angle and inertia in time history are shown in Eqs. (4.32), (4.35) and (4.41).

In order to study the force and displacement relationship in pure heaving the specific parameters used in this theoretical study are tabulated below.

Wing chord (uniform)	$2b$	30mm
Wing span	$s$	150mm
Speed	$V_{\infty}$	4m/s
Frequency	$f$	4Hz
Wing mass	$m$	0.83g
Heaving amplitude	$h_0$	10mm
Pitch angle	$\alpha$	$5^{\circ}$

Table 4.2 Parameters used for heaving motion

#### 4.3.2.1 Forces on the Wing in Heaving Motion

Based on the given parameters in Table 4.2 the lift and inertia force acting on the wing are calculated over a cycle in time history. As shown in Fig. 4.12 the blue curve ' $AF$ ' is the lift in heaving. The pink curve ' $Inertia$ ' indicates the inertia force. The yellow curve ' $Dis$ ' is displacement which indicates the wing movement as defined in Eq. (4.32) that positive value indicating the upper position of motion.

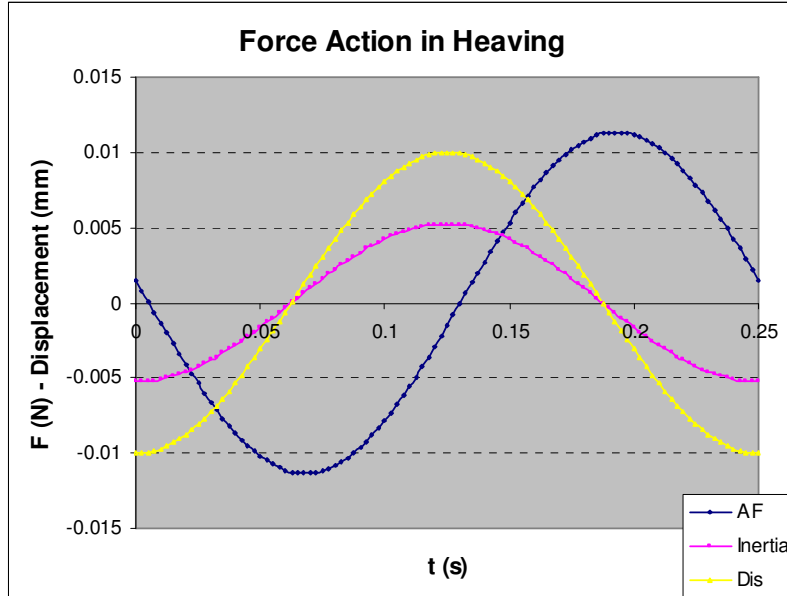


Figure 4.12 Forces due to heaving motion in time history

To understand the interaction of the lift and inertia, the heaving simple harmonic motion is divided into five cyclic positions as shown in Fig. 4.13.

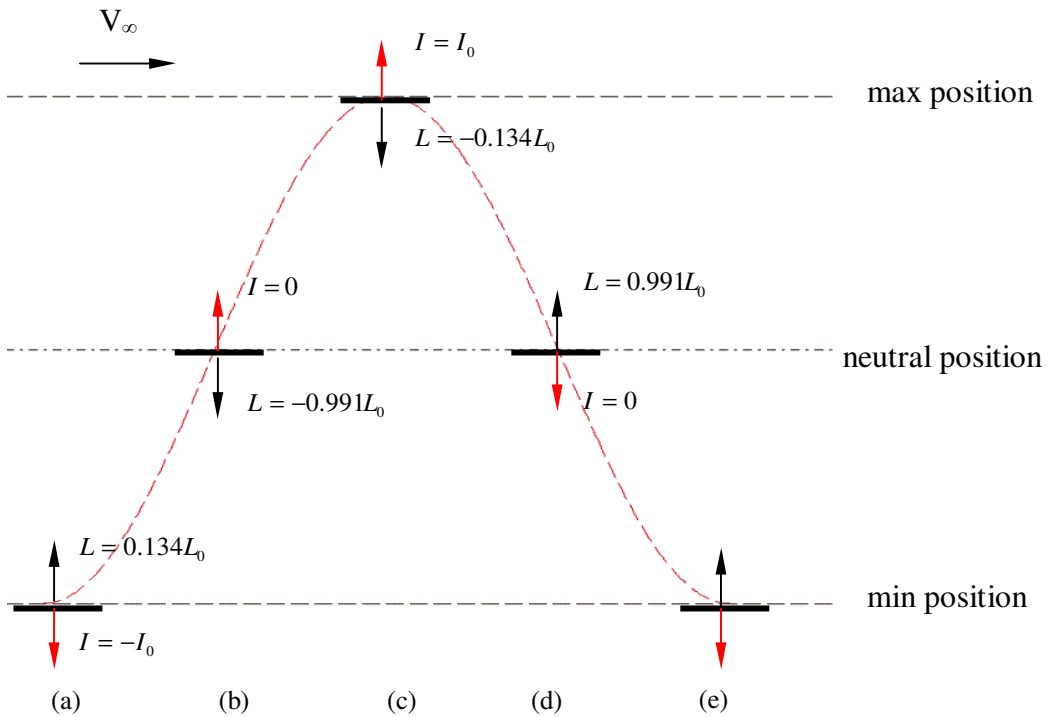


Figure 4.13 Simple harmonic motion of heaving

According to the computed results of the forces acting on the wing in Fig. 4.12 the relative magnitudes of the forces at neutral, maximum and minimum positions are shown in Fig. 4.13. The black arrow is the lift and red arrow indicates inertia force. In position (a) the wing starts moving upward and the lift is also upward. This is mainly due to term  $\pi\rho b^2\ddot{h}$  which is the so-called apparent mass lift representing only 13.4% of the peak lift amplitude. At this position since  $\ddot{h}$  reaches its maximum while  $\dot{h}$  is zero and lift is dominated by term  $\pi\rho b^2\ddot{h}$  and inertia force also reaches to its maximum value. In position (b) lift term  $\dot{h}$  reaches maximum value at 99.1% of peak lift amplitude while  $\ddot{h}$  is zero. Therefore the lift is dominated by term  $2\pi\rho V_\infty bC(k)\dot{h}$  while inertia reduces to zero refer to Eq. (4.10). In position (c) the wing moves to its maximum position while at the same time term  $\ddot{h}$  reaches maximum and  $\dot{h}$  reduces to zero. The lift is dominated by term  $\pi\rho b^2\ddot{h}$  again and inertia force reaches to its maximum. In position (d) the wing moves back to its neutral position. The term  $\dot{h}$  increases to maximum value and  $\ddot{h}$  is zero. The lift is dominated by term  $2\pi\rho V_\infty bC(k)\dot{h}$  and inertia is zero. In position (e) the wing returns to its minimum position again and repeats the motion in the next cycle.

Based on the calculation the lift on the wing at its peak displacement positions is totally dominated by the apparent mass term but is very small compared with its inertia force. However the lift becomes the dominant force when the wing returns to its neutral position and the inertia force reduces to zero. Regard displacement as a reference in time history the inertia is in phase with displacement and the phase shift between lift and inertia is almost  $\pi/2$ .

#### 4.3.2.2 Forces on the Wing in Pitching Motion

Based on the specified parameters shown in Table 4.2 the aerodynamic force is calculated over a cycle of time history. As shown in Fig. 4.14 the blue curve 'AF' is the aerodynamic force in pitching. The yellow curve 'Angle' indicates the pitch angle

displacement which has been factored down by 10 to facilitate its plotting with the lift in the same graph.

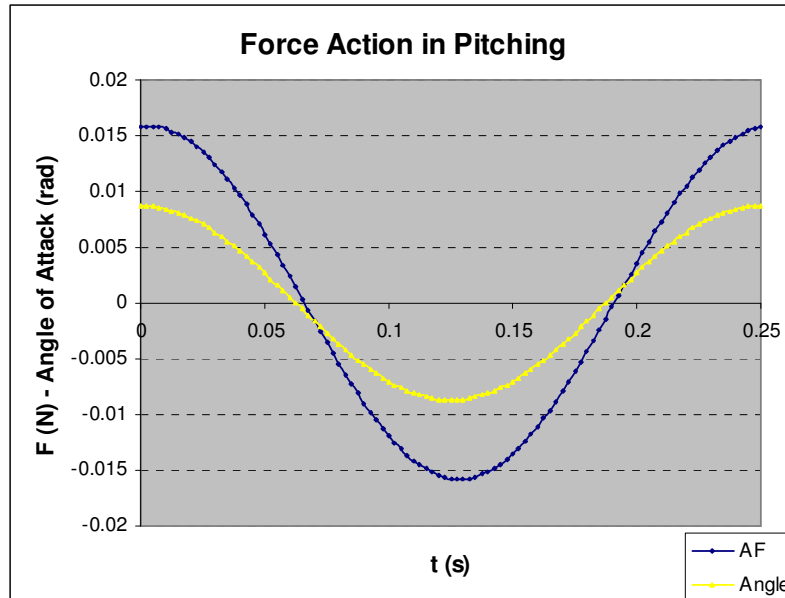


Figure 4.14 Forces due to pitching motion in time history

To understand the relationship between the lift and the pitch angle the simple harmonic motion of pitching about its mid-chord is divided into five cyclic positions as shown in Fig. 4.15.

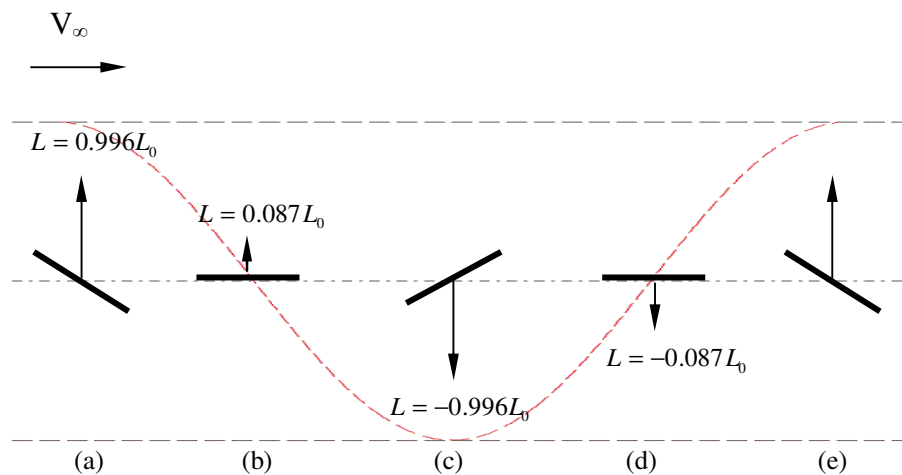


Figure 4.15 Simple harmonic motion of pitching

According to the computed results of total force acting on the wing in Fig. 4.14 the relative magnitudes of forces at neutral, maximum and minimum positions are shown in Fig. 4.15. Based on the computed the magnitude of lift is governed by terms  $\pi\rho b^2 V_\infty \dot{\alpha}[C(k)+1]$  and  $2\pi\rho b V_\infty^2 \alpha C(k)$  as shown in Eq. (4.19). In position (a) the wing starts rotating anticlockwise (nose down) from  $\alpha = 5^\circ$ . A positive lift is generated due to this angle of attack. Since term  $\alpha$  is at its maximum value while  $\dot{\alpha}$  is zero the lift is dominated by the term  $2\pi\rho b V_\infty^2 \alpha C(k)$  with 99.6% of peak amplitude. In position (b) term  $\dot{\alpha}$  reaches to maximum and  $\alpha$  is zero. At this moment the lift is dominated by term  $\pi\rho b^2 V_\infty \dot{\alpha}[C(k)+1]$  with only 8.7% of peak amplitude. When the wing rotates to a negative angle of  $\alpha = -5^\circ$  in position (c) term  $\alpha$  reaches the maximum and  $\dot{\alpha}$  is zero. The lift at this position is dominated by term  $2\pi\rho b V_\infty^2 \alpha C(k)$ . In position (d) term  $\alpha$  decreases to zero and  $\dot{\alpha}$  reaches to maximum. Lift is dominated by term  $\pi\rho b^2 V_\infty \dot{\alpha}[C(k)+1]$ . The next cycle repeats itself when the wing returns to position (e).

### 4.3.2.3 Forces on the Wing in Combined Heave and Pitch Motion

In the heaving and pitching combined motion case the lift magnitude is governed by the heaving and pitching motion respectively and its phase shift  $\varphi_C$  between heaving and pitching.

$$L_C = L_H + L_P \quad (4.90)$$

The equations for the wing motion are given by

$$\left. \begin{aligned} h &= h_0 \cos \omega t \\ \alpha &= \alpha_0 \cos(\omega t + \varphi_C) \end{aligned} \right\} \quad (4.91)$$

By defining the pitch axis is at mid-chord the combined motions in different modes are illustrated below.

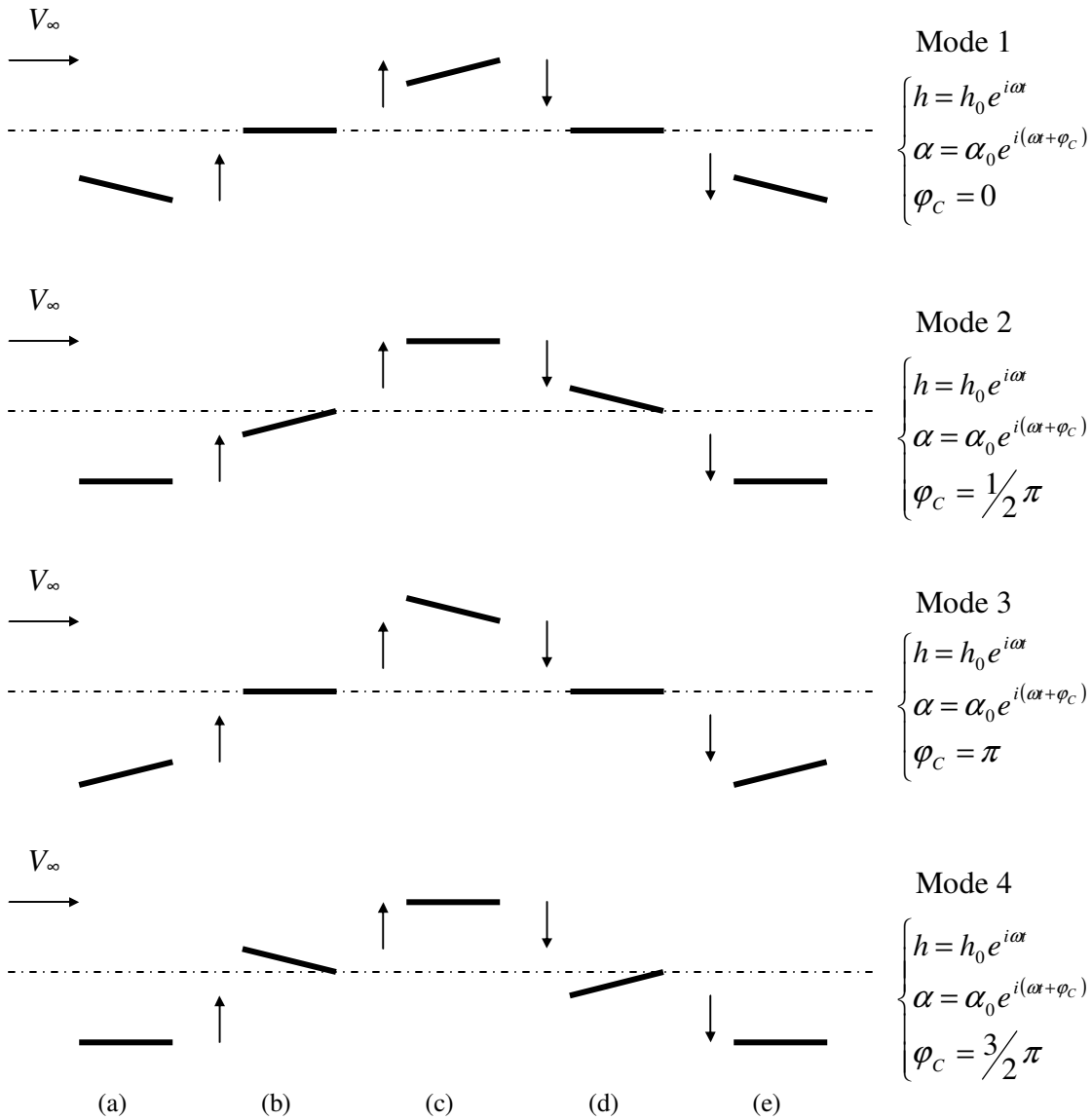


Figure 4.16 Heaving and pitching combined motion

For a range of phase shift angles  $\varphi_C$ , the lift over a cycle of oscillation for the combined motion is calculated and analysed in time history. As shown in Fig. 5.9 to Fig. 5.12 the blue curve ' $L(H)$ ' is the lift due to heaving, the pink curve ' $L(P)$ ' is the lift due to pitching, the turquoise curve ' $L(C)$ ' is the total lift due to heaving and pitching combined motion, the yellow curve ' $Dis$ ' is the wing displacement and the red curve ' $Angle$ ' indicates the wing pitch angle. By setting the phase shift  $\varphi_C$  between heaving and



pitching from 0 to  $\frac{3}{2}\pi$  the peak value of the aerodynamic force can be changed from 22% to 138% of the lift amplitude compared with mode 1 as reference. Therefore by proper control the wing pitch angle the total aerodynamic force of flapping wing can be controlled.

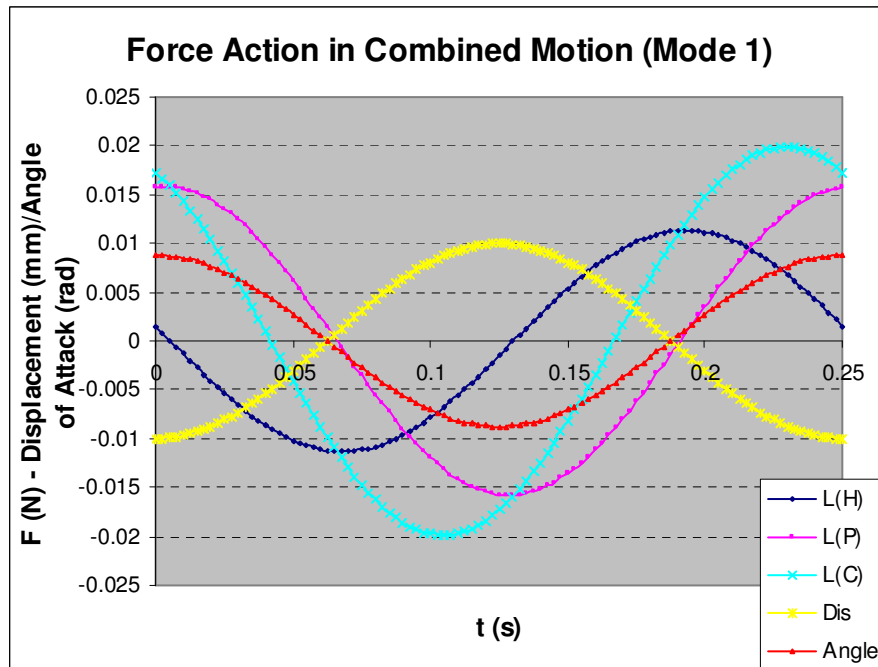


Figure 4.17 Combined motion of mode 1

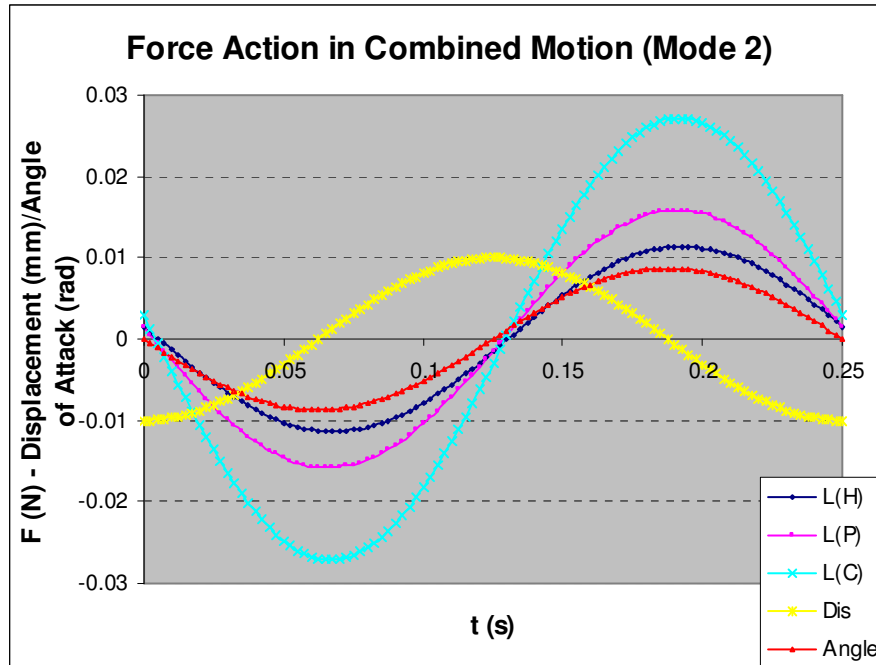


Figure 4.18 Combined motion of mode 2

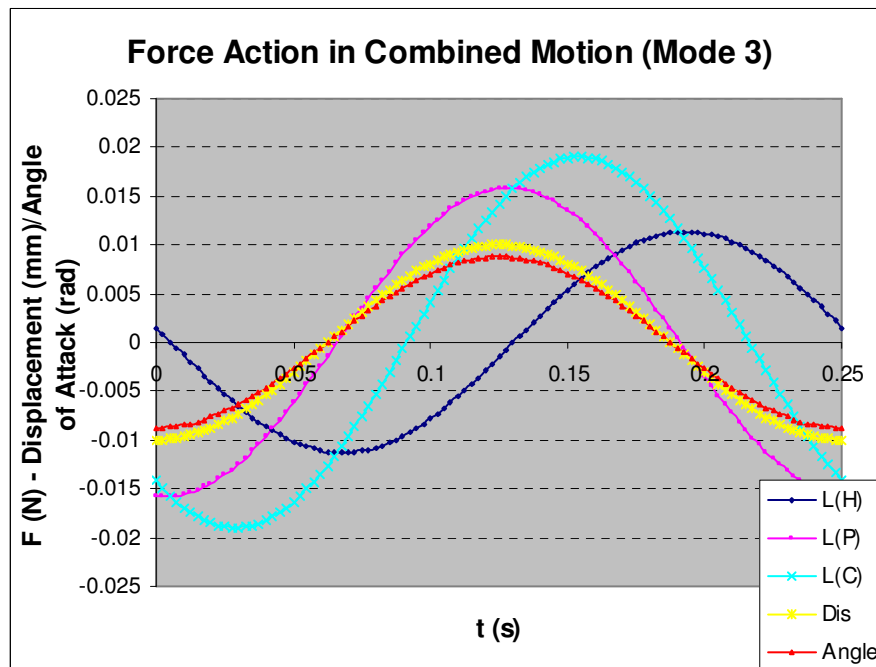


Figure 4.19 Combined motion of mode 3

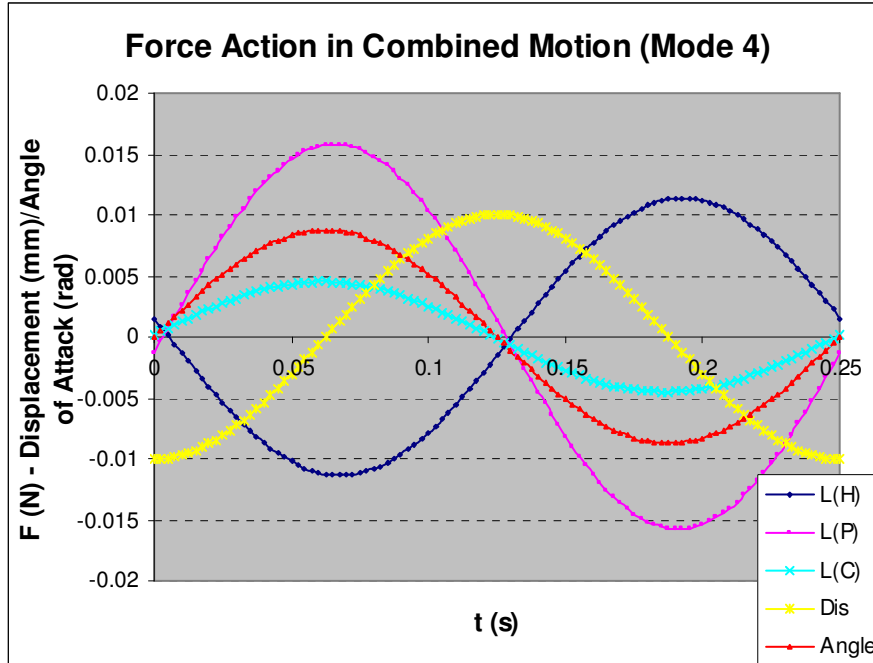


Figure 4.20 Combined motion of mode 4

#### 4.3.2.4 Wing Propulsion and Propulsive Efficiency

In Garrick's report the mathematical equations are derived to calculate the thrust and propulsive efficiency as mentioned in Eq. (4.44) and Eq. (4.46). In heaving motion the propulsive efficiency is calculated and plotted against  $1/k$  as shown in Fig. 4.21. According to Eq. (4.48) the propulsion efficiency for heaving depends on term  $F(k)$  and  $G(k)$ . Fig. 4.21 shows that the efficiency varies from 50% to 100% as  $1/k$  increases from zero to infinity. Heaving motion at low speed and high frequency gives rise to poor efficiency 50%, whereas at higher speed and lower frequency the efficiency can be improved theoretically nearer to 100%.

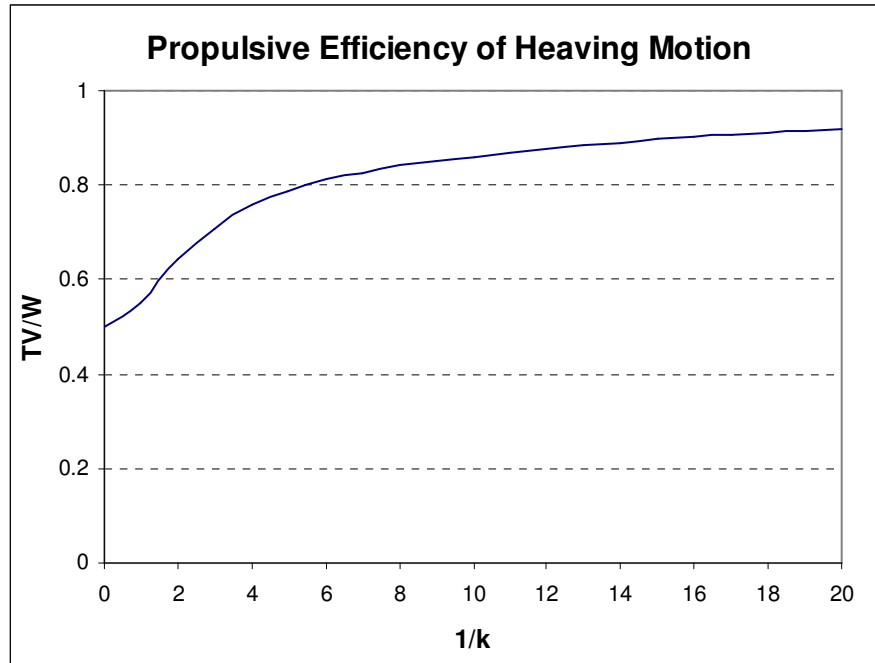


Figure 4.21 Propulsive efficiency of heaving motion

For pitching case the propulsive force is given by Eq. (4.49) in terms of pitch axis location  $a$  depicted in Fig. 4.1. To evaluate the variation of propulsive efficiency with pitch axis  $a$  the energy formula is given in Eq. (4.51) is used. Theoretical results of  $\overline{E}/\overline{W}$  against  $1/k$  for pitch motion have been obtained as shown below.

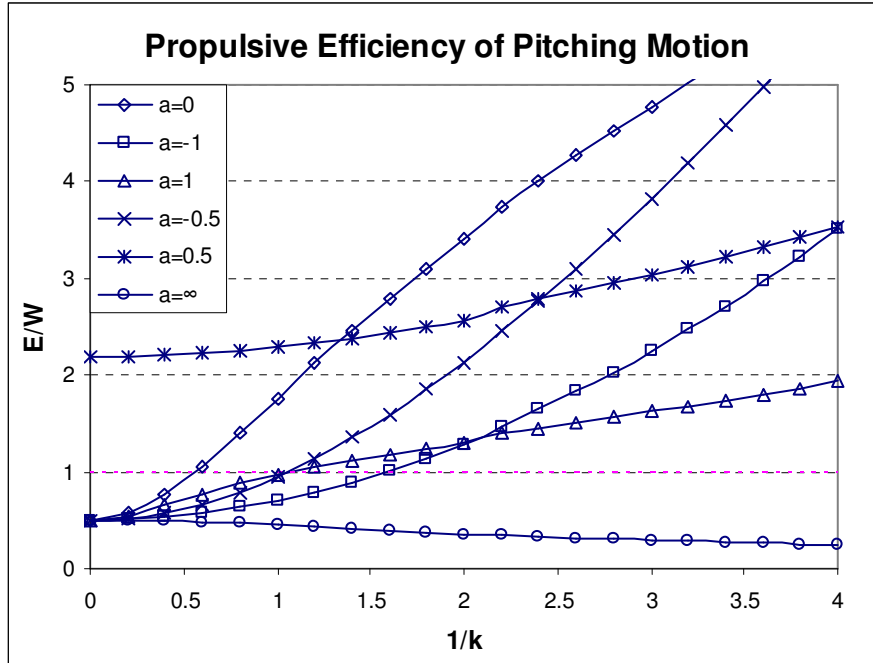


Figure 4.22 Energy dissipated in the wake for pitching about axis  $a$

In the figure above the ratio  $\overline{E}/\overline{W}$  is plotted in this case for several positions of the pitch axis  $a$ . These curves give the ratio of the energy per unit time released in the wake as work per unit time required to maintain the oscillations. In the range of values  $0 < \overline{E}/\overline{W} < 1$ ,  $T$  is positive and denotes a thrust or propelling force; for other values it is negative and denotes a drag force. It should be noted that thrust is always obtained when the pitch axis approaches infinity regardless of  $k$ . Therefore heaving motion always provides the thrust. However most pitching motion induces drag throughout the high range of  $1/k$  except for  $0 < 1/k < 2.0$  where thrust can be obtained depending to some extent on the pitch axis  $a$ .

## 5 Experimental Investigation

In this chapter the experimental investigation is carried out to measure the aerodynamic forces on wings undergoing simple harmonic oscillations. Wind tunnel measurements are carried out on rigid and flexible wings over a range of wind tunnel speeds and wing oscillatory frequencies and results are compared with numerical calculations obtained using the methods described in previous chapters.

### 5.1 Wind Tunnel Test of Rigid Wings

It is very important for flapping wing wind tunnel test that the wing should be very light weight because it helps in the measurement of the aerodynamic forces from wind tunnel testing using strain gauges. A heavy wing will induce a large inertia force which may dominate the total force measurement and therefore reduces the accuracy of aerodynamic force measurement.

#### 5.1.1 *Wing and Test Rig Design*

As part of the experimental investigation in order to measure useful data for comparing with theoretical predication, a test rig is purposefully designed and built for the wind tunnel test. The test rig is designed to achieve the three different wing motions which are pure heaving, pure pitching and heaving pitching combined motions. Based on a small wing the weight of the wing is kept as light as possible to minimize the effect of inertia force but at the same time it must be reasonably stiff so as to minimize excessive bending during the motion.

Three small wings made of balsa wood are constructed for the three different motion test cases respectively. All three sample wings are of the same geometry of 150mm spanwise, 30mm chordwise and 1mm thickness as shown in Fig. 5.1. Two strain gauges (FLA-6-11) are securely attached at the root of the wing on both sides to measure the strain due to bending moment induced by the forces on the wing surface subject to different airflow

speeds and oscillatory frequencies. Tissue paper is selected as the wing skin and spread on the wing frame. To get a smooth surface dope is used to stretch the skin tightly.

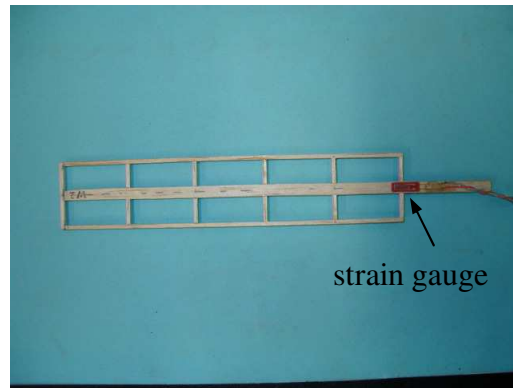


Figure 5.1 Wing frame with strain gauge attached at the root

The test rig consists of a gear box, a circular floor and several linkages. By replacing different sets of linkage pure heaving, pure pitching and heaving pitching combined wing motions can be achieved. A one-to-one gear box is designed for the power transmission, see Fig. 5.2. The gear box is mounted on a side panel which is shown in Fig. 5.3. The gear box is fitted onto a side panel which in turn is fitted onto the circular floor shown in Fig. 5.4. The motor (9904-120-52602) is powered by a power plant to control the input voltage and achieve different speeds.

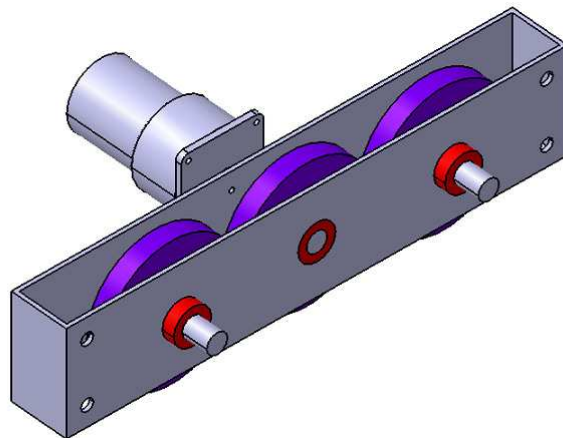


Figure 5.2 Gear box design

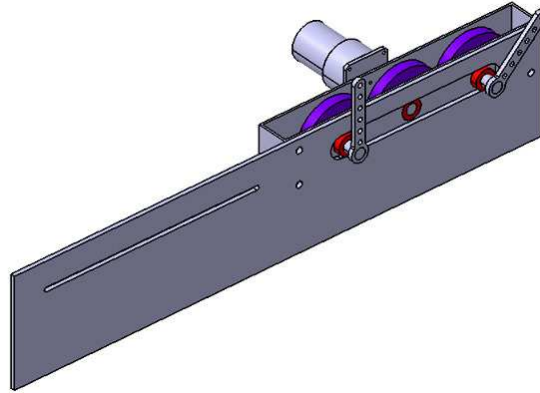


Figure 5.3 Side panel with gear box

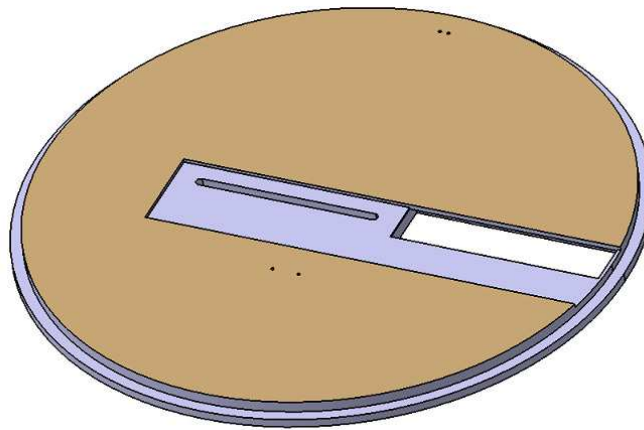


Figure 5.4 Floor

An assembled test rig is shown in Fig. 5.5. A heaving unit driven by an arm is located on the slot of the side panel to move up and down in a simple harmonic motion. The heaving unit and arm is connected by a rod. A position sensor is connected on the shaft of the gear box to monitor the rotation speed, see Fig. 5.6. In Fig. 5.7 a wooden beam is clamped at the edge of the floor and another side is connected to the heaving unit and two strain gauges are fitted at the root of the beam on both sides to measure the displacement of the wing from its neutral position during the oscillation.



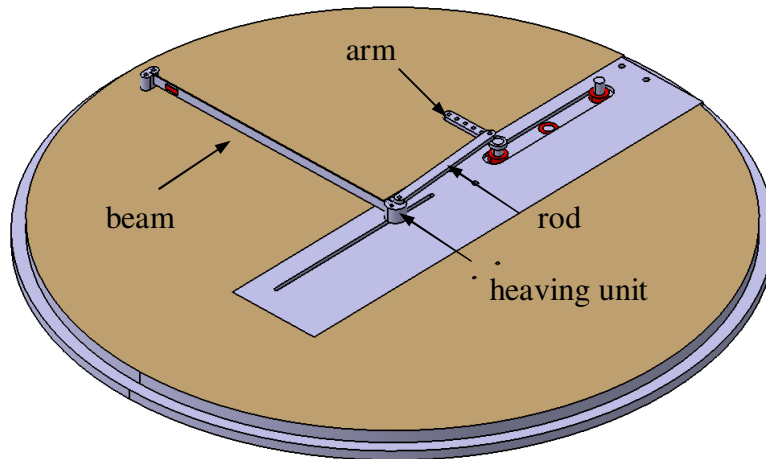


Figure 5.5 Assembled test rig

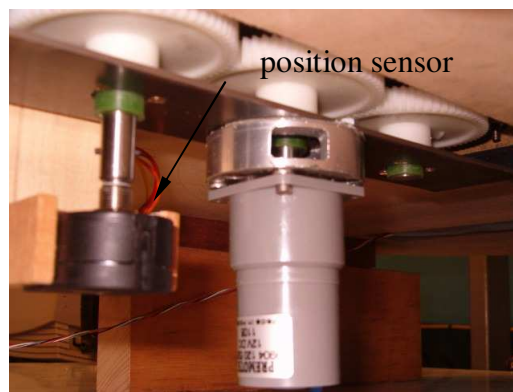


Figure 5.6 Position sensor

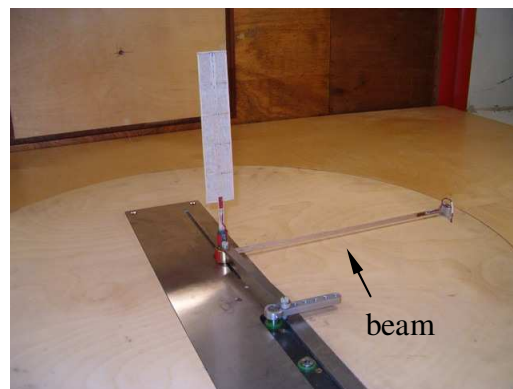


Figure 5.7 Beam for displacement test

### 5.1.2 Construction of Test Rig for Different Motions

By replacing different linkages three different wing motions can be achieved which are described as below. Detailed engineering drawings are shown in Appendix A from Figs. A1 to A6.

#### 5.1.2.1 Pure Heaving Motion

Fig. 5.8 shows the test rig for the pure heaving case. The wing is clamped on the heaving unit which is driven by an arm to move in the slot up and down. The maximum heaving amplitude is 10mm. The heaving frequency depends on the rotation speed of the arm which is powered by the power unit underneath. By adjusting the input voltage different oscillatory frequencies can be achieved.

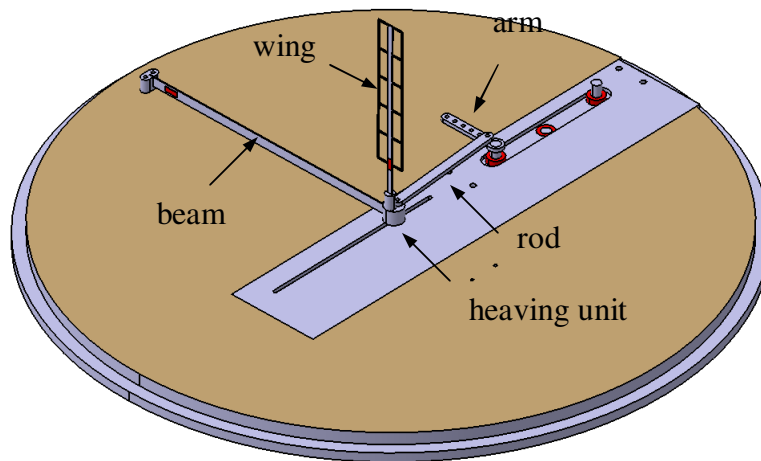


Figure 5.8 Test rig design for pure heaving motion

#### 5.1.2.2 Pure Pitching Motion

Fig. 5.9 shows the test rig for the pure pitching case. The wing is clamped on the pitching linkage which can be set to rotate only motion on a fixed pitching step. The step on which the wing sits is linked to a heaving unit which is driven by the arm to move in the slot. The upper surface of the heaving unit on the slot is connected to the pitching step via a pitching linkage. When the heaving unit is moving up and down on the slot on the side

panel on the test rig the pitching linkage is driven by the heaving unit and causing rotation on the pitching step and producing a simple harmonic pitching motion. The maximum angle of attack is controlled at 5 degree.

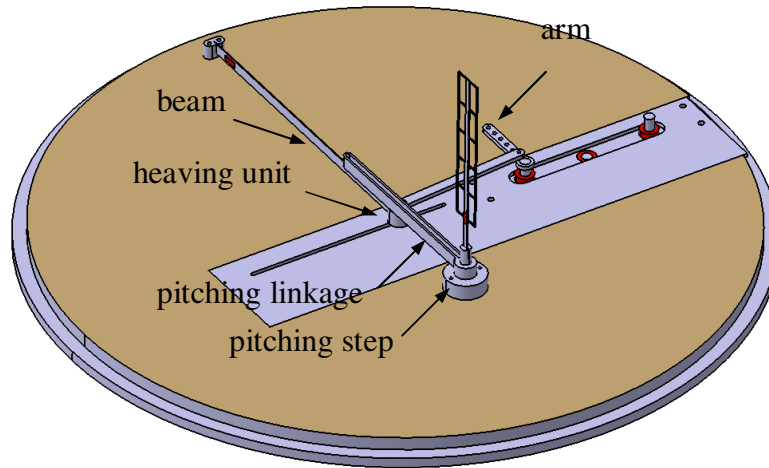


Figure 5.9 Test rig for pure pitching motion

### 5.1.2.3 Heaving and Pitching Combined Motion

Fig. 5.10 shows the test rig for the pure pitching case. The wing is clamped on the pitching linkage and the heaving unit is located underneath to give a pure heaving motion. A fixed step is connected on the other edge of the pitching linkage to achieve a pure pitching motion. Finally a heaving and pitching combined simple harmonic motion is achieved by this mechanical linkage system. The angle of attack is set at maximum constant amplitude 5 degree and the heaving displacement is 10mm.

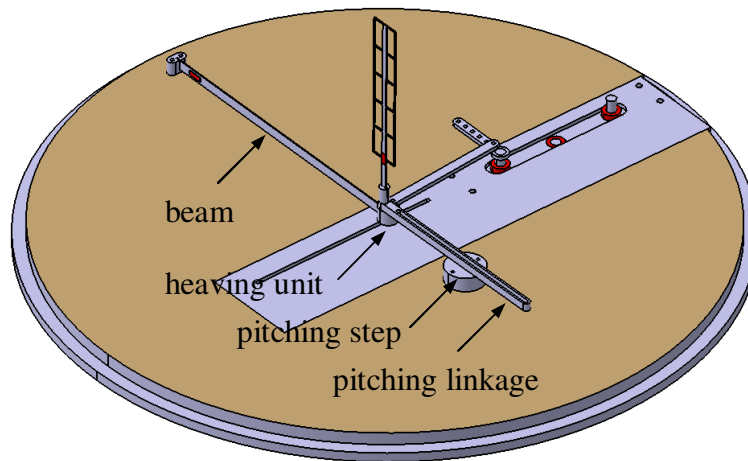


Figure 5.10 Test rig for heaving and pitching combined motion

### **5.1.3 Wind Tunnel Test Equipment**

The wind tunnel used for the experimental investigation is the T3 wind tunnel located in the Handley Page wind tunnel laboratory at City University. The geometry of the wind tunnel sectional test space is  $1.15\text{m} \times 0.89\text{m} \times 1.5\text{m}$ . The range of the available airflow speeds is 0-55m/s. In the wind tunnel test section a floor with a circular cut-out is constructed and mounted inside the tunnel about quarter way from the true tunnel floor in order to hold the test rig shown in Fig. 5.11.

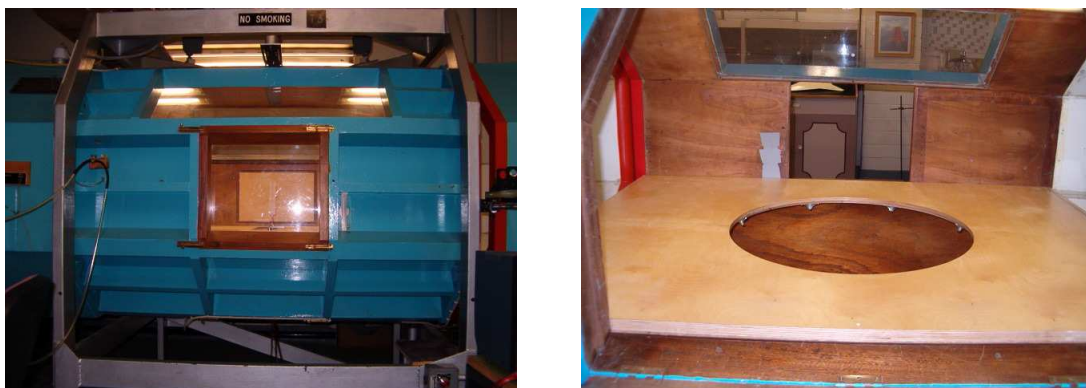


Figure 5.11 Test section of the T3 wind tunnel

A Pitot tube is located on the wall in front of test section to measure the airflow speed as shown in Fig. 5.12. A casella micro-manometer with vernier scale is connected to the Pitot tube to measure the pressure of the airflow which is illustrated in Fig. 5.13. Relevant equations are shown as below.

$$\frac{1}{2} \rho_{air} V_{\infty}^2 = K \rho_{water} g (h - h_0) \quad (5.1)$$

$$V_{\infty} = \sqrt{\frac{2K \rho_{water} g (h - h_0)}{\rho_{air}}} \quad (5.2)$$

where

$$\rho_{air} = \frac{P_{lab}}{R \cdot T_{lab}} \quad (5.3)$$

$$R = 287 \text{ KJ/kgK} \quad (5.4)$$

' $h - h_0$ ' is the variation of the water height which is obtained by the micro-manometer.  $P_{Lab}$  and  $T_{Lab}$  are lab atmosphere pressure and temperature respectively. And  $k = 1.02$  which is the calibration factor. The pressure  $P_{Lab}$  measured by mercury barometer is in 'mbar' and  $T_{Lab}$  is in '°C'. To calculate air density by Eq. (5.3) the pressure should be in 'Pa' and temperature is in 'K'.



Figure 5.12 Pitot tube



Figure 5.13 Micro-manometer

The test data logging setup is illustrated in Fig. 5.14. An installed piece of software called ‘Spike5’ is used for the data analysis. After amplifying the measured voltage from the strain gauge the electrical signal is converted to digital datum by the digital transformer.



Figure 5.14 Test data logging set up

Three channels are used to record the test results. Channel 0 records the output rotation speed of the gear box by the position sensor. Channel 1 measures the bending moment at the root of the wing due to the aerodynamic force and inertia via stain gauges fitted at the wing root. Channel 2 records the displacement of the wing by the strain gauges at the beam.

### 5.1.4 Wind Tunnel Test

The wind tunnel test is carried out in different wing motions subject to different airflow speeds and oscillatory frequencies in the low speed wind tunnel. The objective of this experiment is to measure the aerodynamic forces under the simple harmonic motion in a steady mainstream flow. The test is carried out with wind speeds ranging from 2m/s to 8m/s at 2m/s increment and the flapping frequencies from 4Hz to 8Hz at 1Hz step.

#### 5.1.4.1 Force Calibration

The calibration is necessary to convert the voltage signal to force. The calibration is carried out by placing unit loads at the wing tip to get the calibration scale factor  $CSF$  which is the relationship between voltage and force based on the wing structure stiffness.

In Fig. 5.15 the wing is moving in a simple harmonic heaving motion. The inertia force due to the wing mass is distributed along the wingspan  $s$ . The contribution of the inertia applies at the mid-span  $s/2$ . The bending moment due to inertia force  $I$  is shown in Eq. (5.5). In the calibration the unit load ‘ $W_c$ ’ is placed at the wing tip with a bending moment  $M_c$  shown in Eq. (5.6).

Bending moment due to inertia force

$$M_I = I \frac{s}{2} = ma \cdot \frac{s}{2} = m\ddot{h} \cdot \frac{s}{2} \quad (5.5)$$

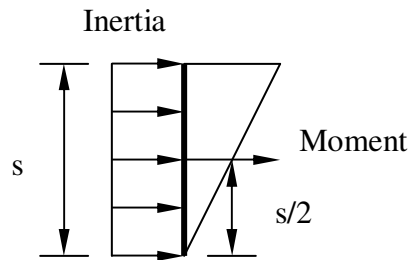


Figure 5.15 Spanwise inertia distribution

Bending moment due to a tip load for calibration

$$M_c = W_c \cdot s \quad (5.6)$$

where  $W_c$  is a unit load (N) at the wing tip for calibration

Put Eq. (5.5) and Eq. (5.6) together

$$I = ma = 2 \cdot \frac{W_c}{M_c} \cdot M_I = 2 \cdot M_I \cdot \frac{W_c}{M_c} = 2 \cdot V_m \frac{W_c}{V_c} \quad (5.7)$$

Therefore the calibration scale factor  $CSF = \frac{W_c}{V_c}$

where  $V_m$  and  $V_c$  are the measured strain gauge signal (mV) from the inertia test and static calibration test respectively.

In the wind tunnel test the strain gauges record the total bending moment at the root due to the aerodynamic force which is in a parabolic distribution along spanwise, see Fig. 5.16. Based on elliptical lift distribution along the wingspan (refer to Eq. (4.52)) the total aerodynamic force (  $AF$  ) and moment is shown below.

$$\text{Total } AF \quad F_a = Ls \left( \frac{\pi}{4} \right) \quad (5.8)$$

$$\text{Total Moment} \quad M_a = Ls \left( \frac{s\pi}{8} \right) \quad (5.9)$$



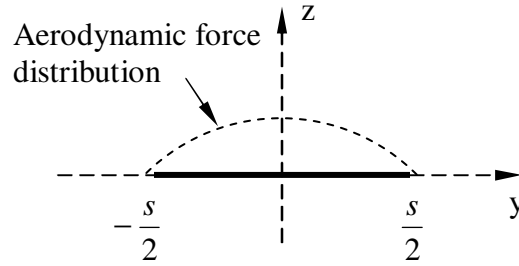


Figure 5.16 Spanwise aerodynamic force

Bending moment due to aerodynamic force acting on the wing

$$M_a = F_a \cdot \frac{s}{2} \quad (5.10)$$

where  $F_a$  is the total aerodynamic force on the wing

Put Eq. (5.10) and Eq. (5.6) together

$$F_a = 2 \cdot W_c \frac{M_{AF}}{M_c} = 2 \cdot V_a \frac{W_c}{V_c} \quad (5.11)$$

Therefore the calibration scale factor  $CSF = \frac{W_c}{V_c}$

where  $V_a$  and  $V_c$  are the measured strain gauge signal (mV) from the wind tunnel test and static calibration test respectively.

An experiment for the calibration scale factor ( $CSF$ ) is carried out by placing a load at the tip of the wing. By setting different weight of 0.2g, 0.5g, 1g, 2g, 5g at the wing tip, the relationship between  $W_c$  and strain gauge signal (mV) is shown in Fig. 5.17, Fig 5.18 and Fig. 5.19 for heaving, pitching and combined motion.

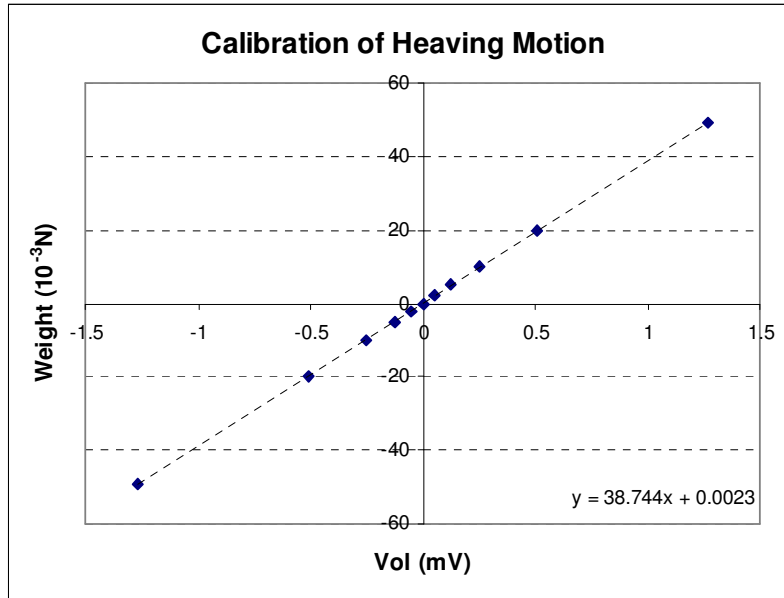


Figure 5.17 Relationship between tip load  $W_c$  and strain gauge signal in heaving motion

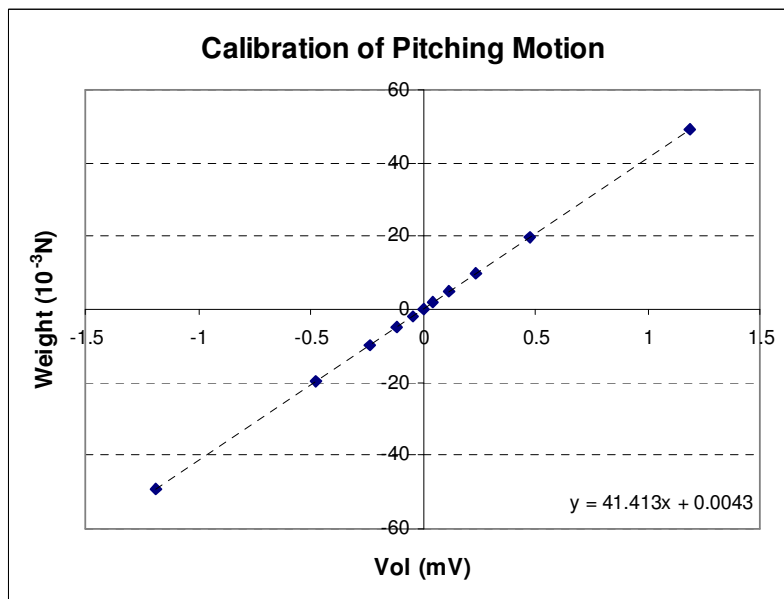


Figure 5.18 Relationship between tip load  $W_c$  and strain gauge signal in pitching motion

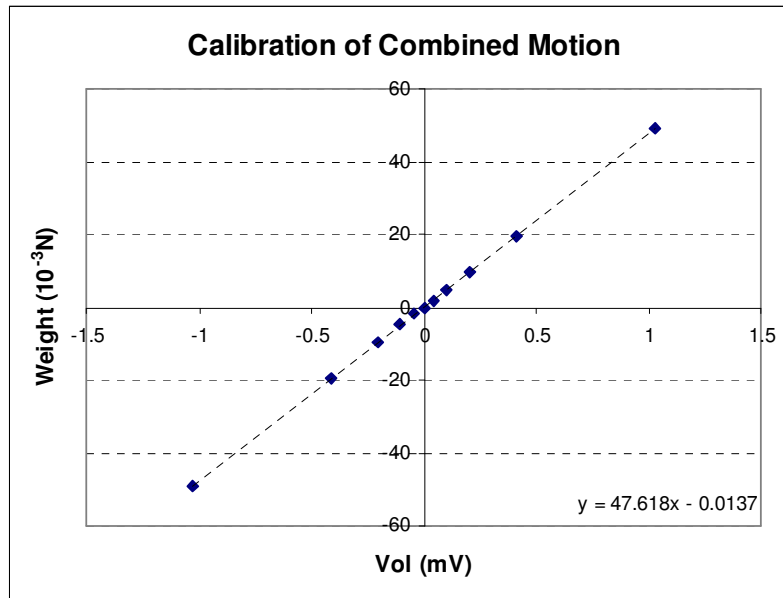


Figure 5.19 Relationship between tip load  $W_c$  and strain gauge signal in combined motion

Since a high density dope is used to attach the skin on the wing frame meanwhile the skin is fully stretched by the dope the rigidity of these three wings are slightly different due to the slight different quantity of the dope on the wing skin. Hence the calibration scale factors (*CSF*) for heaving, pitching and combined motion are slightly different given as:  $38.744 \times 10^{-3}$  N/mV,  $41.413 \times 10^{-3}$  N/mV and  $47.618 \times 10^{-3}$  N/mV.

#### 5.1.4.2 Inertia Force Measurement

In the flapping wing aerodynamic force measurement the inertia force due to the weight of the wing have to be carefully measured in such a way that the aerodynamic force can be accounted for accurately. However, the readings recorded by the strain gauges at the root of the wing consist of inertia and aerodynamic forces. Hence the aerodynamic force has to be obtained by subtracting the inertia force from the total force measured by the stain gauge in the same time history.

As a means of measuring the total inertia force due to the motion of the small wing (150mmx30mm), the wing skin is rolled up and placed along the spar so that no

aerodynamic force is produced when the wing is set in motion. In this way the voltage from the strain gauge at the root is only due to the bending moment of the wing inertia without any aerodynamic force effect. The inertia force test is illustrated in Fig. 5.20. Subject to different frequencies (4Hz-8Hz) and wing motions the inertia force test results are shown below.

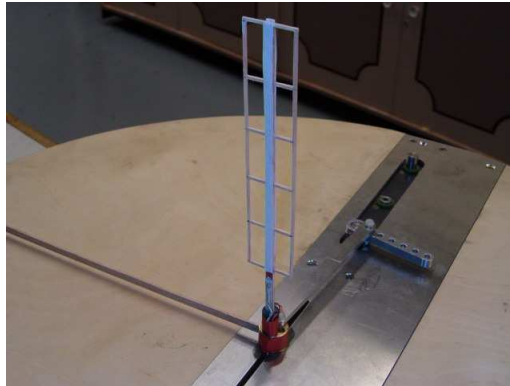


Figure 5.20 Inertia force test

For the inertia test of heaving motion the wing weight is 0.83g. For the pitching motion the wing has 0.85g weight and in the combined motion test the wing has 0.88g weight. By measuring the inertia force in terms of voltage (mV) against frequency square  $f^2$  the results are shown in Fig. 5.21.

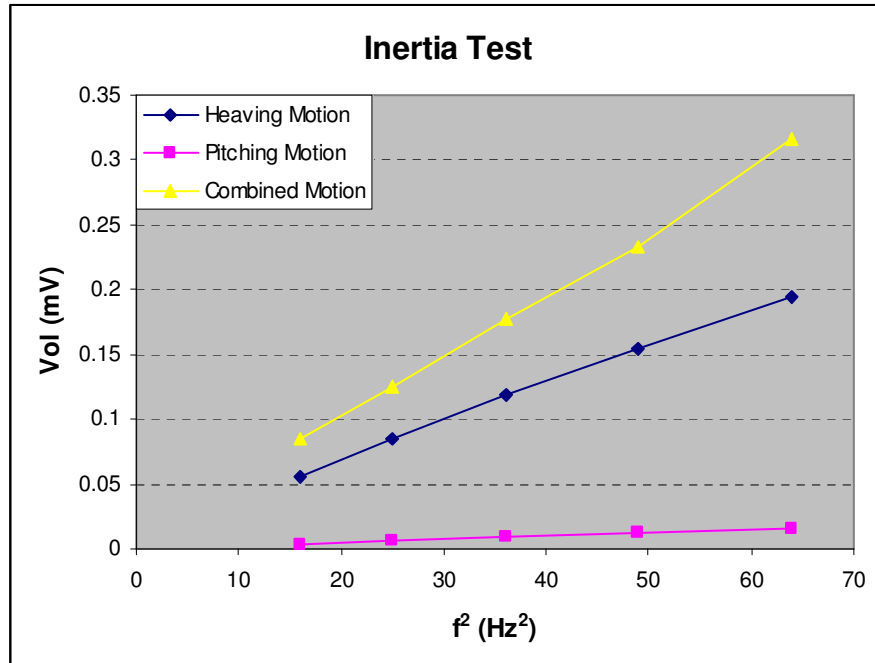


Figure 5.21 Inertia test results

From the test results the measured inertia in voltage is proportional to frequency square which shows the trend as expected. However these results are later converted to actual inertia force by the calibration scale factor to compare with theoretical calculation.

#### 5.1.4.3 Force Measurement in Heaving Motion

In the heaving motion test the wind speed increases from 2m/s to 8m/s with 2m/s increment while the frequency increases from 4Hz to 8Hz with 1Hz variation. And the heaving amplitude is 10mm. As stated earlier, the total force measured in the test consists of aerodynamic and inertia forces. To obtain the pure aerodynamic force the inertia force is subtracted from total force in the same time history. The wing motion is illustrated in Fig. 5.22. The wing starts moving upward from its minimum to maximum position and then moves downward to minimum position again from position (a) to position (e). By subtracting the inertia strain the strain measured due to the heaving aerodynamic force in voltage is shown in Fig. 5.23. The results show the peak amplitude in different cases with different frequencies from 4Hz to 8Hz and different speeds from 2m/s to 8m/s.

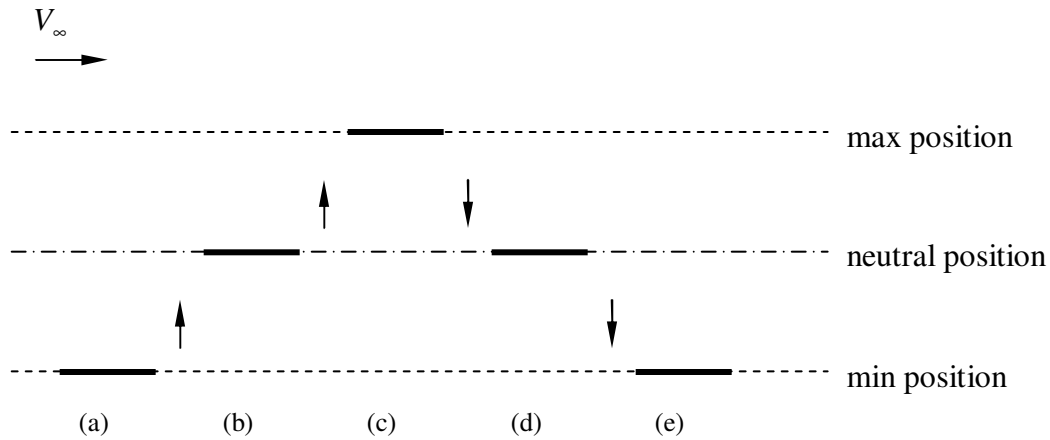


Figure 5.22 Heaving motion in wind tunnel test

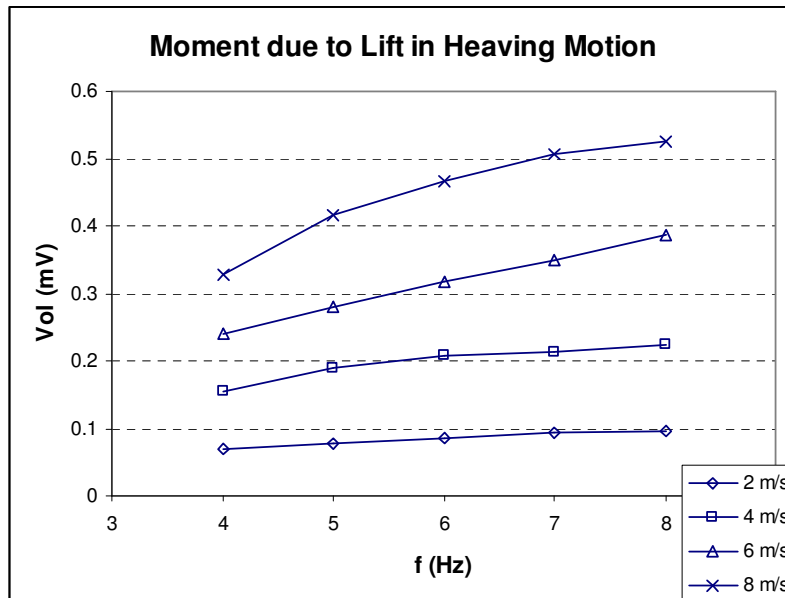


Figure 5.23 Moment due to lift in heaving motion

#### 5.1.4.4 Force Measurement in Pitching Motion

In the pitching motion test shown in Fig. 5.24 the wing starts moving with a maximum negative angle of attack  $\alpha = -5^\circ$ . In position (a) the wing is rotating clockwise to the neutral position to position (b). Then it reaches to position (c) with a positive angle of attack  $\alpha = 5^\circ$ . From position (c) to (d) the wing is moving anticlockwise till neutral position again. In position (e) the wing is repeating the next cycle. By subtracting the

inertia strain the strain due to the pitching aerodynamic force in voltage is shown in Fig. 5.25. The results show the peak amplitude in different cases with different frequency from 4Hz to 8Hz and different speed from 2m/s to 8m/s.

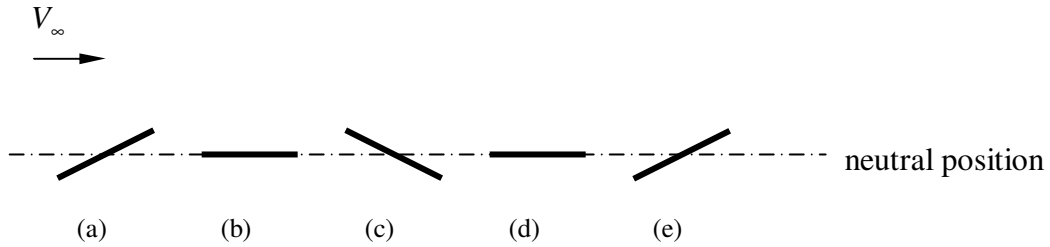


Figure 5.24 Pitching motion in wind tunnel test

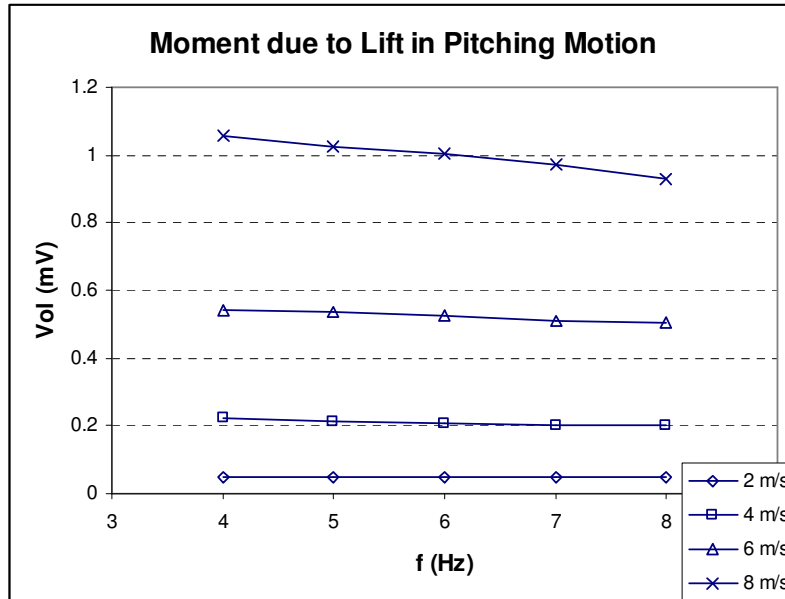


Figure 5.25 Moment due to lift in pitching motion

#### 5.1.4.5 Force Measurement in Heaving and Pitching Combined Motion

In the heaving and pitching combined motion test illustrated in Fig. 5.26 the wing starts moving from minimum position with a positive angle of attack  $\alpha = 5^\circ$  in position (a). When it reaches to the neutral position in position (b) the angle of attack is zero. In position (c) the wing moves to the maximum position with a negative angle  $\alpha = -5^\circ$ .

Then the wing moves back to the neutral position again in position (d) with zero angle of attack. After it reaches to position (e) the wing is repeating the next cycle. By subtracting the inertia strain the strain due to the aerodynamic force in voltage is shown in Fig. 5.27. The results show the peak amplitude in different cases with different frequencies from 4Hz to 8Hz and different speed from 2m/s to 8m/s.

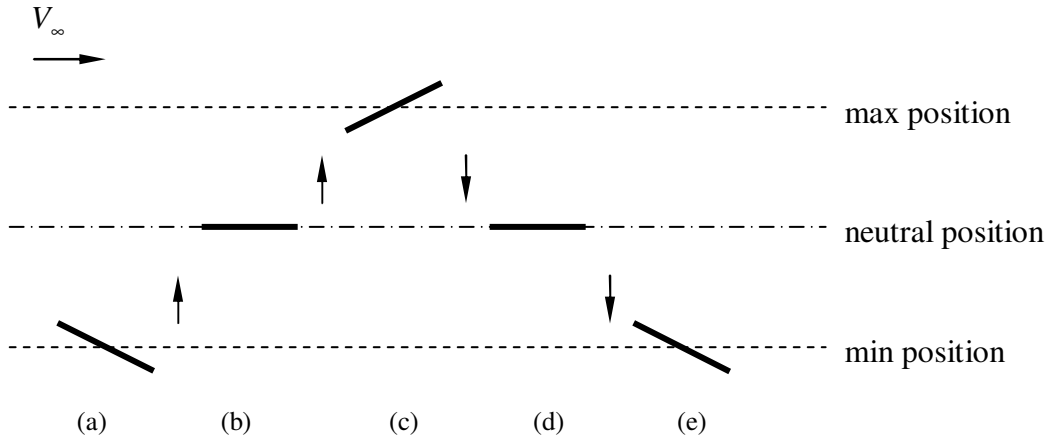


Figure 5.26 Combined motion in wind tunnel test

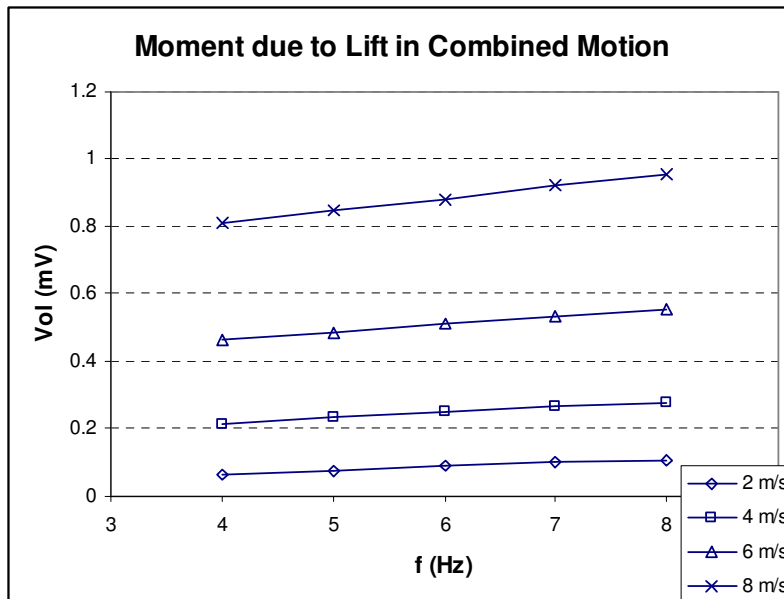


Figure 5.27 Moment due to lift in combined motion



### 5.1.5 Test Results Comparison

In this section the measured forces are converted from voltage to Newton by the calibration scale factor and compared with theoretical calculations.

#### 5.1.5.1 Inertia Force Comparison

In the inertia test of heaving motion the calibration scale factor is  $38.744 \times 10^{-3} \text{N/mV}$  which is the gradient of the curve in Fig. 5.17. The comparison of test results and theoretical calculation is plotted in Fig. 5.28 which shows the converted inertia force against frequency square  $f^2$ . It is seen that the measured inertia force is slightly lower than that predicted by theoretical calculation. The comparison shows the peak value of inertia amplitude. The maximum peak value is obtained when the wing moves to extreme position. Due to the small deformation of the wing frame when the wing root arrives at its extreme position whereas the wing tip does not. Hence the wing root reaches to maximum acceleration and the wing tip does not. The acceleration of the whole wing frame is not able to reach maximum value when the wing moves to its extreme position. This is why the experimental results are slightly lower than theoretical calculation.

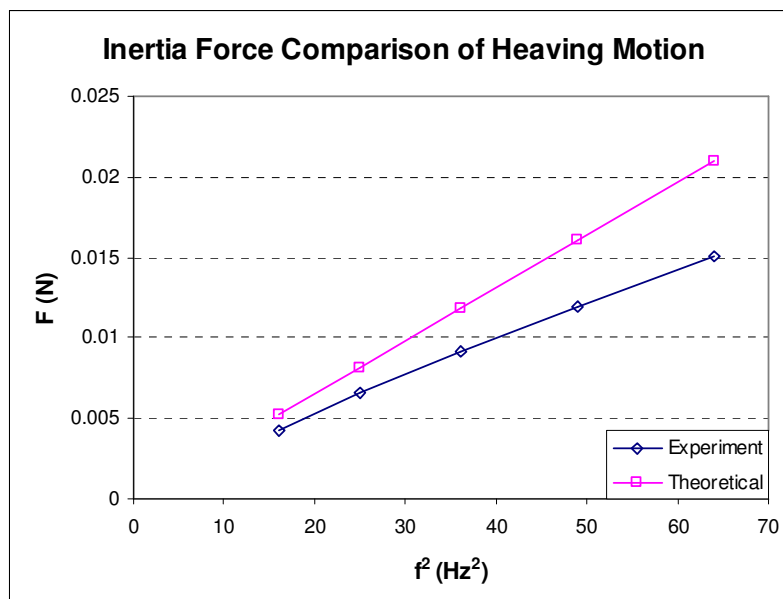


Figure 5.28 Inertia force comparison of heaving motion

In pitching motion test the inertia force is due to the rotation of the wing. By using the calibration scale factor  $41.413 \times 10^{-3} \text{N/mV}$  shown in Fig. 5.18 the force is converted and shown in Fig. 5.29. The force is rather small compared with the inertia force in heaving which caused by the moment of rotation. Therefore the theoretical calculation of inertia is not provided.

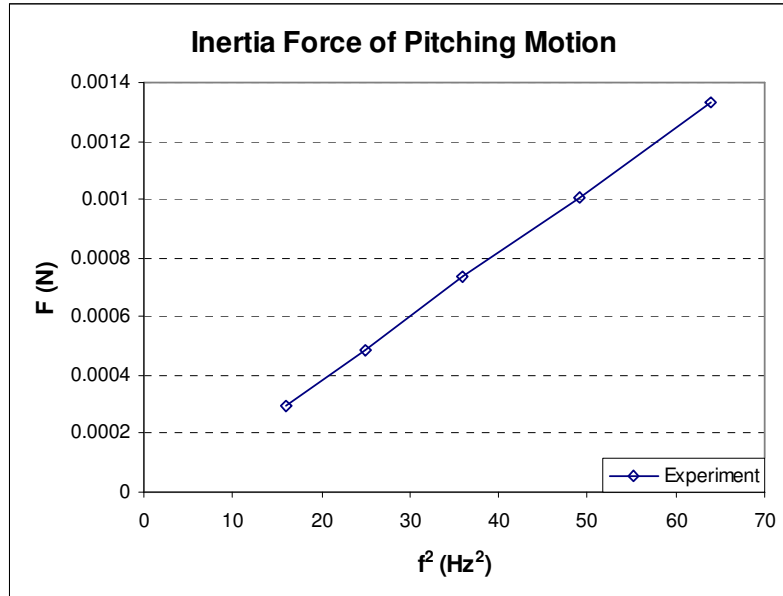


Figure 5.29 Inertia force of pitching motion

By using the calibration scale factor of  $47.618 \times 10^{-3} \text{N/mV}$  shown in Fig. 5.19 the inertia force of combined motion is converted as shown in Fig. 5.30. Similar to the pure heaving case, the test results show a slightly higher inertia force than that predicted by theoretical calculation. In combined motion test more mechanical linkages are placed on the test rig which induced higher noise. Therefore the test results are higher than theoretical calculation.

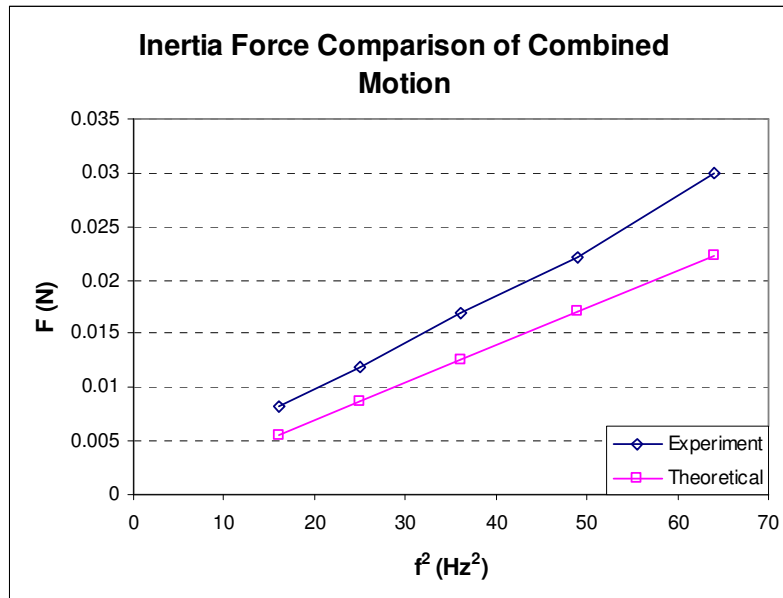


Figure 5.30 Inertia force comparison of combined motion

### 5.1.5.2 Aerodynamic Force Comparison

In this section the aerodynamic force is converted to force in Newton and compared with theoretical calculation by Theodorsen's theory. In different frequencies and speeds the peak amplitude of lift is shown in Fig 6.31, Fig. 5.32 and Fig. 5.33 in heaving motion, pitching motion and combined motion by using Theodorsen's theory. The blue curve with 'Exp' is the experimental result and the pink curve with 'Theo' indicates the theoretical calculation.

Fig. 5.31 shows the peak amplitude of lift for heaving motion in different frequencies and speeds and comparison with Theodorsen's theory. For each speed case the measured force reduces slightly with increasing of frequency. At high frequency the vertical speed  $\dot{h}$  in heaving is proportional to flapping frequency and with increasing frequency the effective incidence of the wing is increased. With the increasing of flapping frequency from 2Hz to 8Hz the vertical speed is increased 4 times subject to the same forward speed which leads to a increasing of effective incidence. When the frequency reaches 8Hz the flow separation might occurs due to a large angle of attack. Hence the test results show an appreciable reduction of 11.6% in lift compared with theoretical calculation.

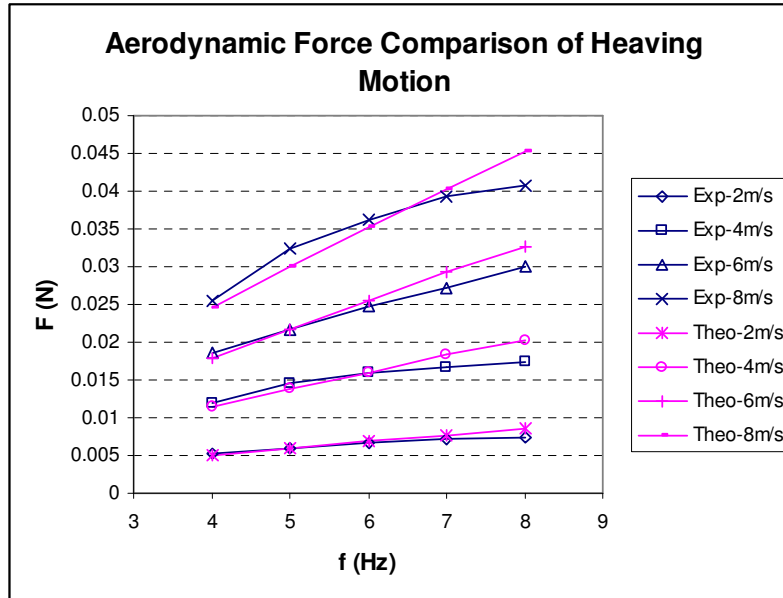


Figure 5.31 Aerodynamic force comparison for heaving motion

The test result of heaving motion in time history for 4m/s and 4Hz is shown in Fig. 5.32 subject to 4m/s and 4Hz case. The blue curve ' $AF$ ' is lift. The pink curve ' $Inertia$ ' is measured inertia force. And the yellow curve ' $Dis$ ' indicates the displacement of the wing which is scaled down five times. Compared with computed results in Fig. 5.33 the test results show a good agreement in time history. The test result confirms that the inertia is approximately in phase with displacement. Note that when the wing is in its extreme position a very small lift is generated due to the inertia of fluid. The lift reaches to maximum at the neutral position. Although the difference between calculated and measured inertia is large as shown in Fig. 5.30, it does not affect the lift as shown in Fig. 5.31. This is because the lift shown in Fig. 5.31 is the peak value which is  $90^\circ$  phase difference from the peak of inertia. The converted inertia and aerodynamic forces of three motions are tabulated in Appendix from Table A1 to Table A3. The raw data of the rest of the other cases in time history are show in Appendix from Figs. A7 to A26.

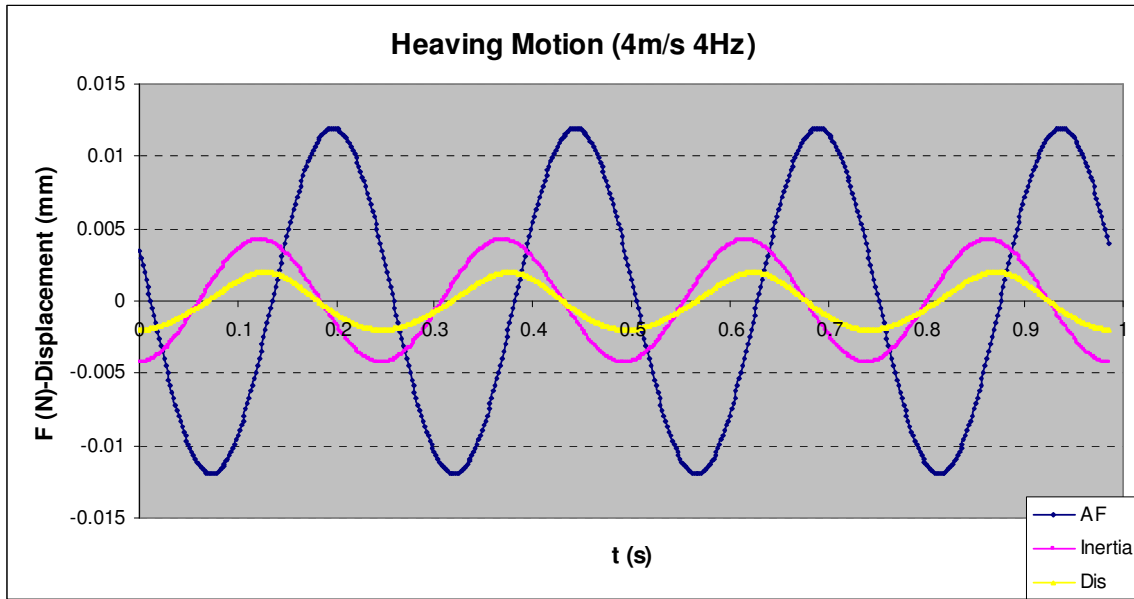


Figure 5.32 Test result of heaving motion in time history for 4m/s, 4Hz

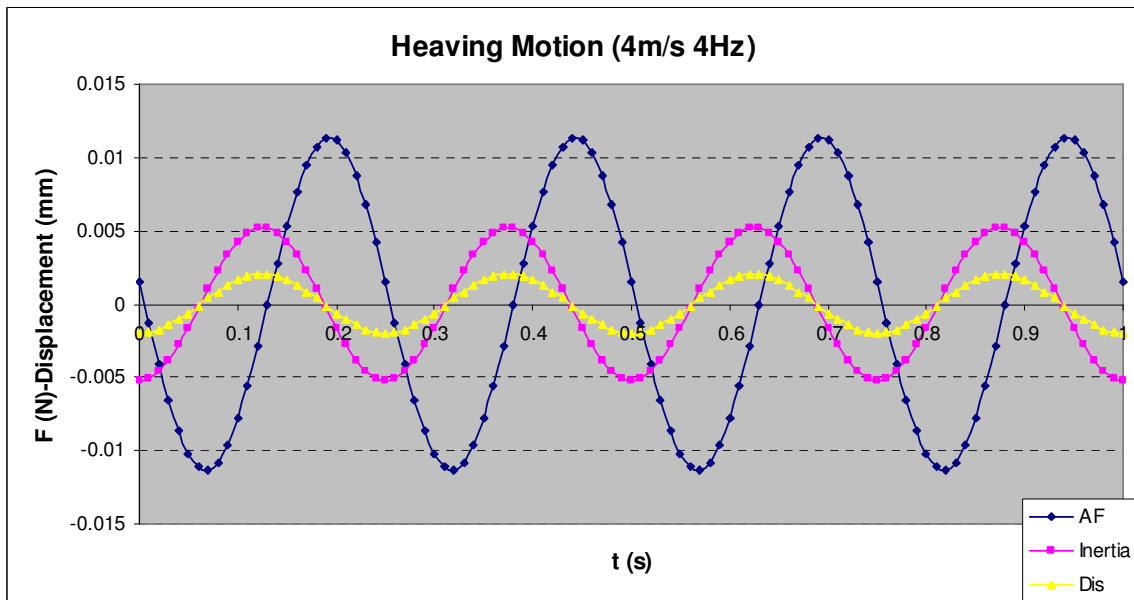


Figure 5.33 Computed result of heaving motion in time history for 4m/s, 4Hz

In Fig. 5.34 the test results of pitching motion is shown and compared with theoretical calculation. The test results are higher than theoretical calculation. The maximum peak is obtained when the wing rotates to the maximum angle of attack which is  $5^\circ$ . However the

wing experiences an additional twist at this moment with maximum aerodynamic force applied on the wing frame. Therefore the lift shows even higher values at the high speeds. With the increasing of speed the additional force due to wing twist is also increased from 15% to 26% compared with theoretical calculation.

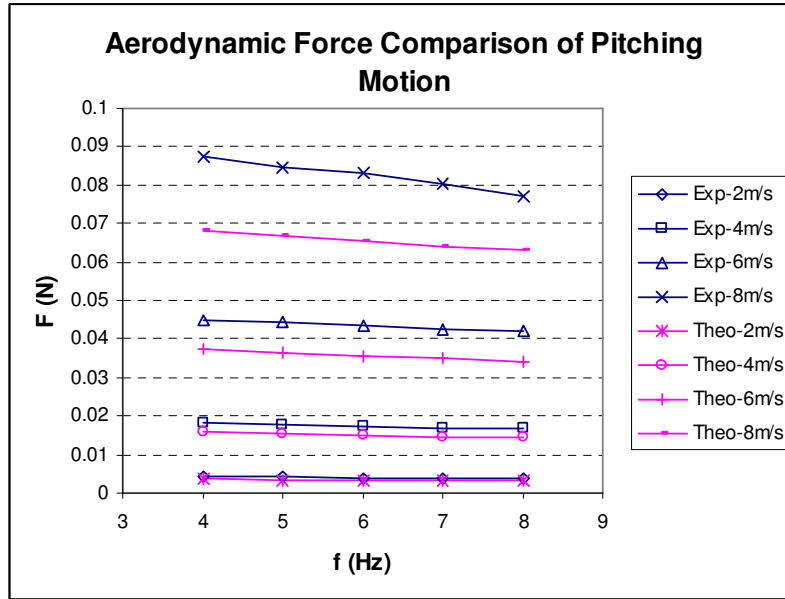


Figure 5.34 Aerodynamic force comparison for pitching motion

The test result of pitching motion in time history is shown in Fig. 5.35 for 4 m/s and 4Hz case. The blue curve '*AF*' is the aerodynamic force of the wing, the pink curve '*Inertia*' is inertia force due to pitching motion which is rather small, and the yellow curve '*AoA*' indicates the pitch angle which is twenty times scaled down. The test result shows a good comparison with computed result shown in Fig. 5.36. When the wing moves to its extreme position with maximum pitch angle the lift reaches maximum and in the neutral position the lift is almost zero. The raw data for the rest of the test cases are shown in Appendix from Figs. A27 to A46.

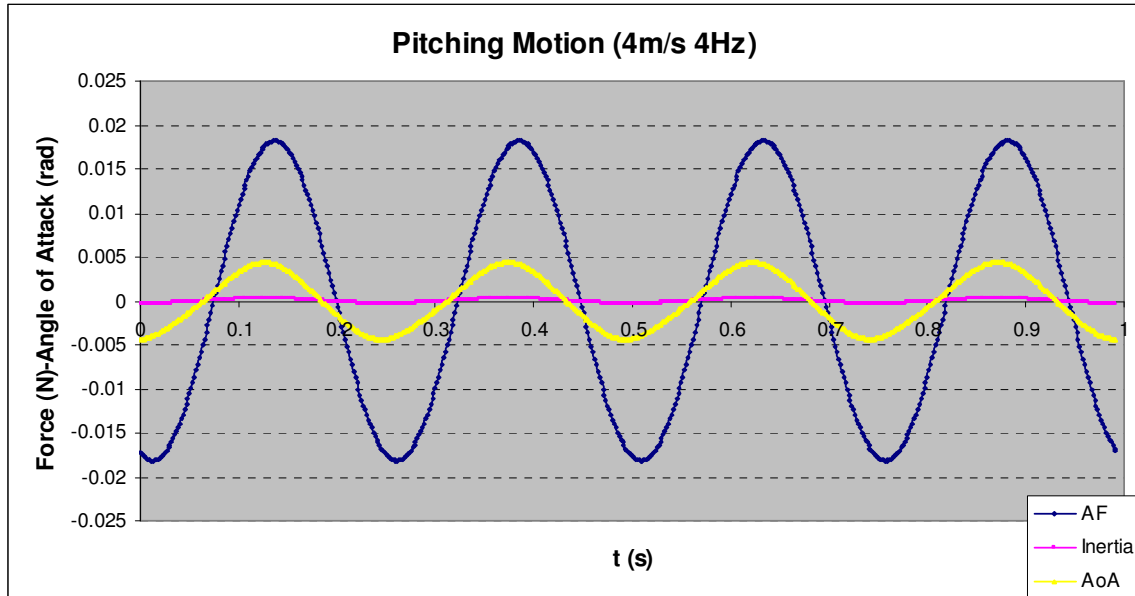


Figure 5.35 Test result of pitching motion in time history for 4m/s, 4Hz

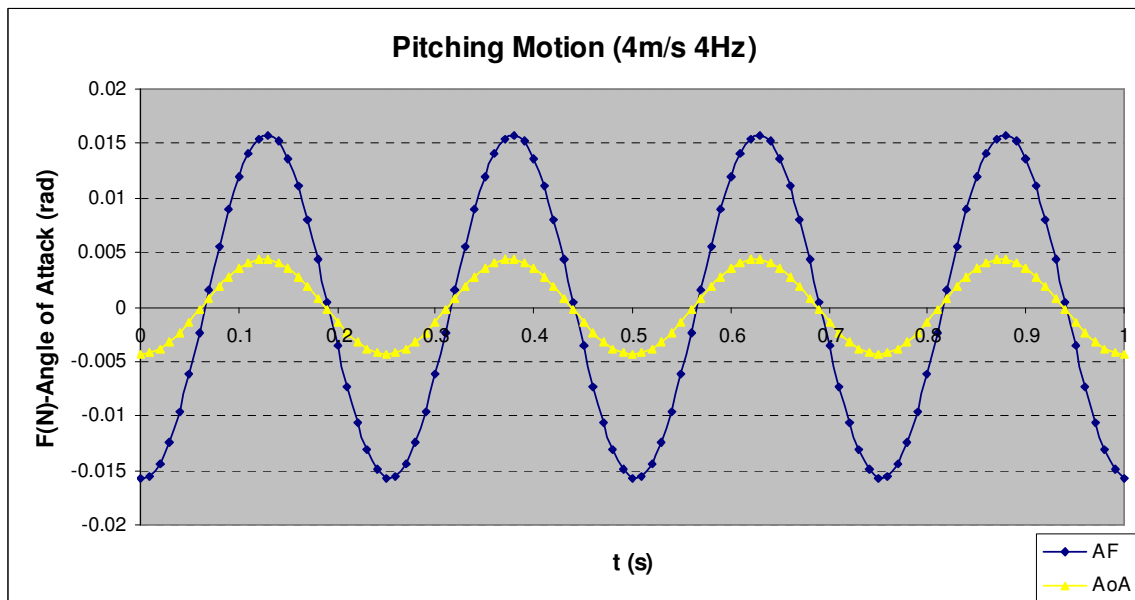


Figure 5.36 Computed result of pitching motion in time history for 4m/s, 4Hz

In Fig. 5.37 the test results of combined motion is illustrated with theoretical calculation. The test results show significantly higher lift measured at high speeds. This is due to the wing twist in high pitch angle with maximum aerodynamic force applied on it.

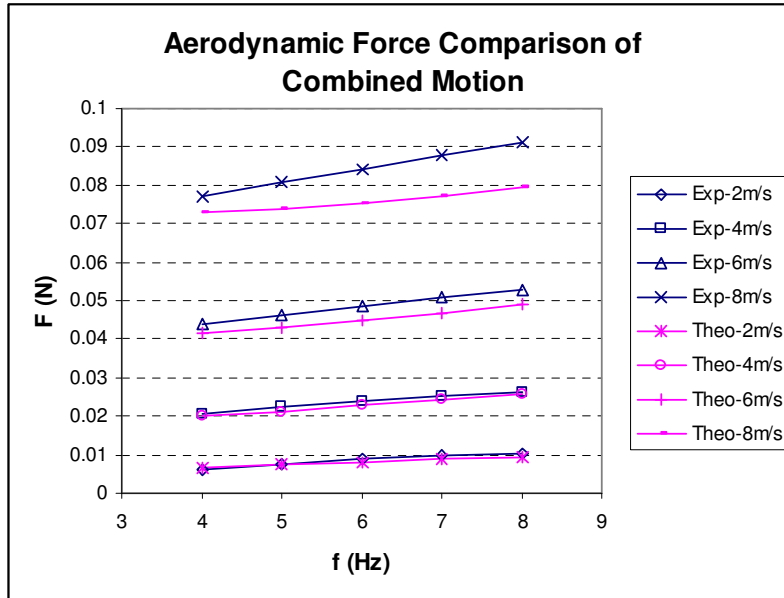


Figure 5.37 Aerodynamic force comparison for combined motion

Overall it is seen that the lift amplitudes measured over the range of frequencies and wind tunnel speeds show a good agreement with theoretical calculation. Due to the flow separation at high frequencies it affects the lift generation for all three motions which shows that the test results are slightly lower in heaving motion compared with theoretical calculation. However the wing frame deformation is more effective and the test results are higher in pitching and combined motion compared with theoretical calculation. With the increasing of speed the additional lift due to wing twist is also increased from 3.7% to 10.9%. Hence the wing flexibility is an essential factor in affecting the aerodynamic force in flapping wing motion.

The test result of combined motion in time history is shown in Fig. 5.38 for the same flow speed and wing frequency. The blue curve ' $AF$ ' is the aerodynamic force of the wing, the pink curve ' $Inertia$ ' is the inertia force, and the yellow curve ' $Dis$ ' indicates the displacement which is five times scaled down. Compared with computed result in Fig. 5.39 the test result shows a good agreement in terms of phase shift between forces and displacement. The raw data of rest of the other cases are shown in Appendix from Figs. A47 to A66.



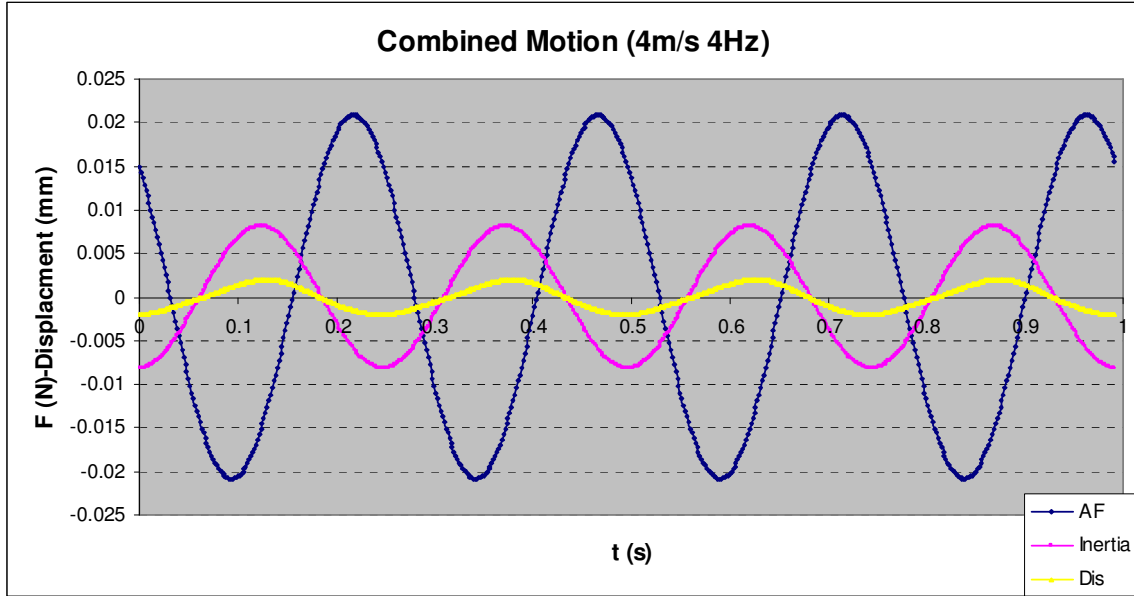


Figure 5.38 Test result of combined motion in time history for 4m/s, 4Hz

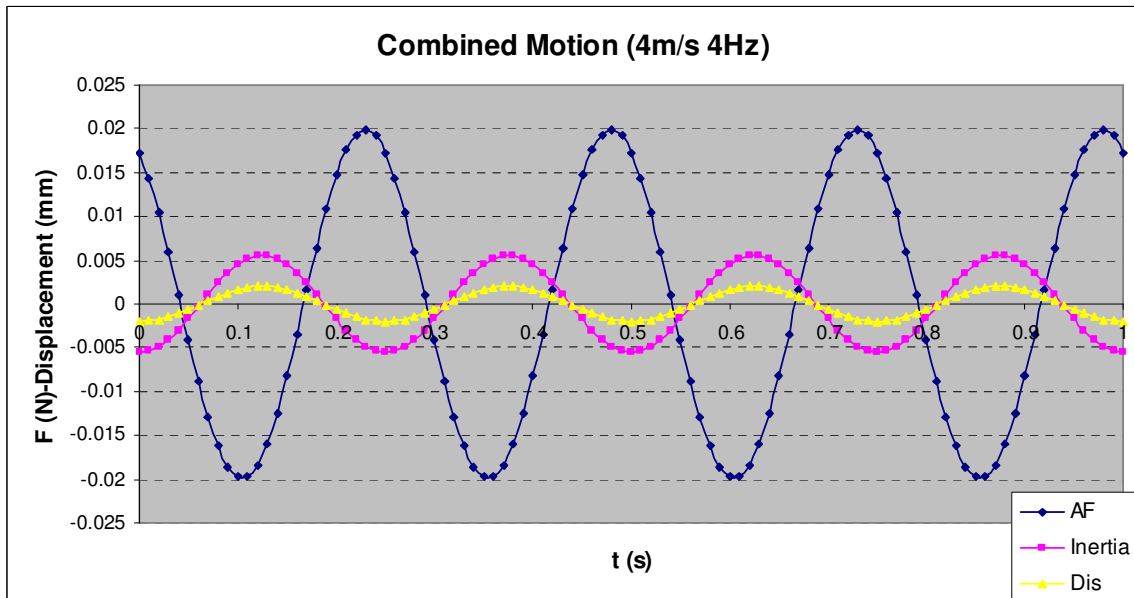


Figure 5.39 Computed result of combined motion in time history for 4m/s, 4Hz

## **5.2 Wind Tunnel Test of Flexible Wings**

The wing flexibility effect is studied in this section. Since the wing is subject to deformation when loads are applied on the frame the wing flexibility becomes a very important issue in affecting the wing performance in flapping motion in terms of force generation, wing motion control and power consumption.

### **5.2.1 Experimental Study of Flexible Wing**

The study is mainly based on the wind tunnel test. The objective of the study is to investigate the flexibility effect of flapping wings on the aerodynamic load and power efficiency. Three wings with similar configurations are manufactured with slightly different degrees of structure flexibility. The investigations are based on the experimental work carried in the same T3 wind tunnel used previously. Aerodynamic loads are measured by 2-component balance.

#### **5.2.1.1 Wing Configuration**

Wind tunnel tests are carried out to investigate the power efficiency and flexibility effect of flapping wings. The wing configurations are illustrated in Fig. 5.40. Three wings are studied with similar configurations with 460mm span and 120mm chord. The wing leading edge and root are made of 2mm CFC rods which are jointed as an L-shape frame. A sweep forward cross bar is placed and connected to the L-shape frame to obtain a triangle shape with rather rigid area. The outer wing is supported by a few piano strings as flexible area compared with inner wing. With same wing area the wing configurations can be quantified as the fraction of rigid area or flexible area over total wing area. The specification of the wing configurations are tabulated in Table 5.1.

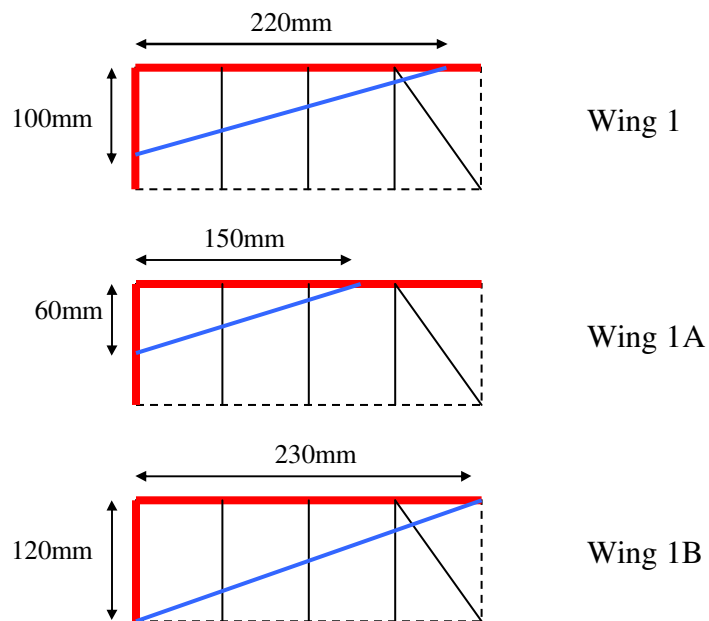


Figure 5.40 Wing configuration

Wing Type	Weight(g)	Rigid Area(m <sup>2</sup> )	Total Area(m <sup>2</sup> )	Rigid Area Fraction
Wing 1	8.09	0.022	0.0552	39.9%
Wing 1A	7.75	0.009	0.0552	16.3%
Wing 1B	8.14	0.0276	0.0552	50%

Table 5.1 Specifications of wing sample

### 5.2.1.2 Experimental Arrangement

A radio control model with flapping mechanism is employed to carry out wind tunnel test. The original wings are replaced by designed wing cases. A two-component balance is constructed by two load cells. The fuselage is mounted on the sting upside down which fixed on the on the load cells. The lift is measured by the horizontal load cell and drag is measured by vertical load cell which is illustrated in Fig. 5.41. Since the model is mounted upside down the vertical displacement is defined as positive down.

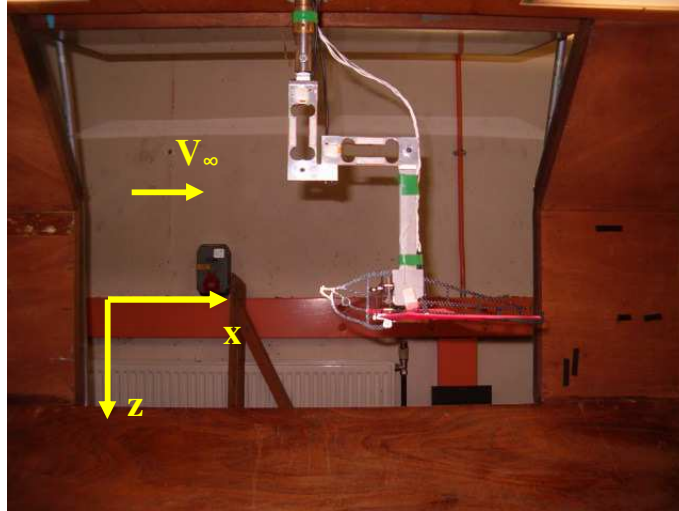


Figure 5.41 Test rig setup

The flapping mechanism is driven by a brushless inrunner motor (BA BL1230 4200kv) which is powered by a power plant. Flapping frequency is controlled by a speed controller and measured by a frequency counter. The control system is illustrated in Fig. 5.42.

The electrical system is shown in Fig. 5.43. The working voltage is fixed at 9Volts. The input power varies by varying the input current  $I$  governed by a speed controller to change the flapping frequency. The consumption of the speed controller is measured as  $I'$  which is 0.292A. The flapping frequency is measured by a frequency counter. Aerodynamic loads are measured by load cells and the wing motion is monitored by a strain gauge placed at the wing root. The power input to the motor is given in Eq. (5.12).

$$P = V \cdot (I - I') \quad (5.12)$$

where  $P$  is the power input to the motor,  $V$  is the input voltage,  $I$  is the current input to the speed controller and  $I'$  is the current consumption of the speed controller

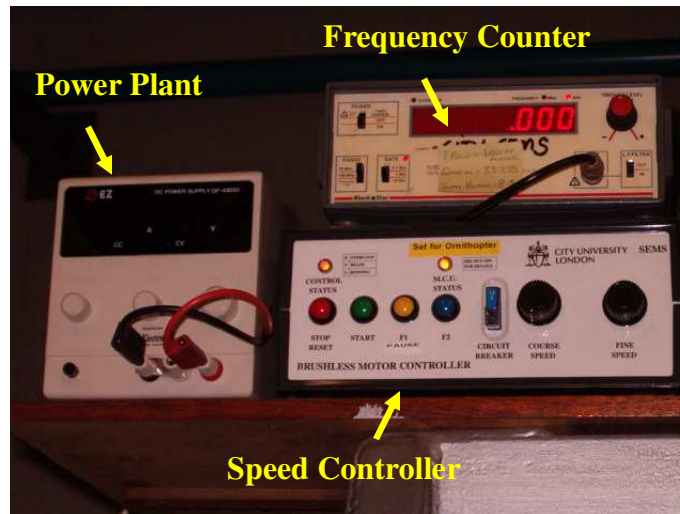


Figure 5.42 Electrical equipment setup

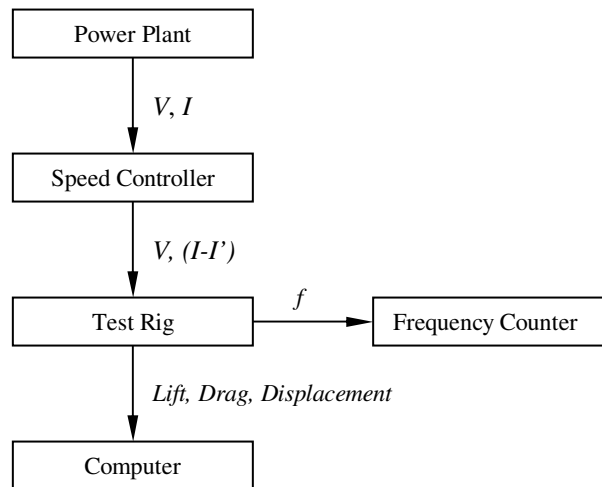


Figure 5.43 Data log setup

### 5.2.1.3 Load Cell Calibration

To convert the load cell readings in counts to force in Newton calibration is carried out by placing unit load in vertical and horizontal direction respectively. The lift force calibration is carried out by hanging unit load on the sting and drag force calibration is carried out by placing horizontal load on the sting through pulley system illustrated in Fig. 5.44.

The sign for loading is based on the coordinate referred in Fig. 5.41. The applied load is set from 0g to 170g with 10g increment and placed on the vertical and horizontal hangers respectively. The calibration tests are carried out by increasing the load from 0g up to 170g and decreasing from 170g down to 0g. The process is repeated for several times for accuracy. The relationship between readings in counts and applied load are illustrated in Fig. 5.45 and Fig. 5.46.

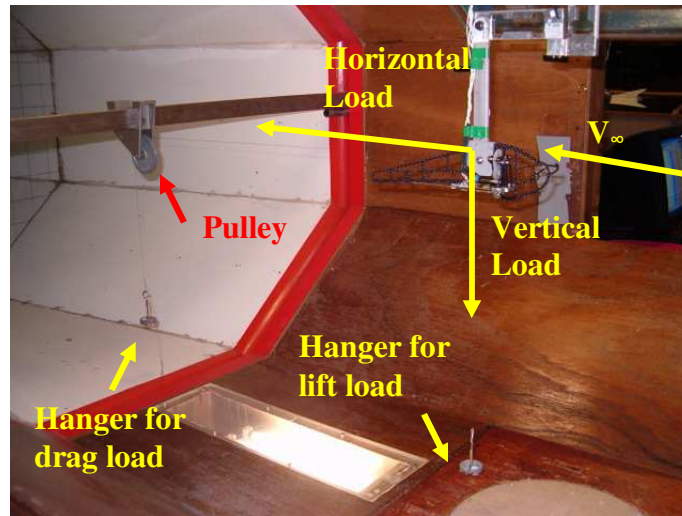


Figure 5.44 Arrangement of balance calibration

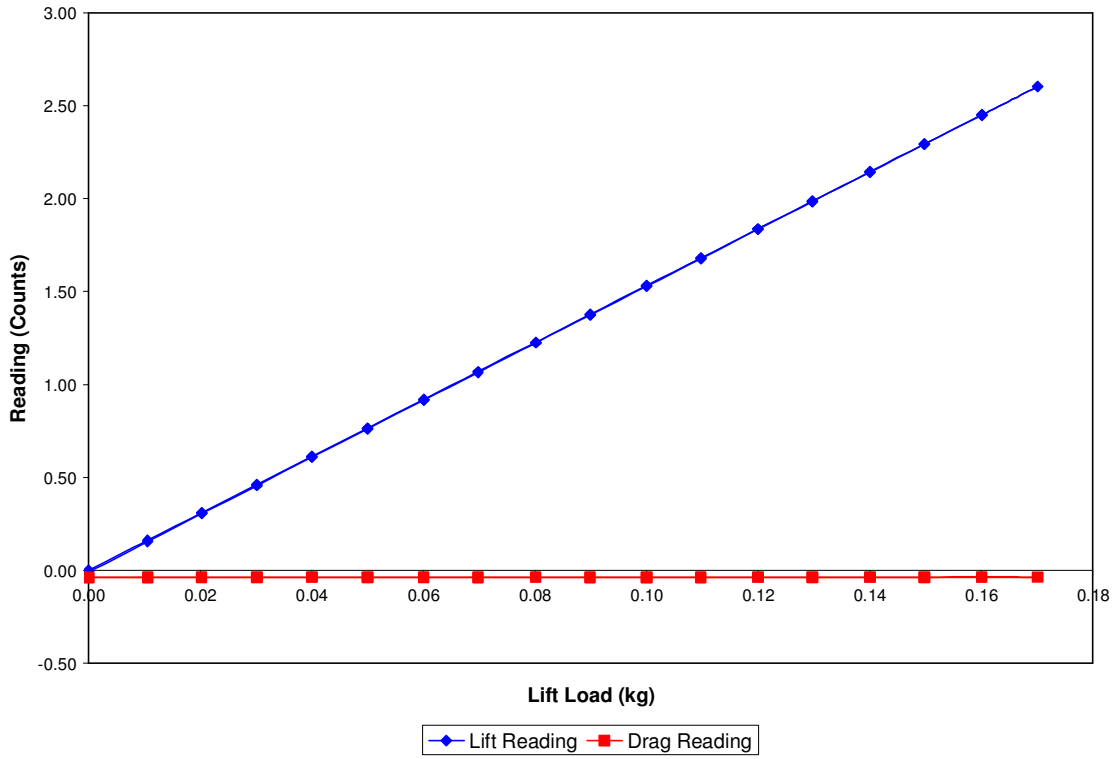


Figure 5.45 Lift force calibration

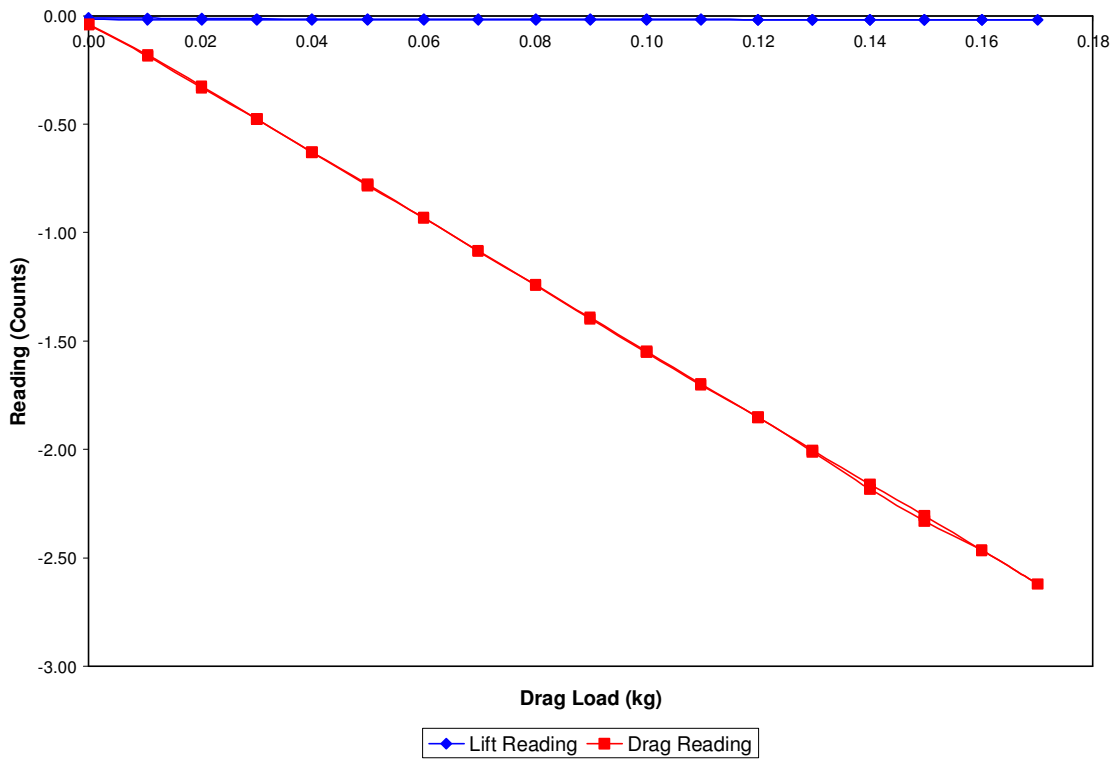


Figure 5.46 Drag force calibration

Based on the setup of the 2-component balance AeroTech's approach assumes that each load is a function of four variables; the two channel output readings and their squares.

$$\begin{cases} L = L(L_c, D_c, L_c^2, D_c^2) \\ D_c = D(L_c, D_c, L_c^2, D_c^2) \end{cases} \quad (5.13)$$

where  $L_c, D_c$  represent the reading in counts for that particular channel,  $L, D$  are the physical loads applied

The equations relating the load (in physical units) to the channel output (in counts) may then be written as

$$\begin{cases} L = a_{0L} + a_{1L} \cdot L_c + a_{2L} \cdot D_c + a_{3L} \cdot L_c^2 + a_{4L} \cdot D_c^2 \\ D = a_{0D} + a_{1D} \cdot L_c + a_{2D} \cdot D_c + a_{3D} \cdot L_c^2 + a_{4D} \cdot D_c^2 \end{cases} \quad (5.14)$$

Or matrix form

$$\begin{bmatrix} L \\ D \end{bmatrix} = \begin{bmatrix} a_{1L} & a_{2L} & a_{3L} & a_{4L} \\ a_{1D} & a_{2D} & a_{3D} & a_{4D} \end{bmatrix} \begin{bmatrix} L_c \\ D_c \\ L_c^2 \\ D_c^2 \end{bmatrix} + \begin{bmatrix} a_{0L} \\ a_{0D} \end{bmatrix} \quad (5.15)$$

The calibration coefficients as provided by Aerotech are shown in Table 5.2.

	$a_0$ (kg)	$a_1$ (kg/mV)	$a_2$ (kg/mV)	$a_3$ (kg/(mV) <sup>2</sup> )	$a_4$ (kg/(mV) <sup>2</sup> )
Lift	5.44E-04	6.46E-02	-7.68E-04	2.17E-04	2.16E-04
Drag	-2.19E-03	-5.62E-04	-6.70E-02	1.90E-04	-5.83E-04

Table 5.2 Calibration coefficients



The uncertainty of the balance is carried out by transferring the converted forces in physical units back to the reading in counts based on the calibration coefficients shown in Table 5.2. Compared with the raw reading in counts the uncertainty of the lift is 0.35% and 0.83% for drag.

#### 5.2.1.4 Sting and Fuselage Calibration

Since the balance is placed in the wind tunnel the aerodynamic effect due to sting, fuselage and balance is first considered without wings. The aerodynamic load due to sting, fuselage and balance are measured from 2m/s to 8m/s with 2m/s increment as shown in Fig. 5.41. To subtract this effect from total aerodynamic forces the vertical and horizontal loads are converted to the lift and drag coefficients with the same characteristic length of the wing. The lift and drag coefficients are plotted against velocity square in Fig. 5.47. The lift and drag forces are shown in Table 5.3. In low speed the coefficient is slightly higher than the coefficient in high speed. This is mainly due to the inaccuracy of the low speed measurement and error in speed control. However the aerodynamic effect of sting and fuselage is rather small compared with the aerodynamic force of flapping wing shown as following.

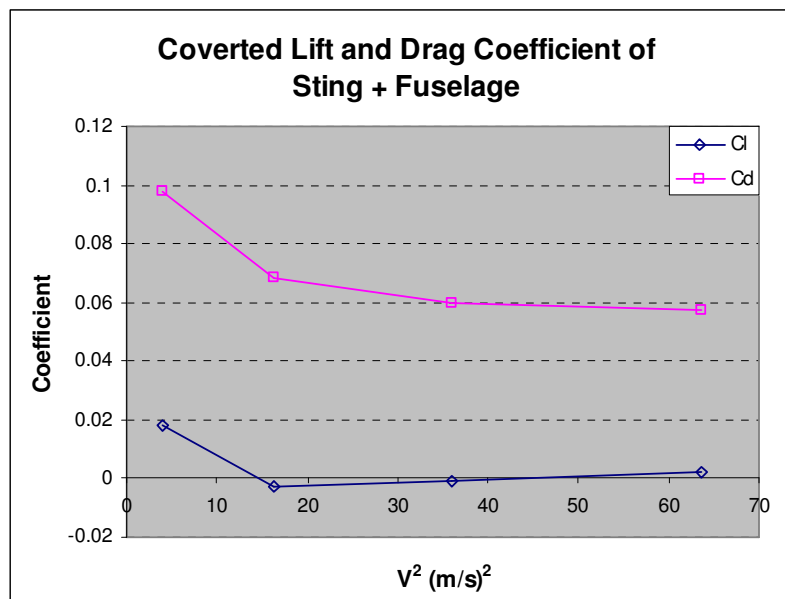


Figure 5.47 Lift and drag coefficients of sting with fuselage

V (m/s)	Lift (N)	Drag (N)
2	0.00232	0.012466
4	-0.00137	0.036143
6	-0.00119	0.069882
8	0.00376	0.118363

Table 5.3 Lift and drag forces of sting and fuselage

### 5.2.1.5 Wing Flexibility Evaluation

To investigate the performance of flexible wing under steady free stream the stiffness of wing frame is calibrated by placing unit load at the trailing edge in 0mm, 50mm, 100mm, 150mm and 230mm away from root in spanwise direction. The deflection at the particular position is shown in Fig. 5.48. Under the same load acting on the wing the deformation of the wing frame varies with the rigid area fraction which can be defined as degree of frame stiffness.

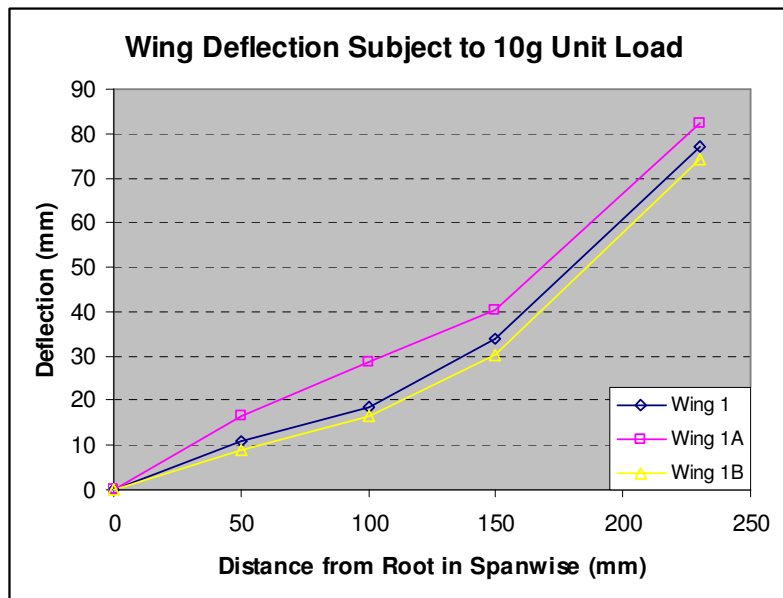


Figure 5.48 Wing frame stiffness calibration

### 5.2.1.6 Steady Aerodynamic Force Test

Steady lift and drag are measured subject to three wing samples with slightly different degrees of stiffness. The test is carried out from 2m/s to 8m/s with the wing placed horizontally in zero angle of attack. By subtracting the effect due to balance and fuselage with sting the lift and drag coefficients of the wing are plotted against velocity square in Fig. 5.49 and Fig. 5.50. Since the wing is constructed by the solid leading edge bar and flexible trailing edge with fabric the wing weight causes an initial camber with trailing edge down in wind off condition. Under almost same wing weight the flexible wing (Wing 1A) deforms the most and stiff wing (Wing 1B) deforms the least giving an appreciable difference in initial angle of attack between the three wings. This difference in turn causes significant difference in lift and drag coefficients at low speeds. However as speed increases more lift is applied on the wing platform and the initial deformation is reduced and the lift and drag coefficients are approaching constant at high speeds.

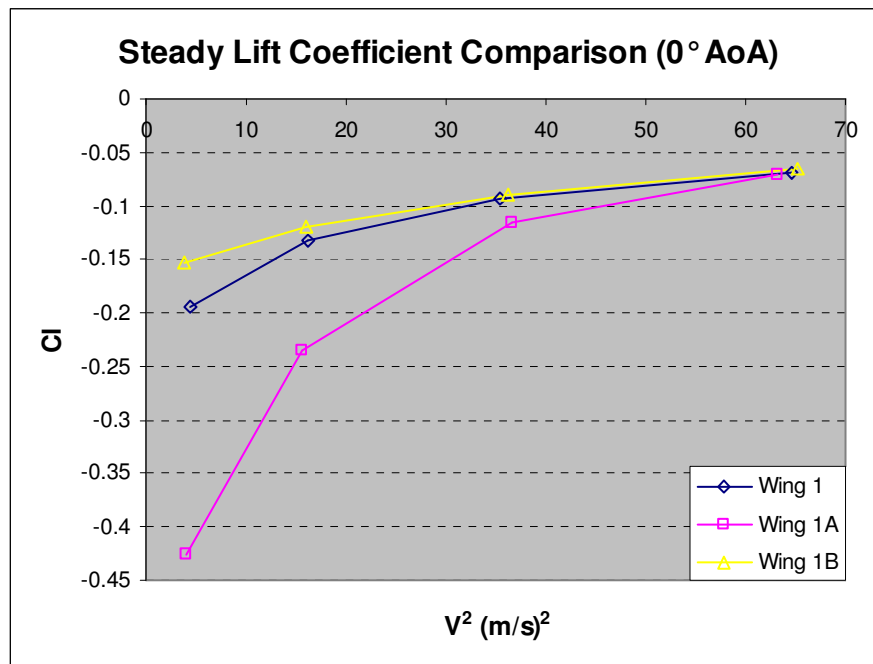
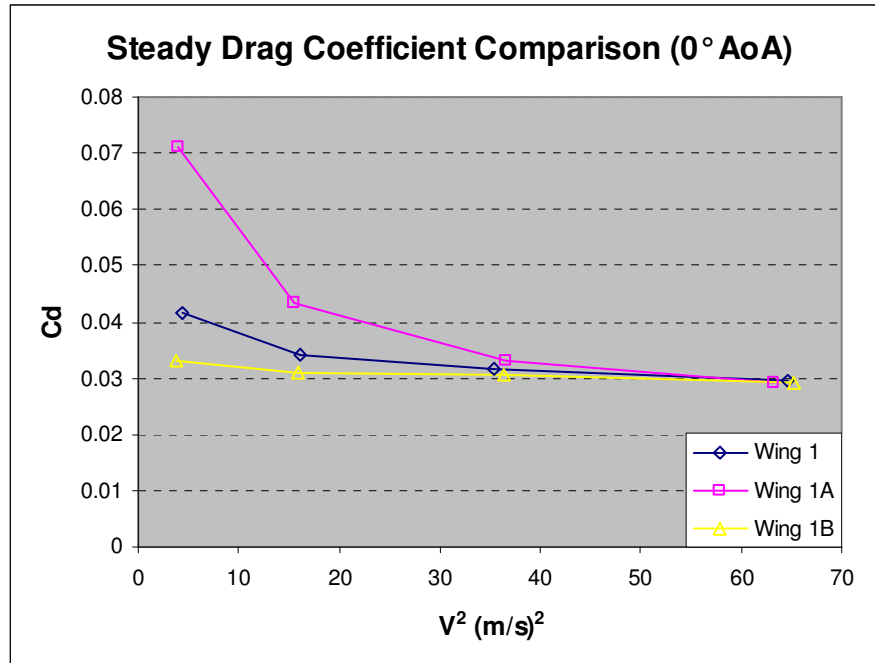


Figure 5.49 Steady lift coefficient at 0° angle of attack

Figure 5.50 Steady drag coefficient at  $0^\circ$  angle of attack

### 5.2.1.7 Inertia Test

The aim of the inertia test is to check the balance is capable of measuring the dynamic force and secondly the inertia test results are essential for the determination of aerodynamic force by subtracting away the inertia force from the total force measured. Consider the weight of the skin and spar placed at the leading edge two beams with the same weight of the wing are employed to simulate the inertia effect. The inertia testing is carried out in 2.5Hz, 3.0Hz and 3.5Hz. The mass of the wing is about 8 gram. As the first step to assess the accuracy of the balance for use to measure dynamic forces the comparisons of test results and theoretical calculations are shown in Fig. 5.51. The difference in inertia force between test results and computed results is 9.6% which indicates the balance is capable of measuring dynamic forces and with reasonable level of accuracy.

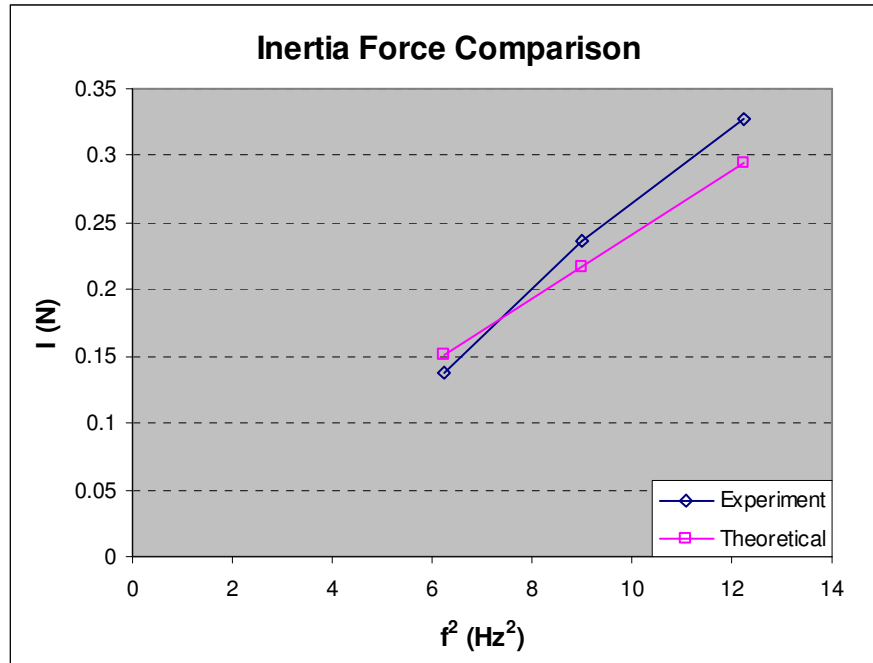


Figure 5.51 Inertia test comparison

### 5.2.1.8 Experiment of Flapping Wing

The wind tunnel test of flapping wings is carried out under  $0^\circ$  angle of attack. The flapping frequency is fixed at 3Hz. The test is carried out from 2m/s to 8m/s with 2m/s increment. The aerodynamic load is measured by the balance. To monitor the displacement of the wing a strain gauge is placed in the centre of the wing. The strain gauge measures the bending moment due to the wing flapping motion. Hence the measured displacement indicates the wing position. The flapping frequency is controlled by speed controller and measured by frequency counter. The data measurement is shown below in Fig. 5.52. The input data and output results are tabulated in Table 5.4.

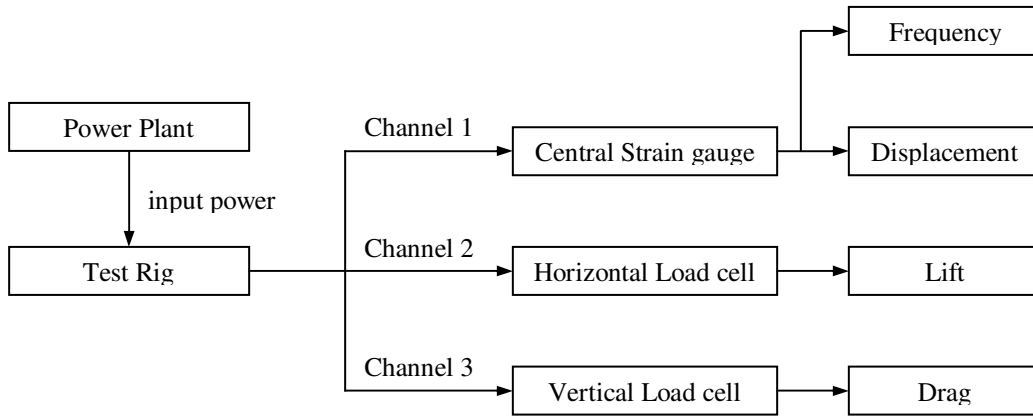


Figure 5.52 Test results measurement

Input		Output	
Speed	$V_{\infty}$	Displacement	$h$
Power	$P$	Frequency	$f$
Angle of Attack	$\alpha$	Lift	$L$
		Drag	$D$

Table 5.4 Input and output data

The loading is measured in terms of reading in counts. By using the calibration coefficients tabulated in Table 5.2 the reading is converted to physical units in Newton. The aerodynamic force of flapping wing is obtained by subtracting the inertia force from total force under the same displacement time history. The lift amplitudes of three wing configurations in  $0^{\circ}$  angle of attack are plotted as shown in Fig. 5.53. The mean horizontal force of flapping wing in terms of either thrust or drag is shown in Fig. 5.54 which is obtained by subtracting the drag of sting with fuselage from total aerodynamic force. The measured net horizontal force is defined negative for thrust and positive for drag. The input power is changed manually during test in order to maintain a constant flapping frequency of 3Hz subject to different flight speeds. The power input to the motor by subtracting the consumption of all electrical equipment is illustrated in Fig. 5.55.

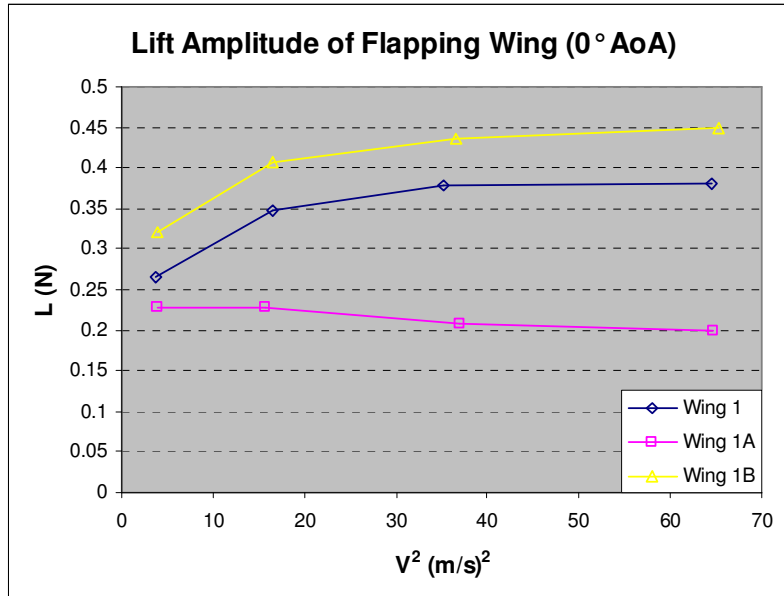


Figure 5.53 Lift amplitude of flapping wings at 3Hz and 0° angle of attack

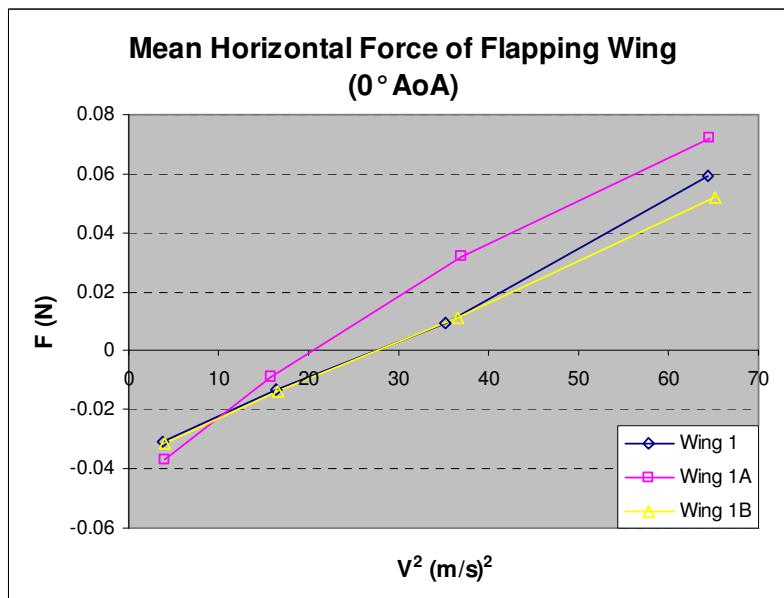


Figure 5.54 Mean horizontal force of flapping wings at 3Hz and 0° angle of attack

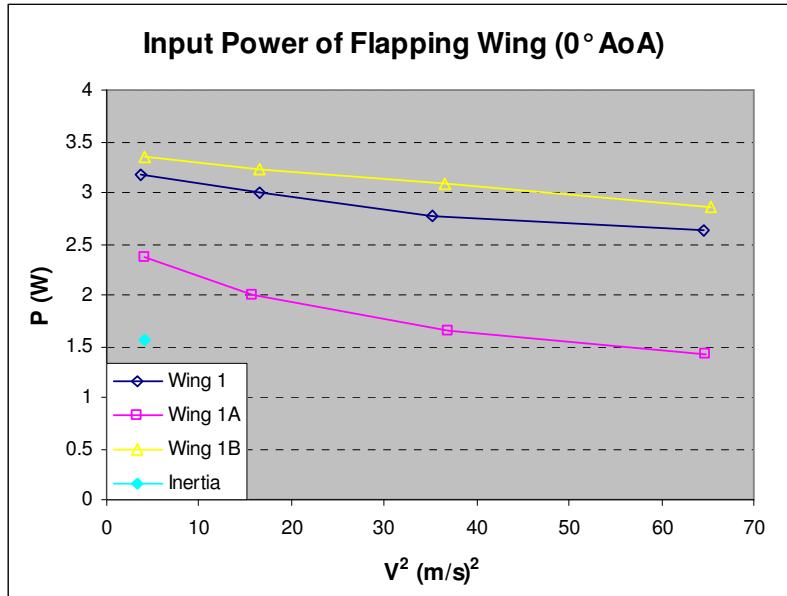


Figure 5.55 Input power of flapping wings at 3Hz and 0° angle of attack

In Fig. 5.53 the lift amplitude is increasing with increasing speed subject to the wing with more rigid area however the most flexible wing generates least amount of lift. This effect of lift loss is due to flow leaking from a larger trailing edge deformation during flapping. In Fig. 5.54 the overall horizontal force of the flapping vehicle is obtained by subtracting the drag force due to sting with fuselage and balance from total force measured. With increased speed the forward force (negative) is reduced and eventually becomes positive drag force. The trend is also slightly affected by the wing frame stiffness with the flexible wing inducing larger deformation during flapping which causes more drag at high speeds. The test results indicate stiffer wing performs better than flexible wing in aerodynamic force generation however it requires more power to actuate flapping motion as seen in Fig. 5.55. The required power, however, is reduced with increasing speed.

Theoretical calculation is carried out by assuming the wing is completely rigid in Fig. 5.56 to compare with the test results of wing 1, Wing 1A and Wing 1B in time history are shown in Fig. 5.57, Fig. 5.58 and Fig. 5.59 at 2m/s and 3Hz. The blue curve 'AF' is the aerodynamic force, the pink curve 'Inertia' is the inertia force of the wing and the yellow curve 'Dis' is the bending moment due to the wing flapping motion which indicates the wing position over a cycle. The measured aerodynamic force and power input to the wing



are tabulated in Appendix from Table B1 to Table B3. The rest of the other test cases in time history are shown in Appendix from Figs. B1 to B12. The test results in time history show a good agreement with theoretical results in Fig. 5.56 in terms of phase shift between forces and displacement.

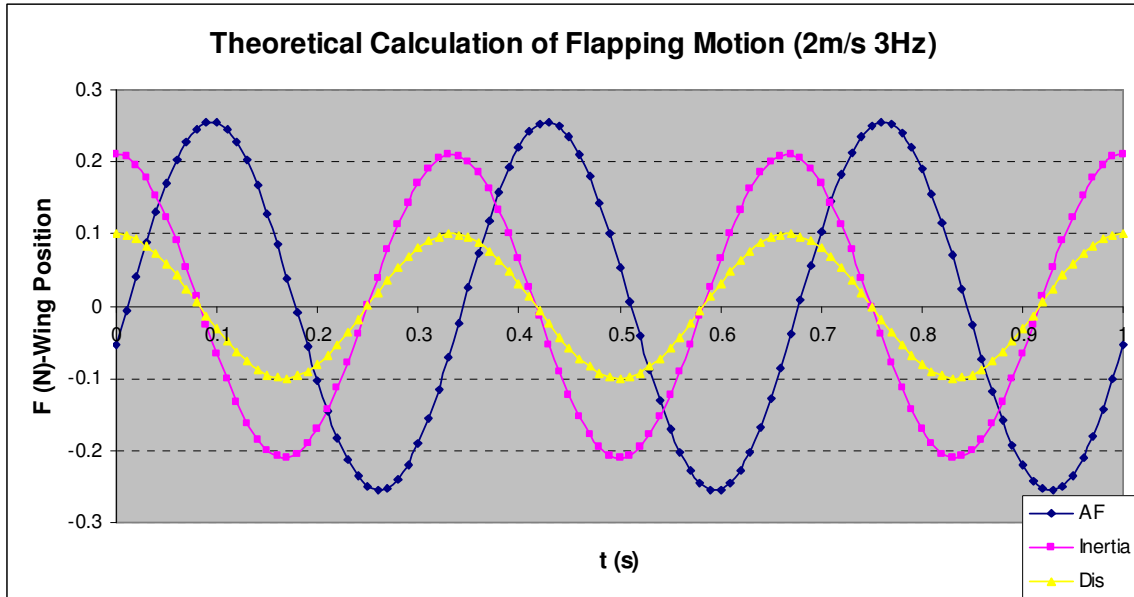


Figure 5.56 Theoretical calculation of flapping motion at 2m/s, 3Hz

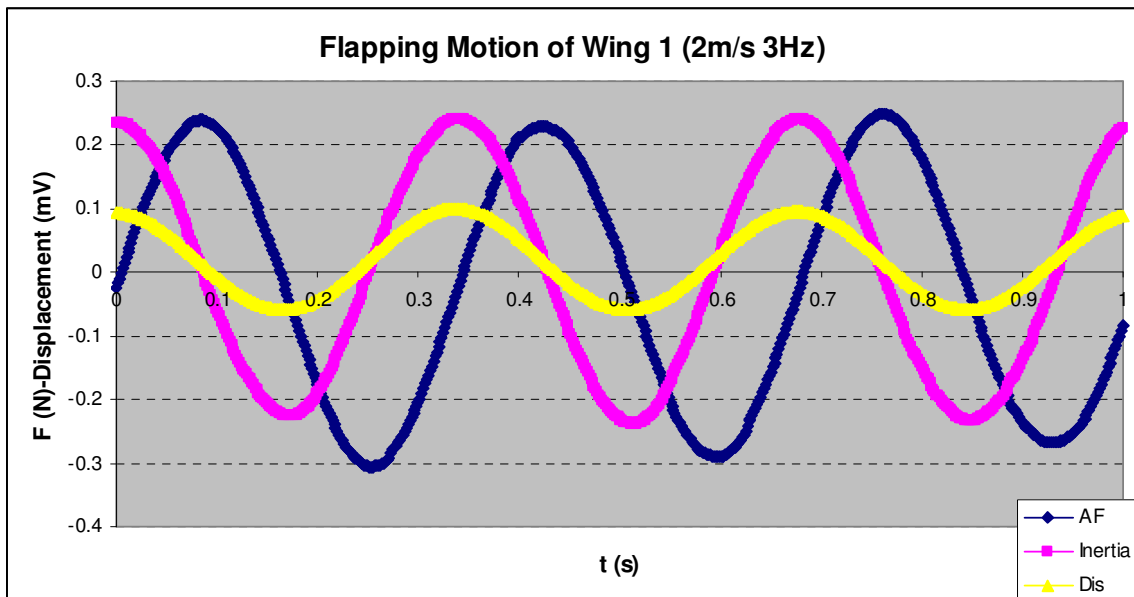


Figure 5.57 Test result of flapping motion of Wing 1 at 2m/s, 3Hz

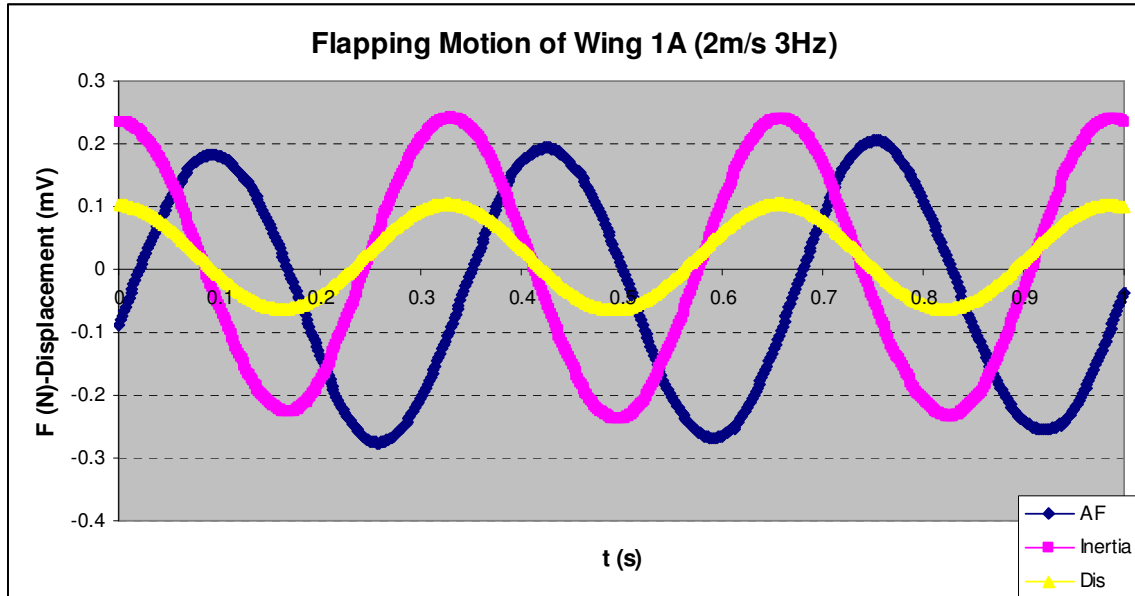


Figure 5.58 Test result of flapping motion of Wing 1A at 2m/s, 3Hz

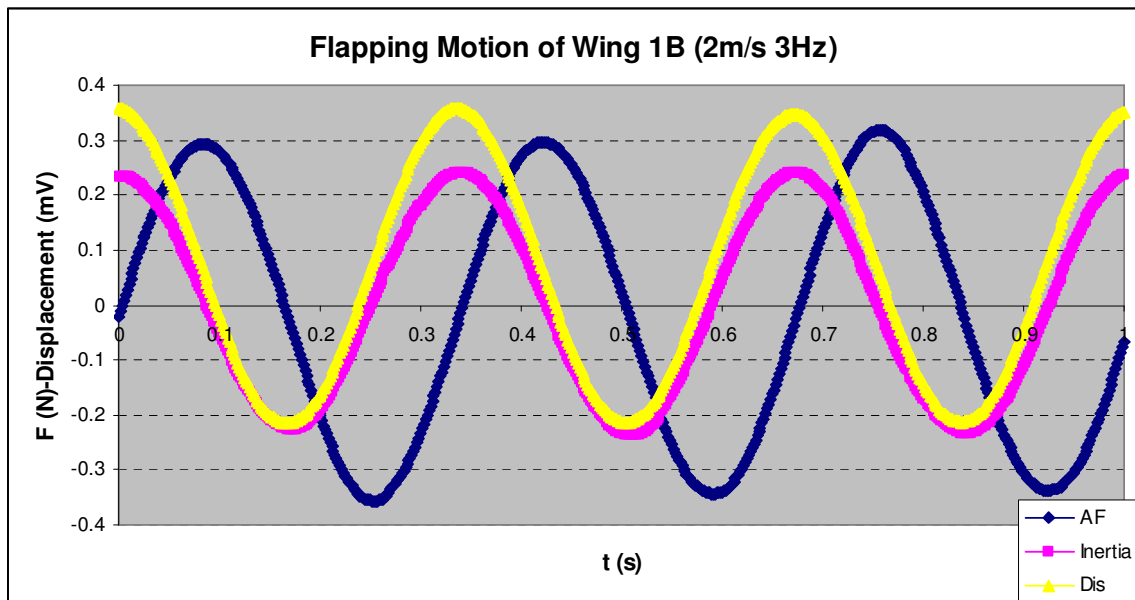


Figure 5.59 Test result of flapping motion of Wing 1B at 2m/s, 3Hz

### 5.2.2 Wing Flexibility Effect

Steady aerodynamic force of the wing with flexible trailing edge is analyzed first. Based on the test rig setup the steady load acting on the wing is illustrated in Fig. 5.60. Since the leading edge is supported by 2mm CFC rod mount on the fuselage the leading edge can be defined as rigid. However the trailing edge is supported by only a few piano strings as ribs and it is rather flexible compared with leading edge. Due to the weight of the wing the trailing edge is deformed downward by an initial amount defined as  $h_{TE}$  in wind-off condition.

The trailing edge deformation induces a small angle of attack. This indicates that any load acting on the wing will induce a trailing edge deformation which is quantified by the frame stiffness  $h_{TE}$  refer to Fig. 5.48. Literally the lift and drag coefficients are supposed to be constant with a fixed angle of attack. With an increased speed the steady lift and drag are increased. This causes a variation of trailing edge deformation.  $h_{TE}$  is reduced due to the increasing of steady aerodynamic force. Therefore the steady lift and drag coefficients are decreased with decreasing wing deformation. At low speeds flexible wing induces larger deformation which causes larger steady aerodynamic force in terms of coefficients. At high speeds the steady forces are high enough to minimize the effect of the chordwise curvature due to the wing weight. And the coefficients are approaching constant which is validated by test results shown in Fig. 5.49 and Fig. 5.50.

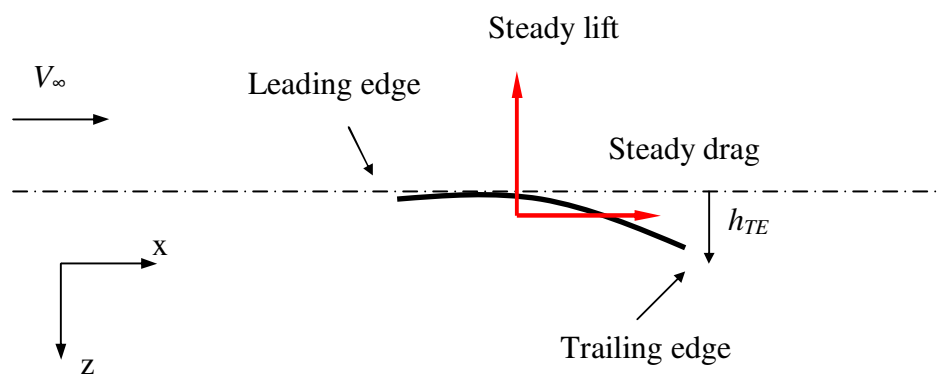


Figure 5.60 Steady loading acting on the flexible wing

The aerodynamic forces from wing tunnel tests and theoretical calculations for flapping wing motions are compared in terms of lift amplitude in Fig. 5.61. Large difference is found at high speeds. The turquoise curve is the computed results based on Theodorsen's theory which assumes the wing is completely rigid with no deformation during flapping. The large difference of the lift amplitude shown in Fig. 5.61 is mainly due to the elastic twist which induced negative angle of attack in downstroke. From the test results flexible wings tend to produce less lift due to larger trailing edge deformation.

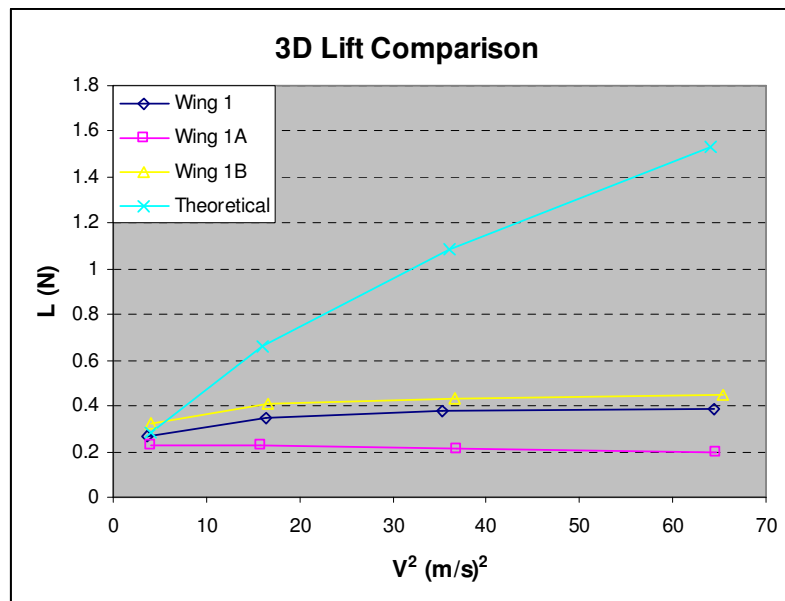


Figure 5.61 Total lift comparison in  $0^\circ$  angle of attack

During flapping test a set of images is recorded using a high speed camera. Since the test rig is mounted upside down the force and displacement are defined as positive down. The upstroke motion and downstroke motion are shown in Fig. 5.62 and Fig. 5.63 respectively. The lift as resistant force acting on the wing causes the wing frame deformation. And this deformation starts from the weakest area which is the trailing edge. Since the aerodynamic force performs as a sinusoidal manner the wing deformation can be treated in phase with aerodynamic force. The deformation of the wing causes the variation of the aerodynamic force generation in flapping motion. The analysis of this effect is stated as following.

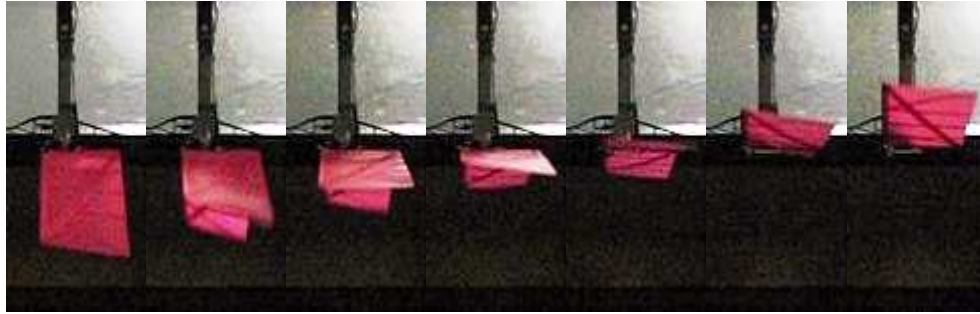


Figure 5.62 Image of flapping wing upstroke motion

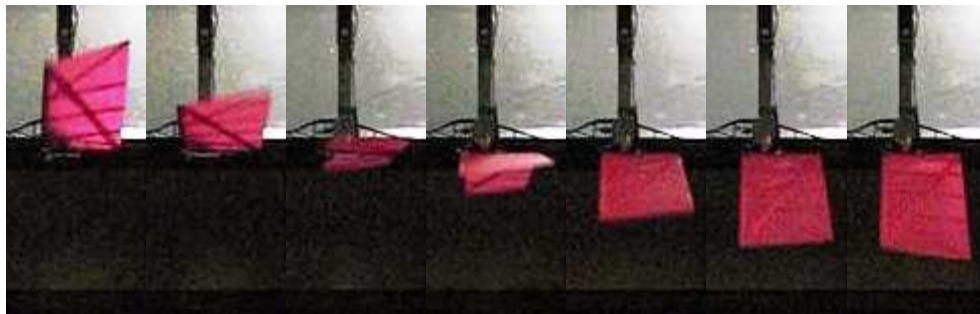


Figure 5.63 Image of flapping wing downstroke motion

The performance of flapping wing with flexible surface is illustrated in Fig. 5.64. In downstroke step the wing is moving down with trailing edge bending up and in upstroke motion the wing is moving up with trailing edge bending down. The lift force  $L_H$  due to heaving is always opposite to the wing motion as resistant force. Meanwhile a trailing edge deformation is induced due to the lift acting on the wing with displacement of  $h_{TE}$ . Hence an additional lift  $L_p$  is generated by this trailing edge deformation. And the trailing edge deformation varies with the variation of  $L_H$  the trailing edge flapping. With the above images of the wing performance during flapping the wing deformation nearly matches simple harmonic motion. The phase shift  $\varphi_C$  between flapping and wing chord twisting is  $\frac{3}{2}\pi$  with observation from Fig. 5.62 and Fig. 5.63 which just matches combined motion mode 4 mentioned in Chapter 4 in Fig. 4.20. Theoretically by increasing velocity the aerodynamic force of flapping wing is increased subject to the rigid wing as shown in Fig. 5.61 (turquoise curve). For flexible wing the increasing

aerodynamic force induces an increased wing deformation  $h_{TE}$  at the trailing edge and more  $L_p$  is produced to compromise the total aerodynamic force. Since the total lift is reduced down due to  $L_p$  the required power to maintain the flapping flight is also reduced.

In the theoretical calculations Theodorsen's theory assumes the wing is rigid with no twist and flow separation. Based on two-dimensional flow the chordwise aerodynamic force is integrated from tip to root. The sectional lift per unit span is linearly proportional to heaving amplitude shown in Fig. 5.65(a) by assuming the wing span is infinite. However at the wing tip the pressure on the top and bottom surface supposed to be balanced as shown in Fig. 5.65(b) based on DeLaurier's method for finite wing. Obviously the theoretical calculation therefore over estimated the total lift. And a proper calculation should be employed to predict the aerodynamic force subject to flexible wing under flapping motion.

Therefore the difference between the theoretical calculation and test results in Fig. 5.61 is mainly due to the wing trailing edge deformation that is believed to have responsible for the over prediction in the computed results.

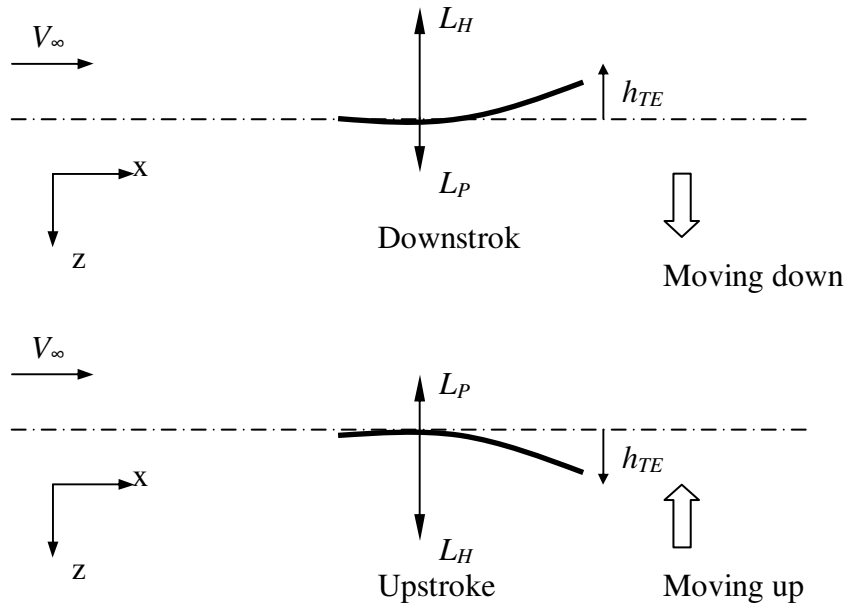


Figure 5.64 Flexible wing performance in flapping motion

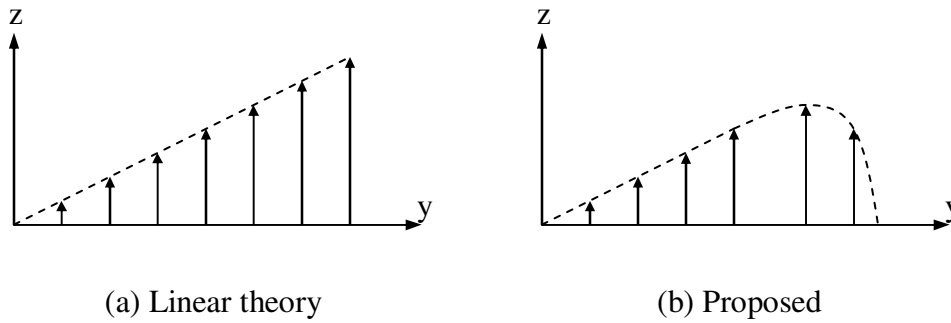


Figure 5.65 Theoretical and proposed lift distribution on half span

In flapping flight the wing is deformed based on elastic axis due to aerodynamic and inertia effect. Since the flapping wing is in a simple harmonic motion the aerodynamic force also acts in a sinusoidal manner. Hence the wing twist can be assumed as simple harmonic pitching. The flapping motion can be treated as a heaving with pitching combined motion. The effect of this chordwise twist is studied in terms of effective angle of attack.

Since the wing is constructed with rigid leading edge and flexible trailing edge in flapping flight the wing motion can be separated as a vertical translation with twist as shown in Fig. 5.66. In downstroke the wing is rotated counter-clockwise (leading edge down and trailing edge up) due to aerodynamic effect. And in upstroke the wing behaves in opposite manner due to the reverse of aerodynamic force. Hence the flexible trailing edge rotates based on the rigid leading edge.

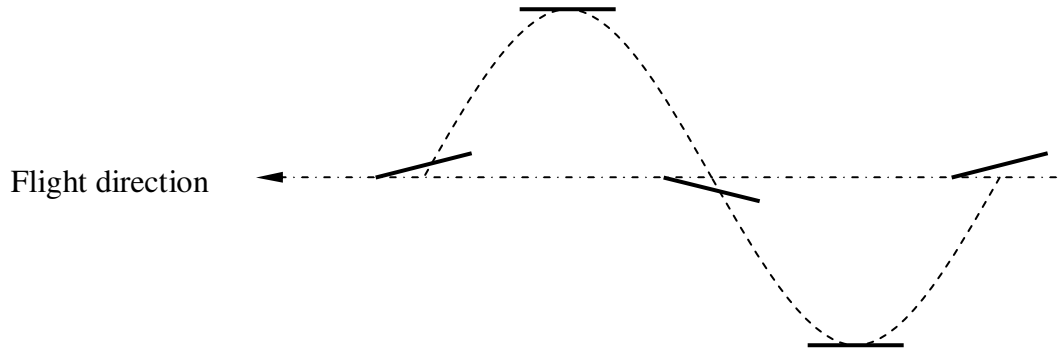


Figure 5.66 Flapping flight with wing twist

In this section the effect of twist angle on flapping flight is studied. In Theodorsen's theory four combined motions are investigated according to the phase shift between heaving and pitching shown in Fig. 5.67. The flapping flight with chordwise twist can be assumed as Mode 4 with phase shift  $\varphi = \frac{3}{2}\pi$ . The combined motion consists of heaving and pitching. The expression of sectional lift due to heaving and pitching are shown below.

$$L_H = \pi\rho b^2 \cdot \ddot{h} + 2\pi\rho V_\infty bC(k) \cdot \dot{h} \quad (5.16)$$

where  $h$  is heaving amplitude given by  $h = h_0 e^{i\alpha t}$

$$L_P = \pi\rho b^2 [V_\infty \dot{\alpha} - ba\ddot{\alpha}] + 2\pi\rho V_\infty bC(k) \left[ V_\infty \alpha + b \left( \frac{1}{2} - a \right) \dot{\alpha} \right] \quad (5.17)$$



where  $\alpha$  is pitching angle given by  $\alpha = \alpha_0 e^{i(\alpha + \varphi)}$ ,  $\varphi$  is phase shift between heaving and pitching

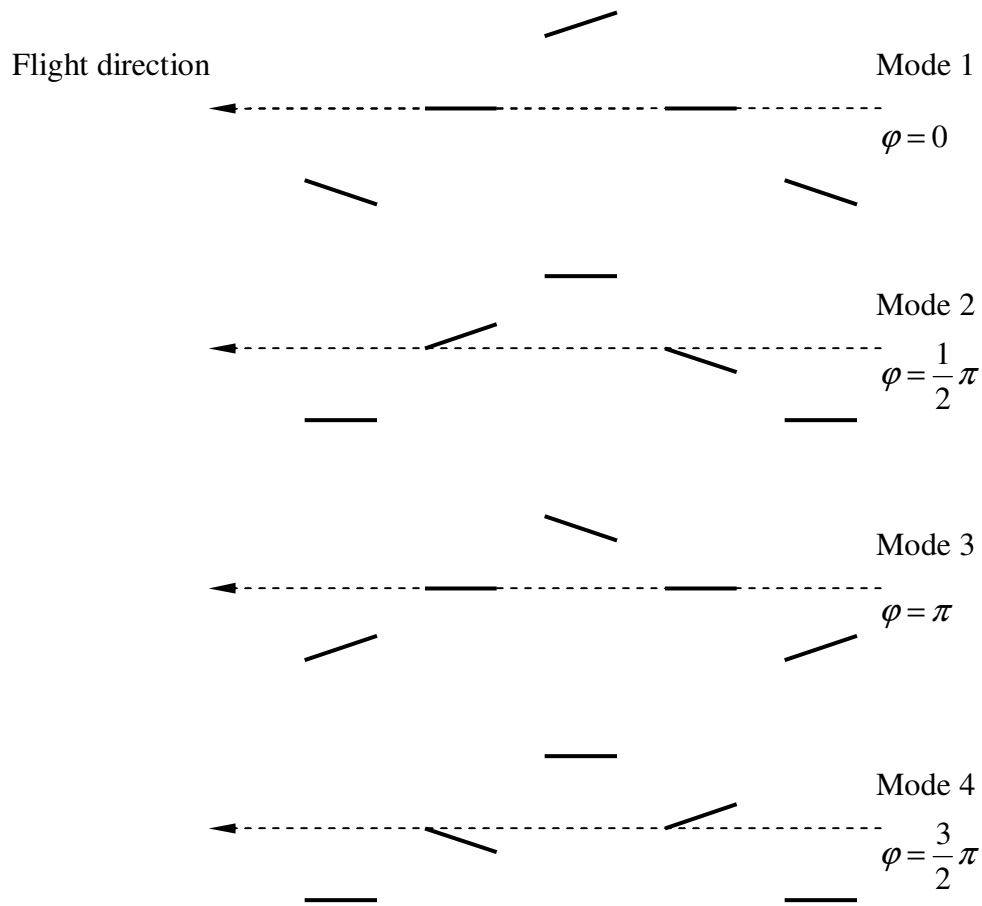


Figure 5.67 Combined heaving and pitching flapping wing motion

A rigid thin airfoil in downstroke movement is demonstrated in Fig. 5.68. Combined the vertical speed  $\dot{h}$  with air speed  $V_\infty$  an angle of attack is formed and approaching to the bottom of the wing. Based on the wing design cases the leading edge area provides a rather rigid surface and trailing edge area is more flexible. Hence the trailing edge flaps during the flapping motion. According to the chordwise twist performance the flapping flight is divided into three flight conditions 'A' 'B' and 'C' based on the location of leading edge. According to the aerodynamic force performance 'A' is defined as propeller mode, 'B' is turbine mode and 'C' is neutral mode.

Region A: (propeller mode)

In this mode the wing twist is small. The wing performs as propeller. The effective angle and thrust are given by

$$\theta = \frac{\dot{h}}{V_{\infty}} \quad (5.18)$$

$$T = L \cdot \theta = L \cdot \frac{\dot{h}}{V_{\infty}} \quad (5.19)$$

Region C: (neutral mode)

When the wing nose-down twist angle increases and approaches to line 'C' which is the direction of resultant velocity the flight is treated as trim flight. Since the angle of attack is zero the lift is zero given by

$$L = L_H + L_P = 0. \quad (5.20)$$

The pitching angle is given by

$$\alpha = \theta = \frac{\dot{h}}{V_{\infty}} \quad (5.21)$$

The neutral mode is between thrust generation and power extraction. In this mode no lift is produced and drag is reduced down to minimum.

Region B: (turbine mode)

In this mode the twist angle is large. The lift reverses down. The wing extracts power from air flow and the extracted power is given by

$$P = L \cdot h \quad (5.22)$$

The wing performs as a turbine. Downward lift and drag are produced. When the wing is in this condition it contributes the wing downstroke movement but compromises aerodynamic force generation.

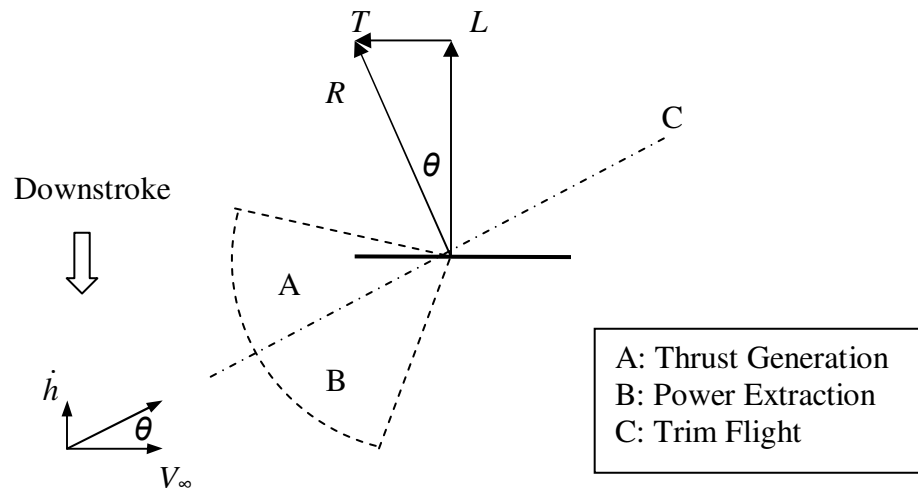


Figure 5.68 Twist angle effect

In comparison of three wing configurations the rigid wing (Wing 1B) produces more lift and forward force than the other two wings as refer to Fig. 5.53 and Fig. 5.54. However it requires more power to maintain the flapping flight at 3Hz as shown in Fig. 5.55. With minimum wing deformation wing 1B can be treated as thrust generation case. Wing 1A with the most flexible structure and minimum input power can be seen as the power extraction case. And Wing 1 is the neutral case in between. Therefore proper modifying the stiffness of the wing frame can achieve different performance for different flight conditions. The test results indicate that by increasing the wing rigid area from 16.3% to 50% relative to total wing area the wing performance can be changed dramatically. Take Wing 1A as reference the lift in amplitude is increased by 88%. However the required power is increased by 72%. Therefore wing chord twist control will be the key issue to conduct the flapping wing design.

## **6 Preliminary Ornithopter Wing Design and Finite Element Modelling**

In this chapter the preliminary ornithopter wing design is carried out based on a hang glider prototype. First the performance of hang glider is studied and design specification is determined. Based on the hang glider geometry the preliminary design of the ornithopter is carried out using calculated aerodynamic forces which have been validated by experimental study on a scale model and finite element modelling. Preliminary design specifications and component parameters of the hang glider are provided by the manufacturer Wills Wing Inc. The performance of the preliminary ornithopter design prototype is evaluated in detail based on the available information from the hang-glider's manufacturer and design analysis carried out in this chapter.

### **6.1 Hang Glider Prototype Design**

The hang glider is selected as a baseline configuration for conducting a detailed feasibility study of ornithopter design. The advantages of using the hang glider are given below which indicate that it is the ideal prototype for the ornithopter design:

- Light weight
- Easy take-off and landing
- High manoeuvrability
- Easy to control
- Low stall speed

#### **6.1.1 Hang Glider Study**

Several types of hang gliders are studied in order to find a suitable glider for use as a baseline configuration for ornithopter design. Following some initial research on hang glider wing designs, it has been found that the Wills Wing class is the most popular wing used in North America. The Wills Wing class consists of four products which are T2, U2,

Falcon 3 and Sport 2. A brief introduction of these four types of hang glider is given below.

### 6.1.1.1 Product of Wills Wing Class

The information in details of these hang gliders is described in Wills Wing hang glider manufacturer's web site [50]. Comparisons are carried out on glider performance, landing characteristics, overall handling qualities and cost subject to four types of hang gliders (T2, U2, Falcon 3 and Sport 2) as shown in Fig. 6.1. The comparative performance characteristics are tabulated in Table 6.1 and they show that Sport 2 has the best balance in performance, landing, handling and cost efficiency.



Figure 6.1 Hang glider comparisons [50]

Specification	T2-144	U2-145	Falcon 3-145	Sport 2-155
Area (m <sup>2</sup> )	13.4	13.5	13.5	14.4
Span (m)	9.8	9.5	8.5	9.6
Aspect Ratio	7.3	6.8	5.4	6.4
Glider Weight (kg)	32	29	20	27
Hook-In Weight (kg)	72-107	64-100	54-86	68-113
Optimum Body Weight (kg)	63-82	64-77	50-64	68-91
$V_{ne}$ (km/h)	85	85	77	85
$V_a$ (km/h)	74	74	68	74
$V_{ms}$ (km/h)	34	32	29	30
$V_d$ (km/h)	120		56	

Table 6.1 Hang glider design specifications

### 6.1.1.2 Definition of Technical Terms for Hang Gliders

In this section several important parameters are defined to help evaluate the hang glider performance as follows:

- Hook-In Weight

This is the total combined weight of the pilot, clothing, harness, parachute, helmet, and any all other items attached to or carried on the pilot's body or harness.

- Optimum Body Weight

This is the weight range within which a given glider offers the optimum combined levels of performance and control. In general, this weight range is specified without overlap between successive sizes of the same model, so that it can serve as a clear recommendation, for a given pilot, of which size glider is considered optimum.

- $V_{ne}$

The placarded maximum speed that should not be exceeded for safety when flying in smooth air and in straight flight.

- $V_a$

The placarded maximum speed that should not be exceeded for safety when flying in turbulence or when maneuvering.

- $V_{ms}$

The speed at which the minimum descent rate is obtained.

- $V_d$

The maximum steady state speed, at minimum recommended wing loading, for a pilot in a normal prone position, pulled all the way in.

### 6.1.1.3 Structural Components of Hang Gliders

The hang glider wing studied here is a sweepback tapered wing. The leading edge and crossbar forms a relative stiff surface and the wing chord profile is supported by the ribs which are slotted in the wing cloth. For some hang glider designs, a kingpost is mounted on top of the wing and cables are connected from tip to the kingpost to stiffen structure. Control bar is fixed on the keel under the wing to control glider pitching as shown in Fig. 6.2.

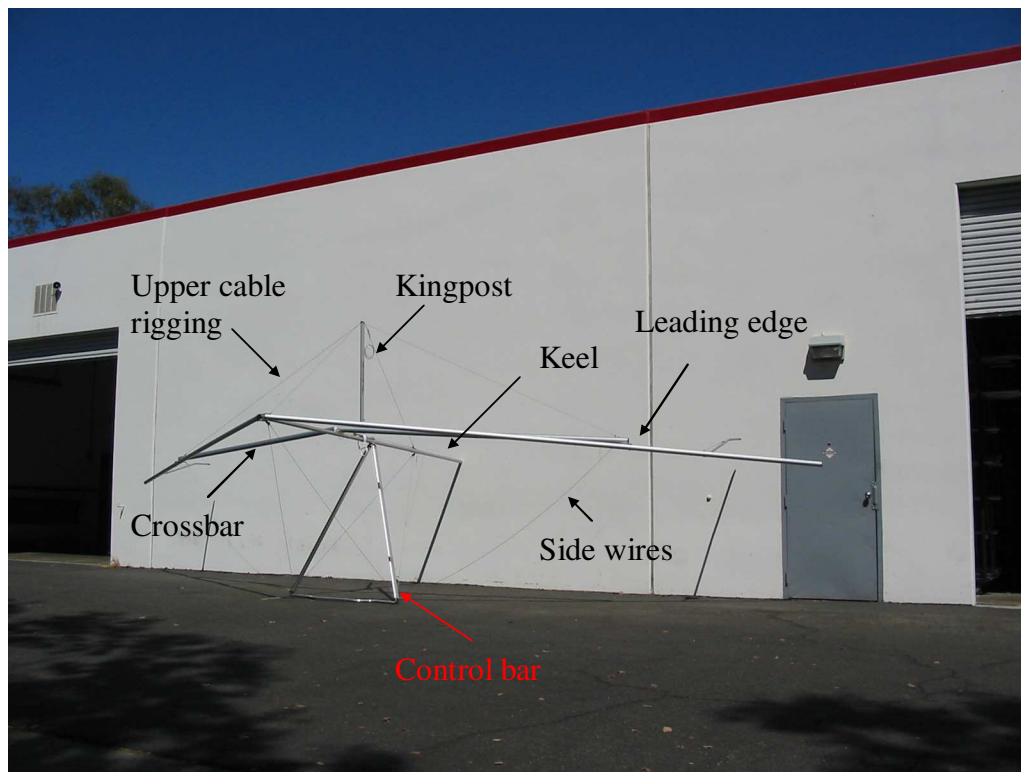


Figure 6.2 Hang glider structure

#### 6.1.1.4 Flight Mechanics of Hang Gliders

In gliding the force and velocity vectors of the wing are shown in Fig. 6.3. The angle  $\gamma$  indicates flight path to horizontal direction. The lift  $L$  and drag  $D$  expressed in terms of the weight  $W$  and glide angle  $\gamma$  are given by

$$L = W \cos \gamma \quad (6.1)$$

$$D = W \sin \gamma \quad (6.2)$$

The vertical and horizontal velocities are given by

$$V_G = V \cos \gamma \quad (6.3)$$



$$V_{sk} = V \sin \gamma \quad (6.4)$$

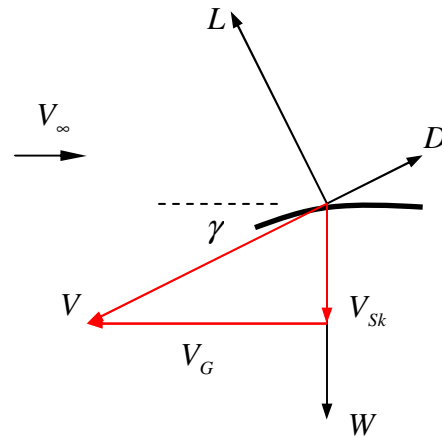


Figure 6.3 Force and velocity vectors for gliding flight

Two key parameters are normally used to evaluate the hang glider performance which are glide ratio and sink rate. The glide ratio is the ratio of the forward distance travelled to the vertical distance lost by an aircraft when gliding without any power; and the sink rate is the rate of loss of vertical height per unit of time. The theoretical equations for these two parameters are given by

$$\text{Glide Ratio} = \frac{L}{D} = \frac{1}{\tan \gamma} \quad (6.5)$$

$$\text{Sink Rate} = V_{sk} = \sqrt{\frac{2W}{\rho S} \frac{C_D}{C_L^{3/2}}} \quad (6.6)$$

#### 6.1.1.5 The HGMA Airworthiness Program

By 1977 the Hang Glider Manufacture Association (HGMA) had been formed and a set of airworthiness testing standards had been developed and implemented. One of the main purposes of the airworthiness standards was to define a range of operating parameters or limits within which a glider that met the airworthiness standards could be operated with a

reasonable degree of confidence that it would not suffer a loss of control or structural failure.

The HGMA certification standards [51] allow each manufacture, for each model and size of glider, to specify the same basic operating limitations:

- The allowable weight range for the pilot
- The maximum allowable maneuvering speed  $V_a$
- The maximum allowable speed  $V_{ne}$
- The maneuvers permitted, including, if desired, aerodynamic maneuvers

Depending on the operating limits that the manufacture specifies, the HGMA Airworthiness Standards then specify the tests and test values that the manufacture is required to perform and document to obtain certification.

The HGMA Standards also provide a default set of minimum operating limitations which are:

- 46mph maneuvering speed  $V_a$
- 53mph  $V_{ne}$
- Maximum pitch attitude to the horizon of 30 degrees nose up or nose down
- Maximum bank angle of 60 degrees

These minimum requirements are thought to be consistent with the intended use of the hang glider as an aircraft — essentially low speed soaring and gliding flight on a light-weight, foot launchable and foot landable aircraft. (For certain training and entry level type gliders, the HGMA standards allow for slightly lower values of  $V_a$  and  $V_{ne}$  if the glider is, by its design, limited in the maximum speed it can maintain.)

In practice most aeroplane designs use a safety factor of 1.5 for loads but in the HGMA standards, the safety factor is taken as 2. The load compliance test is normally carried out with the glider fixed on a road vehicle travelling at a high speed and angle of attack corresponding to maximum lift rather than using G loading. Three sets of test are carried out as shown below.

1. For the normal default HGMA maneuvering speed of 46mph, the required positive load test speed is 65mph at maximum lift angle of attack. (due to the safety factor of 2)
2. Following standard aviation conventions, a negative load requirement of 50% of positive load requirement is applied, resulting in a test speed of 46mph for the negative 30 degree angle of attack test.
3. The HGMA also has negative 150 degree load test for which the required test speed is 32mph. The purpose of this test is to test the glider's structure at this angle of attack and in the loading condition that would occur approximately halfway through a low speed, turbulence induced forward tumble. (the test speed of 32mph provides a safety factor of 2.0 for a tumble that might occur at 23mph.)

Hence the speed in different conditions is tabulated below:

$V_s$	23mph	Stall speed
$V_a$	46mph	The maximum maneuver speed in rough air
$V_{ne}$	53mph	Max speed never exceed in smooth air $1.15V_a$
$V_t$	65mph	Ground test speed $\sqrt{2}V_a$

Table 6.2 Speed in different conditions

### 6.1.2 Design Specifications

The Wills Wing Sport 2-155 selected for the ornithopter design study is shown in Fig. 6.4.



Figure 6.4 Wills Wing Sport 2-155 hang glider

The planform geometric parameters of Wills Wing Sport 2-155 are shown below.

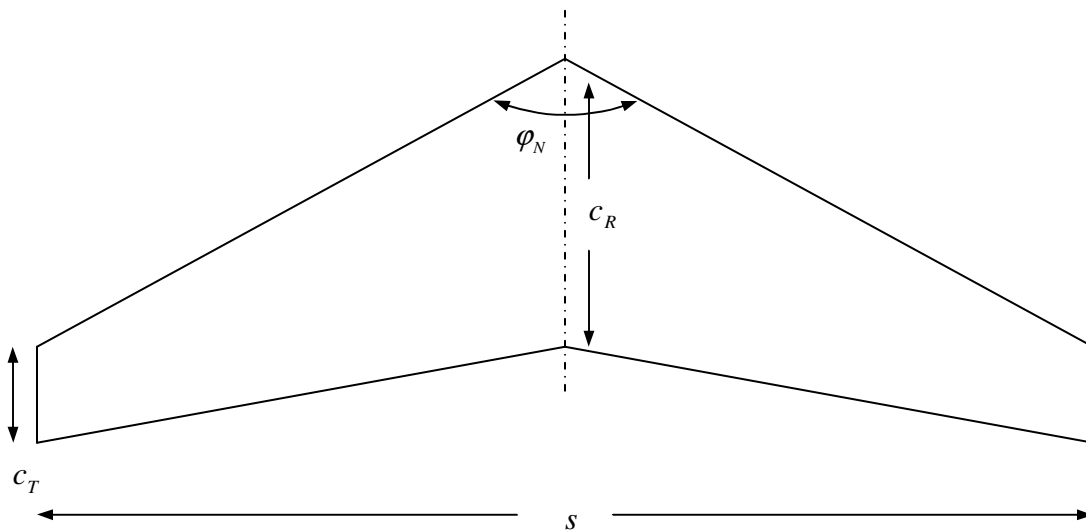


Figure 6.5 Wing geometry

Wing Area	$S$	14.4m <sup>2</sup>
Wing Span	$s$	9.6m
Aspect Ratio	$AR$	6.4
Root Chord	$c_R$	2.2m
Tip Chord	$c_T$	0.8m
Nose Angle	$\varphi_N$	130°
Wing weight	$W_w$	27kg
Hook-in-weight	$W_h$	68~113kg
Max speed	$V_{max}$	20.6m/s
Min speed	$V_{min}$	8.3m/s

Table 6.3 Wing design specification

### **6.1.3 *n-V Diagram and Loading Action***

From the manufacturer the performance of Wills Wing class is obtained as shown in Fig. 6.7. Therefore the lift, drag coefficient and lift-to-drag ratios are obtained. The ‘buildup data’ is obtained from theoretical simulations and the original ‘Wills data’ are the experimental results in the flight test. The ‘buildup data’ is demonstrated in the same graph to compare with the original ‘Wills data’ which shows a good agreement. To understand the performance of Wills Wing Sport 2-155 hang glider the ‘S2-via-Wills-data’ is taken as shown in Fig. 6.6.

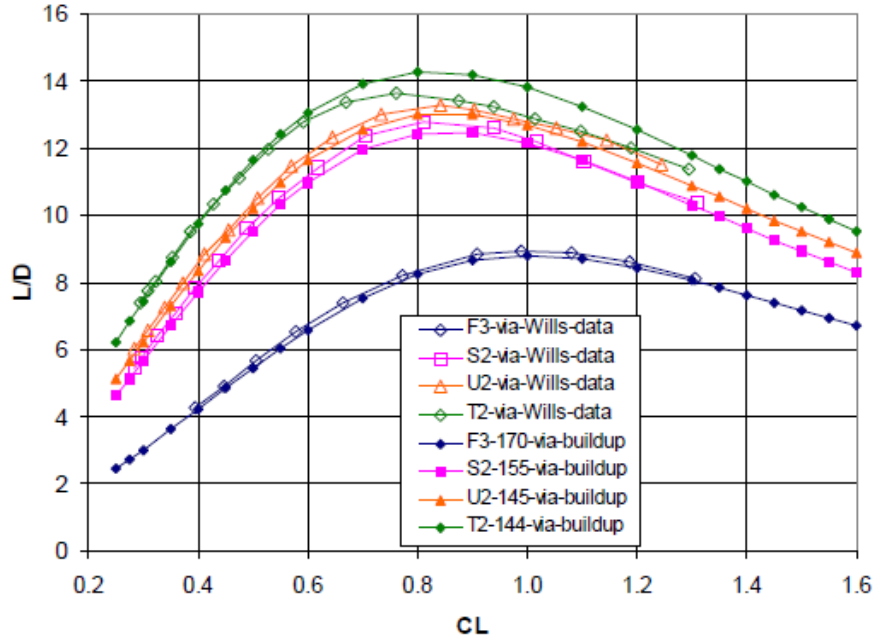


Figure 6.6 Comparison of L/D estimates with manufacturer's data [50]

### 6.1.3.1 Calculation of the Lift Curve Slope

To study the performance of Wills Wing S-155 the lift curve slope is calculated. In general sweepback wing reduces the lift curve slope and moves the aerodynamic centre aft. For transport and general aviation aircraft wing, the theoretical lift curve slope  $\frac{dC_L}{d\alpha}$  is given by

$$\frac{dC_L}{d\alpha} = \frac{2\pi AR}{2 + AR\sqrt{1 + \tan^2 \Lambda}} \quad (6.7)$$

where  $\Lambda$  is sweep angle at  $\frac{1}{4}$  chord, in this case  $\Lambda = 22^\circ$

Therefore the lift curve slope is obtained as 4.52. From the manufacturer the lift coefficient due to camber effect is obtained  $C_L(\text{camber}) = 0.36$ . By using equation shown below the relationship between angle of attack and lift, drag coefficient and lift-to-drag ratio are shown in Fig. 6.7, Fig. 6.8 and Fig. 6.9.

$$C_L = \frac{dC_L}{d\alpha} \alpha + C_L(\text{camber}) \quad (6.8)$$

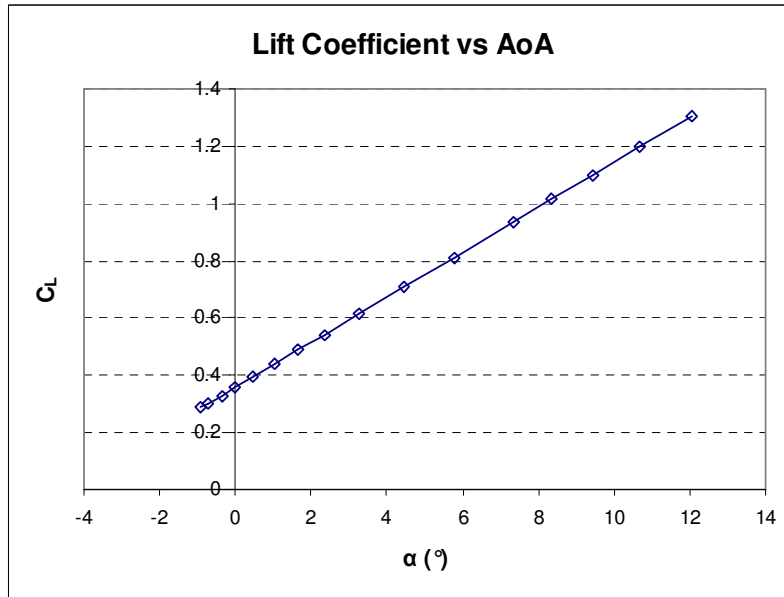


Figure 6.7 Lift coefficient versus angle of attack

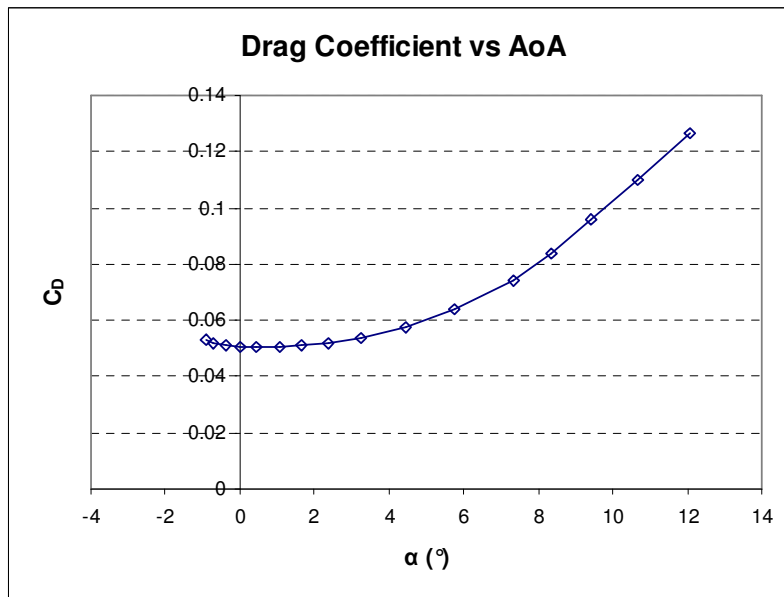


Figure 6.8 Drag coefficient versus angle of attack

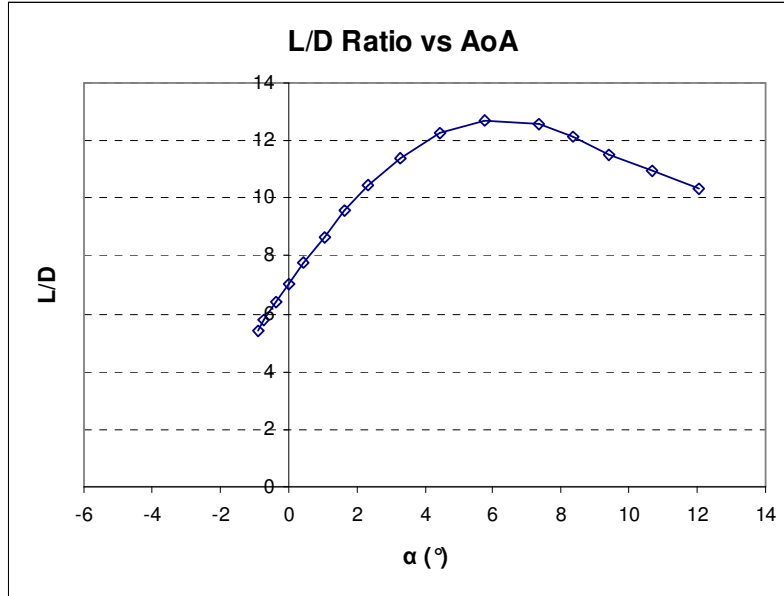


Figure 6.9 Lift-to-drag ratio versus angle of attack

Sink rate is the other important parameter for evaluating the performance of the hang glider which has been given in Eq. (6.6). The total weight of the hang glider is from 95kg to 140kg. The effect of weight on the minimum sink rate is shown below.

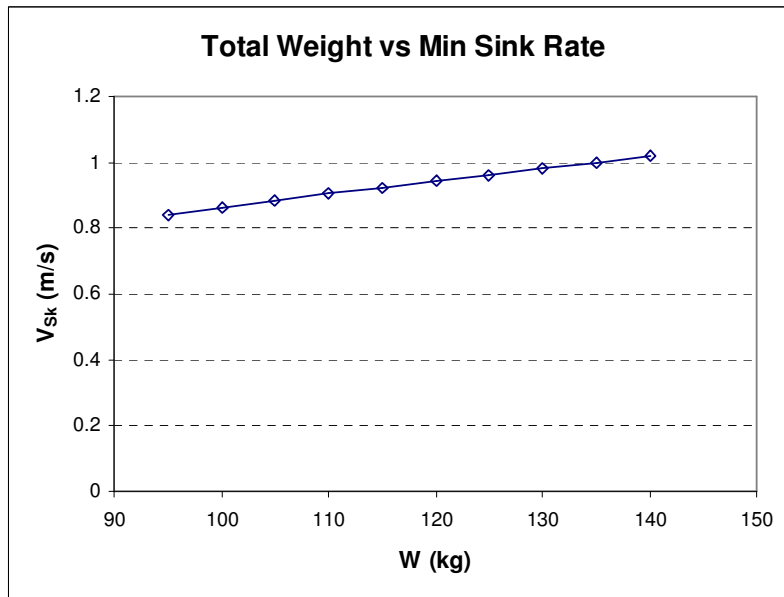


Figure 6.10 Weight effect on minimum sink rate



The sink rate versus angle of attack in maximum weight of 140kg is illustrated below.

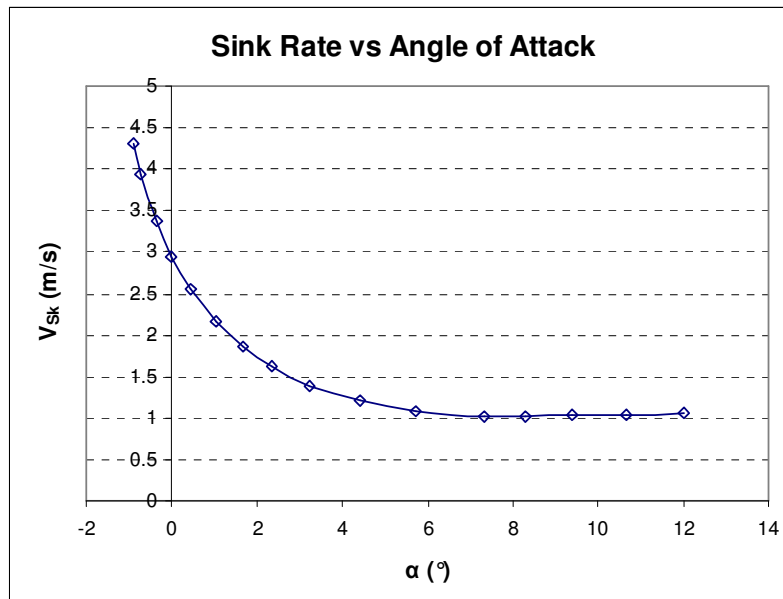


Figure 6.11 Sink rate vs angle of attack

The performance of hang glider is tabulated below.

Total Weight	140kg
Speed	10.9~23.3m/s
Max Glide Ratio	$L/D = 12.7$ at $\alpha = 5.8^\circ$
Min Sink Rate	$V_{sk} = 1.02$ m/s at $\alpha = 8.3^\circ$

Table 6.4 Hang glider performance

### 6.1.3.2 n-V Diagram

In this section the n-V diagram will be constructed. According to Wills Wing Sport 2-155 service manual [52] the limit loads are taken between -1.5 to 3 and the ultimate load factor is 2.0 hence the ultimate loads range from -3.0 to 7.0. The maximum lift coefficient  $C_{L_{max}}$  is taken as 1.31 from Fig. 6.7 and total weight is 140kg.

According to Eq. (6.9) shown below the boundary can be obtained in stall angle with maximum lift coefficient  $C_{L\max}$ .

$$n = \frac{\frac{1}{2} \rho V^2 S C_{L\max}}{W} \quad (6.9)$$

The stall speed is obtained with  $n = 1$

$$V_s = \sqrt{\frac{W}{\frac{1}{2} \rho S C_{L\max}}} \quad (6.10)$$

The cruise speed is obtained when hang glider is at maximum glider ratio given by

$$V_c = \sqrt{\frac{W}{\frac{1}{2} \rho S C_{Lbest}}} \quad (6.11)$$

where  $C_{Lbest}$  is the lift coefficient corresponding to maximum  $L/D$

The maximum maneuver speed  $V_a$  and maximum allowable speed  $V_{ne}$  in rough air and smooth air are obtained in Wills Wing Sport 2-155 service manual [52]. The ground test is carried out at root stall angle of attack at 123% of the placarded speed never to exceed. The speed description is shown in Table 6.5.

$V_s = 10.9 \text{ m/s}$	Stall speed at $n = 1$ and $C_{L_{\max}} = 1.31$
$V_c = 13.8 \text{ m/s}$	Cruise speed when $L/D$ is maximum
$V_a = 20.6 \text{ m/s}$	Max maneuver speed in rough air
$V_{ne} = 23.7 \text{ m/s}$	Max speed never exceed in smooth air
$V_t = 29.1 \text{ m/s}$	Ground test speed obtained by manufacturer

Table 6.5 Flight speed definition

The n-V diagram is shown in Fig. 6.12. In Azaryew’s book [53] it is shown that the downward gust case is neither critical nor dangerous with correct control. Hence the gust load hasn’t been taken into account in n-V diagram.

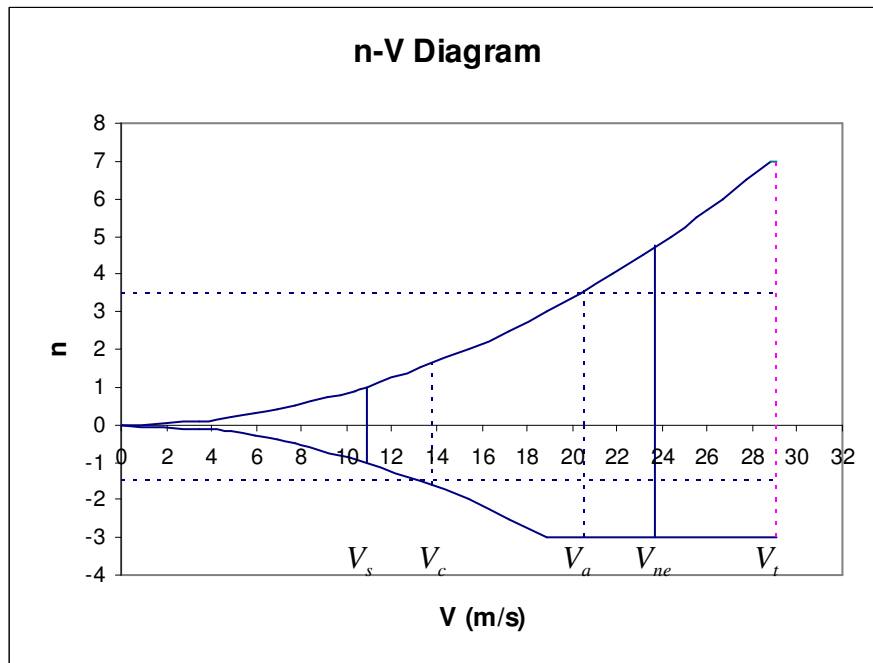


Figure 6.12 n-V diagram

### 6.1.3.3 Spanwise Lift Distribution

A simple evaluation of load distribution on uncranked swept wing is given [54]. The shape of the distribution is completely defined by the position of the semi-spanwise

centre of pressure  $\bar{y}$  (normalized to semi-span) which should lie between the limits  $0.4 < \bar{y} < 0.5$  for the method to give acceptable results. The relevant formulae are:

$$\bar{y} = 0.42 + \frac{AR}{10^3} \left[ (4.4 + 5\lambda) \tan \Lambda + 10.4\lambda^{1/2} - 6.7 \right] \quad (6.12)$$

$$\begin{aligned} \frac{c(y)C_l(y)}{\bar{c}C_L} &= 1.28(1 - \eta^2)^{1/2} + (14.13\eta - 6.35)(\bar{y} - 0.425) && \text{for } \eta < 0.7 \\ &= 1.28(1 - \eta^2)^{1/2} + [4.25 - 53.8(\eta - 0.815)^2](\bar{y} - 0.425) && \text{for } \eta \geq 0.7 \end{aligned} \quad (6.13)$$

where  $\bar{c}$  is the geometric mean chord

$c(y)$  is the local wing chord at a spanwise station  $y$

$C_l(y)$  is local lift coefficient at spanwise station  $y$

$C_L$  is the overall lift coefficient of the wing

$\lambda$  is the taper ratio of the tip to root chord

$\eta$  is  $2y/s$

$\Lambda$  is sweep angle at  $1/4$  chord

The semi-span is divided into 4800 elements with 1mm width. The local chord length  $c(y)$  of each element is given by

$$c(y) = c_R \left[ 1 - \frac{2y}{s} (1 - \lambda) \right] \quad (6.14)$$

The lift coefficient  $C_l(y)$  of each element is calculated based on the local chord  $c(y)$  and its location  $y$  taken from root. By taking  $C_L = 0.81$  when the hang glider is in its best glide ratio the spanwise lift coefficient is shown below.

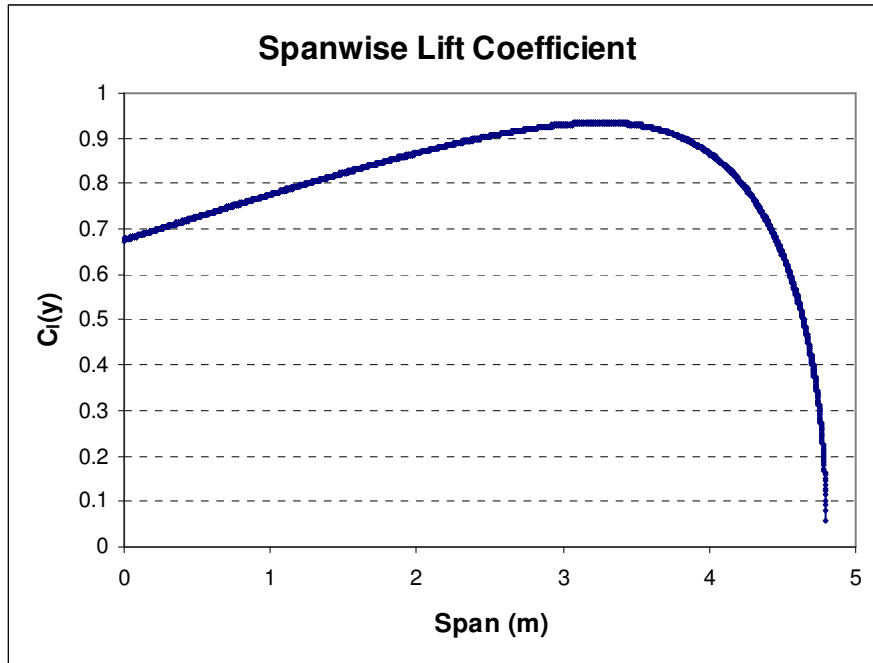


Figure 6.13 Spanwise lift coefficient distribution

Corresponding to overall wing  $C_L = 0.81$  the required speed to maintain level flight is 13.8m/s. The spanwise lift distribution is shown below.

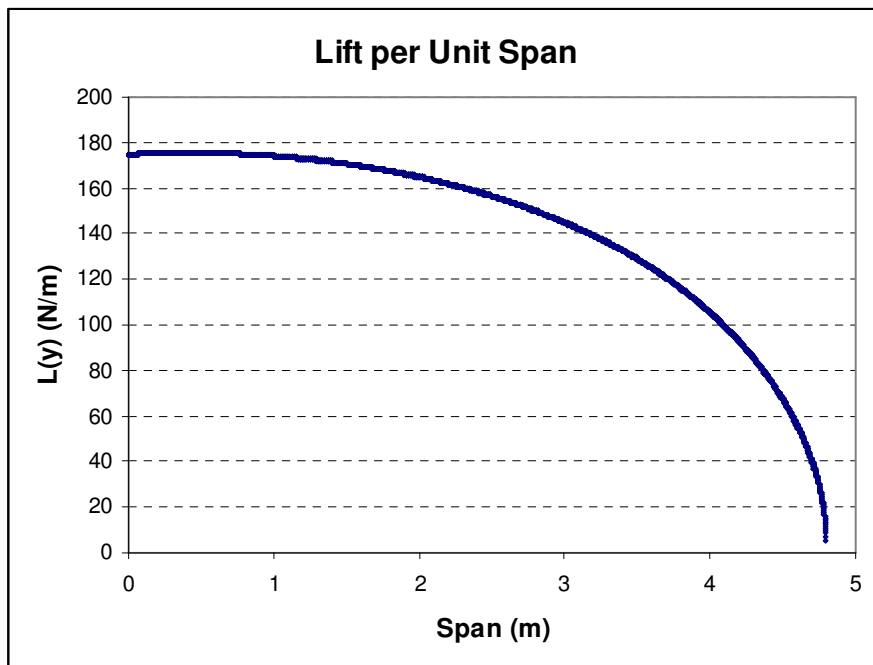


Figure 6.14 Spanwise lift distribution

### 6.1.3.4 Shear Force and Bending Moment

As shown in Fig. 6.15 the semi-span wing is assumed as a cantilever fully clamped at root (point A). The semi-span is divided into 4800 elements. The lift and weight of the wing applied on each element has been taken into account in the shear force and bending moment calculation.

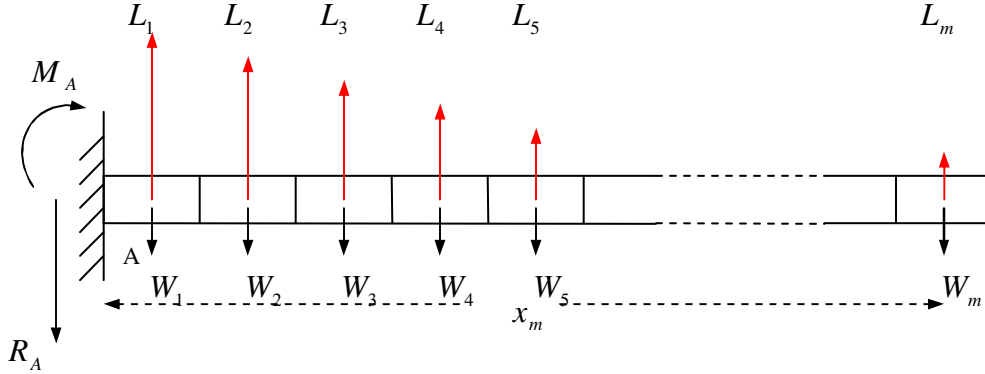


Figure 6.15 Loading action on cantilever

Assume the lift and weight are applied at the centre of each element and  $x_m$  is the distance from point A to the  $m^{\text{th}}$  element centre. Since the beam is clamped at point A the reaction force  $R_A$  and moment  $M_A$  are given by

$$R_A = L_1 + L_2 + \dots + L_m + \dots + L_{4800} - (W_1 + W_2 + \dots + W_m + \dots + W_{4800}) \quad (6.15)$$

$$M_A = (L_1 - W_1)x_1 + (L_2 - W_2)x_2 + \dots + (L_m - W_m)x_m + \dots + (L_{4800} - W_{4800})x_{4800} \quad (6.16)$$

where  $n$  is load factor and the range of  $m$  is  $1 \leq m \leq 4800$

The shear force  $Q$  on each element is given by

$$\begin{cases} Q_1 = R_A \\ Q_2 = R_A - L_1 + W_1 \\ Q_3 = R_A - (L_1 + L_2) + (W_1 + W_2) \\ Q_4 = R_A - (L_1 + L_2 + L_3) + (W_1 + W_2 + W_3) \\ \vdots \\ Q_m = R_A - (L_1 + L_2 + \dots + L_m) + (W_1 + W_2 + \dots + W_m) \end{cases} \quad (6.17)$$

Hence the expression of shear force on  $m^{\text{th}}$  element is given by

$$Q_m = R_A - \sum_{m=1}^m L_m + \sum_{m=1}^m W_m \quad (6.18)$$

The bending moment  $M$  on each element is given by

$$\begin{cases} M_1 = M_A - R_A x_1 \\ M_2 = M_A - R_A x_2 + (L_1 - W_1)(x_2 - x_1) \\ M_3 = M_A - R_A x_3 + (L_1 - W_1)(x_3 - x_1) + (L_2 - W_2)(x_3 - x_2) \\ M_4 = M_A - R_A x_4 + (L_1 - W_1)(x_4 - x_1) + (L_2 - W_2)(x_4 - x_2) + (L_3 - W_3)(x_4 - x_3) \\ \vdots \\ M_m = M_A - R_A x_m + (L_1 - W_1)(x_m - x_1) + (L_2 - W_2)(x_m - x_2) + \dots + (L_{m-1} - W_{m-1})(x_m - x_{m-1}) \end{cases} \quad (6.19)$$

The expression of bending moment on  $m^{\text{th}}$  element is given by

$$M_m = M_A - R_A x_m + \sum_{m=2}^{m-1} (L_{m-1} - W_{m-1})x_m - \sum_{m=2}^{m-1} (L_{m-1} - W_{m-1})x_{m-1} \quad (6.20)$$

According to the spanwise lift distribution the shear force and bending moment diagrams at  $n=1$  are shown below.

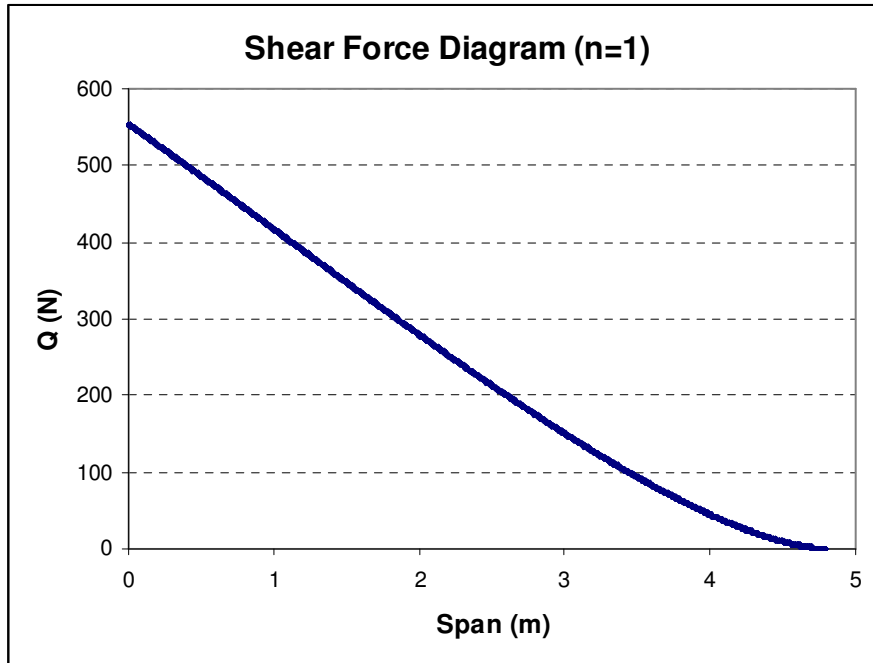


Figure 6.16 Shear force diagram at  $n = 1$

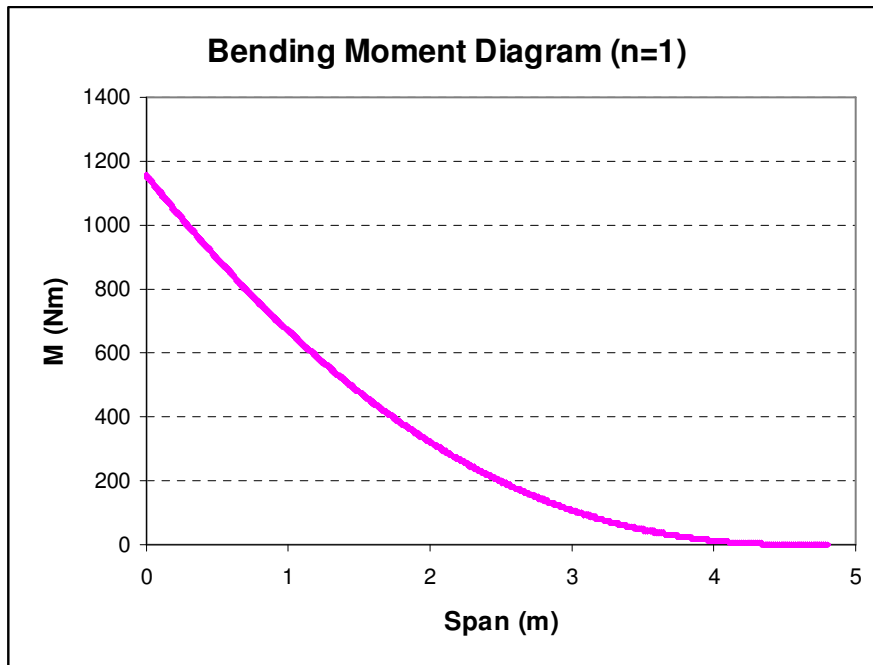


Figure 6.17 Bending moment diagram at  $n = 1$



### 6.1.4 Dimension of Wing Component

According to Wills Wing Sport 2-155 service manual [52] the component parameters of the wing frame are shown below.

Component	Material	Length (in)	Weight (lb)
Front Leading Edge	50mm×0.9mm 7075-T6	141	3.463
Rear Leading Edge	50mm×0.9mm 7075-T6	65	1.399
Cross Bar	62mm×0.9mm 7075-T6	114	3.205
Keel	42mm×0.9mm 7075-T6	168.13	3.032

Table 6.6 Wing frame dimension

As illustrated in Fig. 6.18 the wing frame consists of front leading edge, rear leading edge, cross bar and keel.

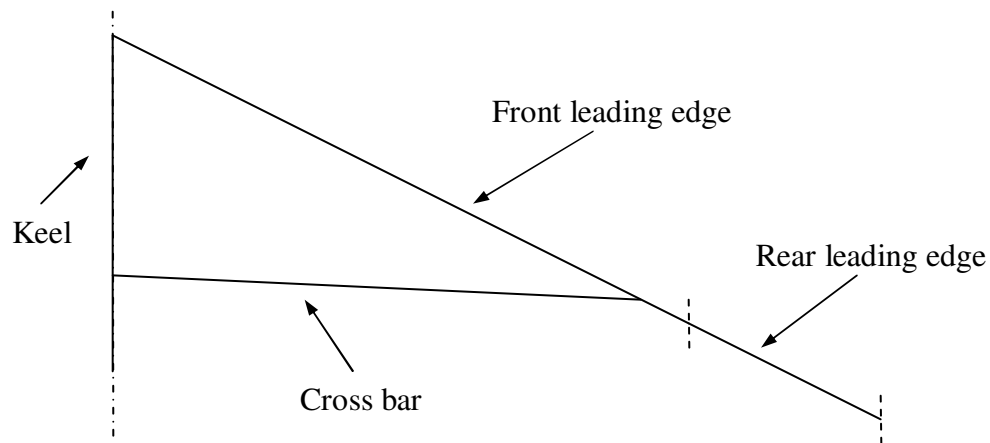


Figure 6.18 Wing frame construction

For Sport 2-155 the skin is made of V170 4.0 Ounce Woven Polyester Fabric which has a weight of 4.0 ounces per sailmaker's yard. Converting the data into metric units the material weight is about  $135.6\text{g/m}^2$ . Hence the weight of skin can be estimated as 3.4kg.

### 6.1.5 CATIA Model of Hang Glider

In this section the engineering drawing of the hang glider Wills Wing Sport 2-155 is carried out using CATIA P3 V5R15. By recovering the dimensions of the hang glider based on the manufacture data the drawing is shown below.

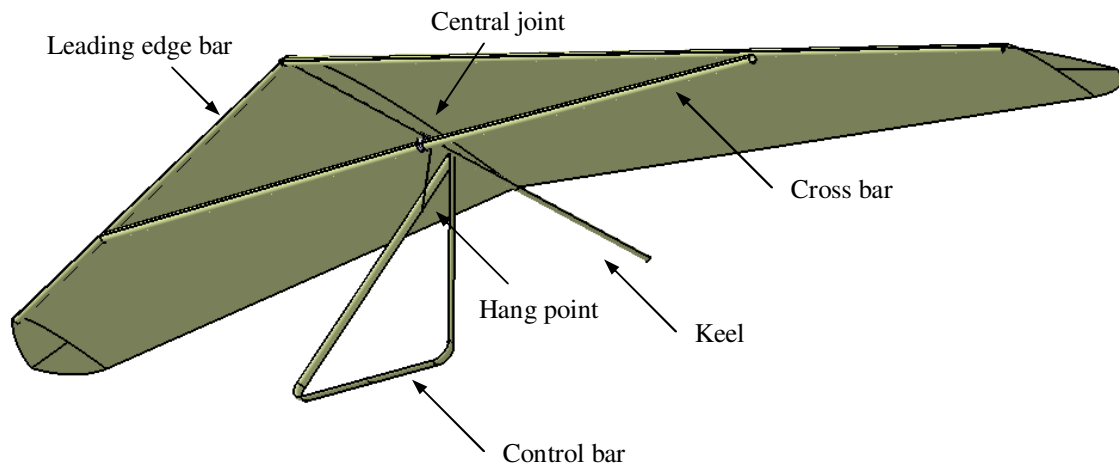


Figure 6.19 Schematic drawing of the Wills Wing Sport 2-155 hang glider

The main components of the hang glider as shown in Fig. 6.19 are leading edge bar, cross bar and keel as main frame constructs the hang glider wing planform. Control bar is mounted underneath to hold the pilot which is hanged on the hang point. The hang glider is controlled by shifting the pilot's body position to achieve pitching and banking action. The cross bar is connected to the leading edge bar by two joints on both sides and the central joint is placed on the keel to connect cross bar and keel. The detail dimensions are illustrated below.

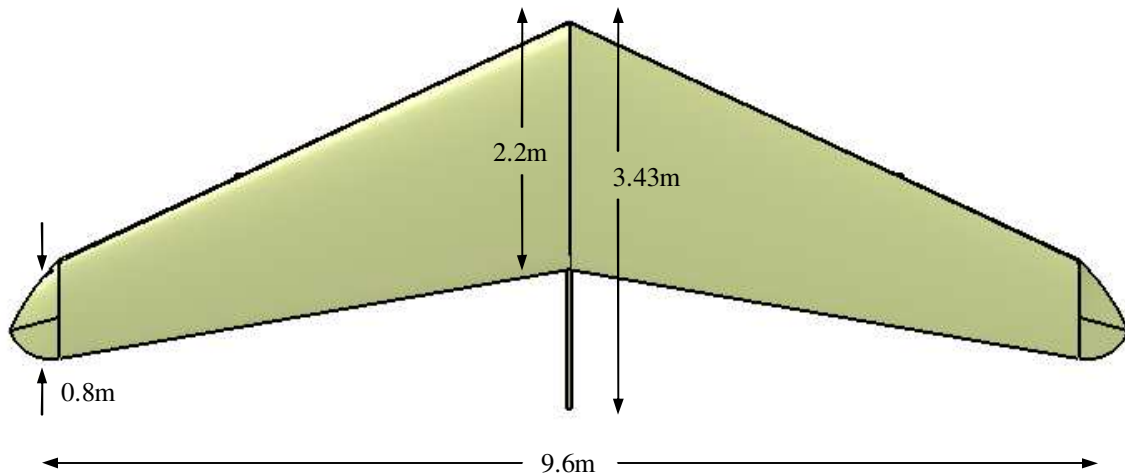


Figure 6.20 Top view of hang glider

As shown in Fig. 6.20 the root is 2.2m and the tip is 0.8m. The total length of the hang glider is 3.43m. The span is 9.6m. Fig. 6.21 shows the bottom view of the hang glider with main components of wing frame. The length of cross bar is 5.94m. From hang glider nose to the central joint is 1.34m. The distance from the root of control bar to the nose is 1.58m. And the wing root chord length is 2.2m.

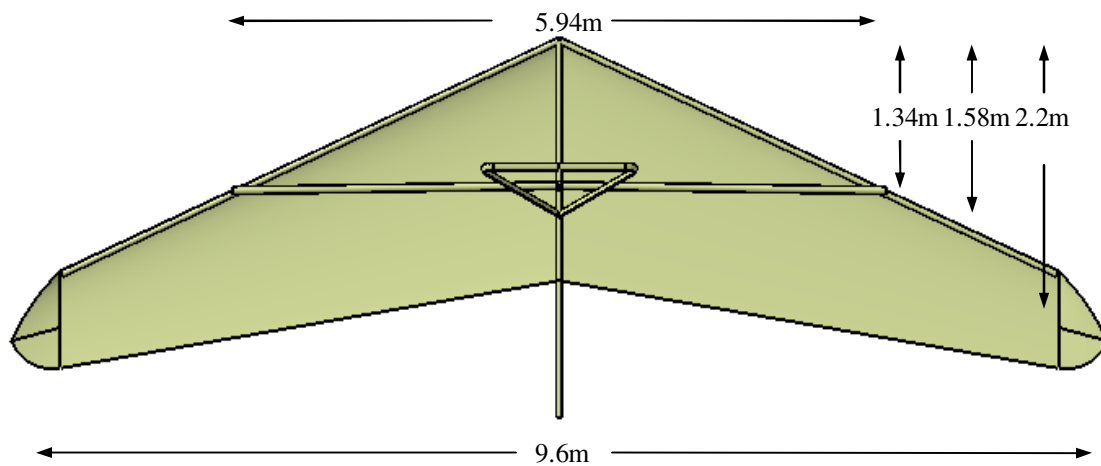


Figure 6.21 Bottom view of hang glider

In Fig. 6.22 the front view of hang glider is illustrated. The triangle control bar is mounted under the main frame to hold the pilot and its width at the bottom is 1.5m and overall height is 1.8m.

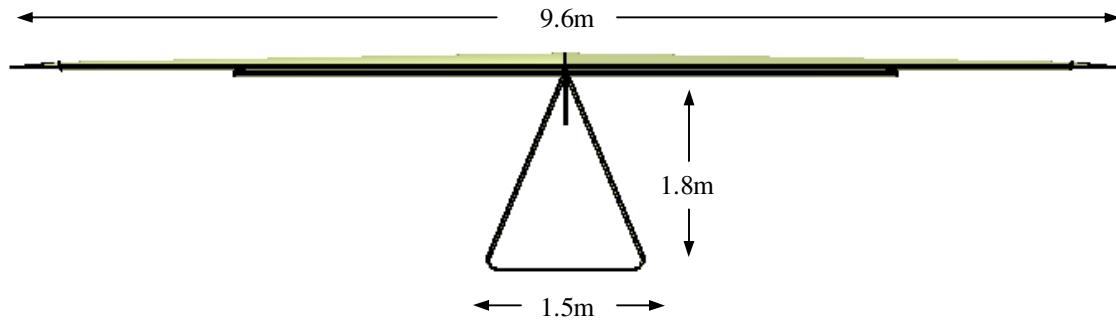


Figure 6.22 Front view of hang glider

The side view of hang glider is illustrated in Fig. 6.23. The hang point is the location where the pilot is hanged on the glider frame. The distance from hang glider nose to the hang point is 1.41m

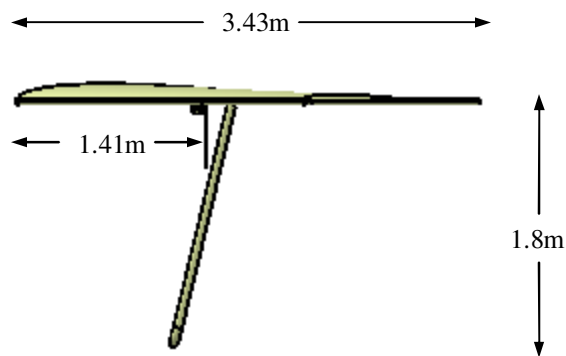


Figure 6.23 Side view of hang glider

By setting all the dimensions of the hang glider the finite element modelling has been carried out to evaluate the structural strength under different flight conditions in order to conduct the ornithopter design.

## 6.2 Ornithopter Design

Based on the Wills Wing Sport 2-155 hang glider the design of ornithopter is carried out by using the existing wing frame. Flapping mechanism is added on the wing structure and driven by an engine. The detailed structural design is described below.

### 6.2.1 Design Specification

For ornithopter design the estimated weight of flapping mechanism, engine and pilot is shown in Table 6.7. Engine Radne Racket is employed to drive the flapping mechanism which is widely used in powered hang gliders and cars. Additional mechanical linkages are placed on the wing frame to achieve flapping motion. The total weight of ornithopter is increased to 140kg (with estimated pilot weight of 70kg) which matches the maximum weight limitation of hang glider.

Wing	$W_w$	27kg
Engine	$W_E$	23kg
Mechanism	$W_M$	20kg

Table 6.7 Estimated weight of ornithopter parts

Based on the original hang glider mentioned above as a design prototype the dimension of ornithopter frame is shown below.

Wing Stroke Axis (spanwise distance)	$l_s$	0.32m
Max Weight	$W_{max}$	140kg
Nose Angle	$\phi_N$	130°
Stroke Angle	$\phi_S$	65°

Table 6.8 Design specification of ornithopter

The ornithopter wing consists of central wing and outer wing as shown in Fig. 6.24. The central wing section is fixed and the outer wing is designed as the flapping wing section. The wing frame is constructed with leading-edge bar, crossbar, keel as central reference, and root bars as stroke axes. The two root bars are placed at a spanwise distance 0.32m from the central keel as the stroke axes between outer wing and central wing.

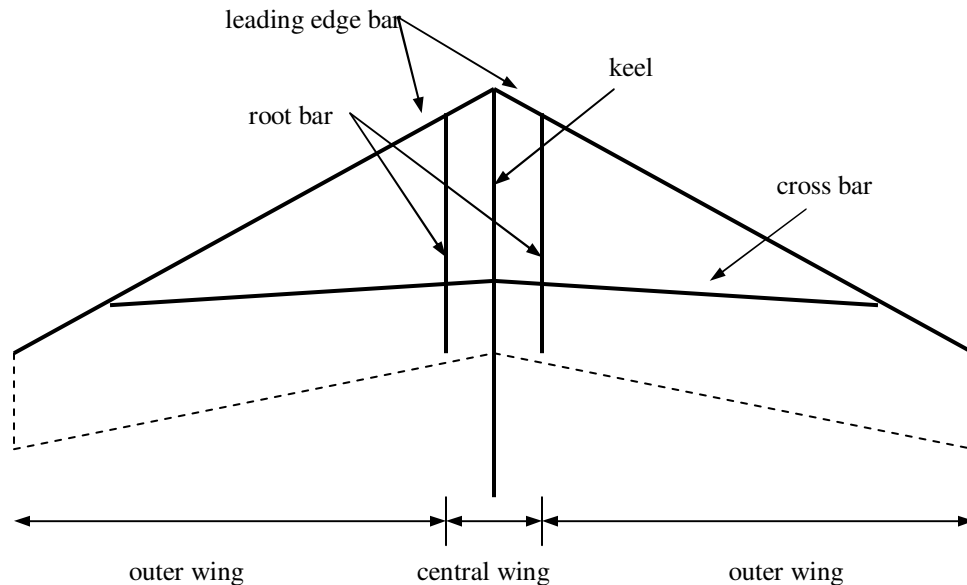


Figure 6.24 Ornithopter wing frame

The dimension of the wing frame is shown in Fig 6.25. The location of the joint adjacent with cross bar and keel is 1340mm taken from nose and another joint adjacent with cross bar and leading edge bar is 3276.6mm away from nose. The stroke axis and fold axis are 320mm and 2400mm respectively taken from root. In Fig. 6.26 the location of hang point and control bar point are illustrated. The hang point indicates where the pilot hangs his body and control bar point represents the connecting point of control bar with central keel.

The ribs used by Wills Wing 2-155 glider is listed in batten diagram 70G-5000 Wills Wing Inc. In the original design the ribs are slotted in without connecting to the leading edge to maintain the aerofoil profile. Seven ribs are placed on each side of wing.

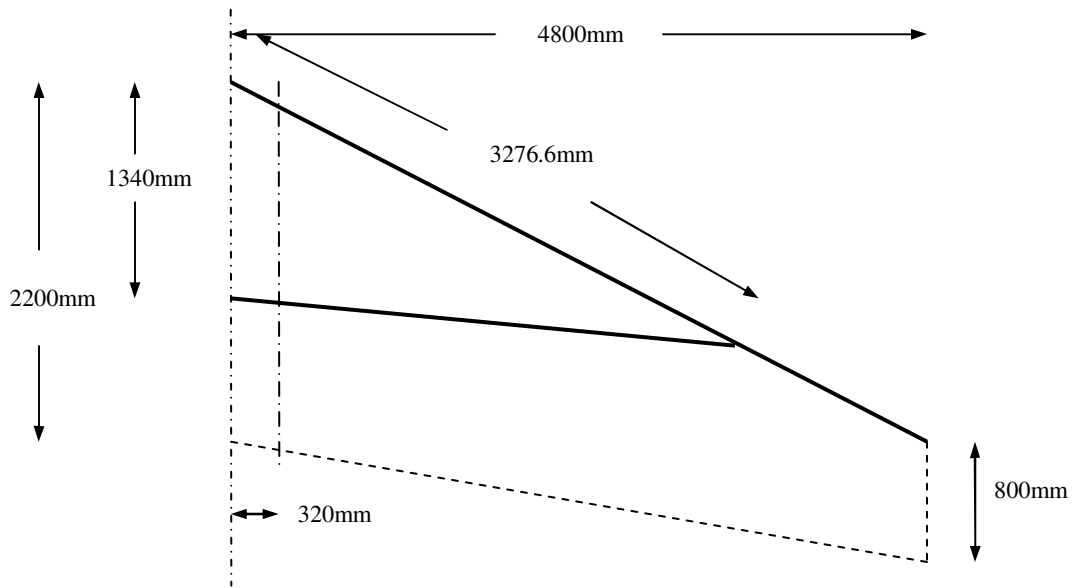


Figure 6.25 Wing frame dimension

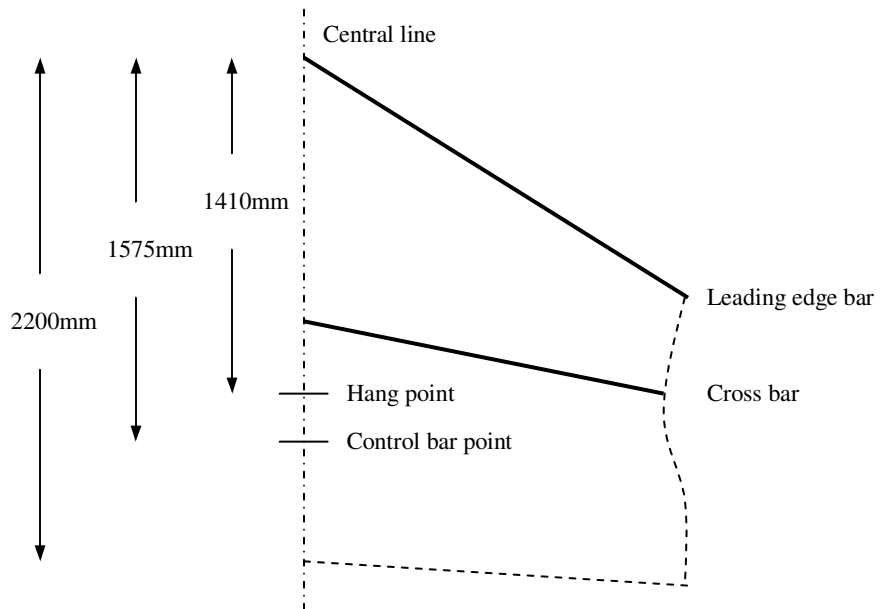


Figure 6.26 Location of the hang point and control bar point

Engine Radne Racket is employed to drive the flapping mechanism which is widely used in powered hang gliders and cars. The details are illustrated below.


Radne Racket	
<ul style="list-style-type: none"> <li>• 120cc air-cooled 14HP</li> <li>• Electric start using sealed lead gel cell batteries</li> <li>• 50kg thrust</li> <li>• Radne reduction drive 3.6 : 1 via gates micro V belt centrifugal clutch</li> <li>• Unleaded (98 oct) 4% oil mix</li> </ul>	

Table 6.9 Radne Racket engine

### 6.2.2 Flapping Motion Control

In the ornithopter design the flapping motion is controlled by properly setting the geometry of flapping mechanism. The maximum amplitude of stroke angle is  $65^\circ$  at stroke axis. As shown in Fig. 6.27 the cross bar is divided into central wing (*bar 1*) and inner wing with outer wing (*bar 2*) at stroke axis. The arm length of *bar 1* and *bar 2* is defined as *arm 1* and *arm 2* in spanwise. The maximum tip amplitude is defined as *amp 1* and *amp 2*. With the maximum stroke angle of  $65^\circ$  and arm length the maximum tip amplitude is calculated as shown in Table 6.10. Theoretically the maximum wing tip amplitude is about 2.4m (*amp 1*) and the root amplitude is 0.1m (*amp 2*).

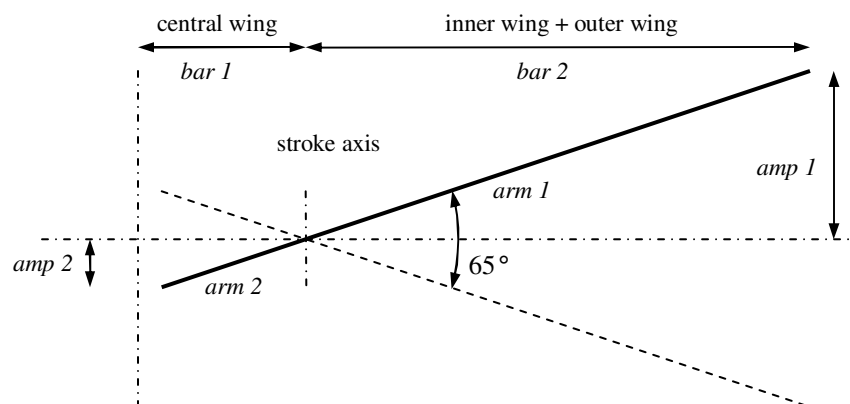


Figure 6.27 Dimension of each section of wing



	arm length	amplitude
<i>bar 1</i>	4480mm	2407.1mm
<i>bar 2</i>	186mm	99.94mm

Table 6.10 Tip amplitude and arm length

### 6.2.3 CATIA Model of Ornithopter

The other original members and components of the hang glider are retained as the rest of the main wing structure. Based on the original hang glider structure additional bars are put on the wing such as the root bars as stroke axes and the support bar to carry the weight of the engine. The CATIA model of the ornithopter design is shown below.

As shown in Fig. 6.28 an isometric view of ornithopter is illustrated. By using the hang glider structure an engine is placed under the wing at the root of the control bar.

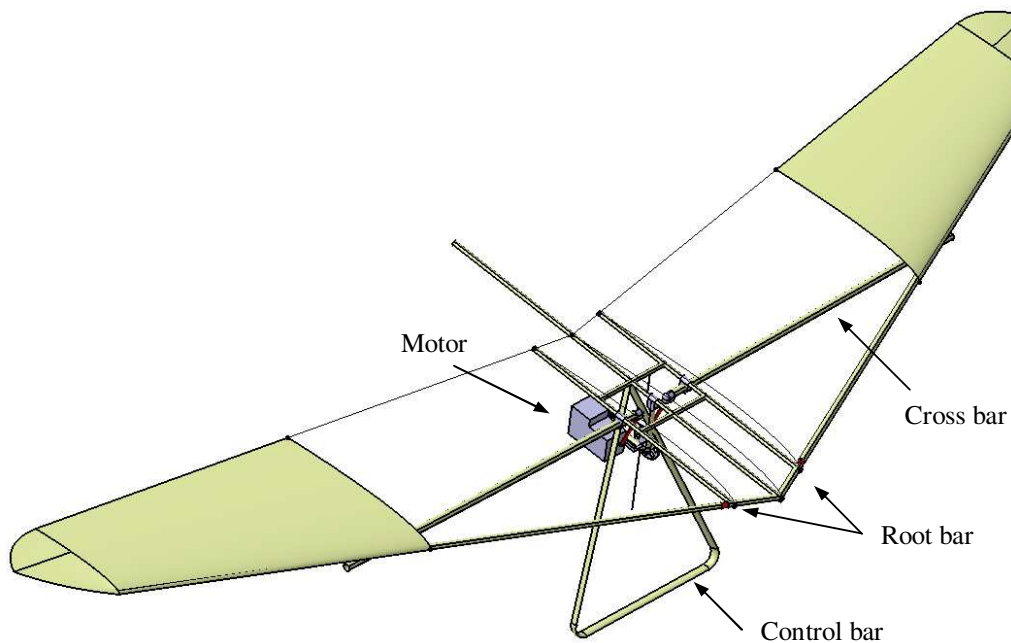


Figure 6.28 Isometric view of ornithopter

Fig. 6.29 shows the details of the flapping mechanism. As the main driving unit the cross bar is cut in the centre. Two stroke ring joints, one on either side, are used to hold the cross bars in place but allow the cross bars rotate about root bar. At the end of the cross bars they are connected to the motor by a crank arm. Two cross rods are placed in the central wing to strengthen the wing structure providing additional support for the engine frame. During flapping the outer wing rotates about the root bar and the leading edge bar will also rotate with the motion of cross bar. To achieve this, a universal joint is used at nose of root bar to connect it up with the leading-edge bar. Therefore the ornithopter structure consists of two main components: the central wing component and outer wing component. The central wing component is a fixed solid base with two root bars which are connected by part of leading edge in the central wing and two cross rods to support the flapping mechanism and hold the engine. The outer wing component is the main flapping wing section used to generate main lift and maintain the flight. The combination of cross bars and leading edge bars construction forming the outer wing and the main central wing structure provides a rather reliable and strong lifting surface. The outer wing is linked to central wing by four joints: two stroke joints on cross bar and two universal joints on leading edge bar.

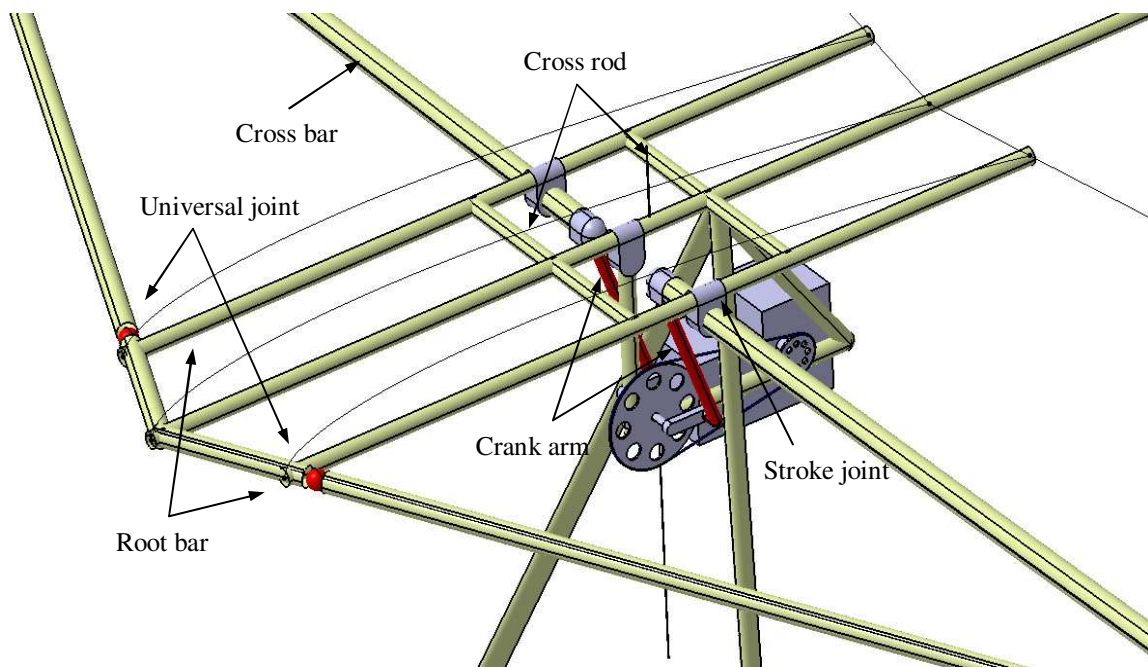


Figure 6.29 Isometric view of flapping mechanism

Another important design consideration is the structural frame which holds the motor. The support frame is required to be strong and steady without changing the original central gravity. Hence the motor with driving mechanism is located at the root of control. As shown in Fig. 6.30 the motor is mounted on the support frame which is just under the root of the control bar. The front support bar is connected to the keel just between those two cross rods refer to Fig. 6.29. And the rear support bar is connected to the root of control bar which is mounted on the keel. The dimension and material of the support frame is same as the keel with 42mm diameter. The rotating amplitude of the arm is 0.1m as given in Table 6.10 in order to achieve the stroke angle of  $65^\circ$ .

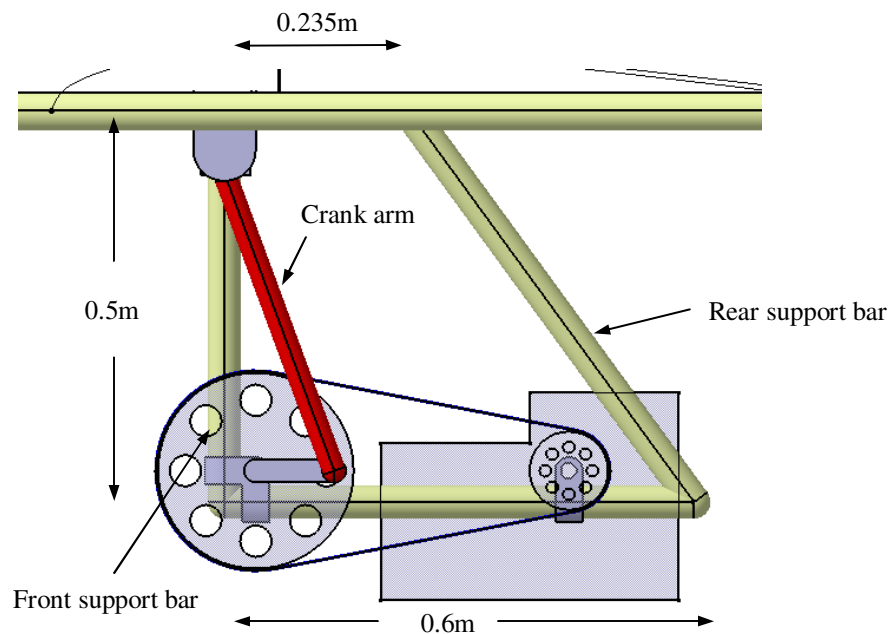


Figure 6.30 Motor support frames

The material used by the ornithopter is same as the original hang glider which is 7075-T6 aluminium alloy. The main dimensions of the wing structural members (single rod) and their masses are given below:

- Leading edge bar                       $\phi = 50 \text{ mm}$        $m = 2.21 \text{ kg}$
- Cross bar                                 $\phi = 62 \text{ mm}$        $m = 1.45 \text{ kg}$
- Keel                                         $\phi = 42 \text{ mm}$        $m = 1.38 \text{ kg}$
- Root bar                                  $\phi = 42 \text{ mm}$        $m = 0.71 \text{ kg}$
- Cross rod                                 $\phi = 42 \text{ mm}$        $m = 0.21 \text{ kg}$
- Motor support frame                 $\phi = 42 \text{ mm}$        $m = 0.57 \text{ kg}$

### 6.2.4 Spanwise Lift Distribution of Ornithopter

In this section the spanwise lift distribution is calculated by using both Theodorsen's theory and DeLaurier's methods. The lift amplitude over a cycle is calculated in order to carry out further structural strength analysis. The initial design of the wing flapping frequency is 2 Hz with total stroke angle of 65°. The parameters of ornithopter are shown below.

Flapping Frequency	$f$	2Hz
Stroke Angle	$\phi$	65°
Stroke Axes	$l_s$	0.32m (from root)

Table 6.11 Ornithopter wing design specification

By dividing the wing into 9600 strips with 1mm width the lift amplitude of flapping wing on each strip over a cycle is calculated over semi-span for cruising flight at the speed of 13.8m/s as shown below.

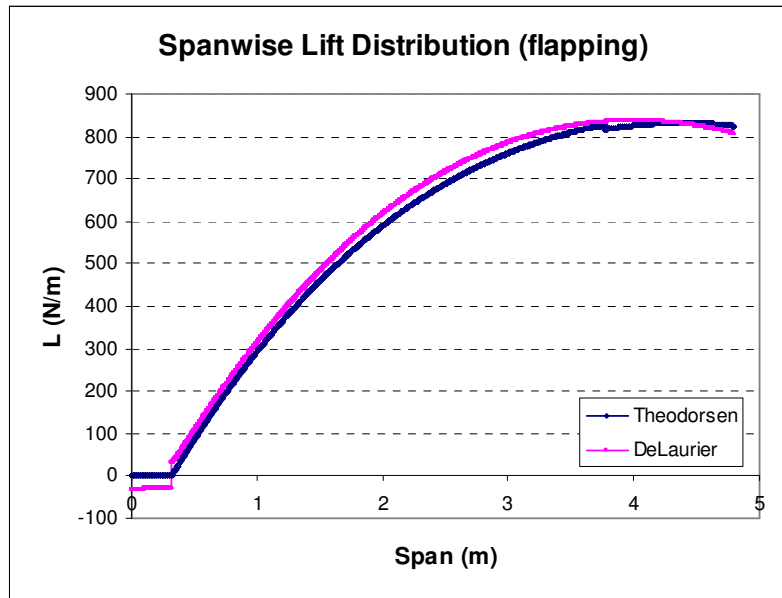


Figure 6.31 Comparison of spanwise lift distribution on semi-span

The total lift computed by Theodorsen's equation is 5.42kN and it is quite closed to the result of DeLaurier's method which is 5.56kN. The total lift is obtained based on the total mass of 140kg in terms of peak lift amplitude when the ornithopter is in cruising speed with 2Hz flapping frequency. By using Garrick's method the thrust generated by the flapping wing is calculated. Refer to Eq. (4.47) the thrust of the wing at 2Hz and cruising speed is 1100N which exceeds the maximum drag of the hang glider of 254 N converted from Fig. 6.8.

Further study will have to be carried out by means of experimental work in order to compare with the theoretical predictions.

### 6.3 Experimental Study

Based on the preliminary design of ornithopter and theoretical studies experimental investigation is carried out in the wind tunnel. A scale down model is manufactured with the scale ratio of 1:20. Two-component balance is constructed and calibrated to measure the forces on the wing with different speed.

### 6.3.1 Scale Down Model

The scale down model 1/20 scale has been designed for the wind tunnel test which fits well onto the test rig and the T3 wind tunnel section. As shown in Fig. 6.32 the wing root chord is 110mm and tip is 40mm. The span is 480mm long and nose apex angle is  $130^\circ$ . The stroke axis is 16mm away from root. 2mm carbon fiber rod is placed as a crossing bar which is connected to the driving mechanism. A 1mm carbon fiber rod is used as the leading edge bar and 0.381mm chordwise piano strings are placed as ribs to hold the wing skin. The total mass of the wing is 7.46g. The central gap between two flapping wing sections represents the fixed central wing. The skin is made of very light flexible ripstop. A strain gauge is placed in the centre and connected to the stroke axis in order to measure the flapping frequency.

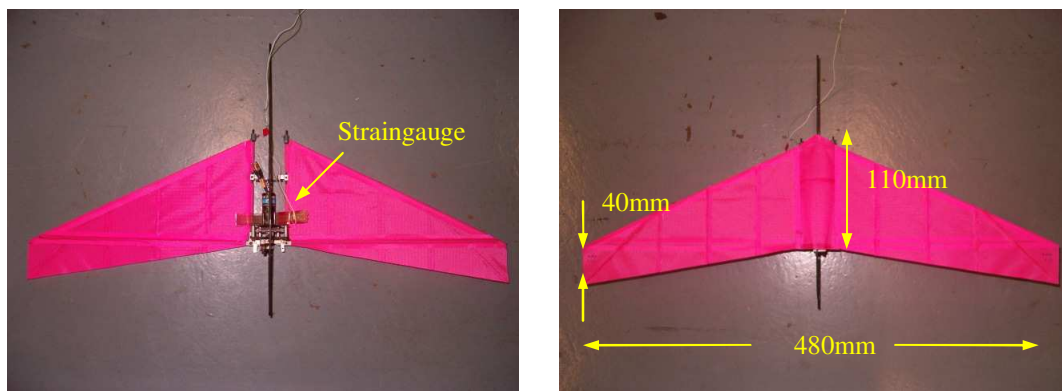


Figure 6.32 1:20 scale wing configuration

### 6.3.2 Test Rig Setup

A two-component balance is constructed by two load cells which is the same layout as the flexible wing tunnel test in Chapter 5. The vertical load cell measures horizontal force and the horizontal load cell measures vertical force. The fuselage is mounted on the end of sting which is fixed on the balance.

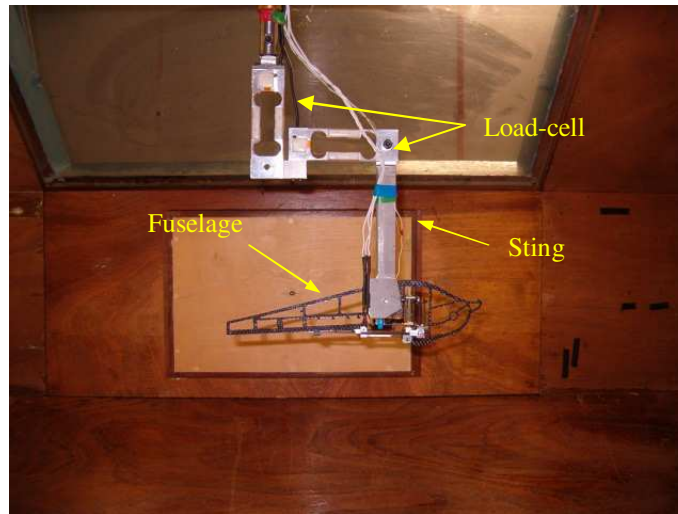


Figure 6.33 Test rig setup

The same set of electrical equipments is employed to control the speed of motor and measure the flapping frequency and input power which has been introduced in Chapter 5 in Fig. 5.42.

### **6.3.3 Balance Calibration**

The loading acting on the flapping wing is measured by the two-component balance. To convert the readings in counts to force in Newtons calibration is carried out by placing unit load in vertical and horizontal directions respectively. The lift force calibration is carried by hanging unit load on the sting vertically and the drag force calibration is carried out by placing horizontal load on the sting through pulley system illustrated in Fig. 5.44. Since a new pair of wing is replaced in this test the calibration is carried out again by using the same method as stated in Chapter 5.

Refer to Fig. 6.31 the total aerodynamic force acting on the flapping wing is 5.56kN at 13.8m/s cruising speed. For 1:20 scale model in low speed less than 10m/s the lift generated by the flapping wing is less than 100g and inertia is less than 20g at 3Hz computed by Theodorsen's theory. Hence the applied load for the calibration is set from 0g to 170g with 10g increment and placed on the vertical and horizontal hanger respectively. The calibration tests are carried out by increasing the load from 0g up to

170g and decreasing from 170g down to 0g. The process is repeated for several times for accuracy. The relationship between readings in counts and applied load are illustrated in Fig. 6.34 and Fig. 6.35. By using the same method motioned in Chapter 5 in Eq. (5.15) the calibration coefficient matrix is obtained in Table 6.12. The uncertainty of the balance is carried out by transferring the converted forces in physical units back to the reading in counts based on the calibration coefficients shown in Table 6.12. Compared with the raw reading in counts the uncertainty of the lift is 0.5% and 0.93% for drag.

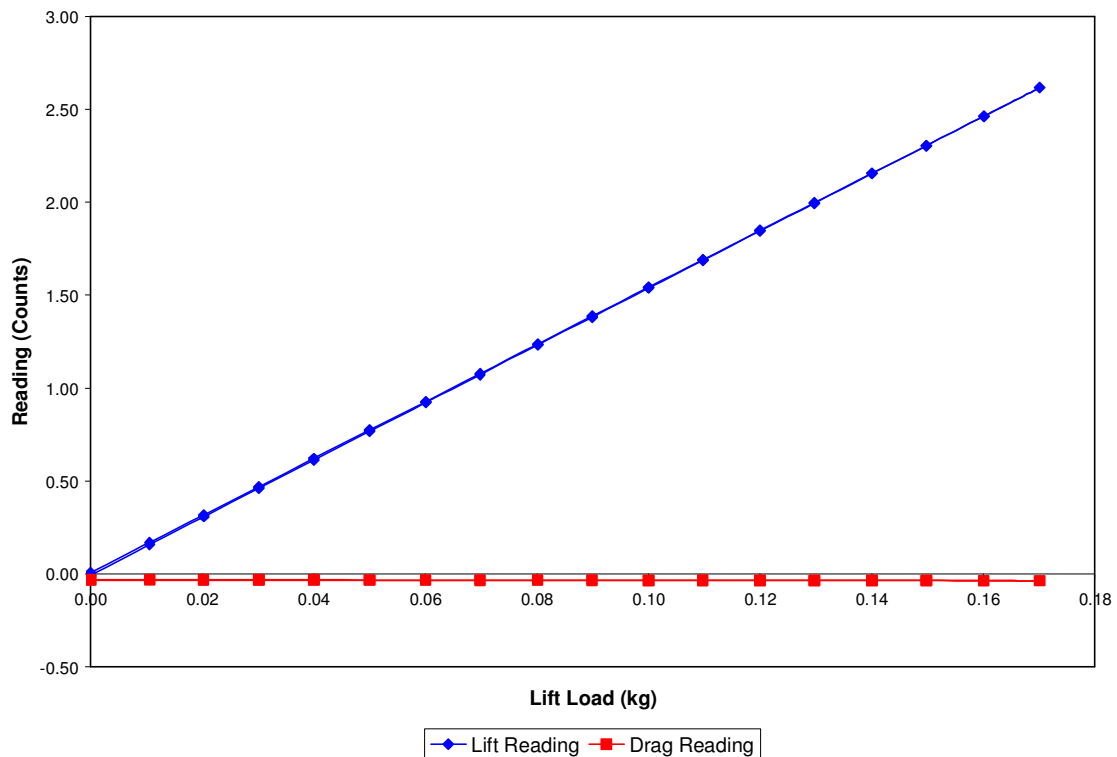


Figure 6.34 Lift force calibration



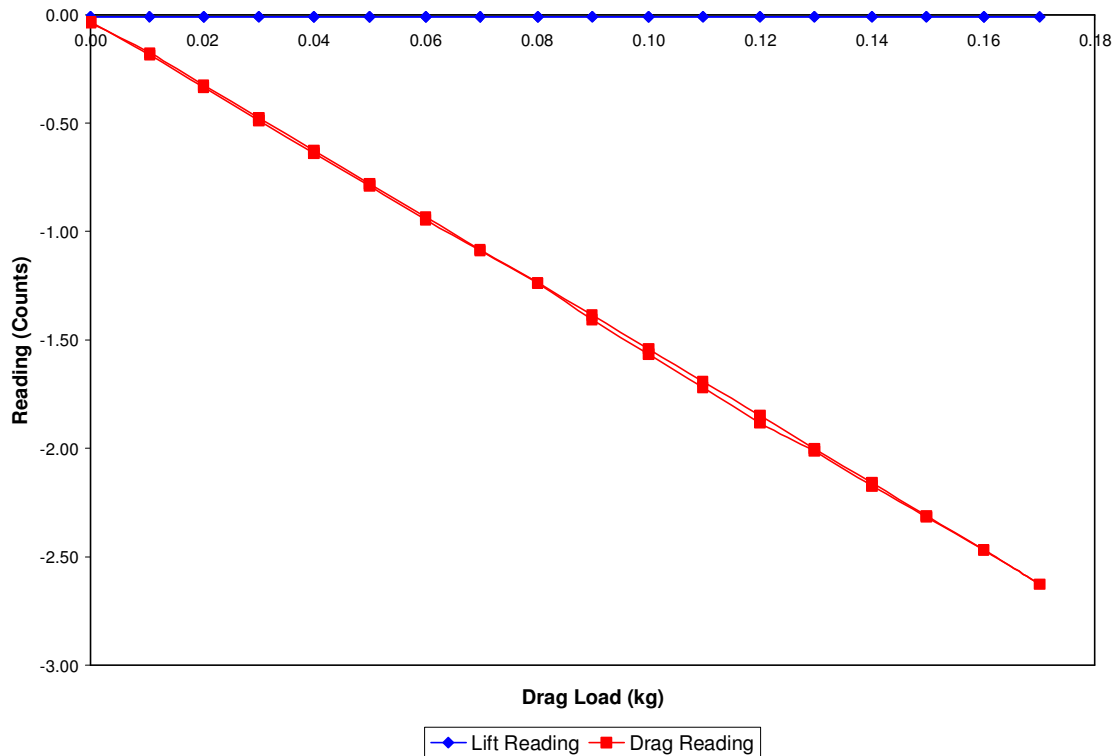


Figure 6.35 Drag force calibration

	$a_0$ (kg)	$a_1$ (kg/mV)	$a_2$ (kg/mV)	$a_3$ (kg/(mV) <sup>2</sup> )	$a_4$ (kg/(mV) <sup>2</sup> )
Lift	2.56E-04	6.44E-02	-5.34E-04	2.17E-04	-1.73E-04
Drag	-1.90E-03	-4.37E-04	-6.62E-02	1.00E-04	-3.15E-04

Table 6.12 Calibration coefficients

### 6.3.4 Wind Tunnel Test

In order to obtain the aerodynamic load of the flapping wing inertia test is carried out first. The total wing mass is 7.46g and inertia force is measured in different frequencies of 2.0Hz, 2.5Hz and 3.0Hz with same mass distributed on the wing frame. By using the calibration matrix shown in Table 6.12 the inertia force is converted to Newton. Theoretical calculations are compared with test results by using amplitude of inertia force against frequency square as shown in Fig. 6.36. The test results show a good agreement with computed results. Therefore the load cell is capable of measuring dynamic forces.

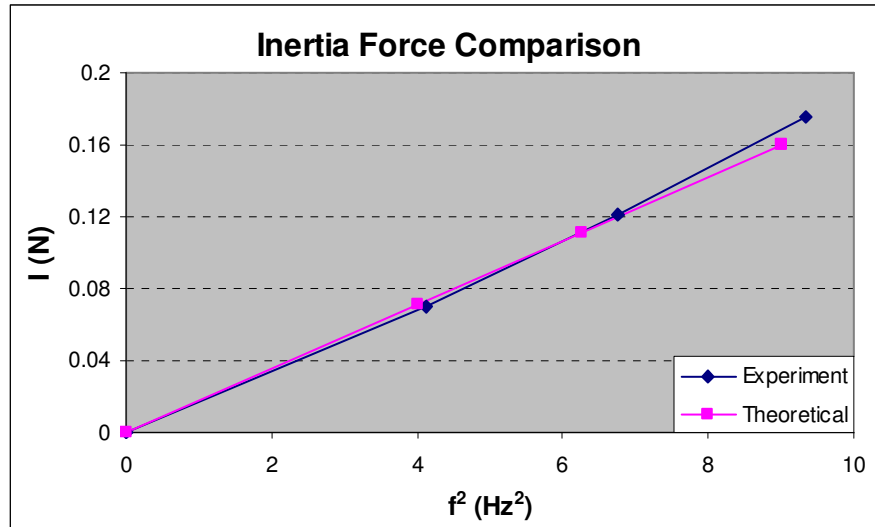


Figure 6.36 Inertia force comparison

Wind tunnel test is carried out subject to this scale model in different speed of 2m/s, 4m/s and 6m/s under 2Hz. Theoretical calculations are carried out by using Theodorsen theory and DeLaurier's method and compared with test results. By subtracting the inertia force from total force the pure aerodynamic force is obtained as shown in Fig. 6.37. The blue curve is the test result of the lift amplitude in different speed. The pink curve and yellow curve represent the theoretical calculation of Theodorsen's method and DeLaurier's method respectively.

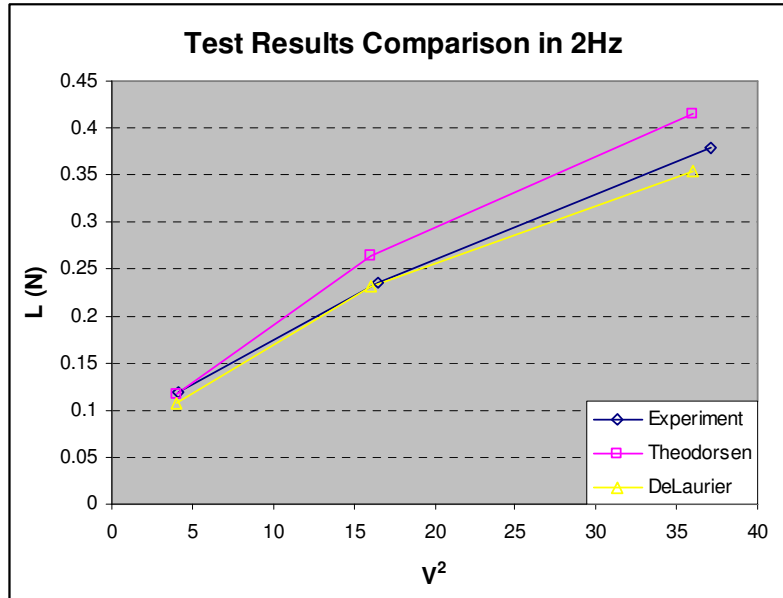


Figure 6.37 Aerodynamic force comparison

Since the Theodorsen's theory assumes the lift is proportional to the heaving amplitude the wing tip produces most of the lift during the flapping. By considering the wing with finite span DeLaurier's method is closest to the test result. Hence the DeLaurier's method is more suitable for predicting the aerodynamic forces of flapping wings. The test results of design case 1 below for 4m/s and 2Hz in Fig. 6.38 show the same tendency in time history compared with theoretical calculation shown in Fig. 6.39. The measured aerodynamic forces are tabulated in Appendix C in Table C1 and the raw data in time history of different test cases are shown in Appendix from Fig. C1 to Fig. C6.

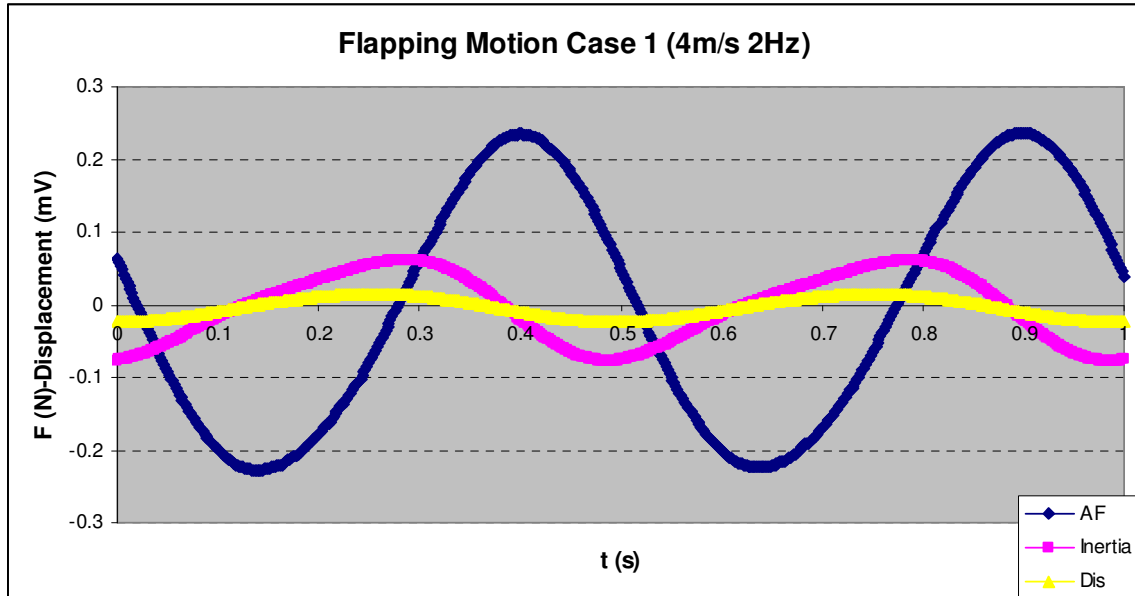


Figure 6.38 Test result of flapping motion of design case 1 for 4m/s, 2Hz

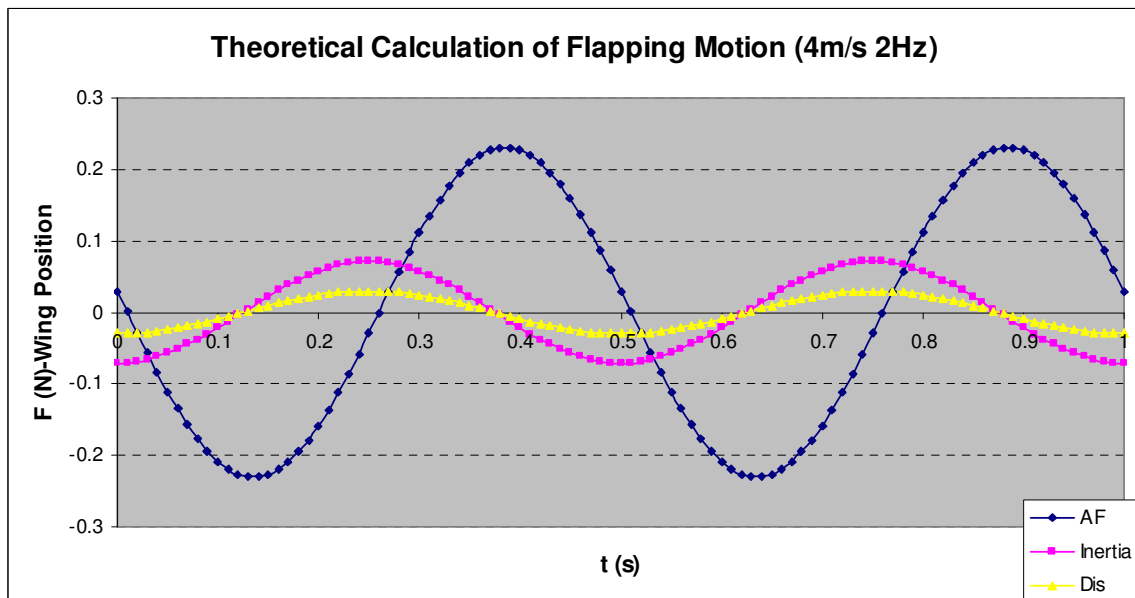


Figure 6.39 Theoretical calculation of flapping motion for 4m/s, 2Hz

## 6.4 Finite Element Modelling

Finite element modelling is carried out to evaluate the structural strength of the wing under different loading cases. MSC Patran/Nastran 2005 is employed to carry out the numerical analysis. The objective of the FE modelling is to analyse the original hang glider structure and thereby help preliminary design of the ornithopter structural integrity. The FE modelling consists of geometry modelling, mesh elements, loading and boundary condition, material and properties selection. The details of FE modelling are described below.

### 6.4.1 FE Modelling of Hang Glider

The FE modelling of the original full-scale hang glider wing is carried out first. As a prototype the wing structural strength is essential for further design optimization of the ornithopter. Due to the complicated shape of the wing around its tip region the wing platform is divided into a number of segments according to the wing frame in the geometry modelling as shown in Fig. 6.40 in order to carry out proper meshing of the entire wing surface.

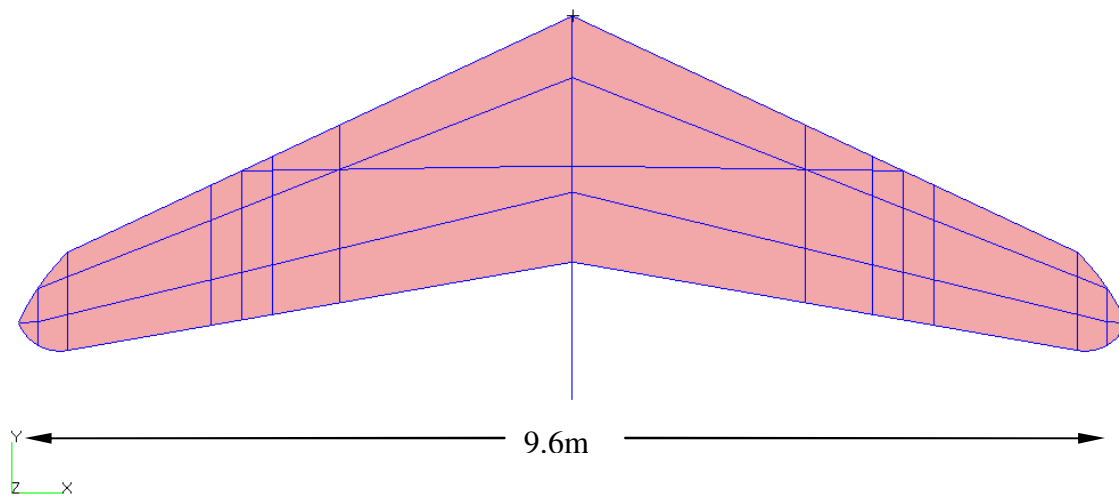


Figure 6.40 Geometry modelling of hang glider

According to the original hang glider structural cables are employed to link the control bar with glider frame as shown in Fig. 6.41. With these wires the control bar is fully strengthened and firmly tied to the main frame.

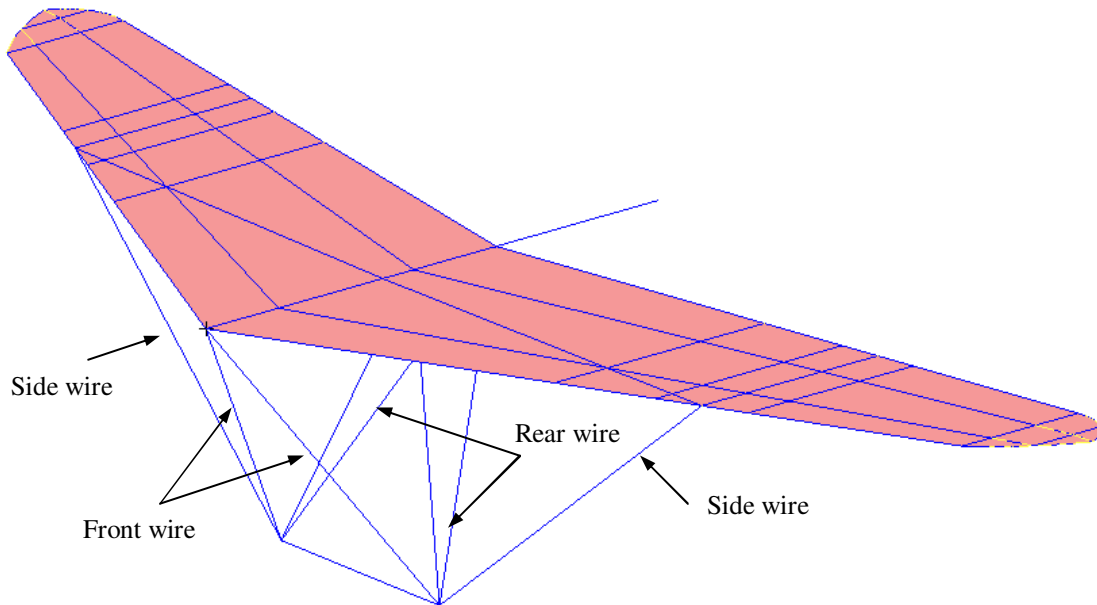


Figure 6.41 Geometry modelling of hang glider wire

Based on the geometry model the mesh is carried out with two types of mesh elements. 2-D shell element is employed for the wing surface and 1-D beam element models for the wing frame and wires. As shown in Fig. 6.42 the isometric trapezoidal (quad) mesh with four nodes is employed for the surface mesh. Fig. 6.43 shows the bar elements with two nodes of the wing frame and wires in blue colour. According to the hang glider structure the control bar is fixed on the keel which is the location of the centre of gravity. Therefore the root of the control is fully clamped in both translation and rotation as shown in Fig. 6.43 in red colour.

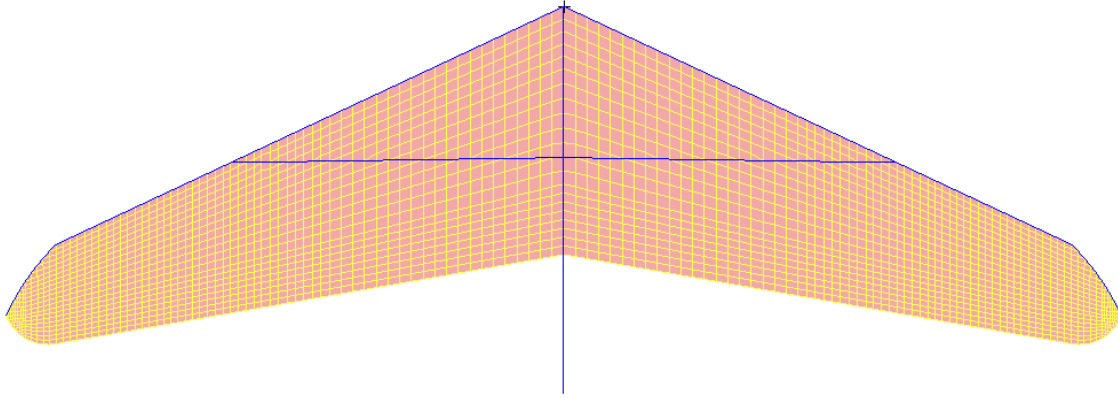


Figure 6.42 Mesh elements of wing surface

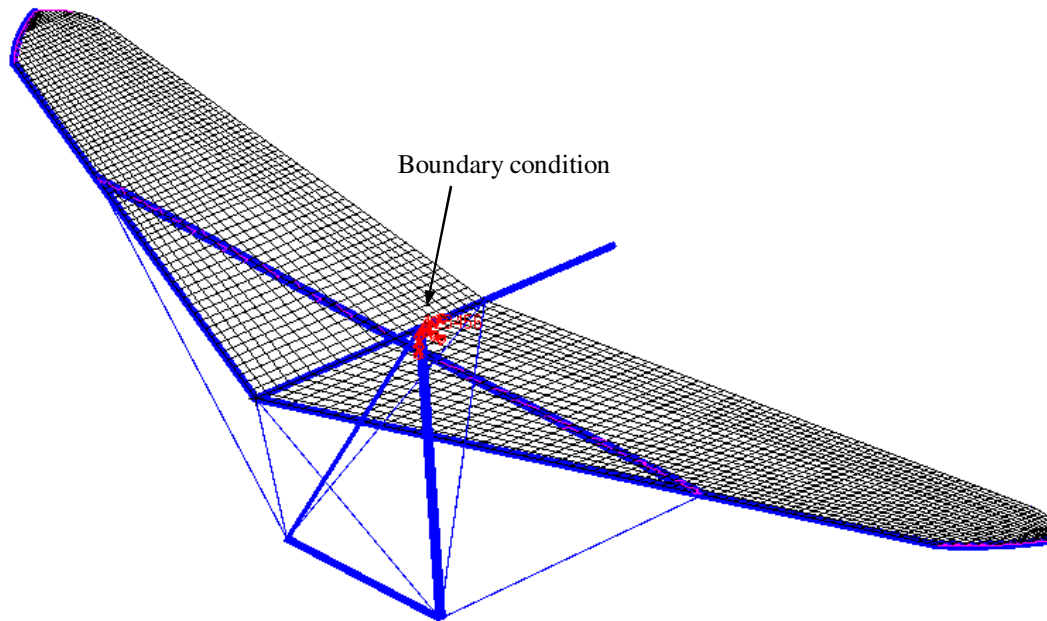


Figure 6.43 Mesh and bar elements of wing frame and boundary condition

In the loading case modelling the aerodynamic force is applied on the wing. Concentrated load is applied on  $\frac{1}{4}$ -chord line. As a reference model the cruising condition is modelled first with load factor of  $n = 1$  with the total weight of 140kg. Refer to Fig. 6.14 the spanwise lift distribution has been calculated and the distributed force is applied on the FE model as shown in Fig. 6.44 in blue colour.

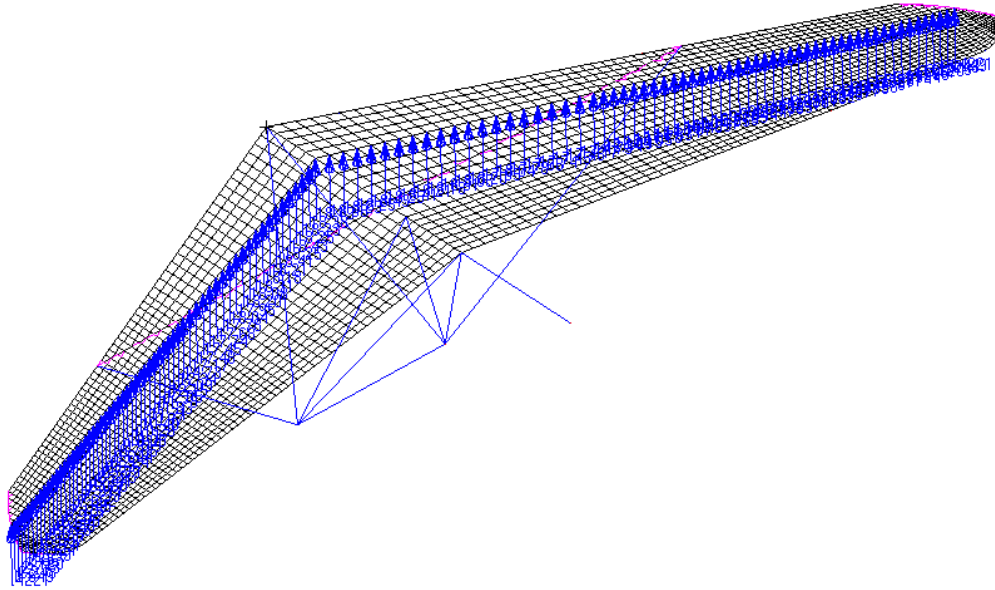


Figure 6.44 Loading case with factor of  $n = 1$

In the material modelling three materials are used for the hang glider components. 7075-T6 aluminium alloy is used for the wing frame and control bar. Glass fiber cloth is used for modelling the wing skin. Steel alloy is used for all the wires. The material properties are tabulated below.

Density	2810kg/m <sup>3</sup>
Ultimate tensile strength	572MPa
Tensile yield strength	503MPa
Poisson's ratio	0.33
Modulus of elasticity	71.7GPa
Shear modulus	26.9GPa

Table 6.13 Material properties of 7075-T6 aluminium alloy



Modulus of elasticity	$E_1=40\text{GPa}$ $E_2=8\text{GPa}$
Poisson's ratio	0.25
Shear modulus	4GPa
Thickness	0.125mm

Table 6.14 Material properties of glass fiber

Density	7850kg/m <sup>3</sup>
Ultimate tensile strength	1882MPa
Tensile yield strength	1793MPa
Poisson's ratio	0.342
Modulus of elasticity	196GPa
Shear modulus	73GPa

Table 6.15 Material properties of steel alloy

The analysis is carried out subject to the entire model with linear static solution type. The wing skin is constructed by 32 layers of glass fiber cloth with the fiber orientation of  $[0/90/45/-45/-45/45/90/0/0/90/45/-45/-45/45/90/0]_S$ . The computed stress on each layer of the skin is tabulated below and Fig. 6.45 shows the first layer with  $0^\circ$  fiber direction.

Fiber orientation	Stress (MPa)
$0^\circ$	10.0
$90^\circ$	15.3
$45^\circ$	13.6
$-45^\circ$	12.6

Table 6.16 Stress on each layer of the skin

The stress level on the wing frame is much higher as shown in Fig. 6.46 which is 66.4MPa due to bending at the joint of cross bar and leading edge bar. In Fig. 6.47 the

axial stress is plotted. The aerodynamic load acting on the wing is transferred by side wire to the control bar with stress level of 225MPa. The deformation of the entire wing structure is illustrated in Fig. 6.48. The maximum displacement is 0.115m at the wing tip.

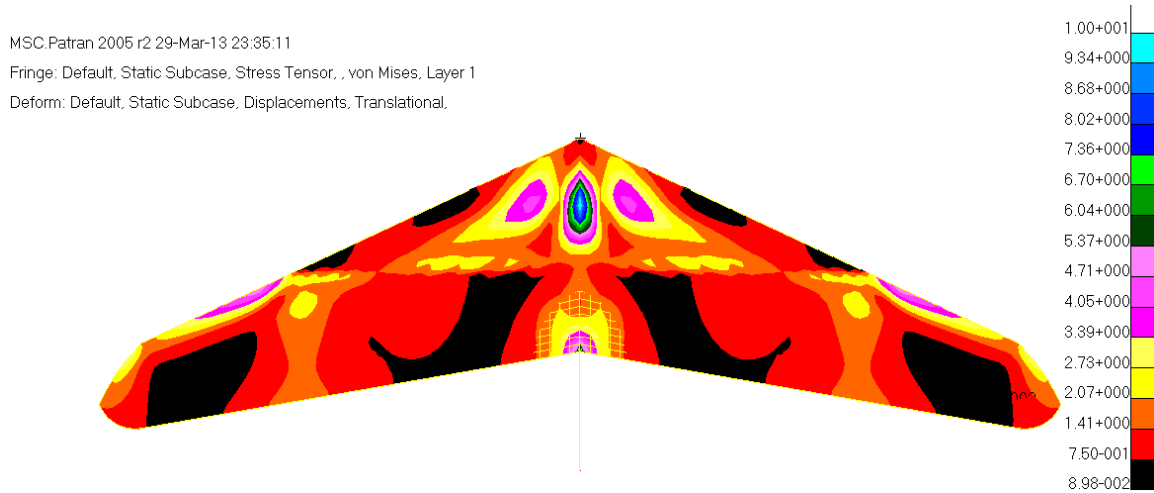


Figure 6.45 Stress on the wing skin

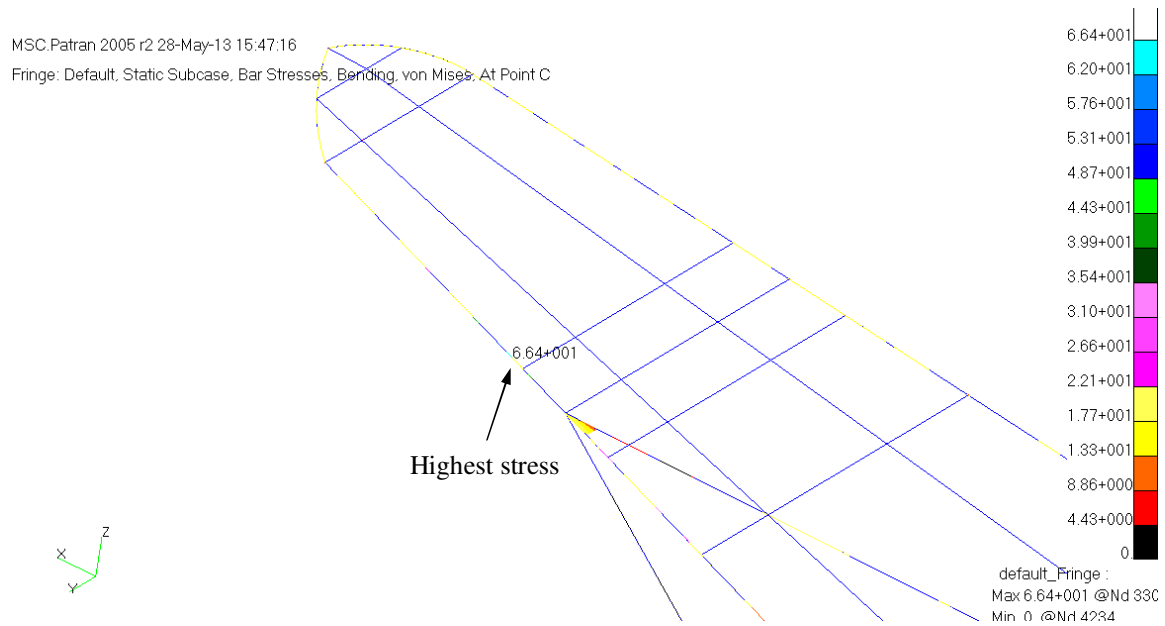


Figure 6.46 Stress on the wing frame

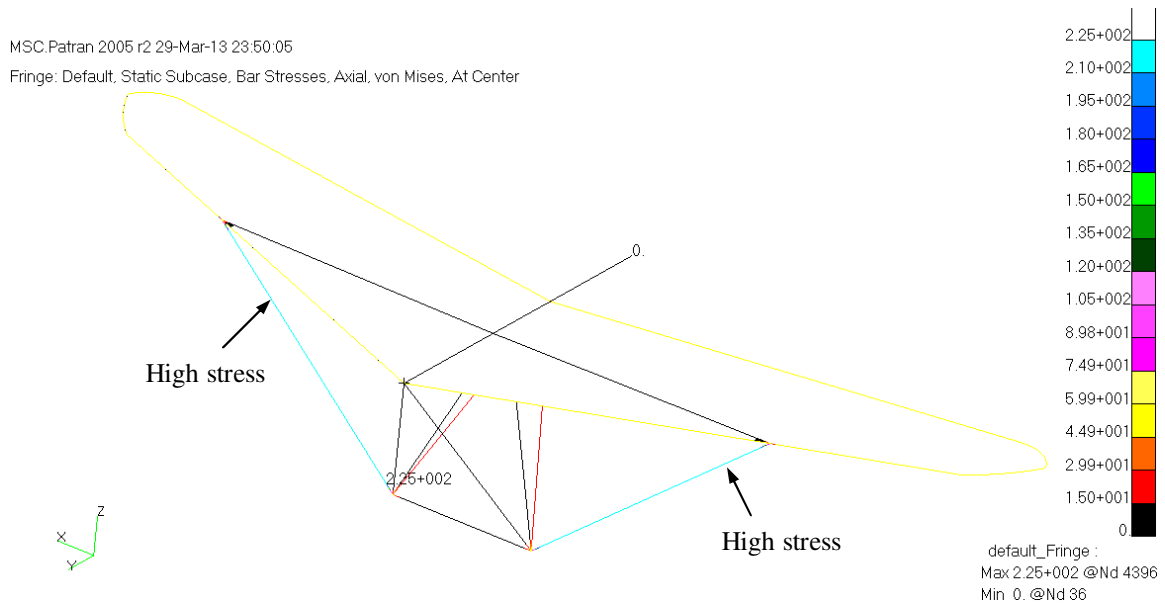


Figure 6.47 Axial stress on the wing frame

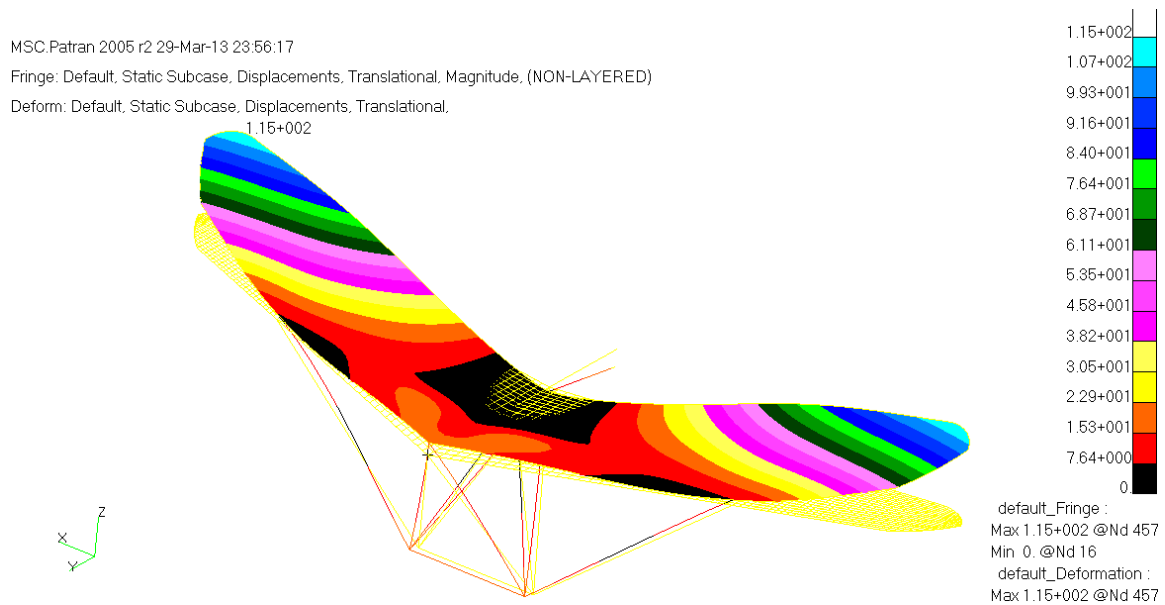


Figure 6.48 Wing deformation

All the results show a reasonable stress level without any structural failure subject to the load factor of  $n = 1$ . Refer to the  $n$ - $V$  diagram in Fig. 6.12 the ground test is carried out by the manufacture under a critical condition at speed of 29.1m/s. And the corresponding load factor at this speed is  $n = 7$ . Therefore the FE modelling subject to this critical case is carried out by increasing the load case from  $n = 1$  to  $n = 7$ . Hence the applied load on

the wing is seven times higher than the cruising condition. By using the same analysis method the results are shown as below. The stress level is still low as shown in Fig. 6.49 which is 70MPa. As shown in Fig. 6.50 the highest stress due to bending occurs at the joint of cross bar and leading edge bar with the stress level of 465MPa. In Fig. 6.51 the highest axial stress occurs on the side wire which is 1570MPa. The deformation in this loading case is demonstrated in Fig. 6.52 with the displacement of 0.8m which occurs at trailing edge of wing tip. Since the wing skin is made of flexible cloth and any load applied on the skin will induce huge deformation the true deformation of the wing frame on the leading edge is 0.695m.

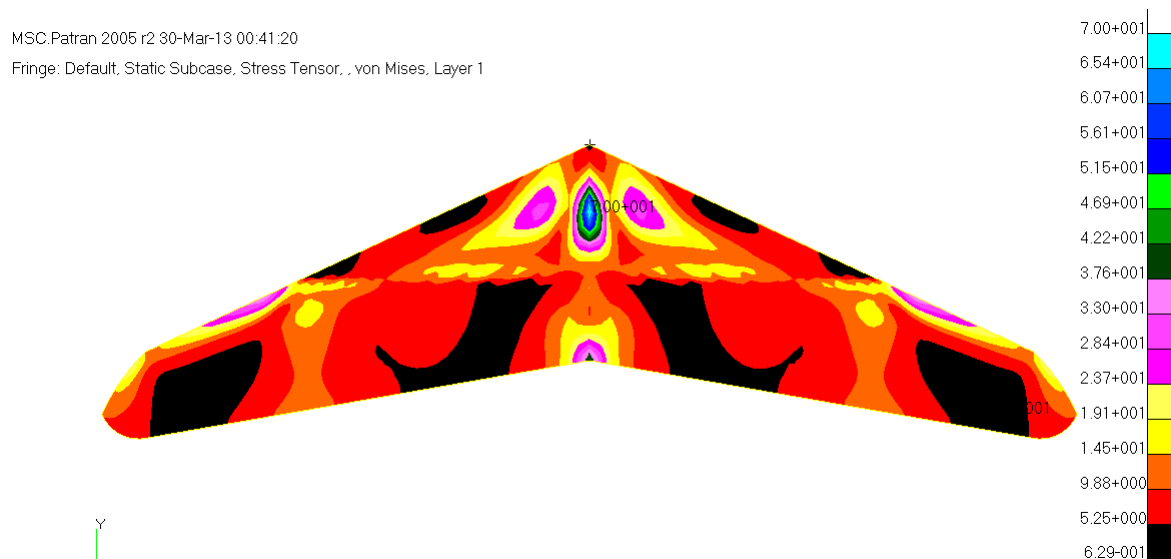


Figure 6.49 Stress on the wing skin (n=7)

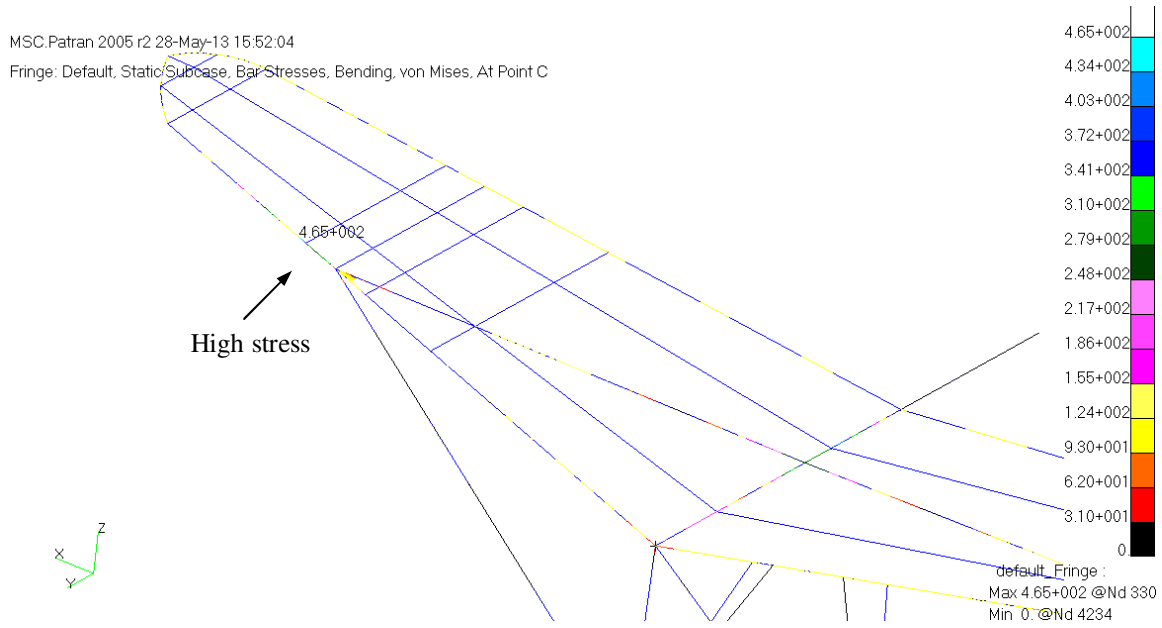


Figure 6.50 Stress on the wing frame (n=7)

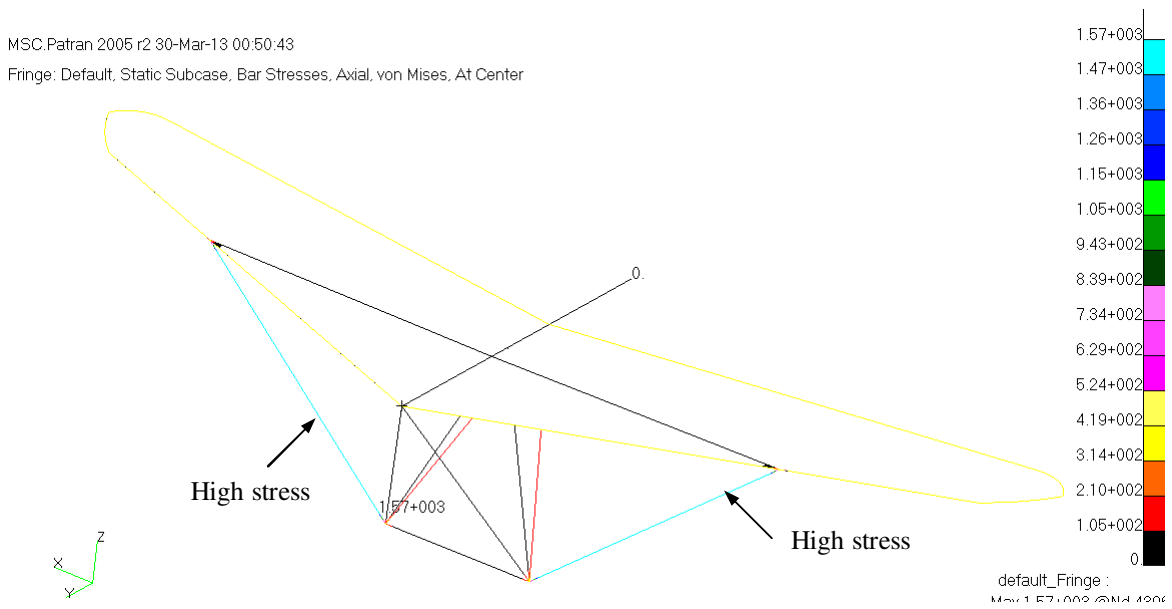


Figure 6.51 Axial stress on the wing frame (n=7)

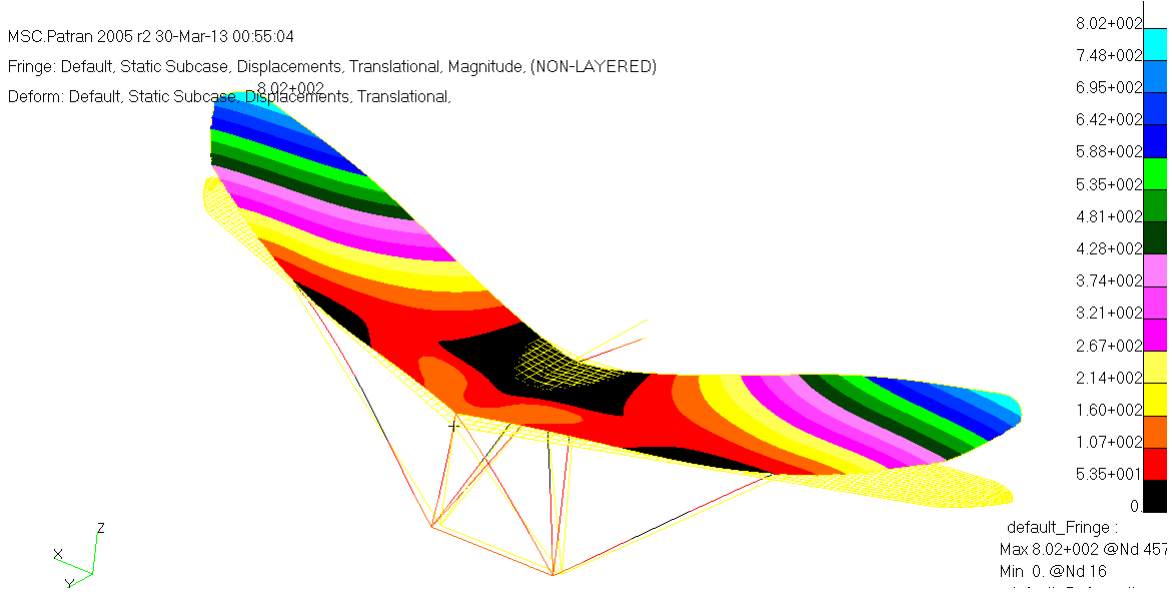


Figure 6.52 Wing deformation (n=7)

Subject to the loading case with load factor of  $n = 1$  and  $n = 7$  the FEA results are tabulated below.

Loading case	$n = 1$	$n = 7$
Stress on skin (MPa)	10	70
Stress in bending (MPa)	66.4	465
Axial stress (MPa)	225	1570
Max deformation (m)	0.115	0.802
Frame deformation (m)	0.099	0.695

Table 6.17 FEA results with load factor  $n = 1$  and  $n = 7$

In gliding condition the aerodynamic load applied on the wing is in elliptical distribution as shown in Fig. 6.14 which bends the wing frame upward. This bending moment is mainly taken by the leading edge bar and cross bar. Hence the maximum stress occurs at the joint of cross bar and leading edge bar with stress level of 465MPa. The aerodynamic load on the wing is transferred by wires to the control bar. The results show the side wires transfer most of load which is 1570MPa axial stress. Since the wing skin is made of

flexible cloth very little stress is taken by skin but large deformation occurs at wing tip. However the maximum displacement occurs at the trailing edge of the wing tip which is not the true deformation of the wing frame. The maximum deformation of the wing frame is 0.609m at wing tip. Compared the FEA results of  $n = 7$  case and  $n = 1$  case the loading is increased 7 times higher and the stress level and deformation are also linearly increased with the factor of 7. Under the critical loading case of  $n = 7$  the structure is in the safe level without failure based on finite element analysis results. And this has also been verified by the manufacture on the ground test with load factor of  $n = 7$ .

Therefore the critical section of the hang glider is the joint of leading edge bar with cross bar. The tip deformation is another important issue that needs to be considered. The side wire is also a key component which experiences the highest axial stress.

#### **6.4.2 FE Modelling of Ornithopter**

Following the above FE analysis on the baseline hang glider structure the FE modelling is carried out on the ornithopter structure. The modelling method for ornithopter is the same as the hang glider modelling. Two modelling cases are carried out subject to different flight conditions which are gliding and flapping. The aerodynamic load is modelled as concentrated load at  $\frac{1}{4}$ -chord line. The mesh elements and materials used for ornithopter model are the same as those used for the glider model. The geometry and mesh of the ornithopter model is illustrated in Fig. 6.53.

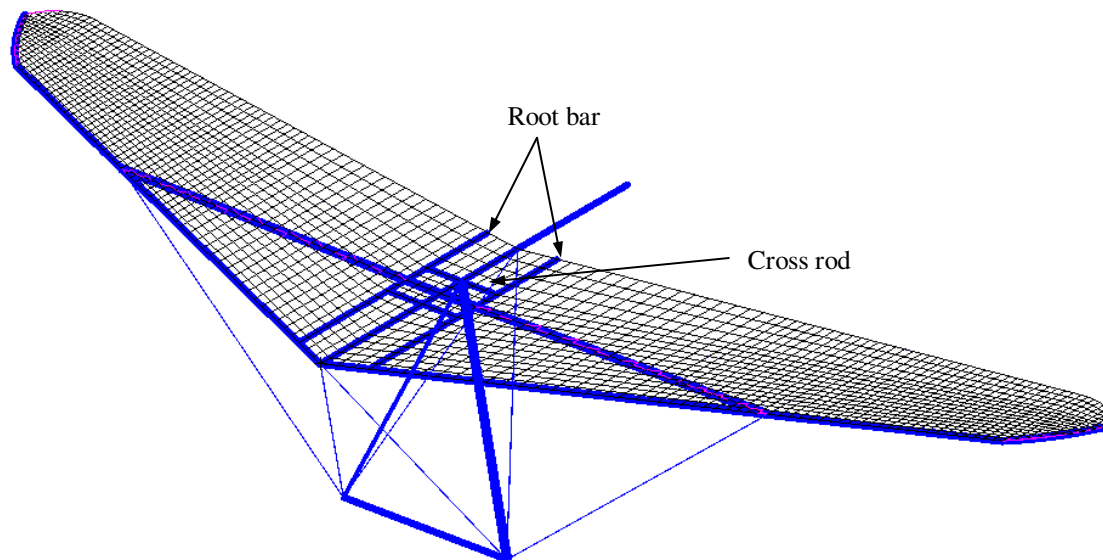


Figure 6.53 FE modelling of ornithopter

#### 6.4.2.1 FE Modelling of Ornithopter in Gliding

In gliding flight the ornithopter wing is locked as fixed steady wing platform which performs like a hang glider. Hence the aerodynamic load distribution is the same as the hang glider as referred in Fig. 6.14. By considering the extreme load condition with load factor of  $n = 7$  the FE analysis is carried out and it shows similar results to the hang glider. The stress on the skin in Fig. 6.54 is 37.8MPa (first layer) and the maximum stress occurs at the root bar which is still in rather low level. Refer to Table 6.17 the stress is reduced from 70MPa to 37.8MPa compared with the skin stress of the glider model in  $n = 7$  loading case. The stress reduction of the skin is mainly due to the additional root bars and cross rods placed on the wing root which forms a rather solid central wing section to take the aerodynamic load. In Fig. 6.55 it shows the stress of the frame due to bending. The maximum stress occurs at joint of leading edge bar and cross bar with stress level of 465MPa. The axial stress as shown in Fig. 6.56 indicates the maximum stress occurs on side wire with stress level of 1560MPa. The wing deformation is shown in Fig. 6.57. The maximum displacement occurs at trailing edge of wing tip in 0.8m. And the deformation of the leading edge bar is 0.694m. Comparing the FEA results of ornithopter with hang glider in the same loading case of  $n = 7$  the stress level and deformation is



slightly reduced which is due to the two root bars and cross bars and cross rods which reinforce the central wing and these results indicate no failure occurs on the entire structure in gliding.

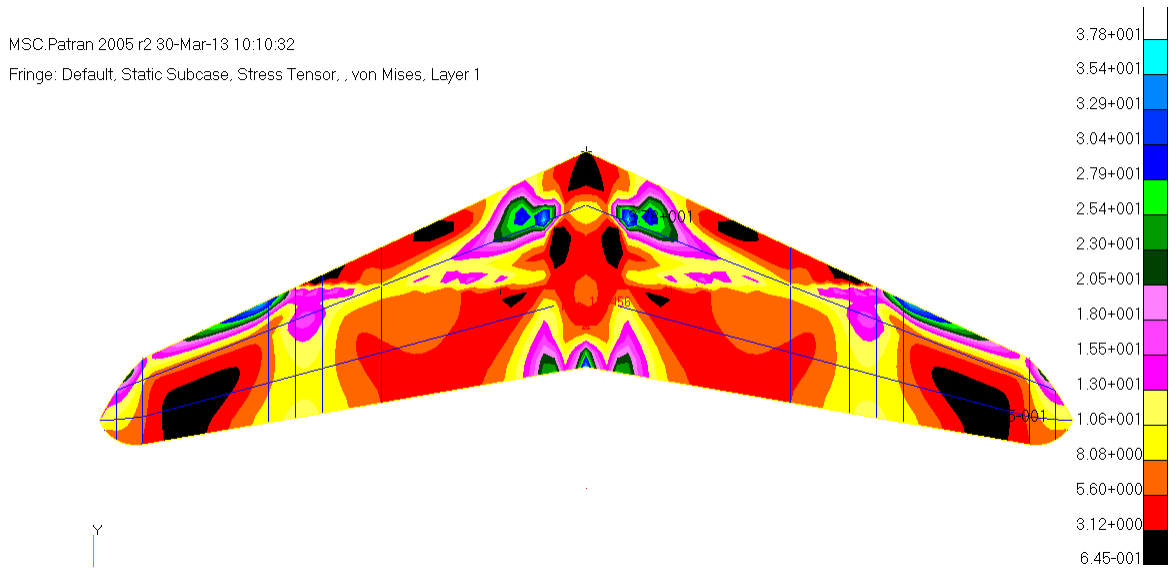


Figure 6.54 Stress on the wing skin in gliding

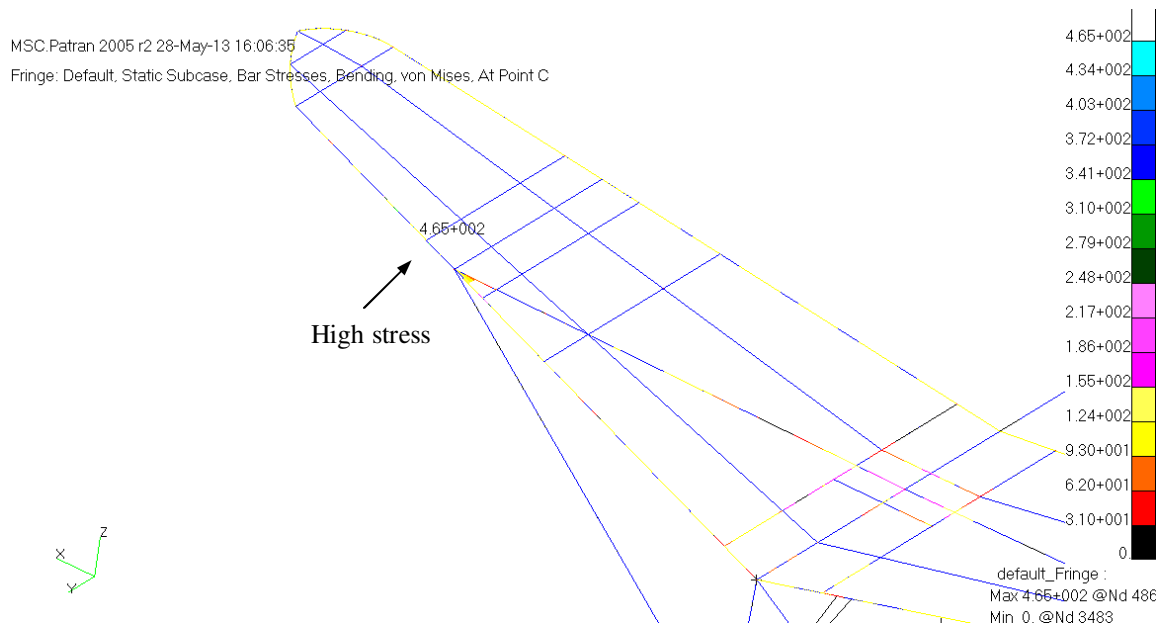


Figure 6.55 Stress on the wing frame in gliding

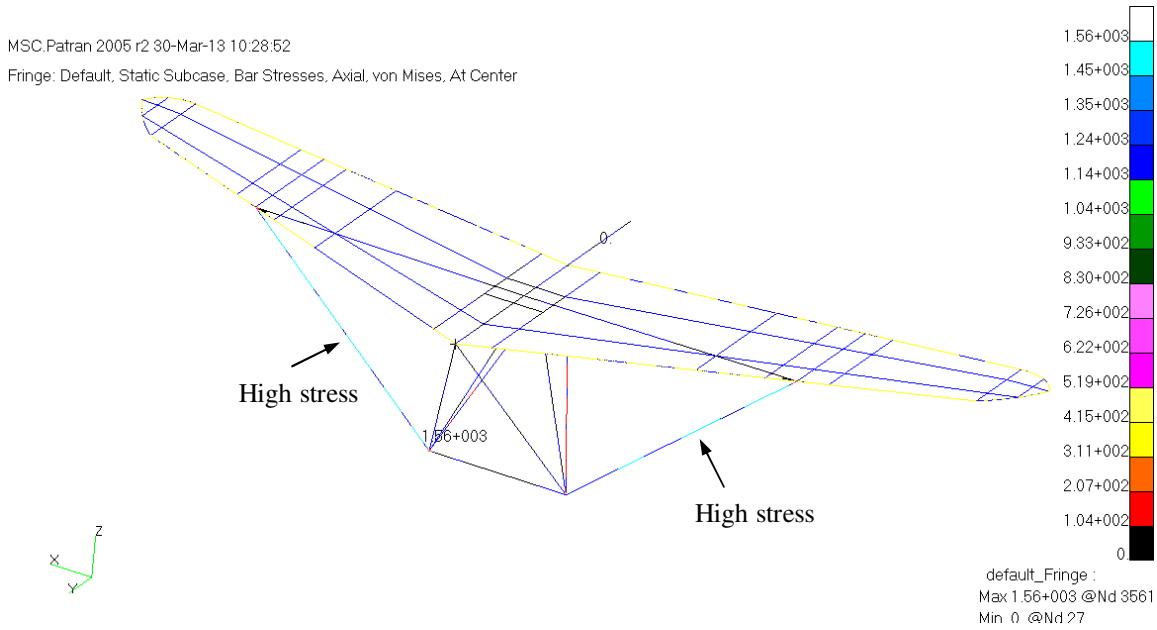


Figure 6.56 Axial stress on the wing frame in gliding

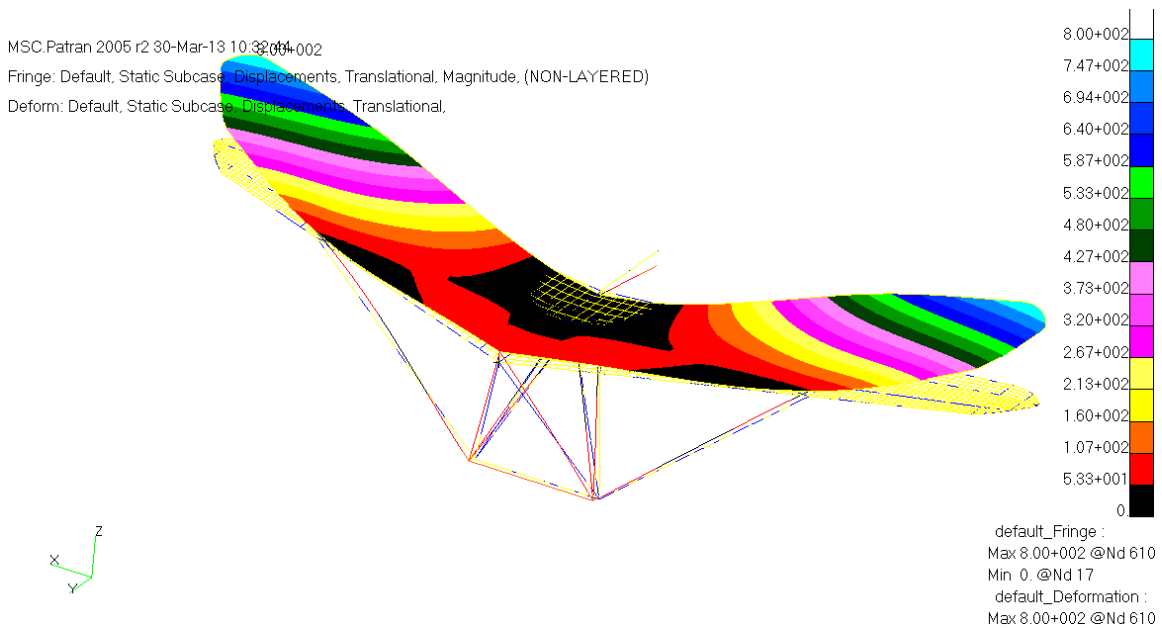


Figure 6.57 Wing deformation in gliding

### 6.4.2.2 FE Modelling of Ornithopter in Flapping

The FE modelling for ornithopter in flapping is carried out by applying the aerodynamic load computed by DeLaurier's method on the wing  $\frac{1}{4}$ -chord line. The aerodynamic load

is computed in flapping condition with 2Hz frequency in cruising speed of 13.8m/s as shown in Fig. 6.31. Compared with the spanwise lift distribution of flapping and gliding in cruising speed as shown in Fig. 6.58 the total flapping lift is four times higher. Since the lift is proportional to the flapping frequency the high lift is generated at outboard of the wing rather than the elliptical lift distribution in gliding. Hence the outboard of the flapping wing turns out to be the critical part in terms of stress consideration.

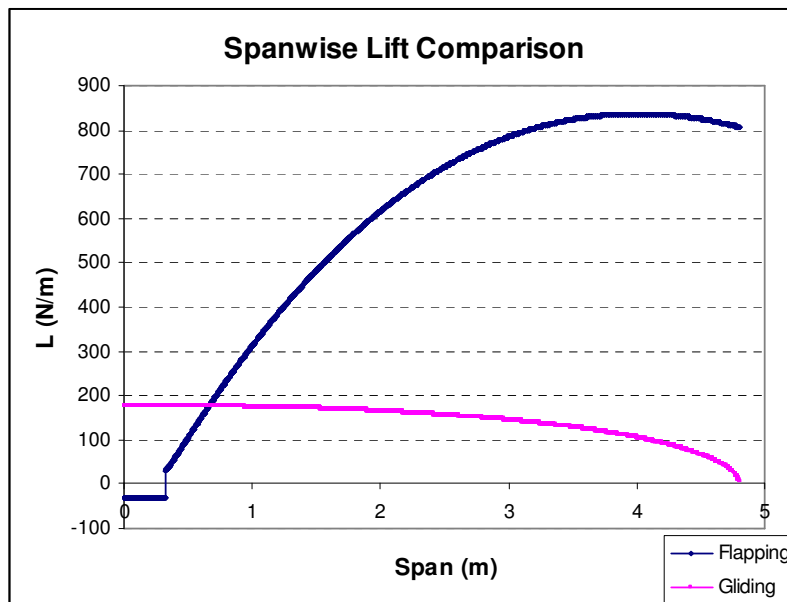


Figure 6.58 Spanwise lift comparison of flapping and gliding

In flapping motion the main forces acting on the wing are aerodynamic force and inertia force. Refer to Table 6.6 the inertia force is calculated based on the mass of leading edge bar, cross bar and the wing skin. The spanwise force distribution of lift and inertia is plotted below at 2Hz in cruising speed. The inertia is  $\frac{1}{4}$  of lift in terms of peak amplitude. The maximum lift is obtained when the wing is in neutral position. And the maximum inertia is obtained when the wing in extreme position. Refer to Fig. 6.39 the phase shift between lift and inertia is almost  $90^\circ$ . Hence the inertia has little effect on the total force of the flapping wing. The following FE analysis is carried out based on the aerodynamic force only as the loading condition.

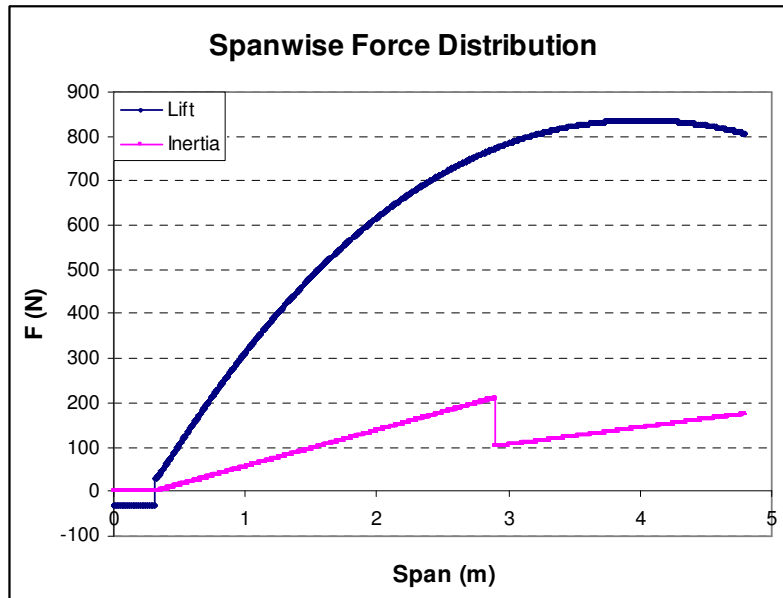


Figure 6.59 Spanwise lift and inertia distribution

The FE modelling is carried out and the FEA results are shown below. In Fig. 6.60 the stress on the skin is illustrated. Unlike the stress distribution of gliding the highest stress occurs at the outboard closed to the leading edge with stress level of 37.3MPa which is in rather low. In Fig. 6.61 it shows the stress on the frame due to bending. The highest stress occurs closed to the leading edge-cross bar joint with a stress level of 674MPa which exceeds the ultimate strength of the aluminium alloy referred to in Table 6.13. Structural failure at this location is mainly due to the overwhelming aerodynamic load at outboard of the wing. Fig. 6.62 illustrates the axial stress taken by wires. The maximum stress occurs on side wire with stress level of 1480MPa. The deformation of the wing is demonstrated in Fig. 6.63. The maximum displacement occurs at rear of wing tip with 1.29m high. The frame at the wing tip also shows high deformation of 1.12m.

MSC.Patran 2005 r2 30-Mar-13 11:06:58

Fringe: Default, Static Subcase, Stress Tensor, , von Mises, Layer 1

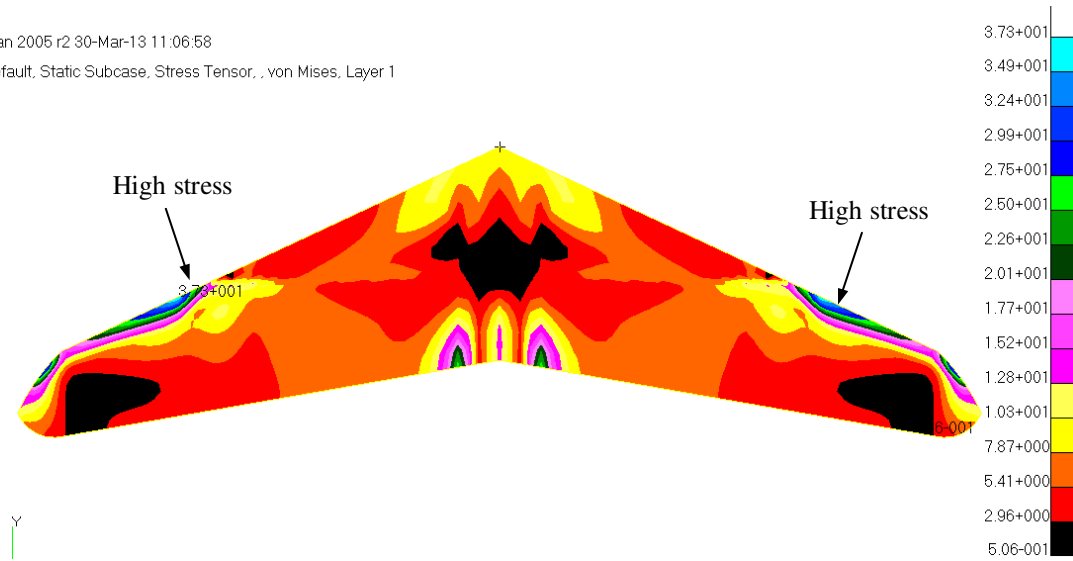


Figure 6.60 Stress on the wing skin in flapping

MSC.Patran 2005 r2 28-May-13 16:15:30

Fringe: Default, Static Subcase, Bar Stresses, Bending, von Mises, At Point C

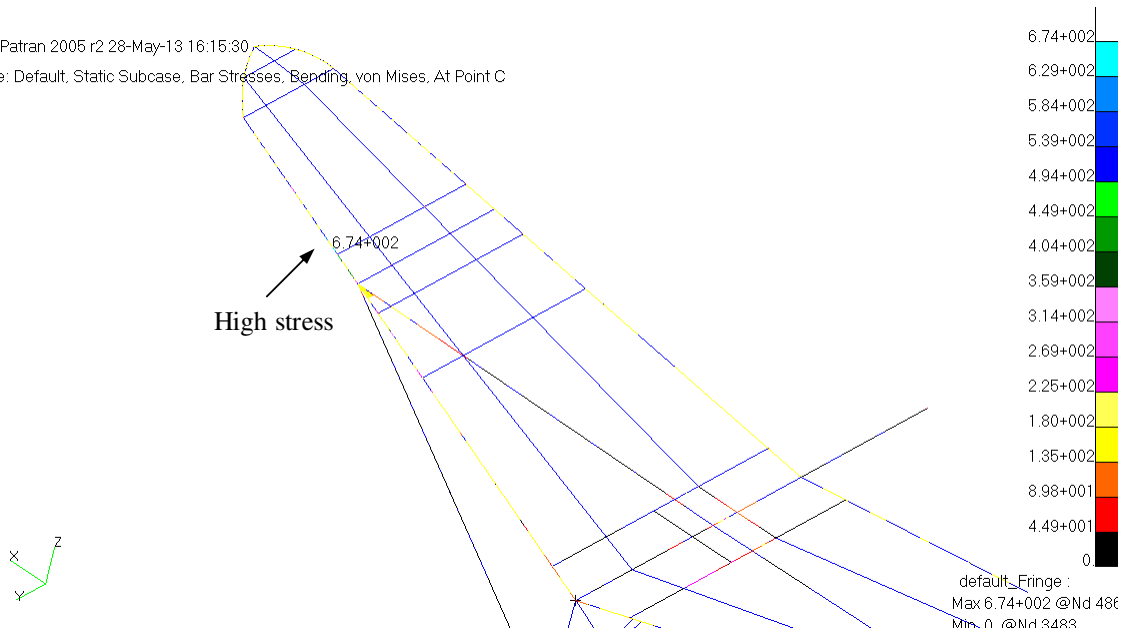


Figure 6.61 Stress on the wing frame in flapping

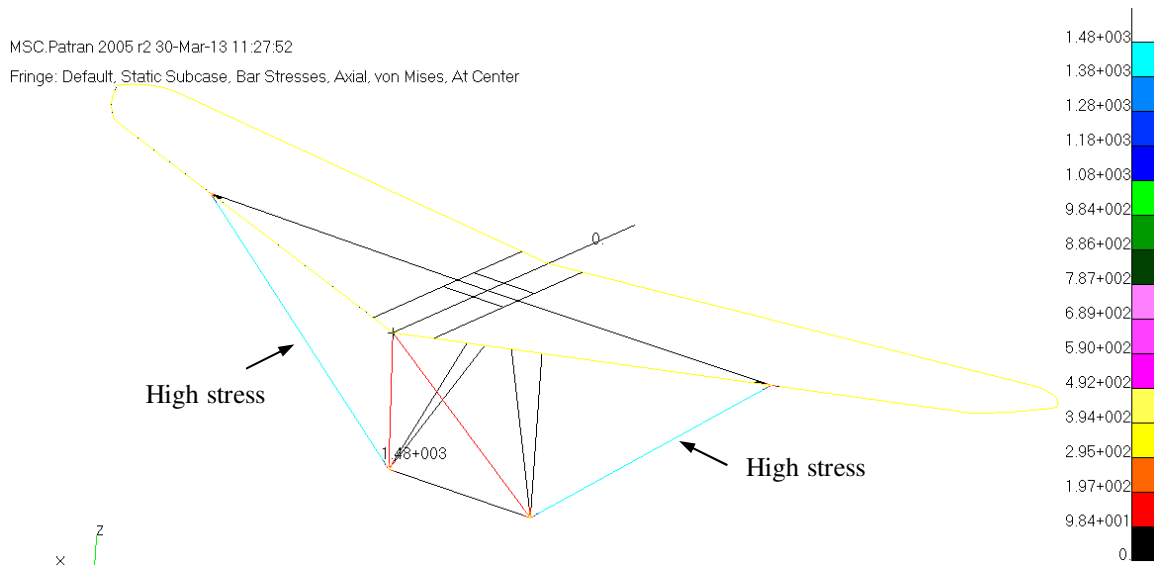


Figure 6.62 Axial stress on the wing frame in flapping

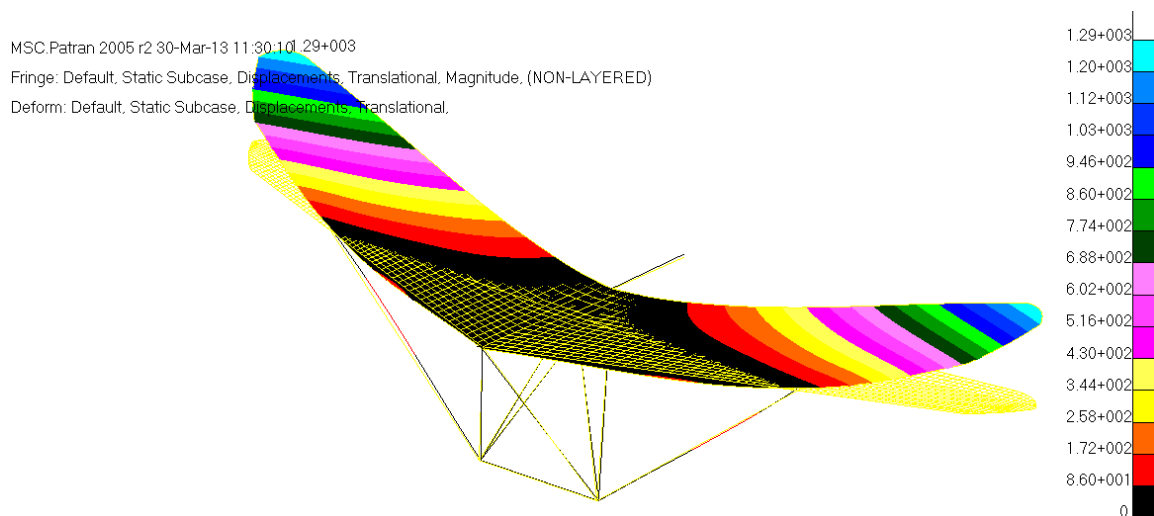


Figure 6.63 Wing deformation in flapping

The FEA results show a structural failure at the joint of leading edge-cross bar. Refer to Fig. 6.58 the aerodynamic force in gliding and flapping is computed based on the load factor of  $n=1$  in cruising speed. The total lift in flapping is four times higher than gliding condition which can be defined as  $n=4$  in flapping condition. The FEA results show the structure is strong enough to hold 7g loading in gliding. However failure occurs in the flapping with 4g load. This is because the aerodynamic centre moves outboard when the wing starts flapping. The outboard wing experiences the highest loading with

large flapping amplitude compared with inboard wing. Based on FEA results the boundary of the inboard wing and outboard wing is the critical location with the highest stress level where the leading-edge and cross bars are jointed together.

In summary the preliminary ornithopter design requirements are shown below:

- The total weight is 140 kg with design specifications shown in Table 6.3 except for the maximum and minimum speeds.
- The ornithopter is designed to achieve same performance as hang glider as shown in Table 6.4 except for the maximum and minimum speeds.
- The maximum design speed is 13.8 m/s which is the same as the cruising speed of hang glider
- The ornithopter is required to maneuver with maximum speed of 13.8 m/s at  $5.8^\circ$  angle of attack to achieve best lift to drag ratio.
- The design flapping frequency is maximum 2 Hz with  $65^\circ$  stroke angle as shown in Table 6.11.
- In level flight at cruising speed the 4g peak lift is generated over a cycle in flapping condition at 2 Hz whereas only 1g loading in gliding.
- Structural failure occurs at leading edge bar due to the bending of the 4g wing loading with stress of 674 MPa as shown in Fig. 6.61.

Hence the ornithopter design optimisation needs to be carried out structurally and aerodynamically in order to achieve better structural reliability and aerodynamic performance which will be presented in the next chapter.

## 7 Ornithopter Design and Optimisation

In this chapter the optimisation of the ornithopter design is carried out based on the theoretical study and finite element analysis results. The objectives of this study are to achieve:

- Better aerodynamic performance of the wing
- Reliable structure in flapping motion

In order to achieve a better performed wing aerodynamically optimal design is carried out based on the preliminary design of ornithopter wing. For the wing structure it requires the modification of the wing frame, flapping motion and aerodynamic load assessment. The wing optimization is mainly conducted by the experimental study subject to different wing design cases. And the structural reassessment is carried out by FE modelling.

### 7.1 Optimisation of Wing Design

The objective of the wing design optimization is to obtain more overall aerodynamic force in term of lift and thrust. Several wing design cases are explored and compared with the preliminary design of ornithopter wing. This investigation is conducted by the experimental results.

#### 7.1.1 Wing Design Cases

Three scale down 1:20 wing samples are designed and manufactured for wind tunnel tests and their results are to compare with the preliminary design of the ornithopter. Together with and based on the original planform (design case 1) the design configurations of these wing samples are labelled and shown as below.



Design Case	Wing Configuration	Weight (g)
Case 1	Original ornithopter wing	7.46
Case 2	Wing with oscillatory camber	7.40
Case 3	Wing can be folded in spanwise	9.07
Case 4	Wing with flexible trailing edge	7.75

Table 7.1 Wing design cases

In design case 1 the wing is based on the reference design case shown in Fig. 7.1. A rigid triangle area is formed by the wing leading edge and cross bars. Piano strings are placed on the wing skin as ribs to hold the wing shape. The weight of the wing is 7.46g which is the same wing studied in Chapter 6 as the preliminary ornithopter wing design.

Base on the structure of case 1 a piece of 12 micro mil polyester film is employed to replace the skin in the rigid triangle area as shown in Fig. 7.2 to produce wing design case 2. During wing flapping the flexible film can be deformed as a parabolic camber driven by the aerodynamic force. Since piano strings are placed underneath the film as ribs it can be only deformed upward to give a positive camber. Therefore a positive camber is generated in downstroke motion. In upstroke motion the negative camber supposed to be achieved due to the downward lift. However the camber is stopped by the ribs placed underneath of the skin and a flat plate is achieved in upstroke. The weight of this wing is 7.4g. Hence the design case 2 can be regarded as wing flapping with asymmetrical camber oscillation.

In Fig. 7.3 two hinges are placed in the middle of the wing's semi-span and the wing is divided into inner wing and our wing by the hinge lines. The hinges are designed to allow the outer wing to fold downward during the upstroke motion while in downstroke motion the outer wing is spread to its full span to contribute to lift generation. This asymmetrical folding allows the entire wing to contribute to the positive lift generation in downstroke while only the inner wing produces negative lift in upstroke. The wing weight in this case is slightly increased to 9.07g due to the addition of hinges.

The fourth wing shown in Fig. 7.4 is constructed by making trailing edge rather flexible compared with rigid area. The piano strings are placed on the top of the trailing edge so that the trailing edge is free to deform downward in upstroke but not in downstroke to achieve asymmetrical trailing edge flap. The weight of the wing is 7.75g.

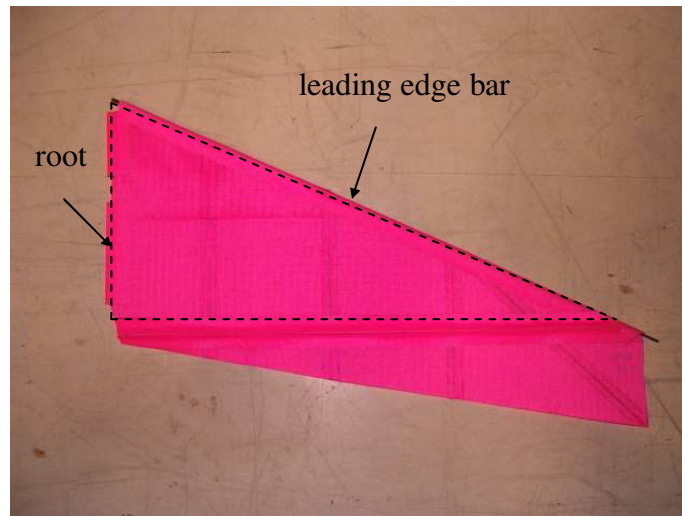


Figure 7.1 Design case 1

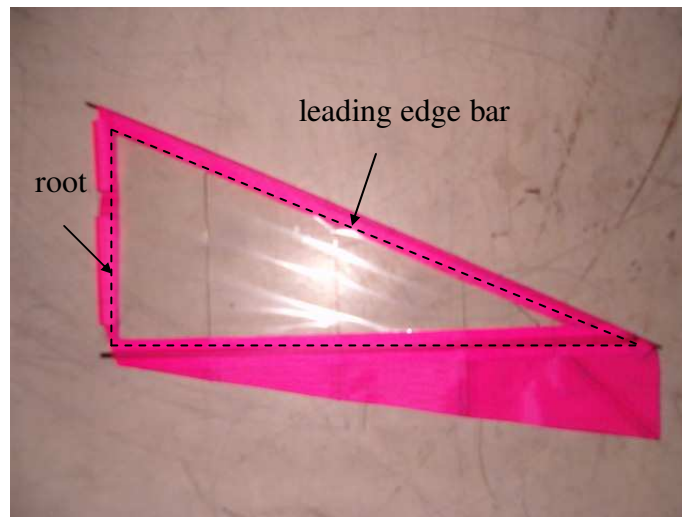


Figure 7.2 Design case 2

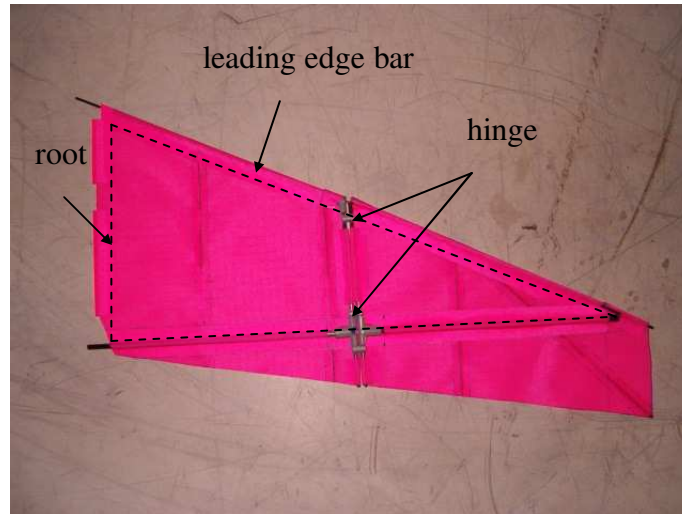


Figure 7.3 Design case 3

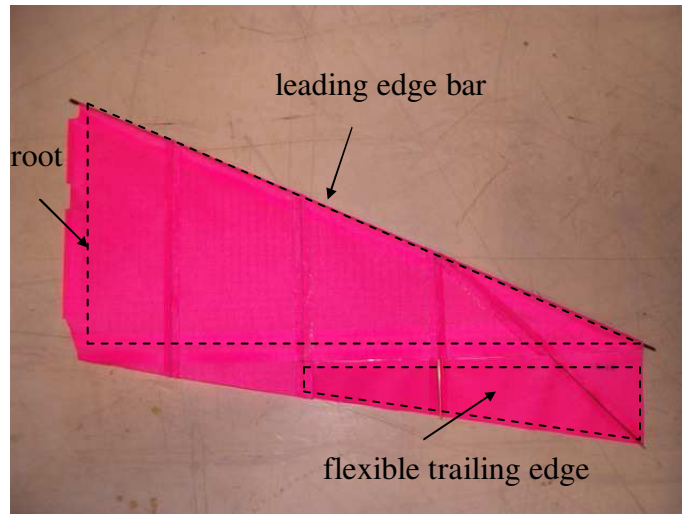


Figure 7.4 Design case 4

In the further study of the wing design cases the wind tunnel tests will be carried out to measure the aerodynamic forces in horizontal direction and vertical direction.

### **7.1.2 Wind Tunnel Tests of the Wing Design Cases**

The main focus and thrust of studying these different wing design cases are on the overall positive lift and horizontal force generation. By employing the asymmetrical flapping motion the positive lift produced in downstroke is increased and negative lift in upstroke

is reduced. Wind tunnel test is carried out to evaluate the effect of these wing design cases. By using the same test rig setup and experimental method for the load cell calibration mentioned in Chapter 6 the wind tunnel tests are carried out for the different wing samples. The inertia force test is carried out first in order to allow its subtraction from the total force. By using the calibration coefficients in Table 6.12 the measured results are converted to inertia force and compared with theoretical calculation which is the same method as design case 1. The test results and theoretical calculations of inertia force at 2Hz are compared in Fig. 7.5 for the four design cases and it shows a good agreement.

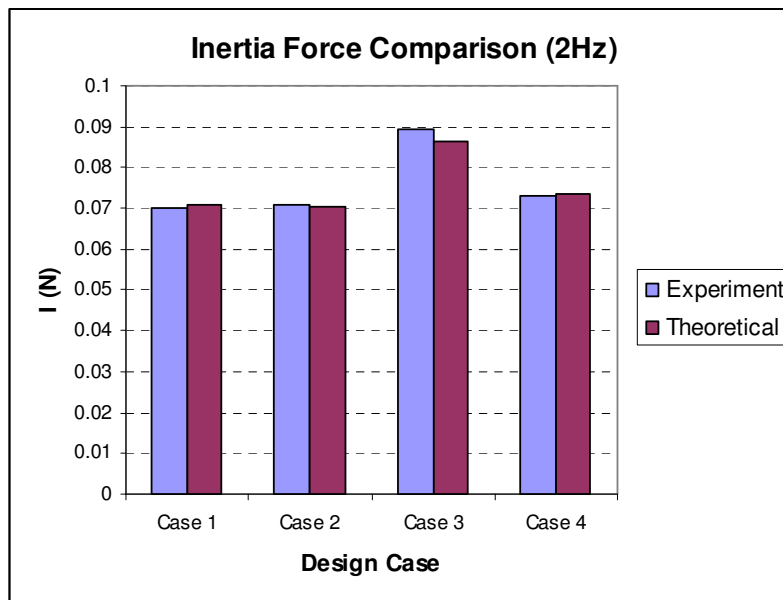


Figure 7.5 Inertia force comparison

After obtaining the measured inertia forces, the wind tunnel tests of the different wing designs are carried out for different speeds of 0m/s, 2m/s, 4m/s and 6m/s at flapping frequency 2Hz. The Reynolds number in this experiment is  $3.08 \times 10^4$  by taking speed of 6m/s and average chord length of 0.075m. The lift amplitude over a cycle is the key parameter being measured. By subtracting the inertia forces from the total forces the measured aerodynamic forces are shown below. Since the optimized wing samples give asymmetrical flapping therefore the lift amplitude is investigated for downstroke and upstroke motions respectively. As shown in Fig. 7.6 the lift amplitude in downstroke is

plotted against speed square. As a reference design case the test result of case 1 has been discussed in Chapter 6 referred to Fig. 6.37 which has indicated a good comparison between the measured results and theoretical results computed by DeLaurier's method. As shown in Fig. 7.6 and Fig. 7.7 the lift amplitude of four design cases in downstroke and upstroke are plotted against velocity square. In downstroke motion positive lift is generated and in upstroke motion negative lift is produced.

In downstroke motion design cases 1, 3 and 4 are supposed to flap down as a flat plate at  $0^\circ$  angle of attack and case 2 achieves maximum camber as designed in Fig. 7.1 to Fig. 7.4. Hence the lift amplitude is supposed to be the same for design cases 1, 3 and 4 and case 2 produces maximum positive lift in terms of lift amplitude as shown in Fig. 7.6 of pink curve. Due to the weight of the trailing edge the wing (case 4) maintains slight degree of curvature which produces additional positive lift as shown in turquoise curve. Case 3 performs more closely to case 1 in downstroke with exactly the same entire wing flap motion as case 1. Therefore case 2 and case 4 seem to be superior in the positive lift generation in downstroke provided by the additional chordwise curvature resulting from oscillatory camber and small trailing edge bending.

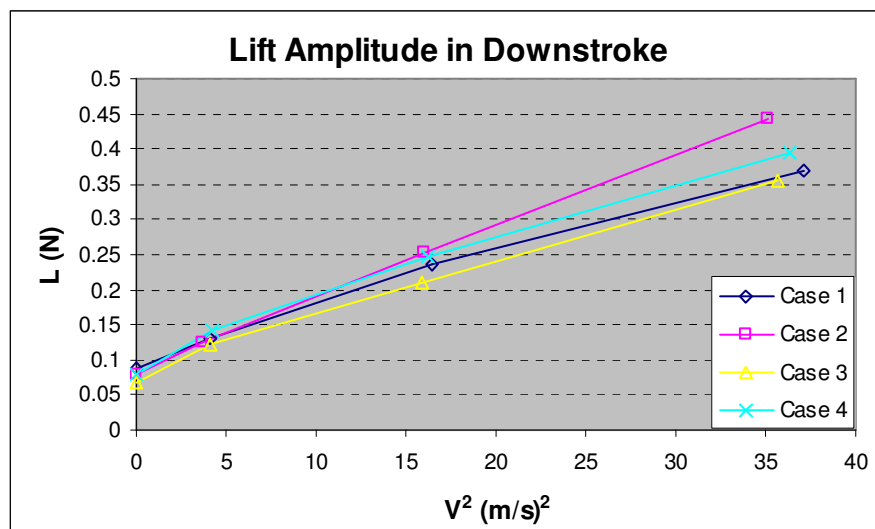


Figure 7.6 Measured lift amplitudes in downstroke at  $0^\circ$  angle of attack

In upstroke motion the measured lift amplitudes are shown in Fig. 7.7. Design case 1 and 2 supposed to flap up as a flat plate. The wing of case 3 should be folded downward at middle of semi-span due to downward lift. Case 4 performs with the downward trailing edge bending. Hence the downward lift of case 1 and 2 should be more closed compared with other cases. However the wing of case 2 still maintains a small positive camber in upstroke motion due to the flexible film used on the camber area which neutralizes the downward lift. Hence the negative lift is reduced (pink curve) compared with case 1 (blue curve). For case 3 and 4 the negative lift is significantly reduced due to the downward wing folding in spanwise and trailing edge bending in chordwise compared with case 1.

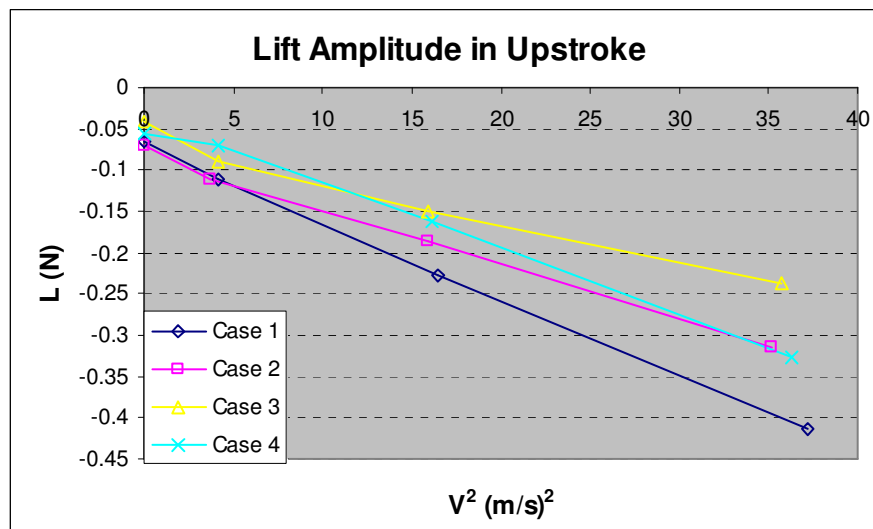


Figure 7.7 Measured lift amplitudes in upstroke

To maintain flapping flight positive overall lift must be obtained. With different wing design cases asymmetrical flapping motion is achieved over a cycle e.g. parabolic camber oscillation, folded wing, trailing edge twisting. However extra drag force is induced by any appreciable deformations of wing structure as shown in Fig. 7.8. Negative force indicates thrust and positive force means drag. Compared with the flat rigid wing planform of case 1, positive lift is obtained at the expense of more drag. For case 2 and case 4 the drag force depends on the degree of the wing chordwise curvature. More chordwise twist and camber leads to higher drag force. For case 3 the wing flaps as a flat plate and the drag level should be the same as case 1. However the complicated hinge

system induced instability in the wing structure which in turn led to further significant wing deformation during flapping. The measured aerodynamic forces of case 2, 3 and 4 are tabulated in Appendix C from Table C2 to Table C4.

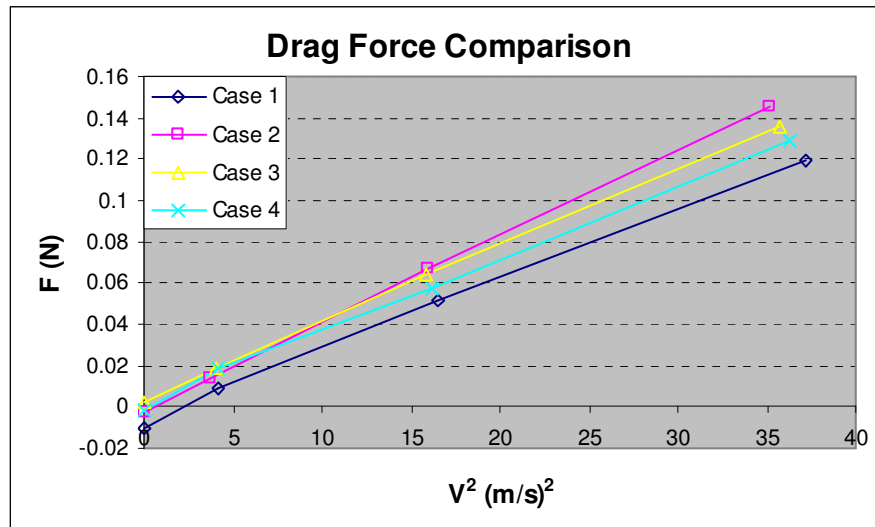


Figure 7.8 Drag force comparison of flapping wing

### 7.1.2.1 Aerodynamic Force Comparison of Case 1 and Case 2

Comparing design case 2 with case 1 the parabolic camber oscillation leads to an increasing positive lift about 16.5% in downstroke and a decreasing negative lift about 24% maximum in upstroke at speed of 6m/s as shown in Fig. 7.9. However the drag force of case 2 is highest as seen in Fig. 7.8. This is mainly due to the camber oscillation compared with flat surface of case 1. The control of the camber in terms of camber profile and oscillatory motion need to be further studied in the real design case.

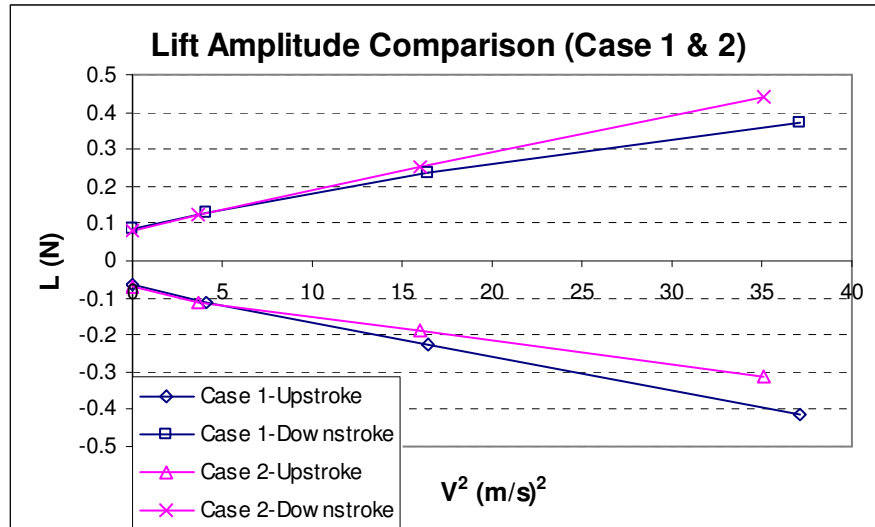


Figure 7.9 Lift amplitude comparison over a cycle (Case 1 & 2)

### 7.1.2.2 Aerodynamic Force Comparison of Case 1 and Case 3

Comparing case 3 with case 1 shown in Fig. 7.10 the positive lift amplitudes are almost on top of each other due to the same wing area and flapping condition in downstroke. However the negative lift in upstroke is dramatically reduced due to the folding of the wing frame with magnitude of 31.5% averagely. Refer to Fig. 7.8 the drag force is still higher compared with case 1. This is due to the complexity of wing structure. Since the hinges are placed in the middle of the wing to achieve downward folding the wing planform is divided by the hinges and more vibration and deformation of wing structure is induced during flapping flight. The complex structure induces significant twist of the wing frame and therefore more drag force during flight. This hinge system also increases the structural weight by about 21.6% compared with case 1. Hence the structural stability and weight control turn out to be some of the most critical and sensitive issues relevant to this design case.



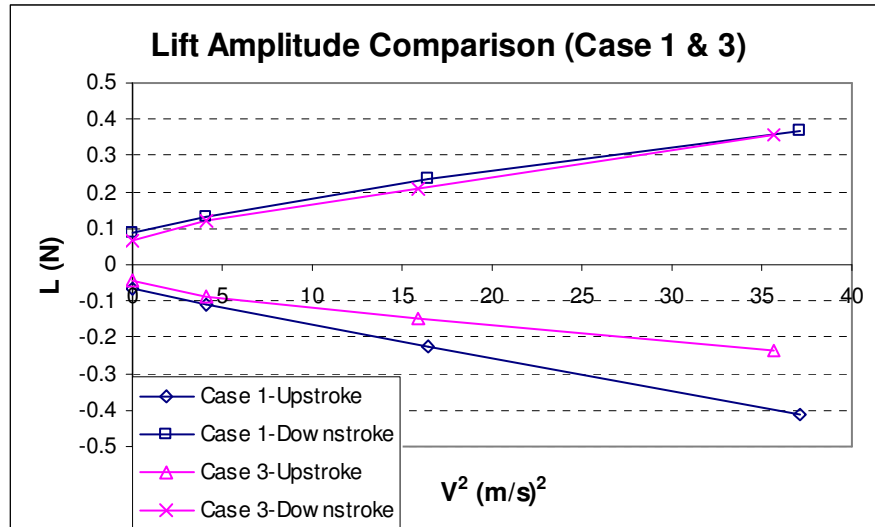


Figure 7.10 Lift amplitude comparison over a cycle (Case 1 & 3)

### 7.1.2.3 Aerodynamic Force Comparison of Case 1 and Case 4

Comparing design case 4 with case 1 the positive lift of case 4 is slightly higher than case 1 with magnitude of 6.9% which is due to the deformation of trailing edge. In upstroke motion since the downward deformation of trailing edge the negative lift is decreased about 29.2% as shown in Fig. 7.11. Without inducing too much drag and weight design case 4 seems to be the best design case. However this trailing edge flapping is simultaneously responding to aerodynamic force which is to achieve proper control. This may not be controlled in real flight under rather high speed compared with wind tunnel test conditions.

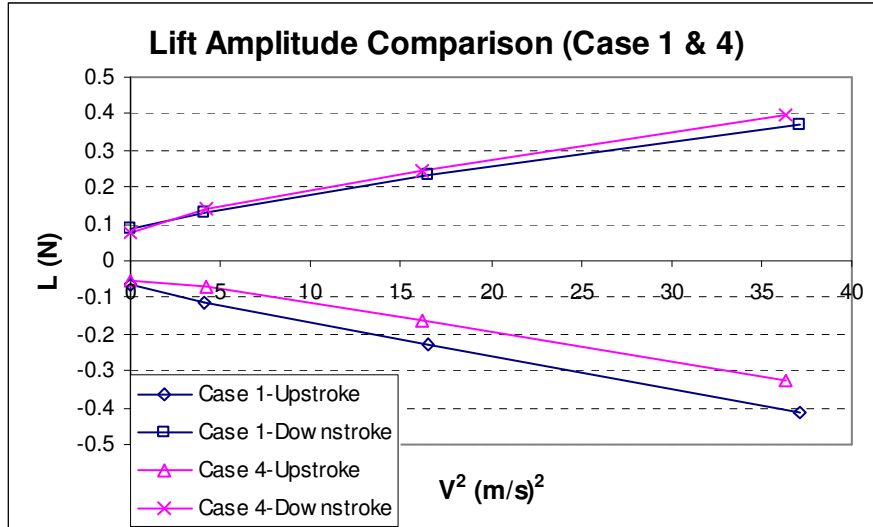


Figure 7.11 Lift amplitude comparison over a cycle (Case 1 & 4)

#### 7.1.2.4 Horizontal Aerodynamic Force Comparison

The horizontal force is also measured in the wind tunnel test subject to four design cases. Comparisons are carried out for steady drag force without flapping and the horizontal force with flapping motion. In the following plots the blue curve ‘steady’ is the steady drag with the wing station at neutral position and the pink curve ‘flapping’ indicates the drag with wing flapping. The steady drag and flapping drag are plotted against velocity square. Positive value means the drag and negative value means forward force. The drag comparison of design case 1 is shown in Fig. 7.12. The design case 1 is the reference wing with flat plate. The test results indicate the drag is decreased about 24% averagely due to the wing flapping motion at 2Hz. Positive force indicates the drag and negative value means the thrust. The results show mostly drag over the speed range tested because the flapping frequency is too low for the size of this scaled model to produce appreciable amount of thrust.

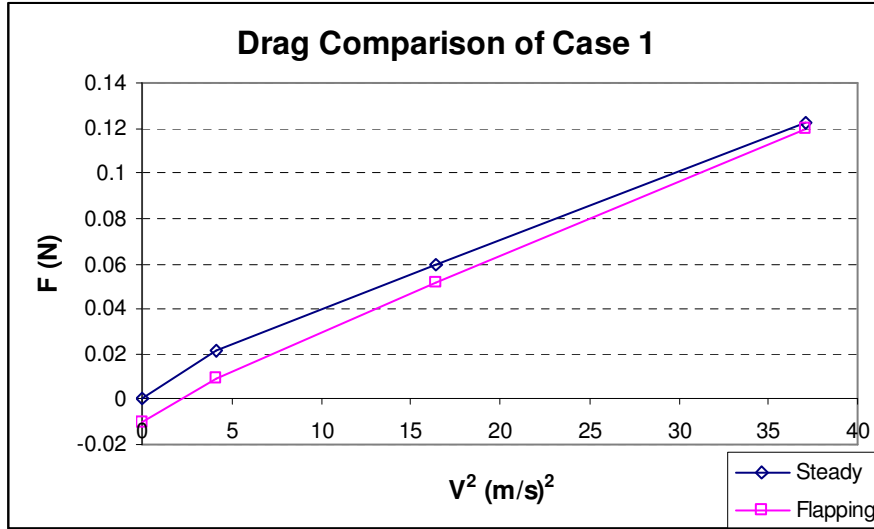


Figure 7.12 Drag comparison of case 1

In Fig. 7.13 it shows the drag comparison of design case 2 with asymmetrical camber oscillation. The steady drag is nearly on top of steady drag which indicates the flapping motion did not contribution on the drag reduction. The camber induces more drag during flapping compared with the steady drag without camber.

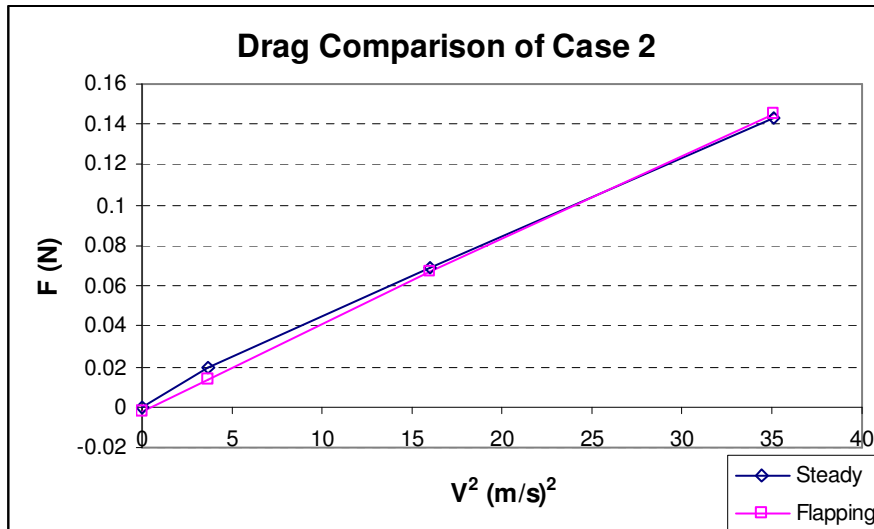


Figure 7.13 Drag comparison of case 2

In Fig. 7.14 the drag force of design case 3 is shown subject the stead and flapping condition. The steady drag is almost the same for case 1 and case 3. The case 3 is

expected to have the same performance as case 1 in the flapping drag measurement. However the flapping drag is higher than steady drag. Since two hinges are placed on each side of wing to allow the wing planform downward bending in upstroke as designed in Fig. 7.3. The wing is expected to have the same performance as case 1 in upstroke motion. However due to the limitation of manufacture condition more structural deformation is induced in the flapping caused by these two hinges. Hence additional drag is produced.

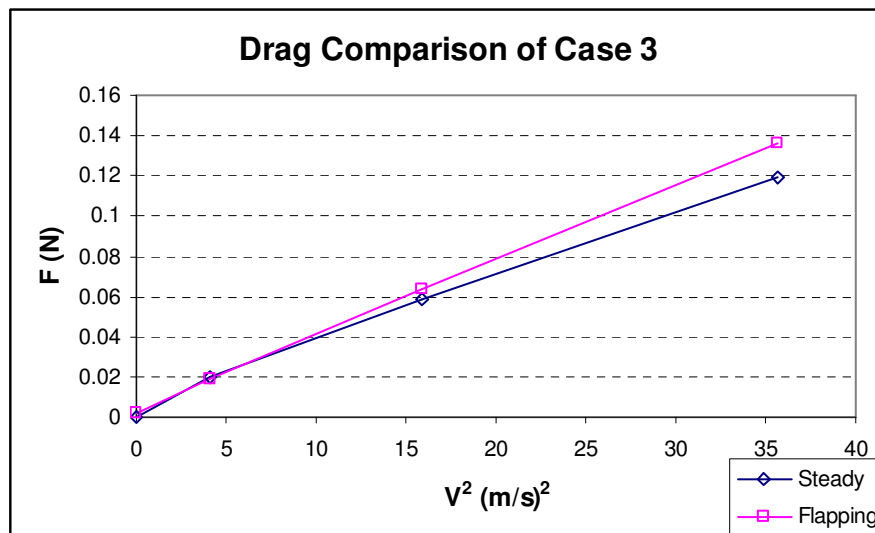


Figure 7.14 Drag comparison of case 3

The drag comparison of design case 4 is shown Fig. 7.15. The test result indicates that the trailing edge flap is not good for the drag reduction. The chordwise deformation is the main reason for inducing extra drag in the flapping flight.

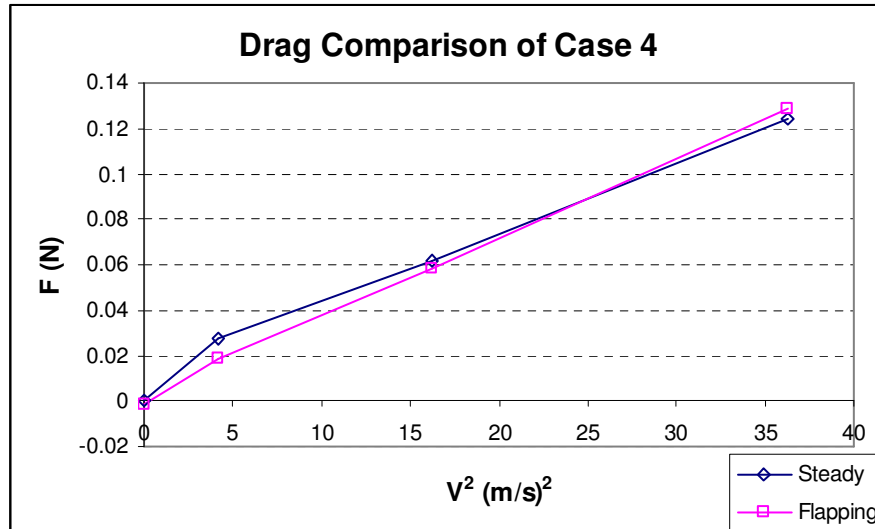


Figure 7.15 Drag comparison of case 4

#### 7.1.2.5 Test Result in Time History

The test result in time history is shown below for case 2, case 3 and case 4 at 4m/s and 2Hz. The blue curve ' $AF$ ' is the aerodynamic force acting on the wing. The pink curve ' $Inertia$ ' is the inertia force due to the wing mass. The yellow curve ' $Dis$ ' indicates the displacement of the wing. Since a strain gauge is placed in the middle of the wing which measures the bending moment in mV due to the wing stroke hence the displacement describes the movement of the wing which is not the true displacement. The test results in Fig. 7.16, Fig. 7.17 and Fig. 7.18 show a good agreement with the theoretical calculation shown in Fig. 6.39 in time history. The rest of test cases in time history are shown in Appendix C from Fig. C7 to Fig. C15.

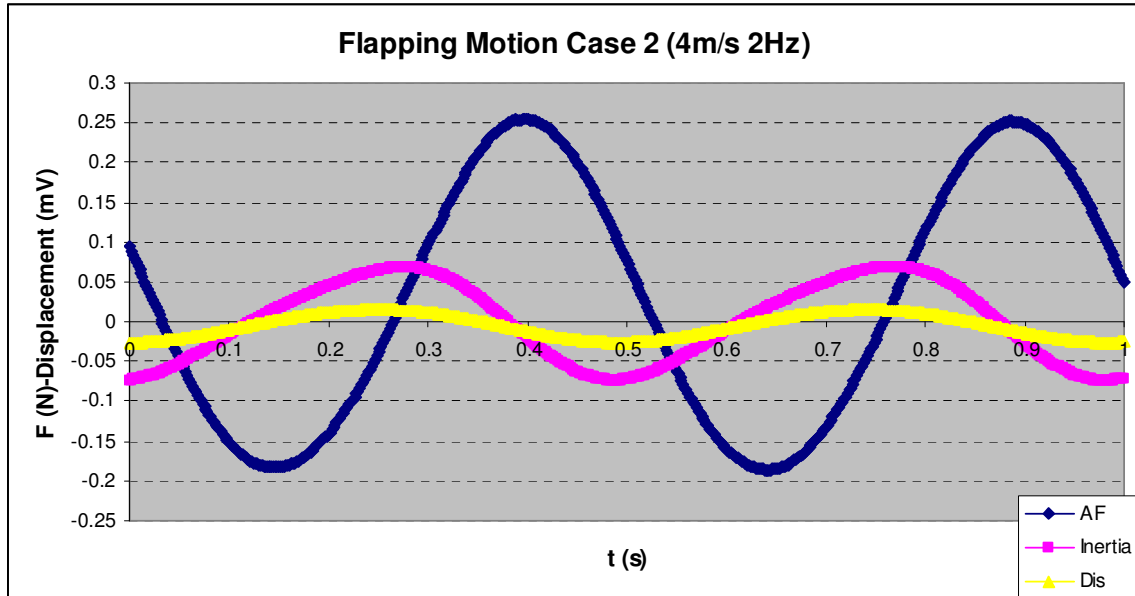


Figure 7.16 Test result of flapping motion of design case 2 for 4m/s, 2Hz

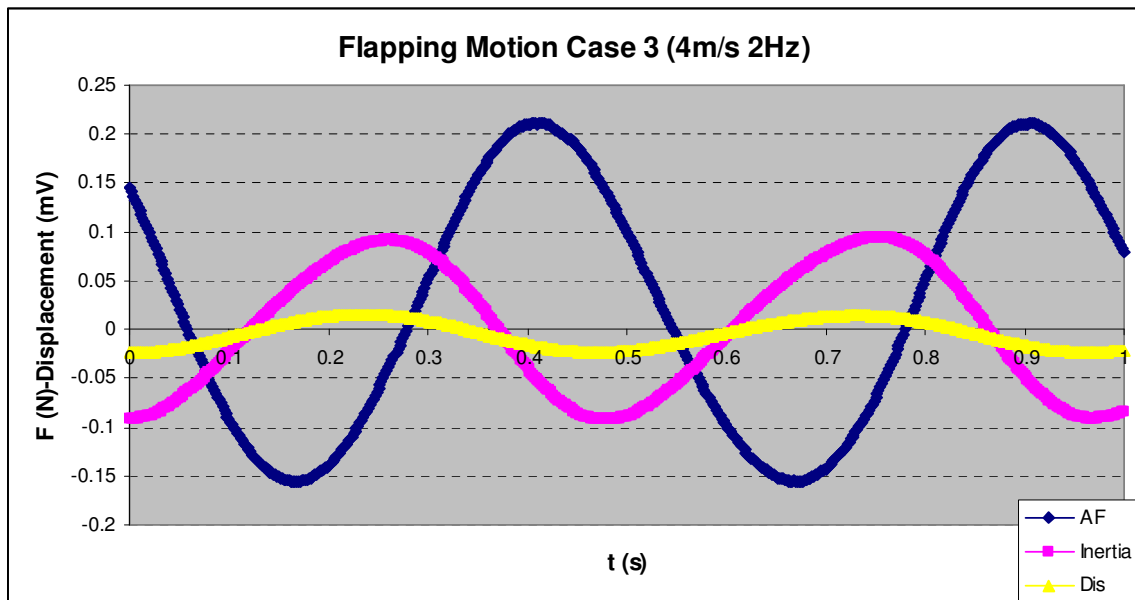


Figure 7.17 Test result of flapping motion of design case 3 for 4m/s, 2Hz

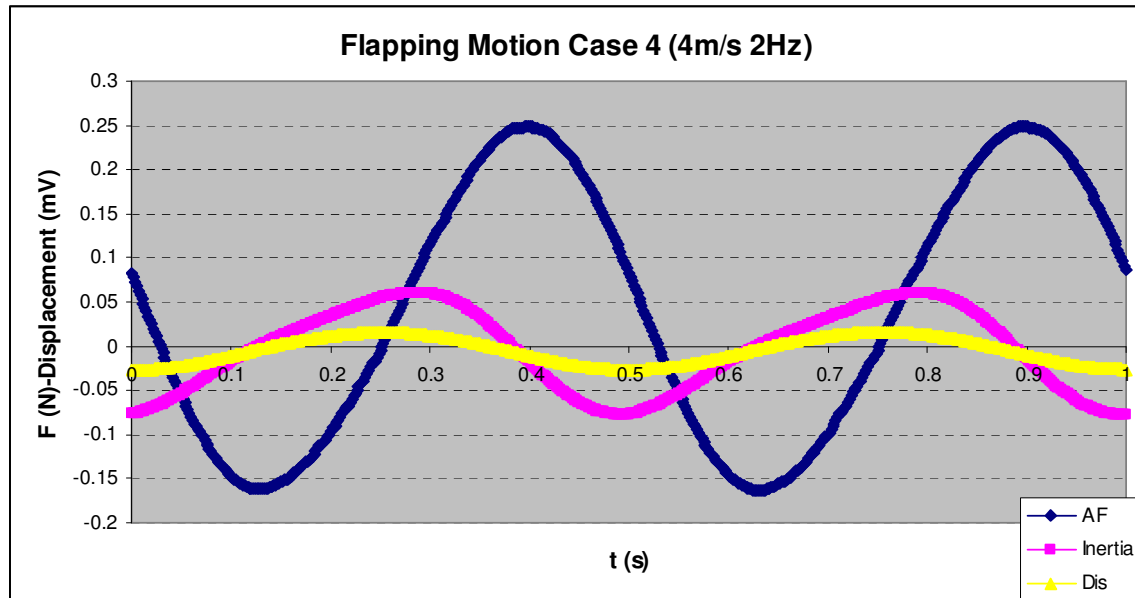


Figure 7.18 Test result of flapping motion of design case 4 for 4m/s, 2Hz

### 7.1.3 Summary of Wing Design Cases

Since the complicated wing motion cannot be accurately calculated by analytical method the design optimization has to be conducted by the experimental studies to estimate the aerodynamic loads acting on the flapping wings. Compared these four wing design cases the overall positive lift is obtained by adopting asymmetrical flapping such as: oscillatory camber, wing fold motion and trailing edge flap. In practical design all these motions require control by the pilot which introduces extra weight for control system and complexity of the structure. By employing the flapping motion to maintain the flight in low speed more lift is generated and applied on the wing. It required higher strength on the frame of the aircraft during the flight. Therefore the idea for an optimal design is to obtain more overall lift and less drag. The design case 3 seems to be the best option by paying little weight penalty and the overall lift is increased by 31.5%. However case 3 is the poorest in the drag reduction as shown in Fig. 7.14. The complexity of the wing folding mechanism induces wing deformation during flapping which is due to poor manufacture of the wing sample. The design case 1 is the best one to reduce the drag without any chordwise deformation. Hence in the design of large ornithopter wing case 3 is the best option in the overall lift generation. However the wing frame should be

reinforced to reduce chordwise deformation such as case 1. Force case 2 and case 3 the camber oscillation and trailing edge flap are difficult to control in the practical design and the chordwise deformation also induces more drag.

## 7.2 Modification of FE Modelling

The FE modelling shows a structural failure of the preliminary ornithopter design with the wing loading calculated for flapping condition shown in Fig. 6.58 at cruising speed and 2Hz flapping frequency with maximum weight of 140kg. The failure is caused by the high aerodynamic load acting on the outer wing leading to the leading edge bar failure as shown in Fig. 6.61. It may be caused by the higher flapping frequency or the over prediction of the aerodynamic load. Hence two methods are explored in order to modify the FE modelling.

### 7.2.1 Frequency Modification of FE Modelling

In the preliminary design the wing flapping frequency is 2Hz with the wing loading of 4g in flapping condition. The aerodynamic forces generated in this condition exceeded the allowable strength of the structure as shown in Fig. 6.61. The stress on the leading edge bar exceeded the ultimate strength of the material. Hence FE model is modified in lower frequency in 1.5Hz and 1.0Hz. The FEA results of these three frequency cases are tabulate below.

Frequency (Hz)	1.0	1.5	2.0
Total Load (N)	2927	4191	5555
Stress on Skin (MPa)	20.2	28.6	37.3
Stress in bending (MPa)	372	523	674
Axial stress (MPa)	795	1130	1480
Max displacement (m)	0.712	1.00	1.29
Frame deformation (m)	0.617	0.867	1.12

Table 7.2 FEA results comparison



Based on the modified FEA results the critical stress and deformation are proportional to the frequency but the stress contour indicates the same distribution in different flapping frequency cases. Therefore the flapping frequency is critical in bring about structural failure. However by reducing the frequency may lead to an insufficient lift to maintain the flight. Therefore other modifications need to be investigated in order to reduce the stress level.

### **7.2.2 Aerodynamic Force Modification for FE Modelling**

Since the structural failure is caused by the excessive aerodynamic load applied on outboard of the wing the force calculation is reassessed. In DeLaurier's method the flow is assumed to be fully attached on the wing. However in the flapping flight the wing tip experiences a rather large angle of attack due to the very high flapping amplitude. Based on the ornithopter structure the effective angle of attack on each strip is calculated by using the equation shown below.

$$\alpha = \frac{\dot{h}}{V_\infty} = \frac{\omega h_0}{V_\infty} e^{i\omega t} = \alpha_0 e^{i\omega t} \quad (7.1)$$

where  $h_0$  is the heaving amplitude and  $\alpha_0$  is the effective angle of attack amplitude and they vary with variation of the location of strip

In cruising speed the angle of attack on each strip is plotted in Fig. 7.19 against span. The computed result shows that from 2m away from wing root the angle of attack has reached to 20° and at wing tip it is even higher than 45°. Hence stall occurs at the outboard of the wing. Refer to Fig. 6.63 the wing tip experiences large deformation by assuming all the load acting on the wing. Based on this FEA result the detailed view of this tip deformation is shown in Fig. 7.20. Since the flexible skin is always adapting the incoming flow the deformed angle of wing tip is calculated based on the FEA results. It

shows about 40° of twist in chordwise which just matches the angle of attack shown in Fig. 7.19.

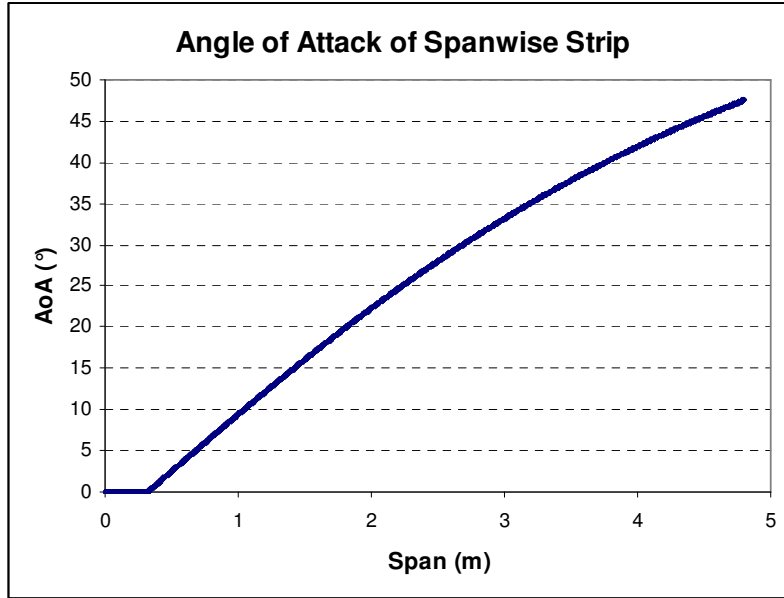


Figure 7.19 Angle of attack of spanwise strip

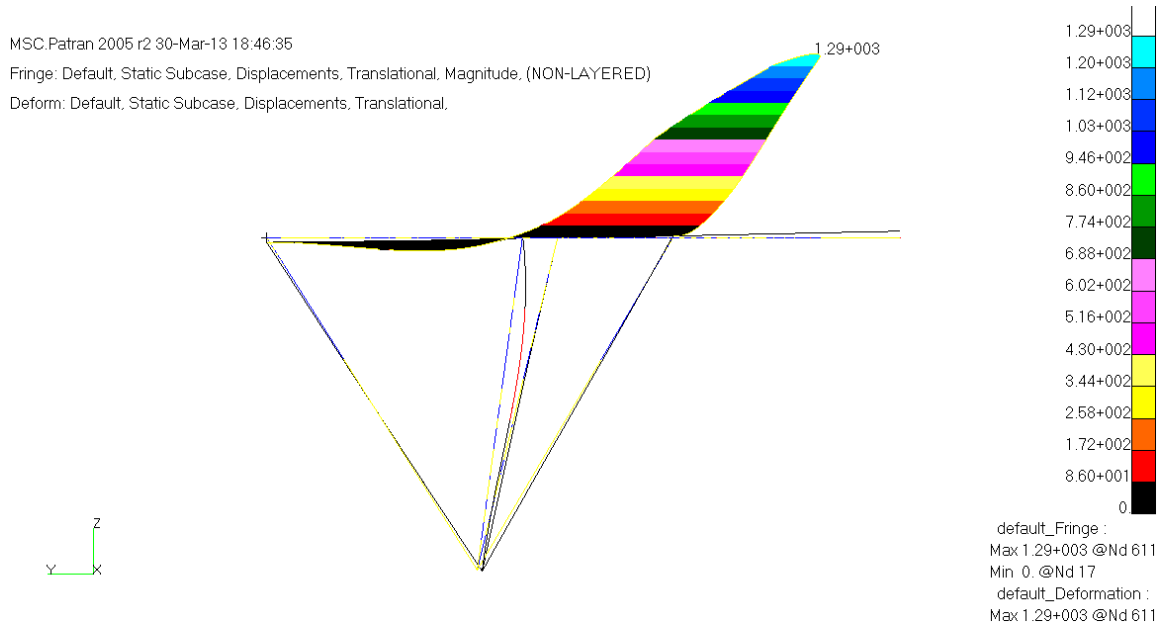


Figure 7.20 Wing tip deformation at 2Hz

Therefore an approximation is carried out by assuming the spanwise lift distribution is one of elliptical. The wing is losing significant amount of lift due to wing tip stall at large angle of attack. The approximated equation is shown below by multiplying a factor to reduce down the force level near on the wing tip.

$$L_{Mod}(y) = L(y) \cdot \sqrt{1 - \left(\frac{y}{s/2}\right)^2} \quad (7.2)$$

where  $L(y)$  is the lift amplitude of the strip computed by DeLaurier's method as plotted in Fig. 6.58,  $s$  is wing span and  $y$  is the location of the spanwise strip.

Compared with the original calculation in Fig. 6.31 the modified lift  $L_{Mod}(y)$  is shown below. This lift distribution may not be an accurate estimation however it can simulate the loading action by taking the wing deformation into account. The total lift is reduced from 4.04g to 2.86g in terms of 'g' loading (normalized by total mass) by 29% especially at the outboard of the wing. However the ornithopter needs to maintain the normal flight with negative lift generated by the flapping wing in the upstroke motion. Based on the test result shown in Fig. 7.10 the downstroke lift can be reduced by 31.5% due to the wing folding. By implementing this factor in the real flight the downward lift is reduced to 0.9g in terms of g loading which can just be neutralized by steady lift. Hence the ornithopter needs to either increase speed or pitch up to gain extra lift to maintain the flight in upstroke which needs to be further investigated. FE analysis is carried out based on this modified loading case at cruising speed and 2Hz frequency. The FEA results are shown below.

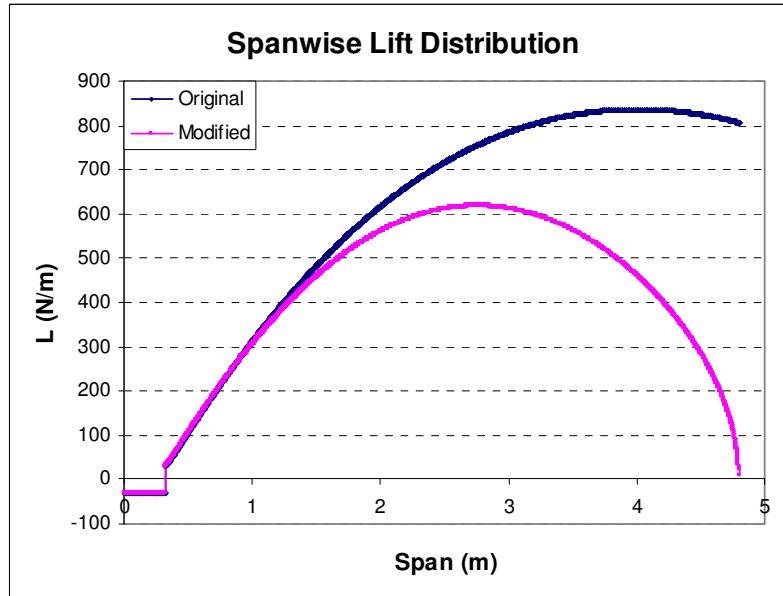


Figure 7.21 Comparison of modified spanwise lift

Fig. 7.22 shows the stress distribution on the skin (layer 1) with modified load. The highest stress occurs at the leading edge with stress level of 22.3MPa. The stress on the frame due to bending is shown in Fig. 7.23. The highest stress is at the joint of leading-edge cross bar with stress level of 287MPa. The axial stress is illustrated in Fig 7.24. The maximum stress occurs on the side wire which is 884MPa. The deformation of the wing is shown in Fig. 7.25. The maximum displacement is 0.576m at the rear of wing tip and the frame deformation is 0.499m.

MSC.Patran 2005 r2 30-Mar-13 19:29:43

Fringe: Default, Static Subcase, Stress Tensor, , von Mises, Layer 1

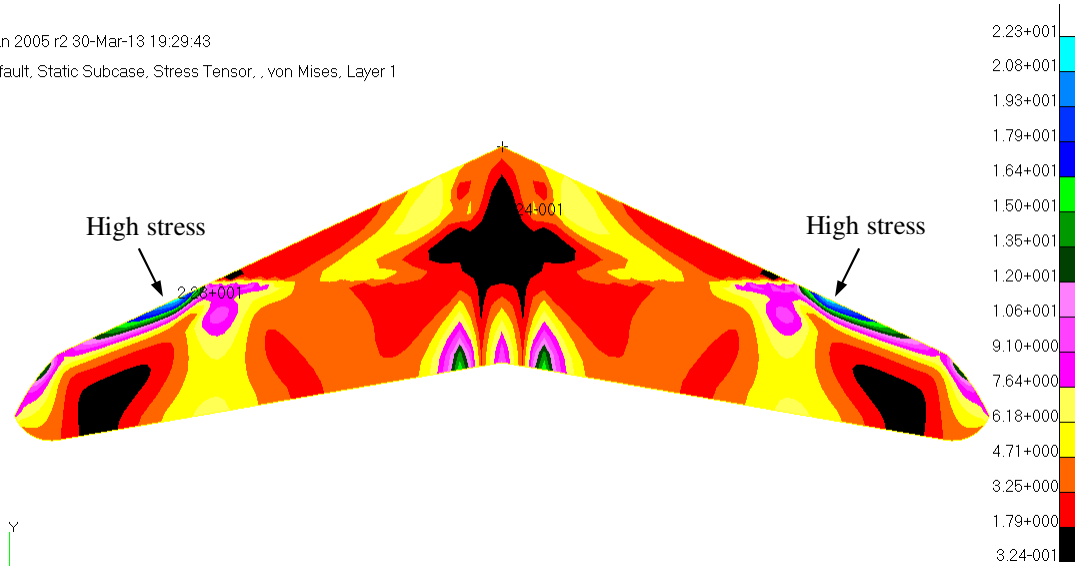


Figure 7.22 Stress on the wing skin with modified flapping aerodynamic load

MSC.Patran 2005 r2 30-Mar-13 19:36:44

Fringe: Default, Static Subcase, Bar Stresses, Bending, von Mises, At Point C

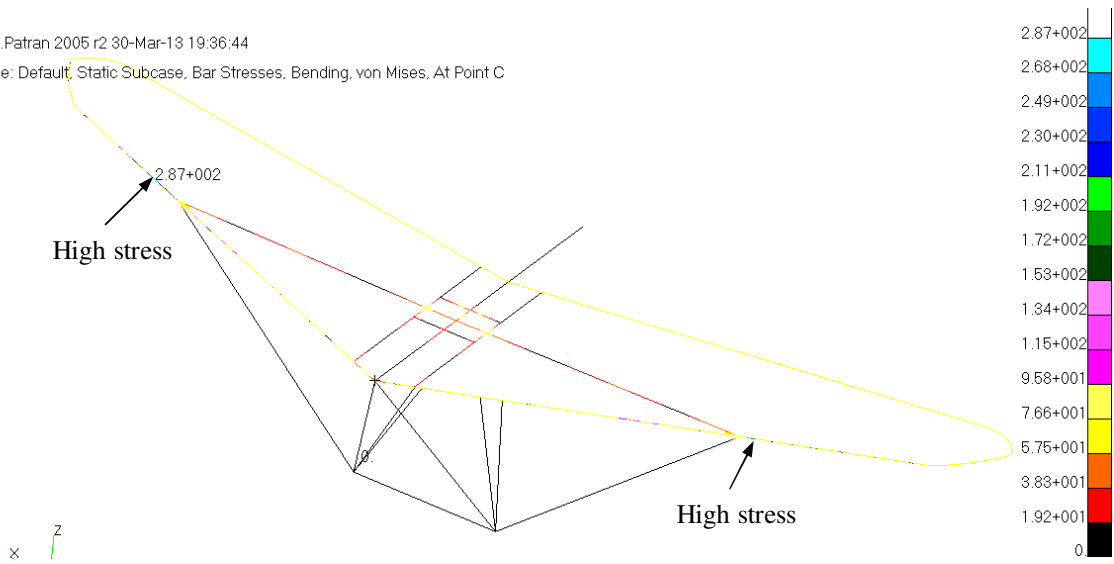


Figure 7.23 Stress on the wing frame with modified flapping aerodynamic load

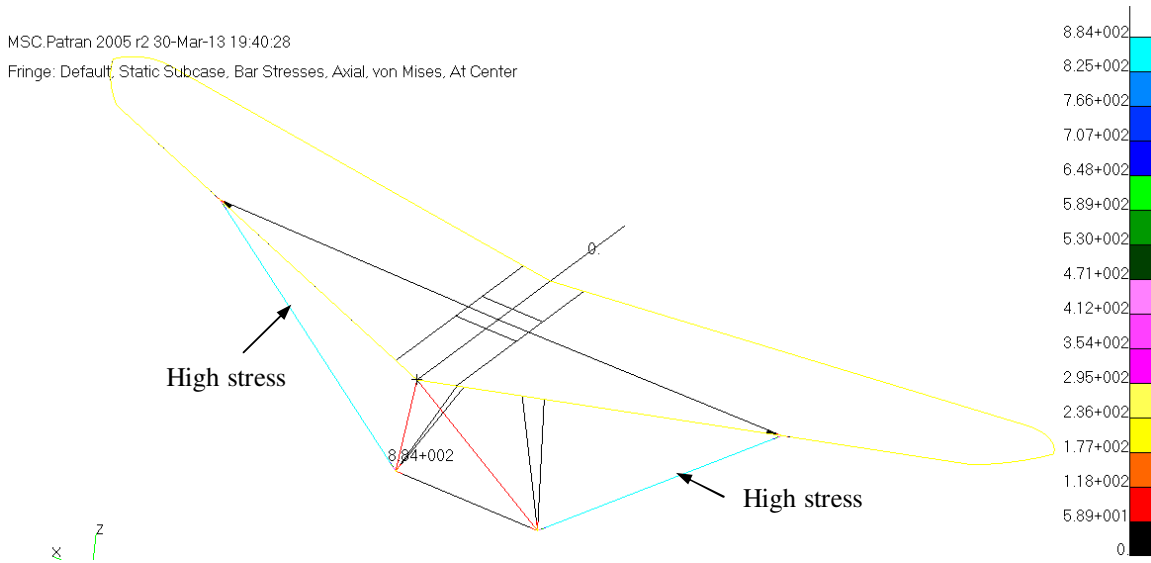


Figure 7.24 Axial stress on the wing frame with modified flapping aerodynamic load

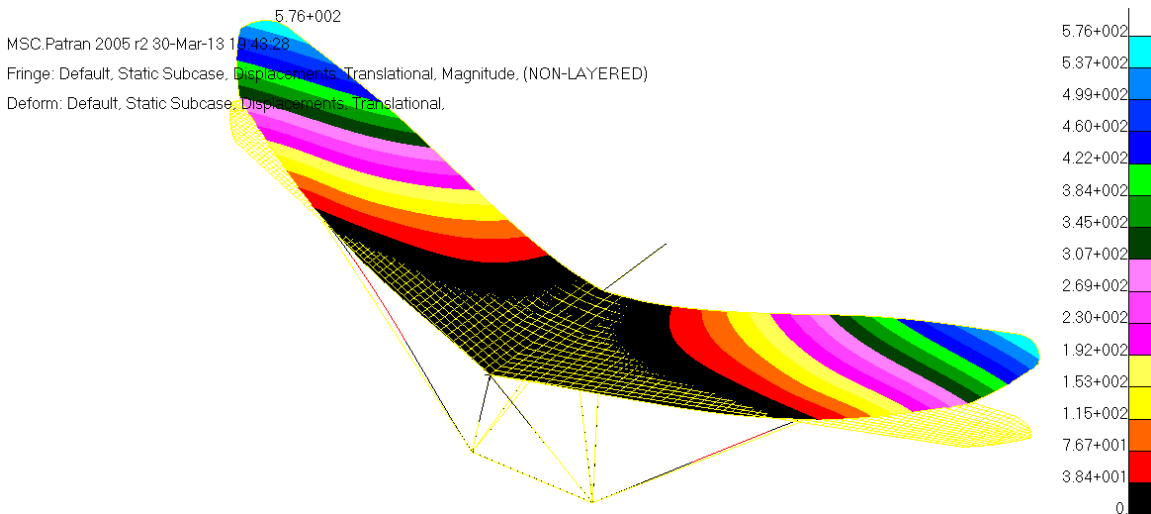


Figure 7.25 Wing deformation subject to modified flapping aerodynamic load

According to the loading case in Fig. 7.21 the stress level is reduced with the modified load distribution. The FEA results are tabulated below. The stress level is reduced down to the safe level by considering the wing deformation effect on the aerodynamic load.

Loading case	Original	Modified
Total load (N)	5555	3929
Stress on Skin (MPa)	37.3	22.3
Stress in bending (MPa)	674	287
Axial stress (MPa)	1480	884
Max displacement (m)	1.29	0.576
Frame deformation (m)	1.12	0.499

Table 7.3 Comparison of FEA results in different loading case

Refer to the original hang glider design specification in Table 6.1 the maximum speed  $V_{ne} = 23.3$  m/s. At this maximum speed the total aerodynamic load is calculated by the modified method at 2Hz. The total load is increased from 3929 N to 6739 N which is 72% higher than the lift at the cruising speed. Since the FE analysis is in linear static solution type the stress level and deformation is proportional to the applied load assuming the load distribution is identical. The FEA results can be scaled up by the factor of the applied load variation. Table 7.4 shows the FEA results in cruising speed of 13.8m/s and maximum speed  $V_{ne}$  of 23.3m/s. According to the material properties listed in Table 6.13, Table 6.14 and Table 6.15 there is no failure on the entire structure at maximum speed and flapping frequency of 2Hz.

Speed case (m/s)	13.8	23.3
Total load (N)	3929	6739
Stress on Skin (MPa)	22.3	38.2
Stress in bending (MPa)	287	492
Axial stress (MPa)	884	1516
Max displacement (m)	0.576	0.988
Frame deformation (m)	0.499	0.856

Table 7.4 FEA results comparison in different speed

In the flight with wing flapping and steady load due to wing camber the total aerodynamic force on the wing consists of the load due to flapping and steady load due to camber. By considering the critical case without structural failure the maximum speed needs to be assessed. Based on the FEA results shown in Table 7.4 in cruising speed of 13.8m/s the critical component is the stress on the frame due to bending. With the maximum speed of  $V_a = 16$  m/s the total lift is 7494N which consists of 4527N generated by flapping motion and 2967N due to steady camber with stall angle. Compared with the cruising condition in Table 7.4 the stress and deformation is tabulated below. The maximum speed for the ornithopter is 16m/s without structural failure.

Speed case (m/s)	13.8	16
Total load (N)	3929	7494
Stress on Skin (MPa)	22.3	42.5
Stress in bending (MPa)	287	547
Axial stress (MPa)	884	1686
Max displacement (m)	0.576	1.099
Frame deformation (m)	0.499	0.952

Table 7.5 FEA results comparison in different speed

### 7.3 Optimisation of Ornithopter Structure

The optimal structural design of ornithopter is carried out by validating the structure strength using FE analysis. Based on the previous investigation of wing design the design maximum overall positive lift is obtained by case 3 of asymmetrical folding which is preferred in this structural modification in order to obtain maximum overall lift. The fold axis is placed on each side of wing which is located in the middle of the semi-span with 2.4m away from root. The hinge allows only downward bending of the outer wing. The graph showed in Fig. 7.26 illustrates the layout of the wing planform.



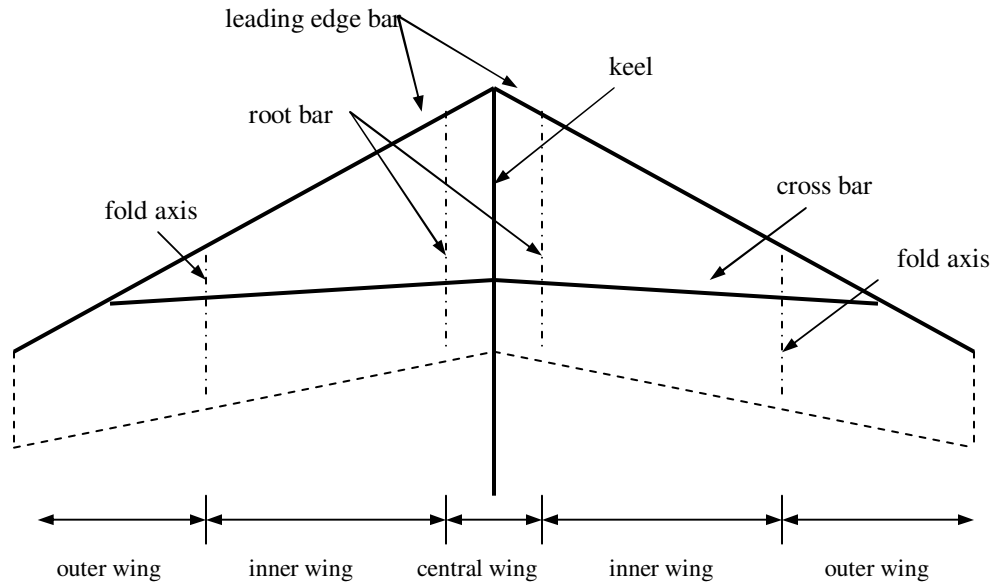


Figure 7.26 Modified ornithopter wing frame

To achieve the asymmetrical folding hinges are placed at fold axis on both leading edge and trailing edge. In order to strengthen the outer wing frame two ribs are added on the edge of inner wing and outer wing on both sides. CATIA model of the wing is illustrated in Fig 7.27. The fold axis in detail is shown in Fig. 7.28.

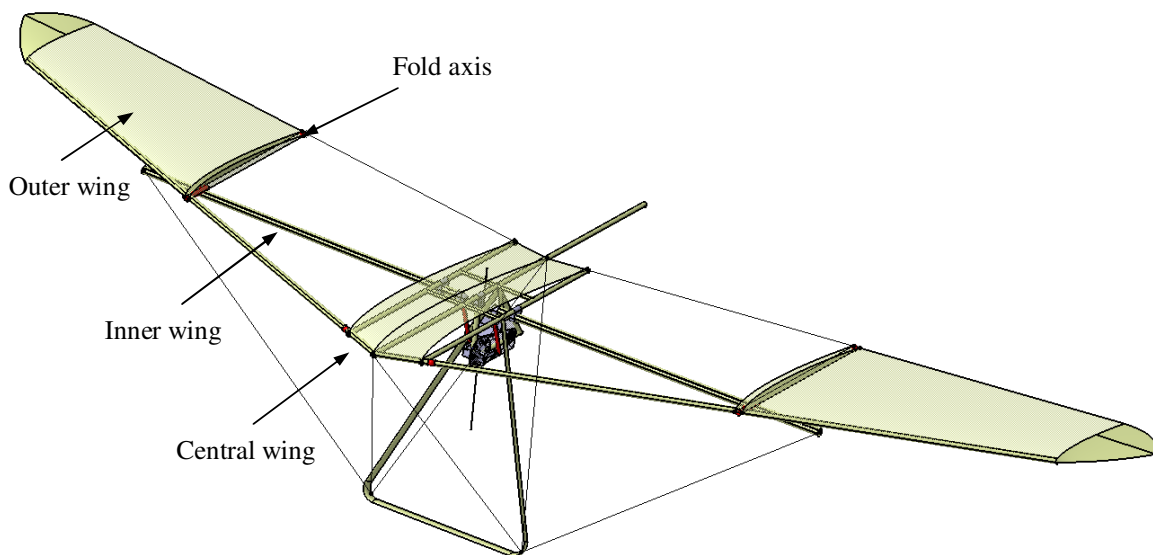


Figure 7.27 CATIA model of optimal design of ornithopter

Two ribs are placed at the edge of inner wing and outer wing to strengthen the wing planform structure. And two joints are placed at the leading edge and trailing edge which allow the outer wing to only fold downward. Due to the folding axis the leading edge bar and cross bar are cut in this location and linked by the joints.

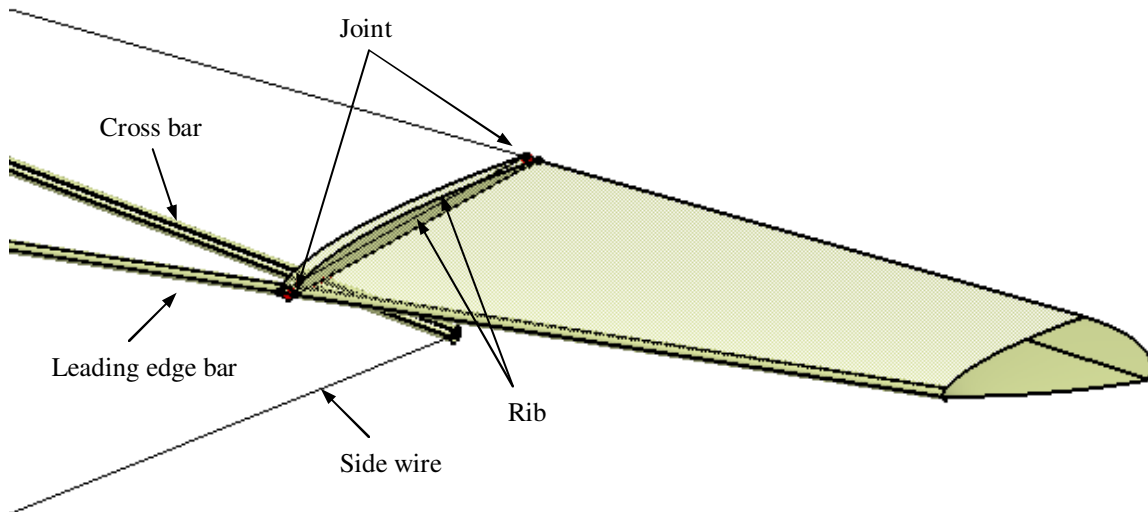


Figure 7.28 CATIA model of fold axis

As shown in Fig 7.29 a simplified CATIA model is presented to illustrate the wing folding motion control. In downward motion the entire wing flaps down as a flat plate. In upward motion the outer wing bends down at fold axis with  $65^\circ$  which is same as the total stroke angle. To achieve the asymmetrical folding motion a VG (variable geometry) system is designed to control the outer wing folding motion. As shown in Fig. 7.30 the side wire is replaced by a VG system consists of main side wire and two sub-wires. The sub-wires A and B are linked by a pulley joint. The end of sub-wire A is connected to the outer wing tip and the other side of sub-wire B is linked with the edge of inner wing as shown in Fig. 7.30 (a). In downstroke motion shown in Fig. 7.30 (b) the entire wing moves down as an identical planform the main wire contracts into control bar by a spring system. The length of sub-wire B is reduced and sub-wire A is increased which is pulled by the main side wire. In upstroke position shown in Fig. 7.30 (c) the main side wire reaches to its maximum length and the sub-wire has to contribute the extension in order to achieve the maximum upstroke angle. Hence the sub-wire B increases and the length

of sub-wire A is reduced. Meanwhile the out wing is able to bend down at the folding axis.

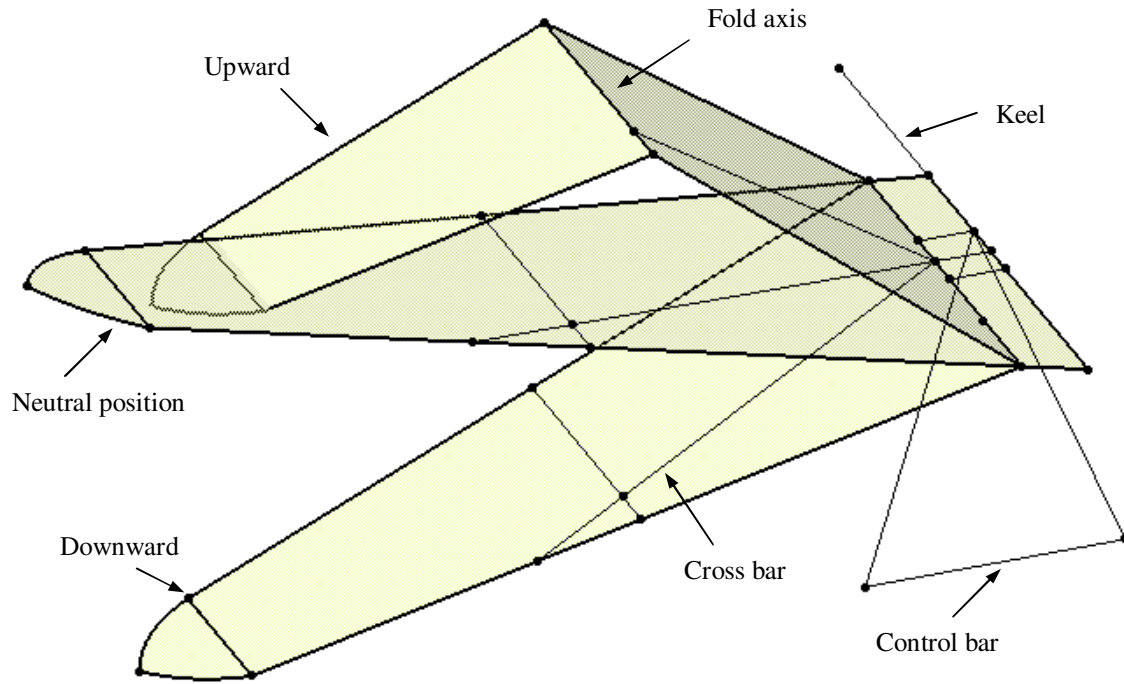


Figure 7.29 Outer wing fold control

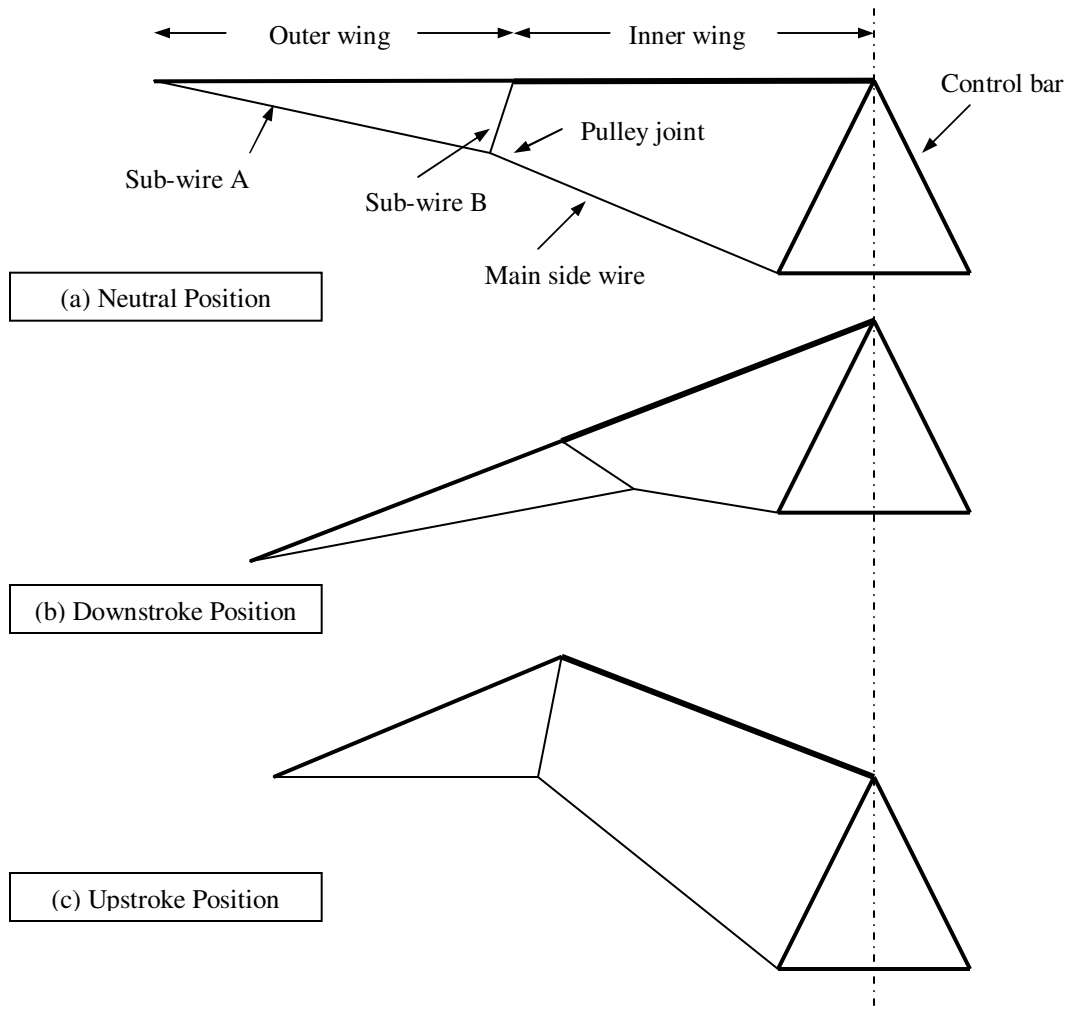


Figure 7.30 VG system

In the ornithopter design several components are placed on the original hang glider frame. The estimated extra weight due to flapping mechanism is 20kg shown in Table 6.7. With the geometry of the final design of the ornithopter the extra weight of the mechanical component is assessed by CATIA model. The weight of the joints is estimated as 0.5kg each. The weight of force transfer system with two gears and a chain is estimated as 2kg. And the VG system with sub-wire is 1kg by estimation. The extra weight of each mechanical component is shown below. The total extra weight is 12.24kg which gives about 8kg allowance for the unexpected parts required.

Component	Material	Total Weight (kg)
Arm	Steel alloy	1.2
Joints	Steel alloy	5
Cross rod	7075-T6 aluminium alloy	0.43
Root bar	7075-T6 aluminium alloy	1.57
Rib	7075-T6 aluminium alloy	1.04
Force transfer system	Steel alloy	2
VG system	Steel alloy	1

Table 7.6 Extra weight of mechanical component

Finally the optimization is achieved by designing an asymmetrical folding wing in order to minimize the negative lift amplitude and obtain positive overall lift. However the VG system needs to be carefully assessed in order to control the outer wing motion precisely.

In summery a practical ornithopter design is achieved based on the hang glider prototype. The total weight of the ornithopter is 140 kg. The ornithopter is designed to fly at 13.8 m/s with  $5.8^\circ$  angle of attack. To maintain the level flight the flapping frequency is 2 Hz to generate adequate thrust. A wing folding mechanism is designed to minimize the negative lift in upstroke to obtain positive overall lift. Finally a variable geometry system is employed to achieve the wing folding motion.

## 8 Conclusions and Recommendations for Future Work

### 8.1 Conclusions

This thesis has provided a practical design of large scale human controlled ornithopter based on the hang glider prototype. Two main research areas have been carried out which are the aerodynamic investigation and structural strength validation of flapping wings.

The study of aerodynamic forces of flapping wings is based on analytical method of Theodorsen's theory and other works extended from his theory such as Garrick's and DeLaurier's method. As far as possible, validation of theoretical data has been carried out by comparing with experimental results. Wind tunnel tests have been carried out with different scale down wing designs in order to investigate the aerodynamic forces in flapping motions. The research began with the theoretical calculation and wind tunnel testing of a straight wing with rigid thin flat plate in small simple harmonic motions. Three flapping motions have been investigated in heaving, pitching and combined heaving and pitching. The test results have indicated a good comparison with the theoretical calculation by Theodorsen equations in terms of lift amplitude over a cycle and phase shift between wing displacement and lift. The theoretical study has been carried out based on a rigid wing with the flow fully attached on the surface and no structural deformation. In the test of heaving motion stall occurs at high frequencies when the wing experiences a large angle of attack. The test results have shown that the wing loses 11.6% of lift at 8Hz compared with theoretical calculation. In pitching motion test the wing pitching amplitude is fixed at  $5^\circ$ . Additional twist occurs when the wing experiences the maximum pitch angle. The wing deformation induces 20.5% extra aerodynamic load compared with theoretical results. In the combined motion test only 6.8% of extra load is induced due to frame deformation. The wing stall at high vertical speeds under heaving motion and structural deformation become the critical issue in flapping wing design.

The wing structural deformation is an important issue in affecting the total aerodynamic force on flapping wings. The wing flexibility effect has been investigated based on wind tunnel testing of various wing designs. With the root flapping motion the wing performs a large deformation at trailing edge. The test results show a significant loss of aerodynamic load due to the wing deformation compared with theoretical results. With the same wing planform configuration flapping at the same frequency the lift varies with the amount of wing flexibility. By increasing 10% of flexible surface the required power is reduced 3% and the total aerodynamic force is reduced 4.8%. Hence the function of the flexible surface is to reduce the required power but less lift is generated. In practical design the flexible surface can be applied on the outboard wing and trailing edge similar to the feather of the bird.

A preliminary ornithopter design has been proposed based on the Wills Wing Sport 2-155 structure. As the prototype the hang glider structural reliability is examined. With the ground test speed of 29 m/s the wing frame is able to take 7g load at the stall angle. Based on the original wing structure and material finite element analysis has been carried out up to 7g wing loading and the FEA results show a reasonable stress level and deformation without any structural failure.

The ornithopter has been designed by adding an engine and flapping mechanism on the original frame. The total mass of this preliminary design is not exceeding 140kg which is the maximum design weight of the baseline hang glider. The wing flaps at stroke axis which is 0.32m away from central keel. The total stroke angle is  $65^\circ$  and the flapping frequency is 2Hz. DeLaurier's method has been employed to estimate the aerodynamic forces of the flapping wing which shows a good agreement with the wind tunnel results. FE modelling has been carried out in order to access the structural strength. The theoretical calculation showed that the flapping wing generated 4g load in cruising speed of 13.8m/s. Based on this wing loading the FEA results indicated structural failure at the joint section between the leading edge bar and cross bar with stress level of 674MPa. Large deformation occurs at wing tip which is 1.29m. Consequently modification has been carried out by reducing the flapping frequency and reassessing the spanwise

aerodynamic load respectively. By considering the effect of significant wing deformation especially near the wing tip the modified aerodynamic load calculated as a result is reduced by 29% in cruising speed and the stress on the frame is also reduced to the acceptable level. Due to the wing flapping motion the aerodynamic load acting on the wing is increased which consists of steady lift from the wing camber and dynamic load due to flapping. Therefore FE analysis has been carried out to exam the critical case of the wing for structural integrity. Due to this additional load on the wing the maximum speed is reduced from 20.5m/s to 16m/s. Structure optimization has been carried out by making use of experimental results with different wing design cases in order to obtain overall positive lift. The test results have shown that the asymmetrical wing folding is the best case which provides the maximum overall lift out of the four design cases considered in Chapter 7. Finally the solution of the outer wing folding motion control is provided by employing a VG system.

Finally the ornithopter is designed with the total weight of 140 kg. To maintain the level flight the flight speed is 13.8 m/s at 5.8° angle of attack at flapping frequency of 2 Hz. A wing folding mechanism is employed to achieve higher overall positive lift. Test results based on the 1:20 scale model show that the total positive lift achieved in downstroke is 31.5% larger than the negative lift in upstroke, resulting in an overall positive average lift on the wing over a complete flapping cycle of the wing.

## **8.2 Recommendations for Future Work**

The current investigation constitutes an initial feasibility study of ornithopter design from an aerodynamic and structural view point. In developing the practical ornithopter design further, some recommendations for the next phase of the research are appropriate. These recommendations are presented below.

The first problem is the stall angle investigation which has become an essential problem for all flapping wing vehicles. Unlike the fixed wing aircraft stall in flapping wings is caused by large flapping amplitude or high frequency inducing large effective angle of



attack. Since this research is focused on the large scale ornithopter design for low frequency flapping and a scale down model has been made for the wind tunnel tests but the stall effect has not been investigated in detail either theoretically or experimentally.

The ornithopter aerodynamic design is mainly conducted by the wind tunnel tests. Scale down model has been employed in order to carry out the wind tunnel tests. The measured aerodynamic loads show a good comparison with theoretical results. However the deformation of the model has not been reflected properly since the structure can be only scaled down in physical size but not so easily in terms of stiffness. A better solution is required to simulate not only the aerodynamic but aeroelastic performance of the flapping wing in wind tunnel tests.

It should be noted that all measurements made during the wind tunnel tests are subject to noise due to mechanical vibration. A proper filtering method is required to delete the noise effect.

Finally a practical design for variable geometry system is required for future work to obtain a better control of the wing folding motion. Also the reliability of the cables needs to be tested.

In concluding, it can be argued that the practical development of ornithopter and the present study has shown that such vehicle can be adapted from basic hang-glider prototype design to provide a much improved performance in terms of lift generation and structural integrity in different flight conditions without any major re-development. However, further convincing evidences and conclusions can only be provided through additional measurements and simulations carried out over a wider range of design and realistic flight conditions.

## REFERENCES

- [1] Henk Tennekes, *The Simple Science of Flight*, Revised and Expanded Edition, 2009, The MIT Press, Cambridge, Massachusetts, London, England.
- [2] Grasmeyer J.M., Keennon M.T.: '*Development of the Black Widow Micro Air Vehicle*'. AIAA 2001-0127, Aerospace Sciences Meeting, Reno, NV, Jan 2000.
- [3] Morris, S., Holden, M., '*Design of Micro Air Vehicles and Flight Test Validation*', Conference on Fixed, Flapping and Rotary Wing Vehicles at Very Low Reynolds Numbers. Nottre Dame University, Indiana, 5-7 June 2000.
- [4] Ifju P.G., Jenkins D.A., Ettinger S., Lian Y., Shyy W.: '*Flexible-Wing-Based Micro Air Vehicles*', AIAA 2002-0705.
- [5] Pornsin-Sisirak T., Lee S.W., Nassef H., Grasmeyer J., Tai Y.C., Ho C.M., Keenon M.: '*MEMS Wing Technology for a Battery-Powered Ornithopter*'. 13<sup>th</sup> IEEE International Conference on Micro Electro Mechanical Systems, Miyazaki, Japan, 23-27 Jan 2000.
- [6] [http://en.wikipedia.org/wiki/James\\_DeLaurier](http://en.wikipedia.org/wiki/James_DeLaurier)
- [7] T.Theodorsen, '*General Theory of Aerodynamic Instability and the mechanism of Flutter*', NACA R/496, 1934.
- [8] I.E. Garrick, '*Propulsion of a Flapping and Oscillating Airfoil*', NACA R/567, 1936.
- [9] Irvin N. Spielberg, '*The Two-Dimensional Incompressible Aerodynamic Coefficients for Oscillatory Changes in Airfoil Camber*', Wright Air Development Center, 1953.

## REFERENCES

---

- [10] J.D.DeLaurier ‘*An aerodynamic model for flapping-wing flight*’, *Aeronautical Journal*, April 1993.
- [11] Evandro Liani, Shijun Guo, Giuliano Allegri, ‘*Aerodynamics and Aeroelasticity of Flexible Flapping Wings*’, 48<sup>th</sup> AIAA 2007-2412.
- [12] K.D. Jones, C.M. Dohring, M.F. Platzer, ‘*Wake Structures Behind Plunging Airfoils: A Comparison of Numerical and Experimental Results*’, AIAA 96-0078, 34<sup>th</sup> Aerospace Sciences Meeting and Exhibit, January 15-18, 1996/Reno, NV.
- [13] K.D. Jones, M.F.Platzer, ‘*Numerical Computation of Flapping-wing Propulsion and Power Extraction*’, AIAA 97-0826, 35<sup>th</sup> Aerospace Sciences Meeting and Exhibit, January 6-10, 1997/Reno, NV.
- [14] K.D. Jones, S.J.Duggan, M.F.Platzer, ‘*Flapping-wing Propulsion for a Micro Air Vehicle*’, AIAA 2001-0126, 39<sup>th</sup> Aerospace Sciences Meeting and Exhibit, 8-11 January 2001, Reno, NV.
- [15] K.D. Jones, B.M. Castro, O.Mahmoud, S.J.Pollard, M.F. Platzer, ‘*A Collaborative Numerical and Experimental Investigation of Flapping-wing Propulsion*’, AIAA 2002-0706, 40<sup>th</sup> Aerospace Science Meeting and Exhibit, 14-17 January 2002, Reno, NV.
- [16] K.D. Jones, C.J. Bradshaw, J.Papadopoulos, M.F. Platzer, ‘*Bio-inspired Design of Flapping-wing Micro Air Vehicles*’, *The Aeronautical Journal*, Vol. 109, No.1098, August 2005.
- [17] K.D. Jones, T.C.Lund, M.F. Platzer, ‘*Experimental and Computational Investigation of Flapping Wing Propulsion for Micro Air Vehicles*’, Naval Postgraduate School, Monterey, CA.

## REFERENCES

---

- [18] T.Nick Pornsin-sirirak, S.W. Lee, H.Nassef, Y.C. Tai, C.M. Ho, M. Keennon, '*MEMS Wing Technology for a Battery-powered Ornithopter*', Caltech Micromachining Laboratory, 136-93, Pasadena, CA 91125.
- [19] C.P. Ellington, '*The Novel Aerodynamics of Insect Flight: Applications to Micro-air Vehicles*', Journal of Experimental Biology, 202, 3439-3448, 1999.
- [20] M. Okamoto, K. Yasuda, A. Azuma, '*Aerodynamic Characteristics of the Wings and Body of a Dragonfly*', Journal of Experimental Biology, vol 199, pp. 281-294, 1996.
- [21] M. Sato, A. Azuma, '*The Flight Performance of a Damselfly Ceriagrion Melanurum Selys*', Journal of Experimental Biology, vol 200, pp. 1765-1779, 1997.
- [22] Graham K. Taylor, Robert L. Nudds, Adrian L.R. Thomas, '*Flying and Swimming Animals Cruise at a Strouhal Number Tuned for High Power Efficiency*', Nature, vol 425, 2003.
- [23] Wei Shyy, Mats Berg and Daniel Ljungqvist. '*Flapping and Flexible Wings for Biological and Micro Air Vehicles*', Department of Aerospace Engineering, Mechanics & Engineering Science, University of Florida, Gainesville, FL 32611.
- [24] K.D. Jones, C.J. Bradshaw, J. Papadopoulos, M.F. Platzer, '*Bio-inspired Design of Flapping-wing Micro Air Vehicles*', AIAA 95-0743, 33<sup>rd</sup> Aerospace Sciences Meeting and Exhibit, January 9-12, 1995/Reno, NV.
- [25] Steven Ho, Hany Nassef, Nick Pornsinsirirak, Yu-Chong Tai, Chih-Ming Ho, '*Unsteady Aerodynamics and Flow Control for Flapping Wing Flyers*', Progress in Aerospace Science 39, 2003, 635-681.

## REFERENCES

---

- [26] David L. Raney, Eric C. Slominski, '*Mechanization and Control Concepts for Biologically Inspired Micro Air Vehicles*', AIAA Guidance, Navigation and Control Conference 11-14, 2003.
- [27] Christopher N. Deal, '*Remote Control Hovering Ornithopter*', AIAA 2008-1421, January 2008.
- [28] Che-Shu Lin, Chyanbin Hwu, Wen-Bin Young, '*The Thrust and Lift of an Ornithopter's Membrane Wings with Simple Flapping Motion*', Aerospace Science and Technology 10, 2006, 111-119.
- [29] Sandra Mau, '*Ornithopter Wing Optimization*', Ornithopter summer internship report, Institute of Aerospace Studies, University of Toronto, August 2003.
- [30] S.A. Combes, T.L. Daniel, '*Flexural Stiffness in Insect Wings and Spatial Distribution and Dynamic Wing Bending*', Journal of Experimental Biology 206, 2989-2997, 2003.
- [31] Pin Wu, Prter Ifju, Bret Stanford, Erik Sallstrom, Lawrence Ukeiley, Robert Love and Rick Lind, '*A Multidisciplinary Experimental Study of Flapping Wing Aeroelasticity in Thrust Production*', 50<sup>th</sup> AIAA 2009-2413, May 2009.
- [32] Lucas Clemons, Hirofumi Igarashi and Hui Hu, '*An Experimental Study of Unsteady Vortex Structures in the Wake of a Piezoelectric Flapping Wing*', 48<sup>th</sup> AIAA 2010-1025, January 2010.
- [33] D.H. Olson, Dmytro Silin, Motoyuki Aki, '*Wind Tunnel Testing and Design of Fixed and Flapping Wing Micro Air Vehicles at the University of Arizona*', University of Arizona, Tucson, Arizona, 85721, USA.

## REFERENCES

---

- [34] P. Prempraneerach, F.S. Hover, M.S. Triantafyllou, '*The effect of Chordwise Flexibility on the Thrust and Efficiency of a Flapping Foil*', 13<sup>th</sup> Intern. Symp. Unmanned Untethered Techn., Durham, NH., Aug. 24-27, 2003.
- [35] Abbs Ebrahimi and Karim Mazaheri, '*Aerodynamic Performance of the Flapping Wing*', Aerospace Systems Center of Excellence, Sharif University of Technology, Iran. ISBN: 978-953-51-0611-1.
- [36] Sergey Shkarayev and Dmitro Silin, '*Aerodynamics of Flapping-Wing Micro Air Vehicles*', 47<sup>th</sup> AIAA-2009-878, January 2009.
- [37] Scott L. Thomson, Christopher A. Mattson, Mark B. Colton, '*Experimental-Based Optimization of Flapping Wing Kinematics*', 47<sup>th</sup> AIAA 2009-874, January 2009.
- [38] Jonathan Warkentin and James DeLaurier, '*Experimental Aerodynamic Study of Tandem Flapping Membrane Wings*', Journal of Aircraft, Vol. 44, No. 5, September-October 2007.
- [39] Norizham A. Razak, Jose. I. Rothkegel, and G. Dimitriadis, '*Experiments on a 3-D Flapping and Pitching Mechanical Model*', IFASD-2009-124.
- [40] Zhang Yafeng, Li Zhanke, Song Wenping, Song Bifeng, '*Lift and Thrust Characteristics of the Flapping Wing Micro Air Vehicle*', 27<sup>th</sup> International Congress of the Aeronautical Sciences.
- [41] A. R. Jones and H. Babinsky, '*Unsteady Lift Generation on Rotating Wings at Low Reynolds Numbers*', Journal of Aircraft, Vol. 47, No. 3, May-June 2010.
- [42] Greenewalt CH. Dimensional relationships for flying animals. *Smithson Misc Collect* 1962:144:1-46.

## REFERENCES

---

- [43] Norberg UM. Vertebrate flight: mechanics, physiology, morphology, ecology and evolution. New York: Springer, 1990.
- [44] <http://www.ornithopter.org/how.fly.shtml>
- [45] Raymond L. Bisplinghoff, Holt Ashley, Robert L. Halfman, 1957, Aeroelasticity, Addison-Wesley Publishing Company, Inc.
- [46] Y.C. Fung, 1955, An Introduction to the Theory of Aeroelasticity, John Wiley & Sons, Inc.
- [47] Joseph Katz, Allen Plotkin, 1991, Low-Speed Aerodynamics From Wing Theory to Panel Methods, McGraw-Hill, Inc.
- [48] Jones, R.T. *'The Unsteady Lift of a Wing of Finite Aspect Ratio'*, NACA Report No.681, 1940.
- [49] Scherer, J.O. *'Experimental and Theoretical Investigation of Large Amplitude Oscillating Foil Propulsion Systems'*, Hydronautics, Laurel, Md, December 1968.
- [50] Wills Wing hang glider manufacture's web site: <http://www.willswing.com>
- [51] 2009 HGMA Airworthiness Standards
- [52] Wills Wing Sport 2-155 owner/service manual
- [53] I.Azaryev *'Aerodynamic of a trike'*. <http://ebooks6.com/TUMBLE-of-a-HANG-GLIDER-download-w84634.pdf>
- [54] Cranfield Lecture Notes, CofA Report 32, Cranfield University.

# APPENDIX A

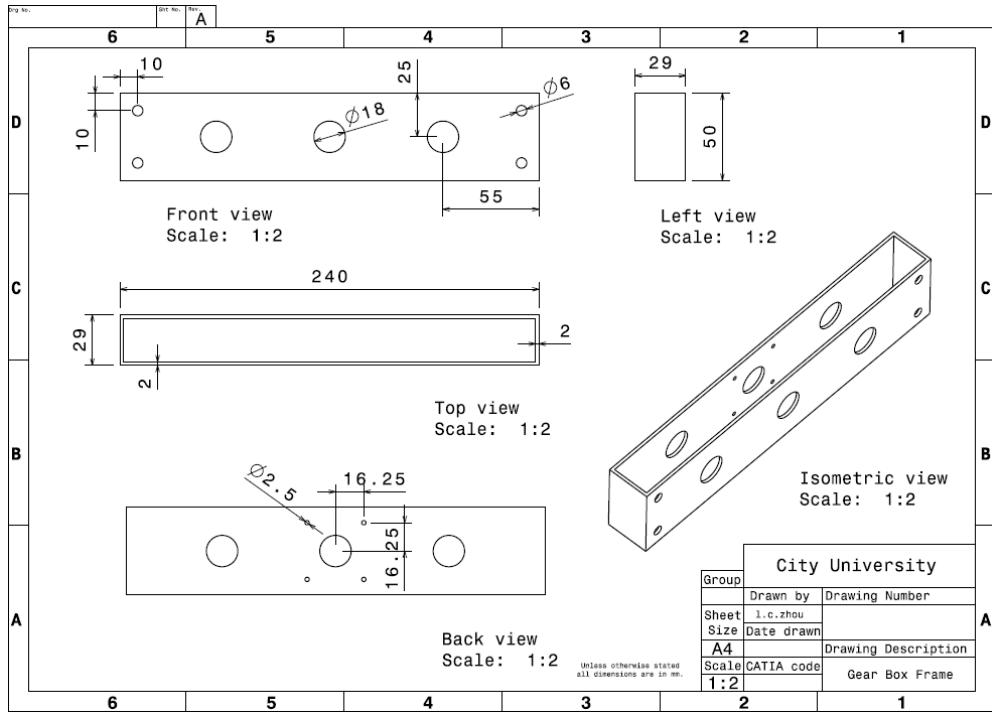


Figure A1 Gear box frame

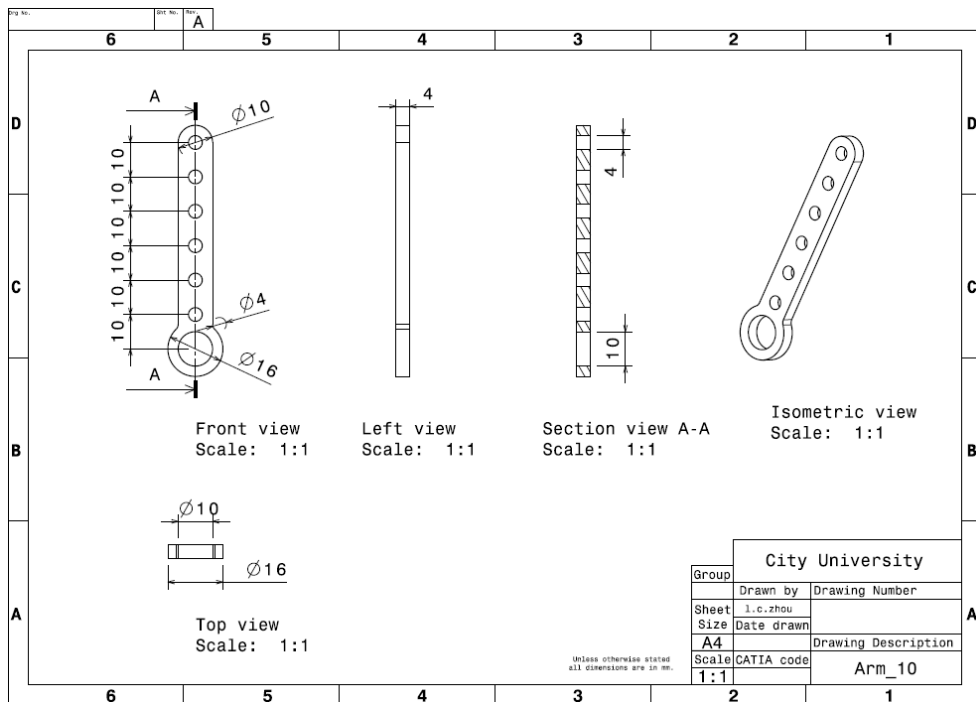


Figure A2 Crank arm



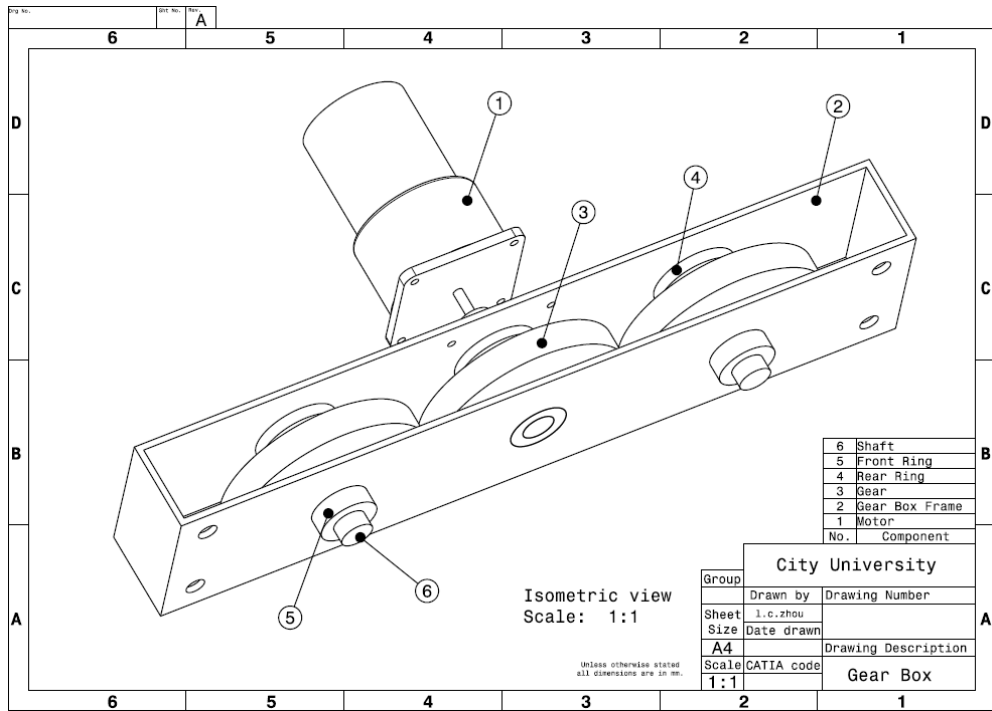


Figure A3 Assembled gear box

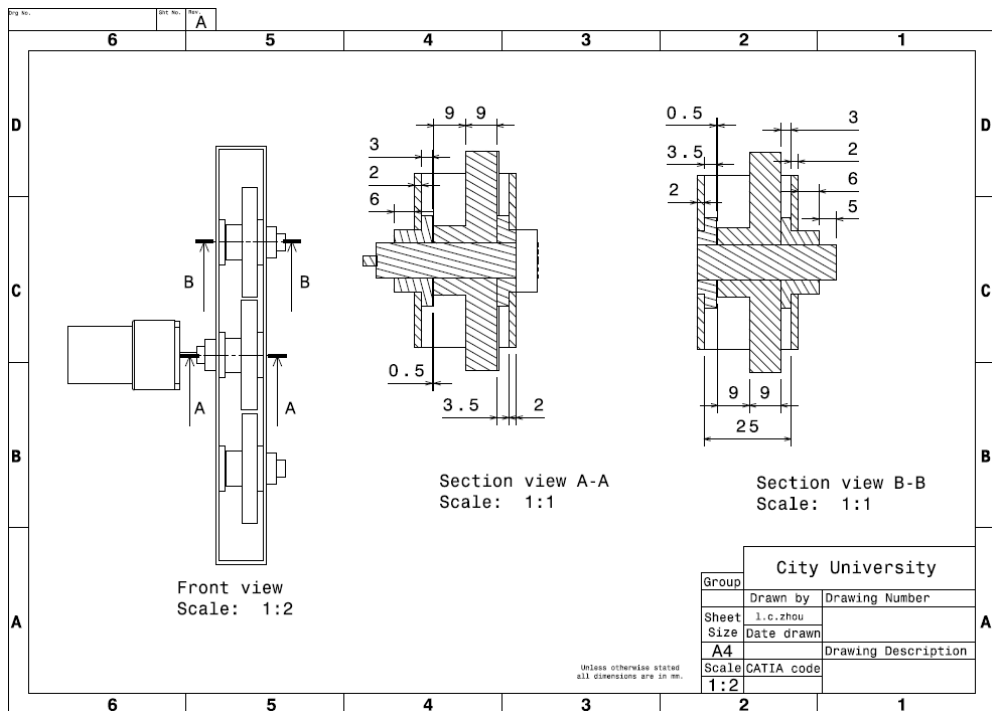


Figure A4 Section view of assembled gear box

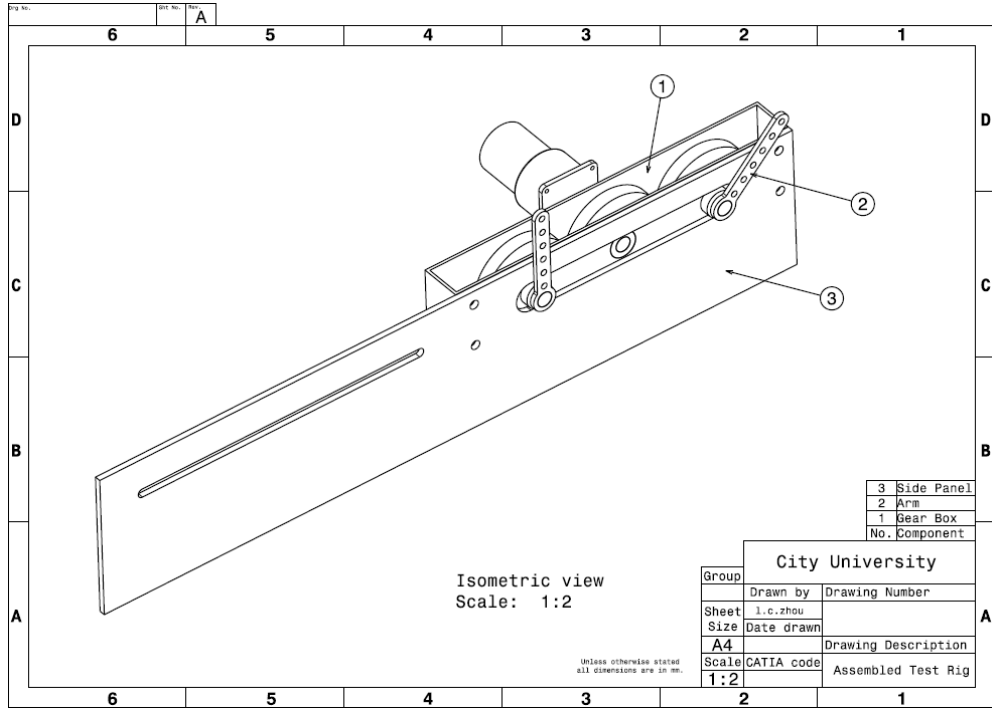


Figure A5 Assembled mechanics

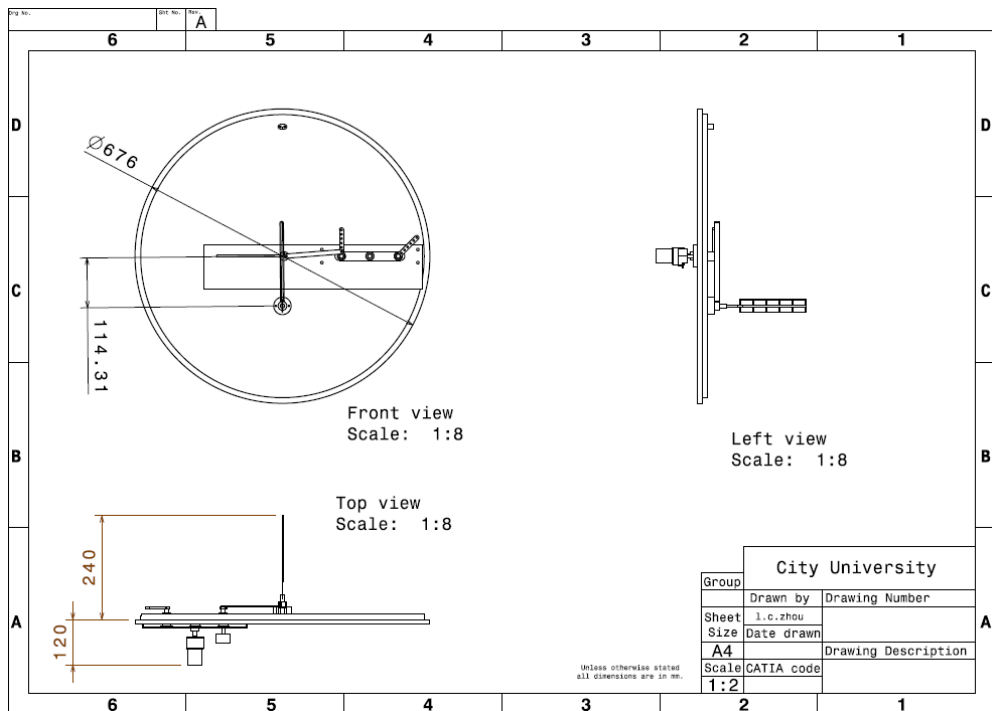


Figure A6 Assembled test rig

Test Result of Heaving Motion ( $10^{-3}$ N)					
	4Hz	5Hz	6Hz	7Hz	8Hz
Inertia	4.26	6.62	9.16	11.94	15.01
2m/s	5.29	6.02	6.61	7.20	7.40
4m/s	11.93	14.57	16.04	16.58	17.27
6m/s	18.55	21.64	24.65	27.11	29.92
8m/s	25.42	32.31	36.21	39.35	40.75

Table A1 Test result of heaving motion

Test Result of Pitching Motion ( $10^{-3}$ N)					
	4Hz	5Hz	6Hz	7Hz	8Hz
Inertia	0.30	0.49	0.74	1.01	1.33
2m/s	4.12	4.02	3.96	3.94	3.93
4m/s	18.33	17.58	17.11	16.80	16.64
6m/s	44.82	44.43	43.46	42.44	41.83
8m/s	87.41	84.74	83.11	80.42	77.17

Table A2 Test result of pitching motion

Test Result of Combined Motion ( $10^{-3}$ N)					
	4Hz	5Hz	6Hz	7Hz	8Hz
Inertia	8.14	11.93	16.96	22.18	30.05
2m/s	6.14	7.36	8.84	9.69	10.39
4m/s	20.45	22.38	23.94	25.31	26.19
6m/s	43.99	46.23	48.52	50.92	52.90
8m/s	77.18	80.65	83.95	87.73	91.14

Table A1 Test result of combined motion

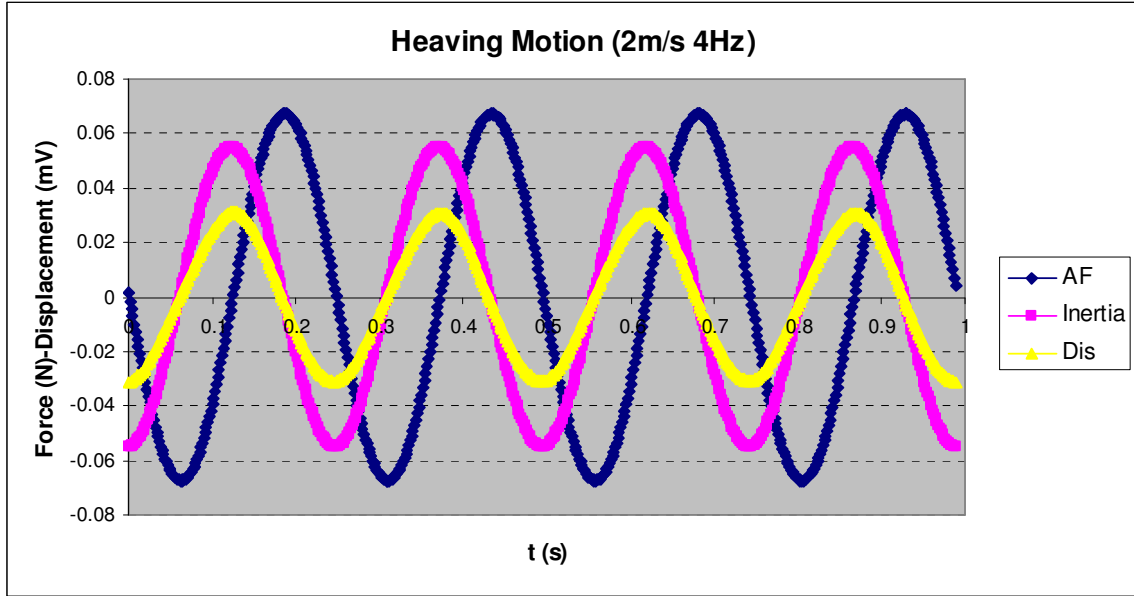


Figure A7 Test result of heaving motion at 2m/s, 4Hz

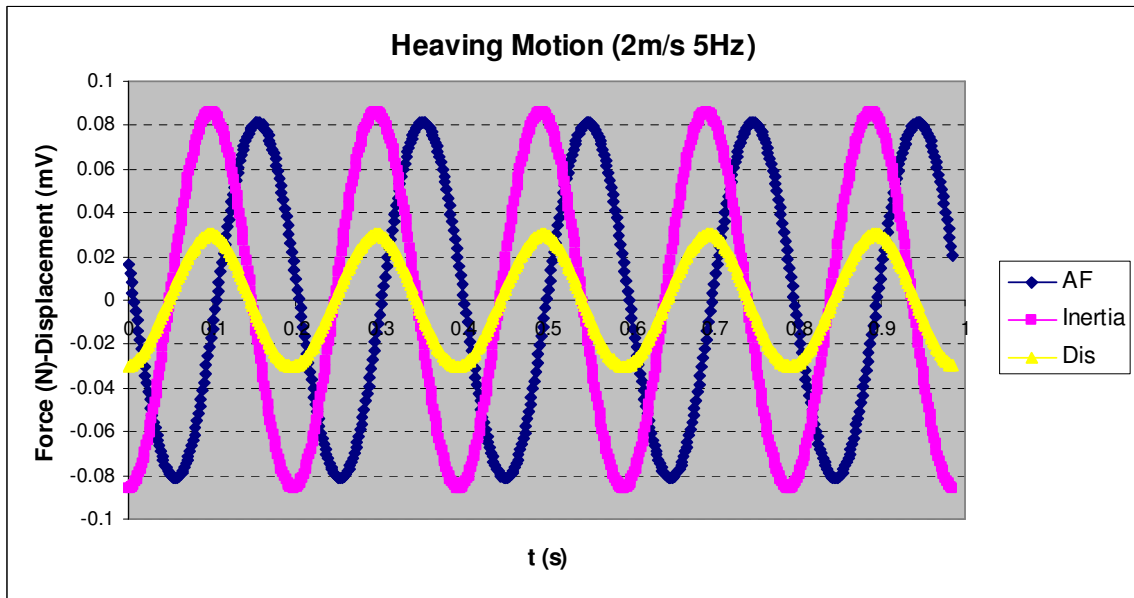


Figure A8 Test result of heaving motion at 2m/s, 5Hz

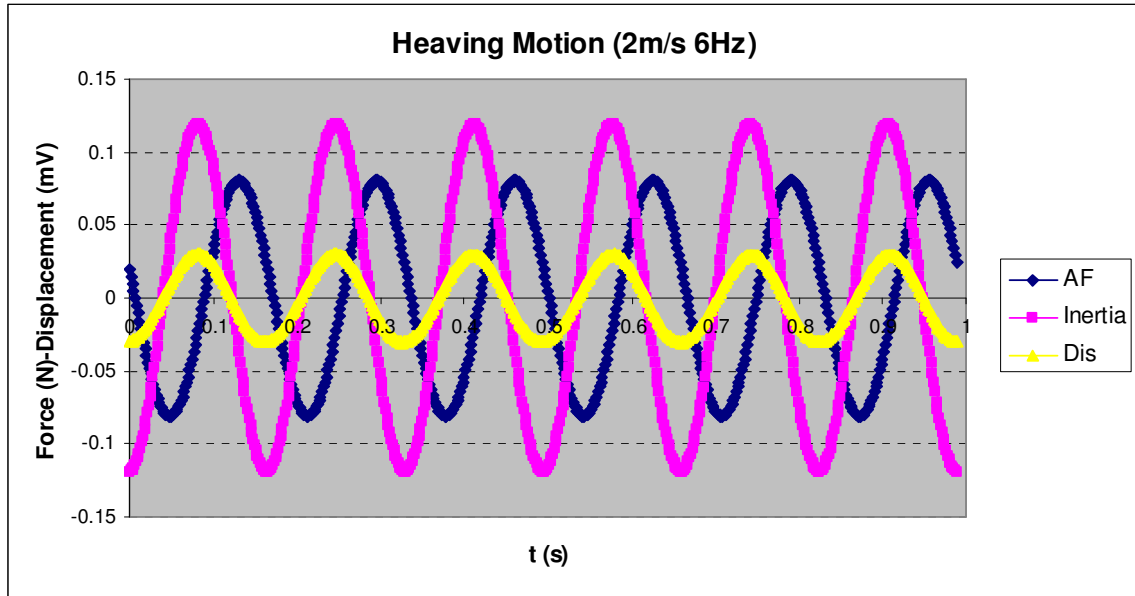


Figure A9 Test result of heaving motion at 2m/s, 6Hz

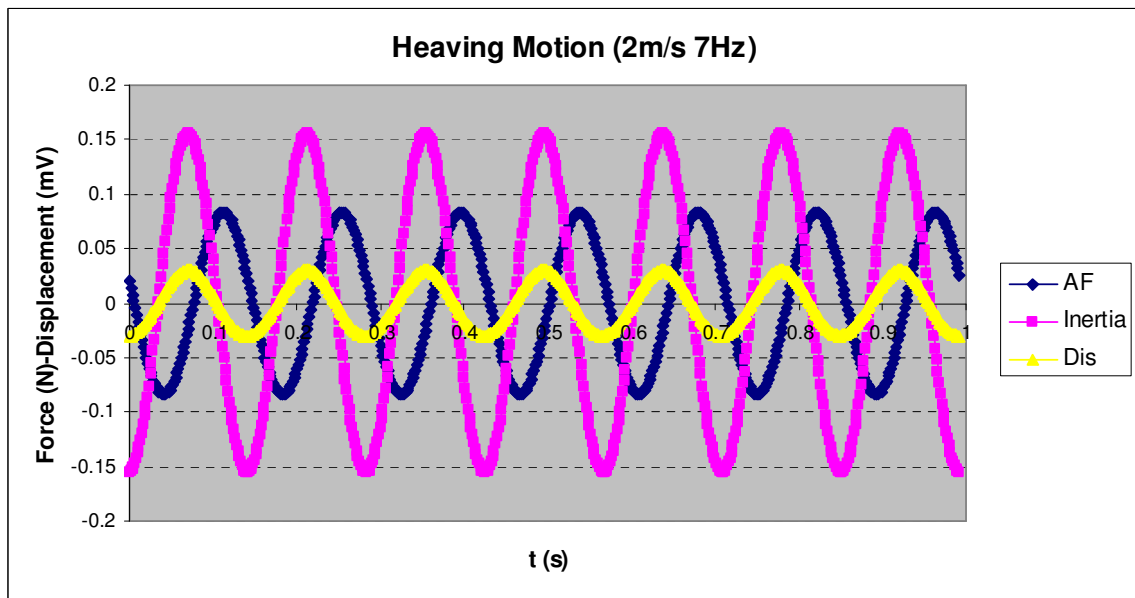


Figure A10 Test result of heaving motion at 2m/s, 7Hz

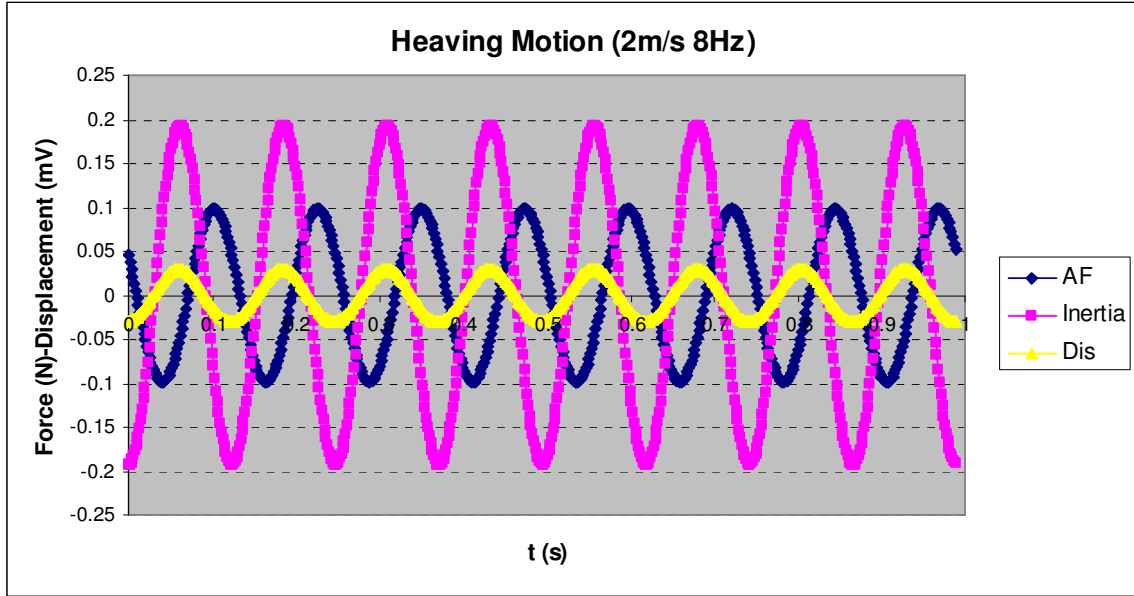


Figure A11 Test result of heaving motion at 2m/s, 8Hz

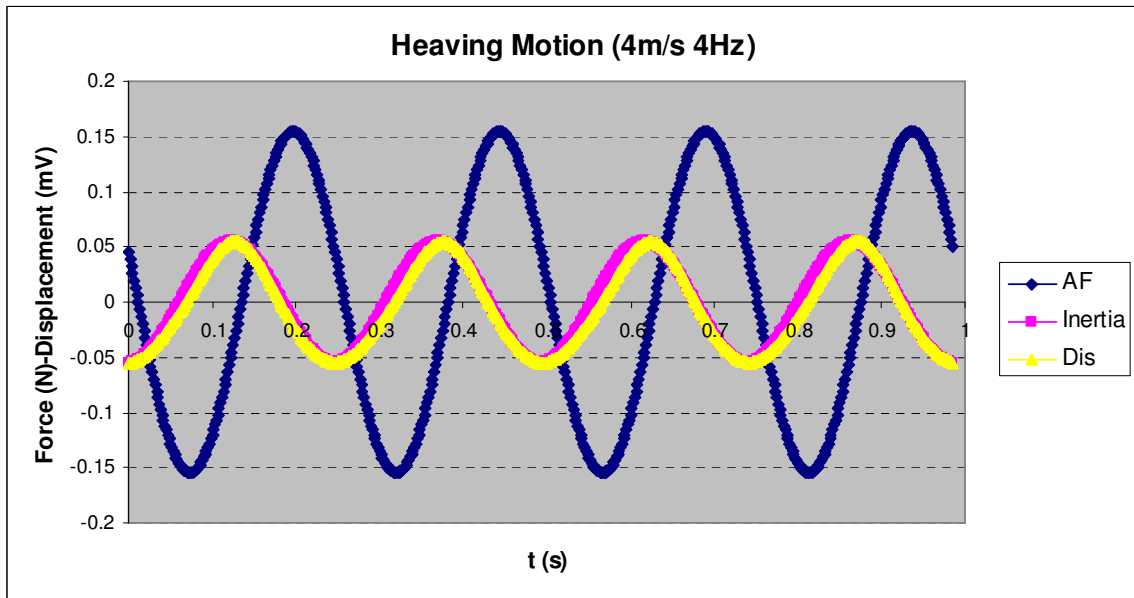


Figure A12 Test result of heaving motion at 4m/s, 4Hz

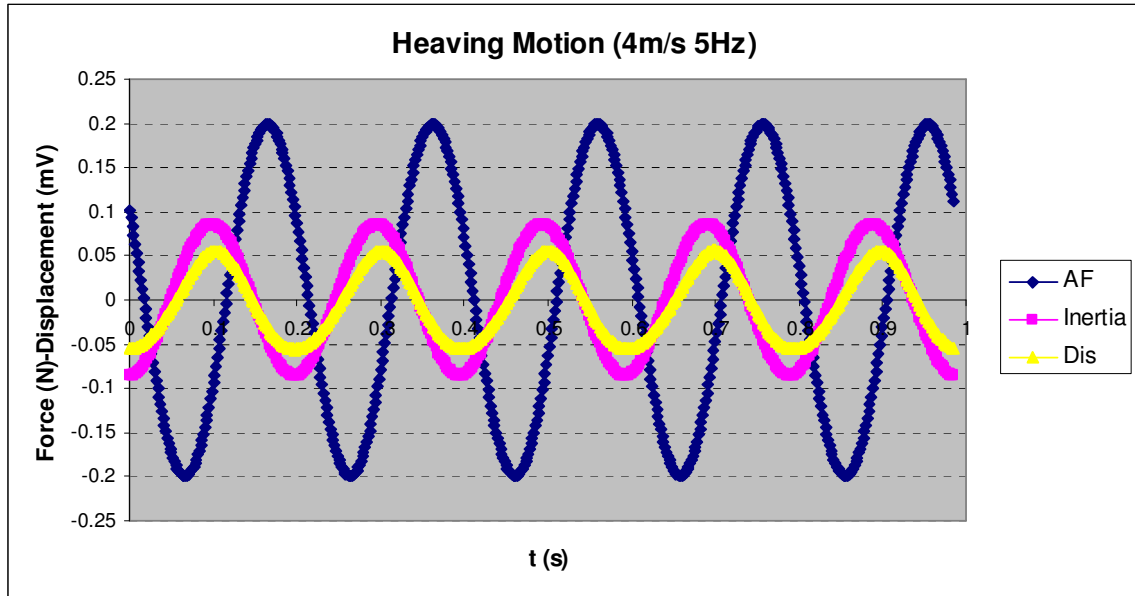


Figure A13 Test result of heaving motion at 4m/s, 5Hz

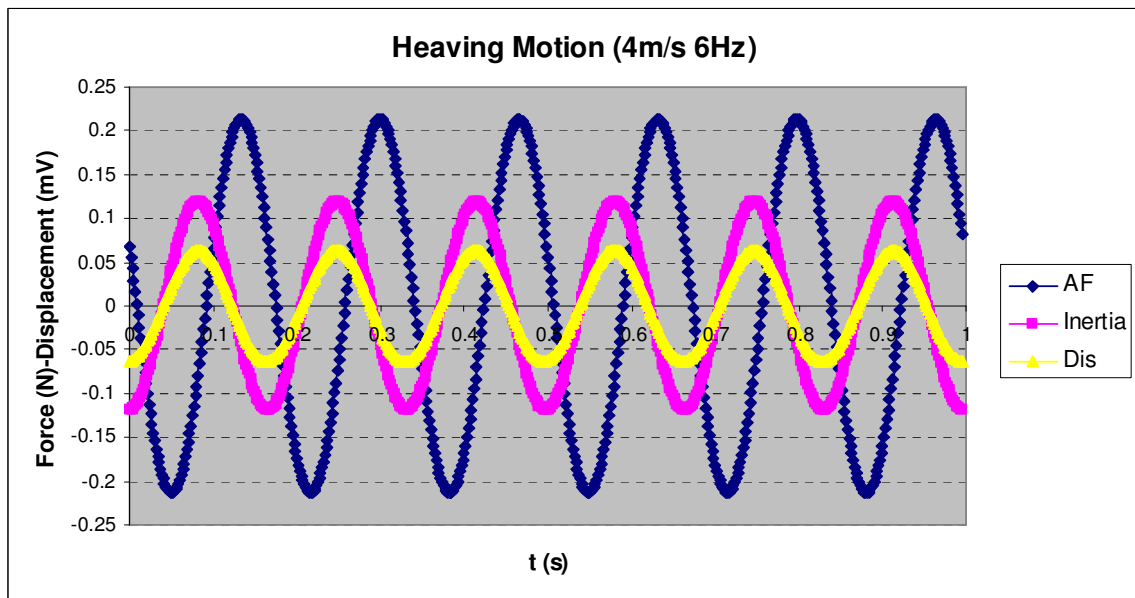


Figure A14 Test result of heaving motion at 4m/s, 6Hz

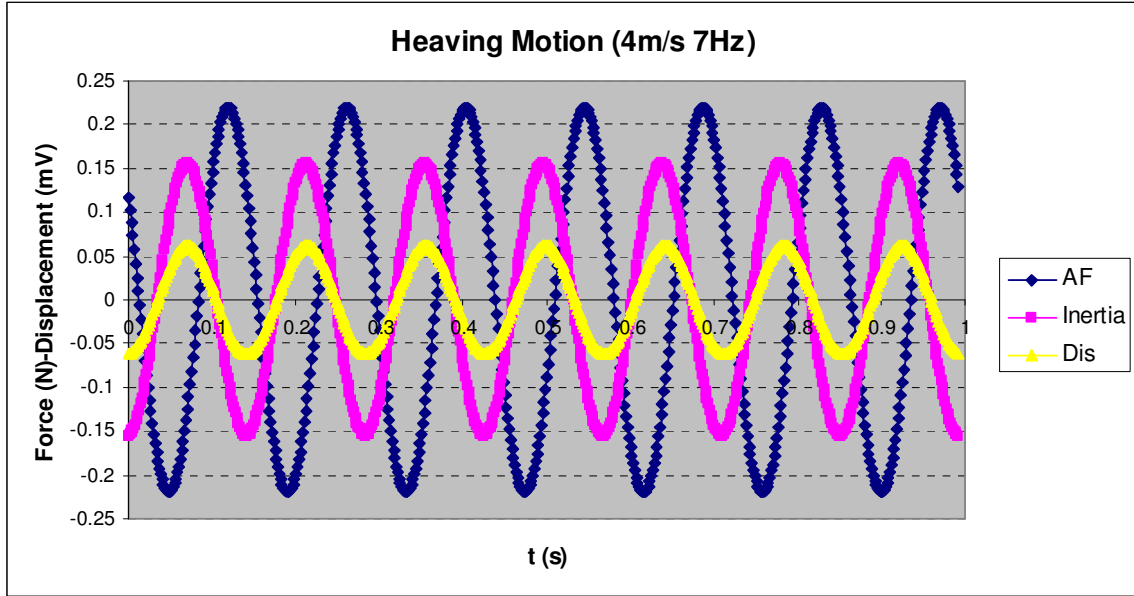


Figure A15 Test result of heaving motion at 4m/s, 7Hz

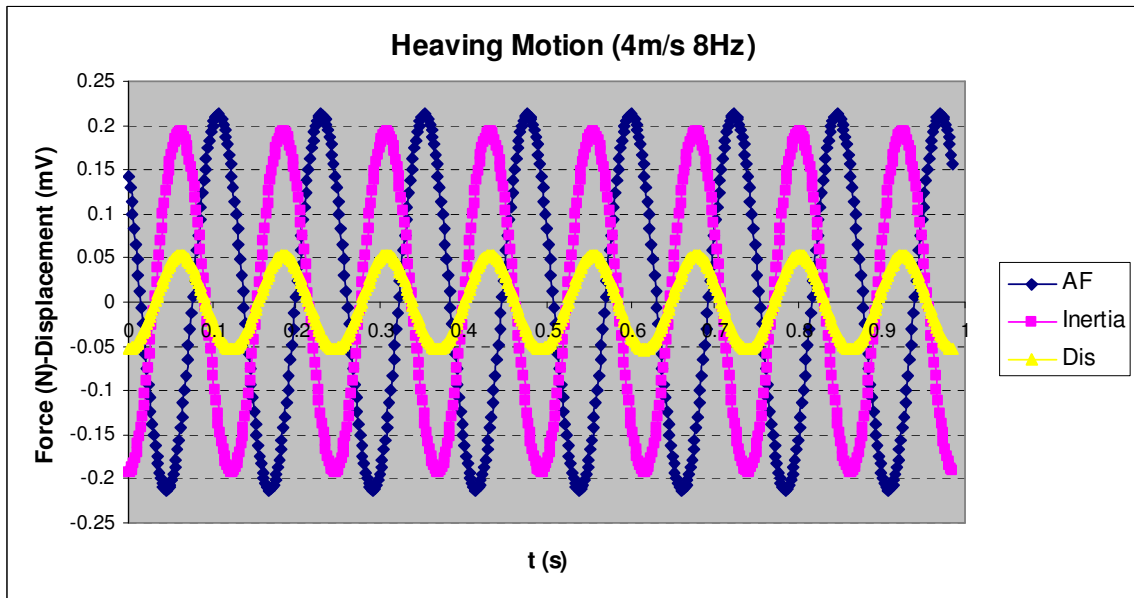


Figure A16 Test result of heaving motion at 4m/s, 8Hz



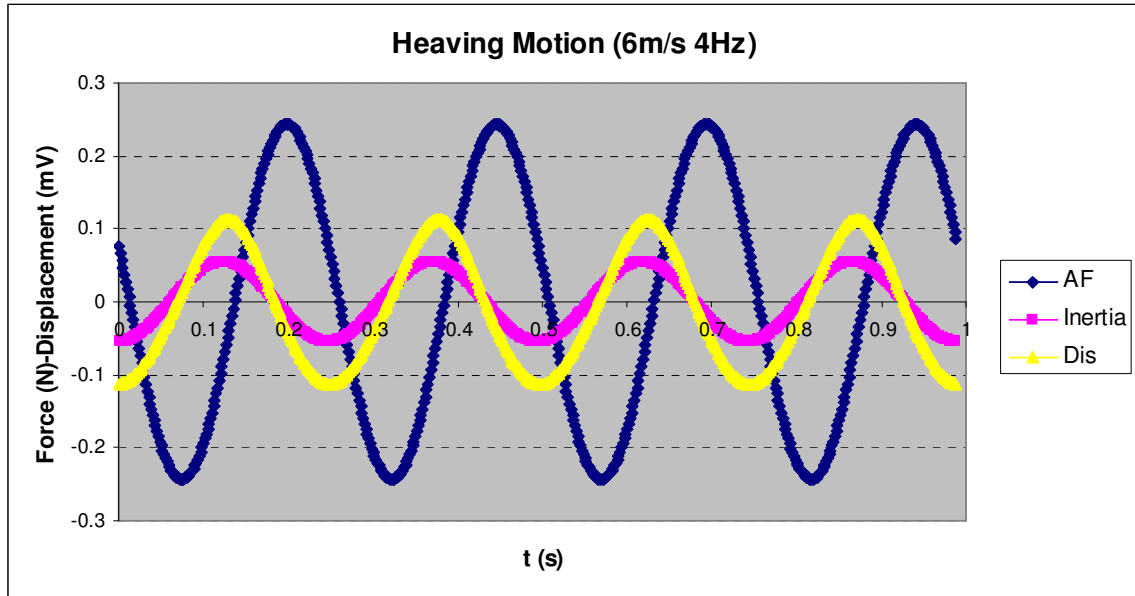


Figure A17 Test result of heaving motion at 6m/s, 4Hz

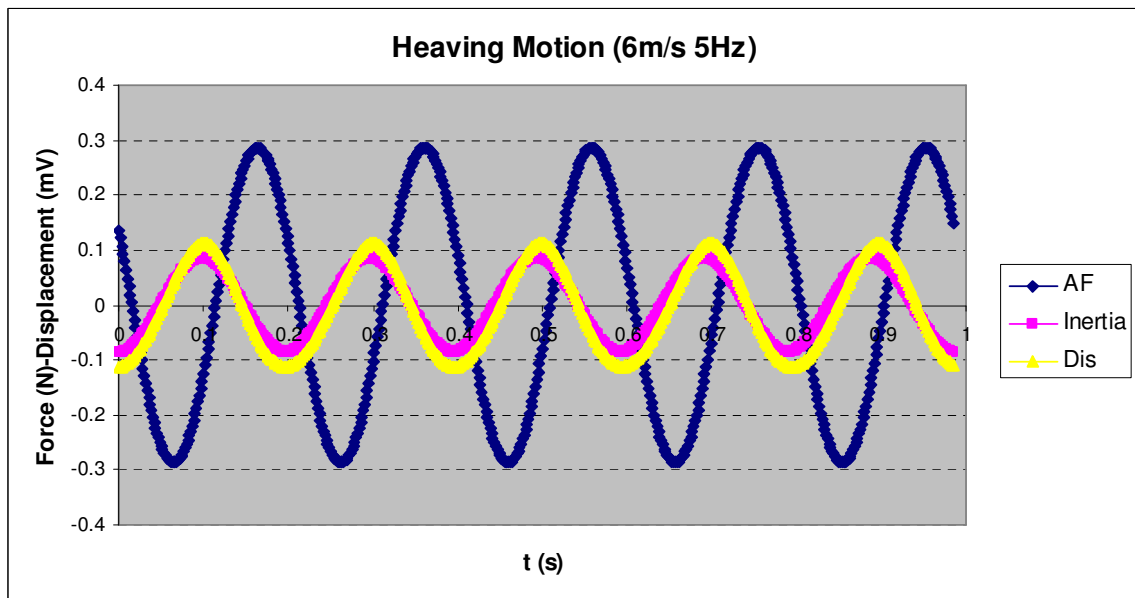


Figure A18 Test result of heaving motion at 6m/s, 5Hz

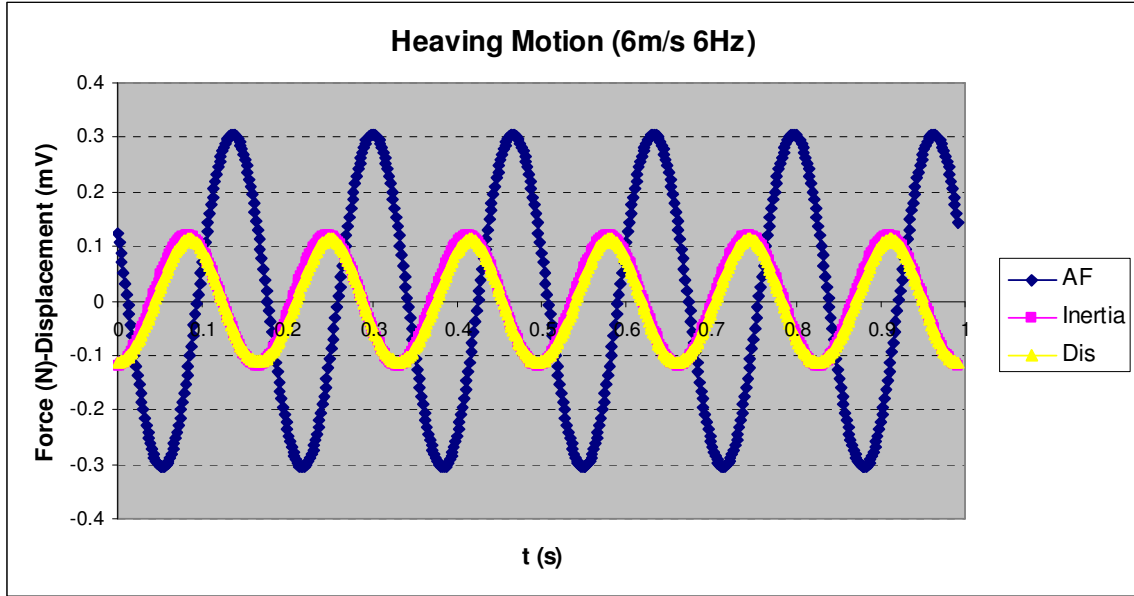


Figure A19 Test result of heaving motion at 6m/s, 6Hz

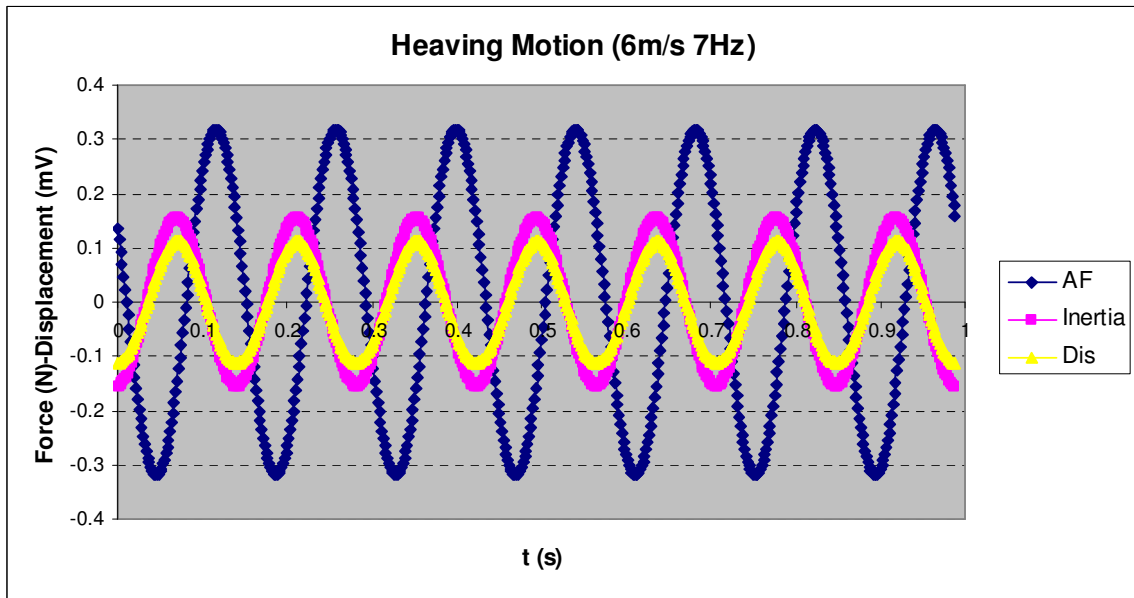


Figure A20 Test result of heaving motion at 6m/s, 7Hz

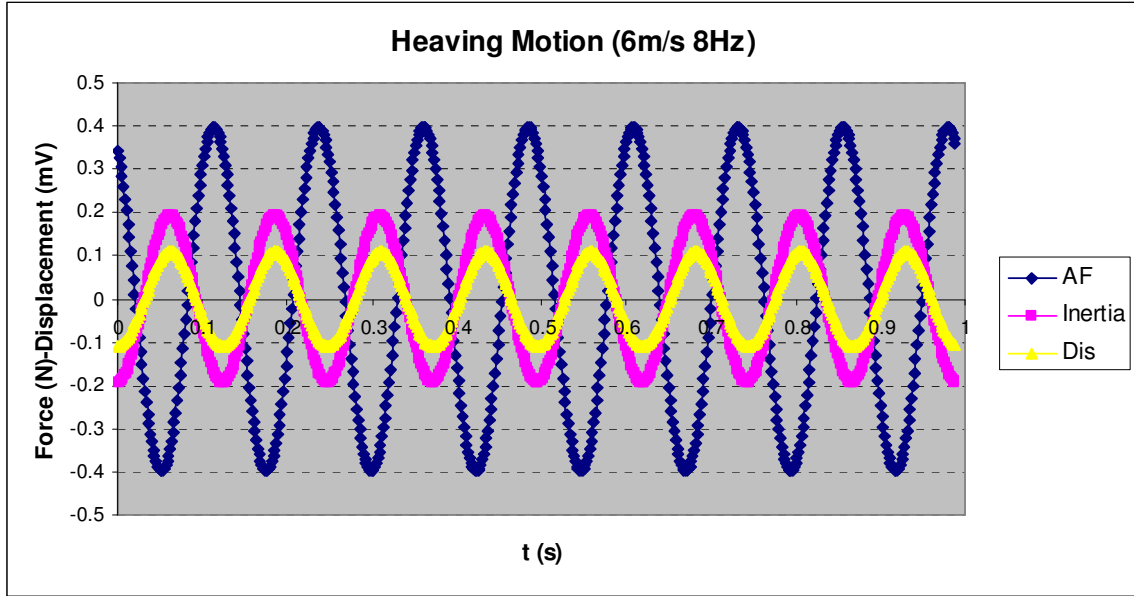


Figure A21 Test result of heaving motion at 6m/s, 8Hz

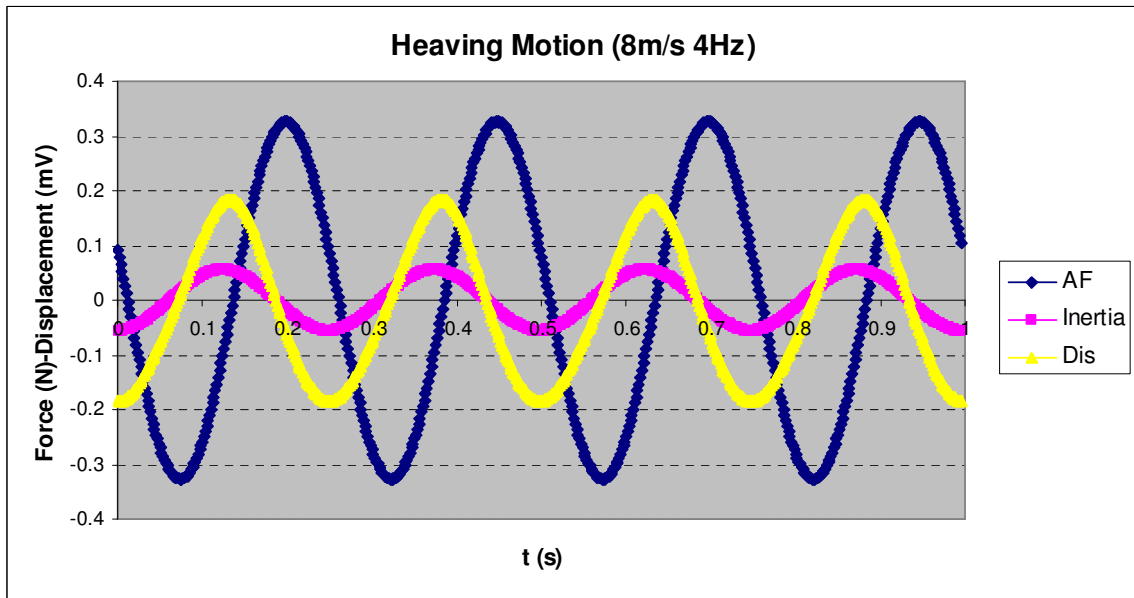


Figure A22 Test result of heaving motion at 8m/s, 4Hz

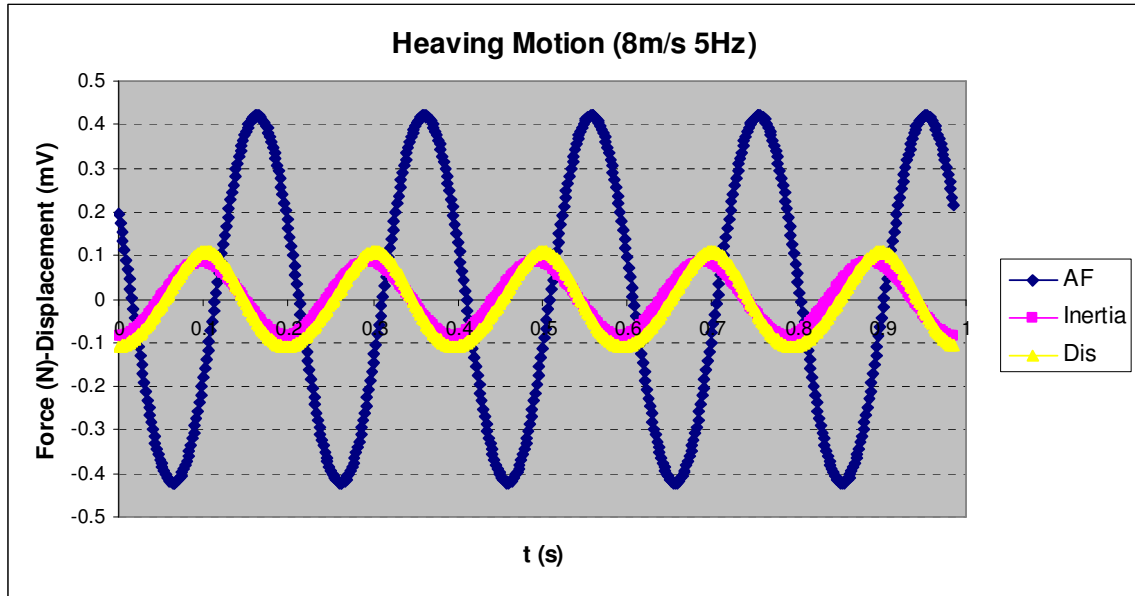


Figure A23 Test result of heaving motion at 8m/s, 5Hz

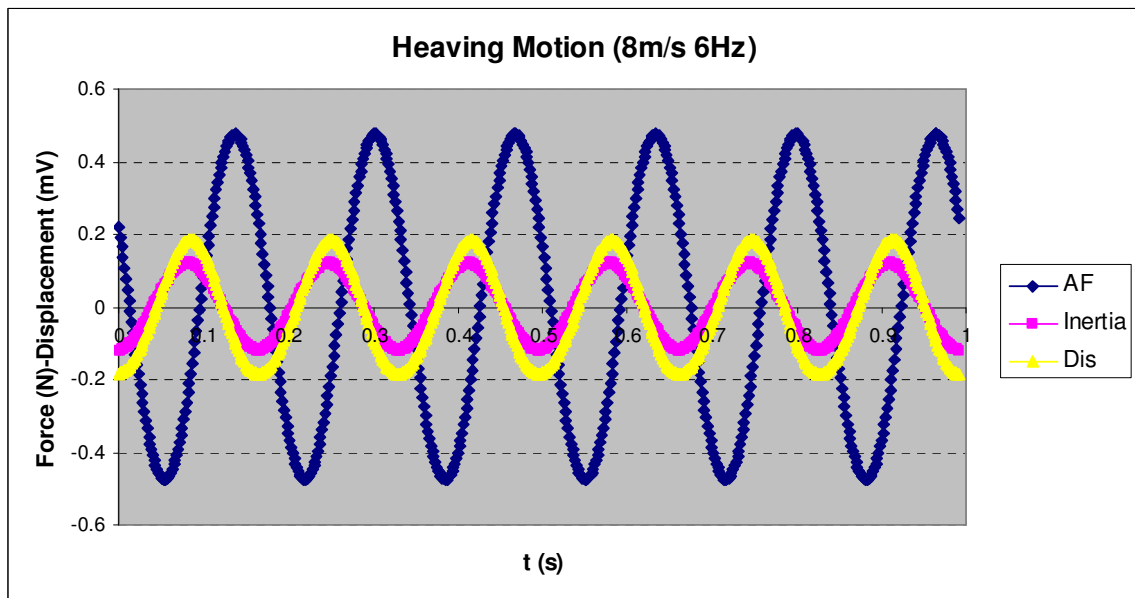


Figure A24 Test result of heaving motion at 8m/s, 6Hz

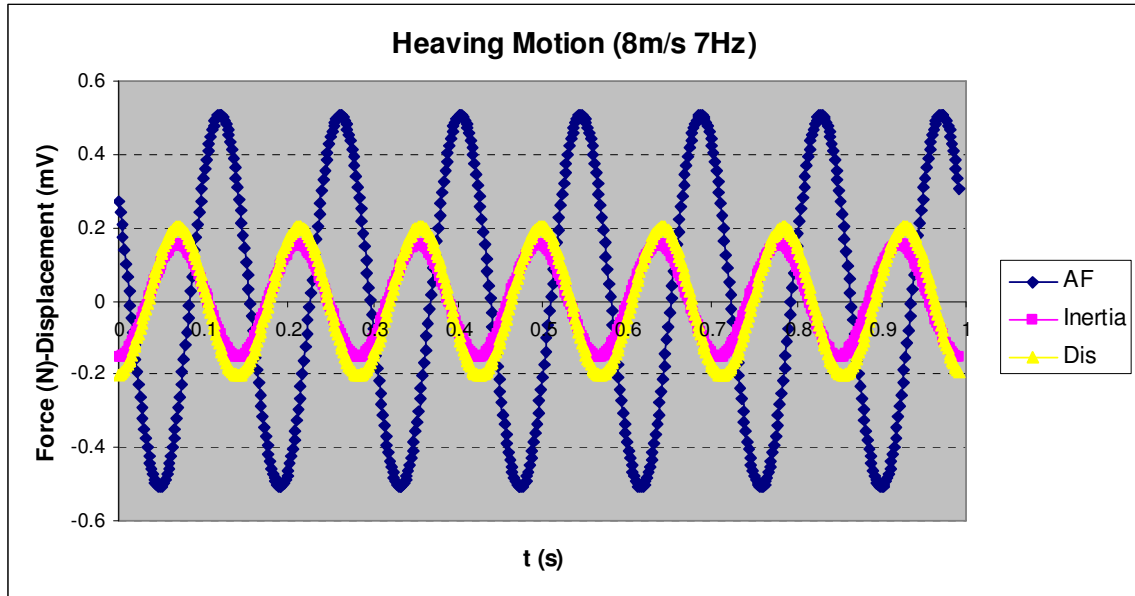


Figure A25 Test result of heaving motion at 8m/s, 7Hz

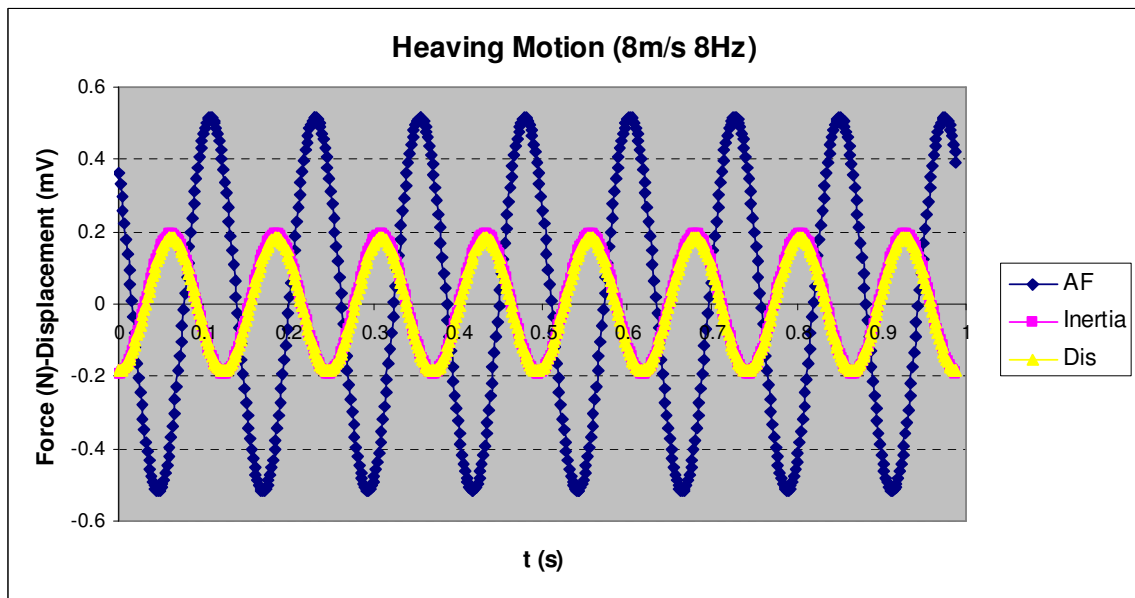


Figure A26 Test result of heaving motion at 8m/s, 8Hz

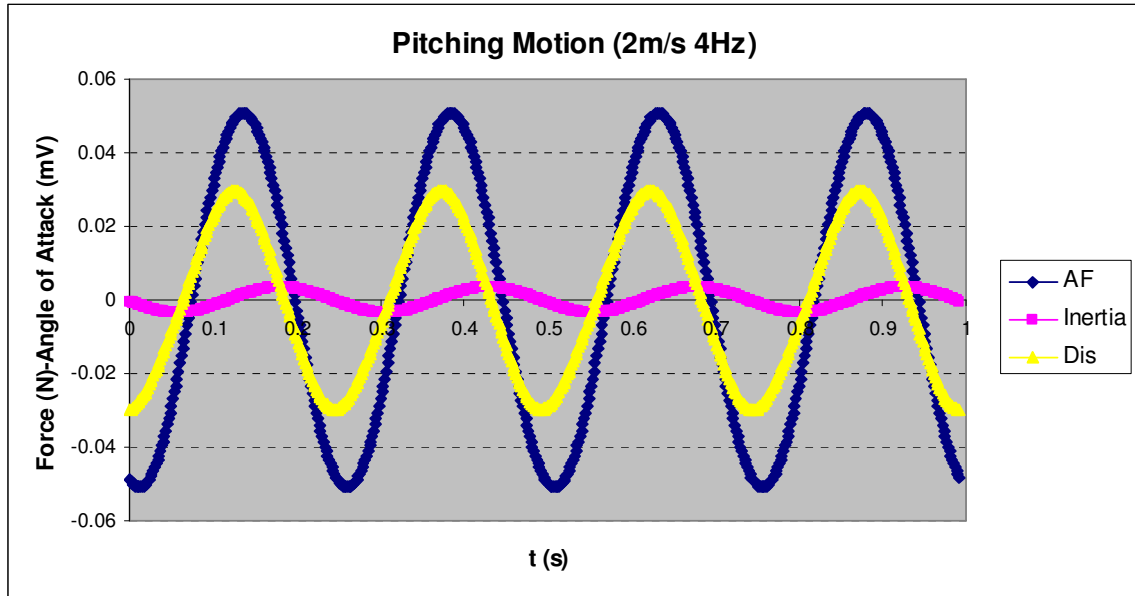


Figure A27 Test result of pitching motion at 2m/s, 4Hz

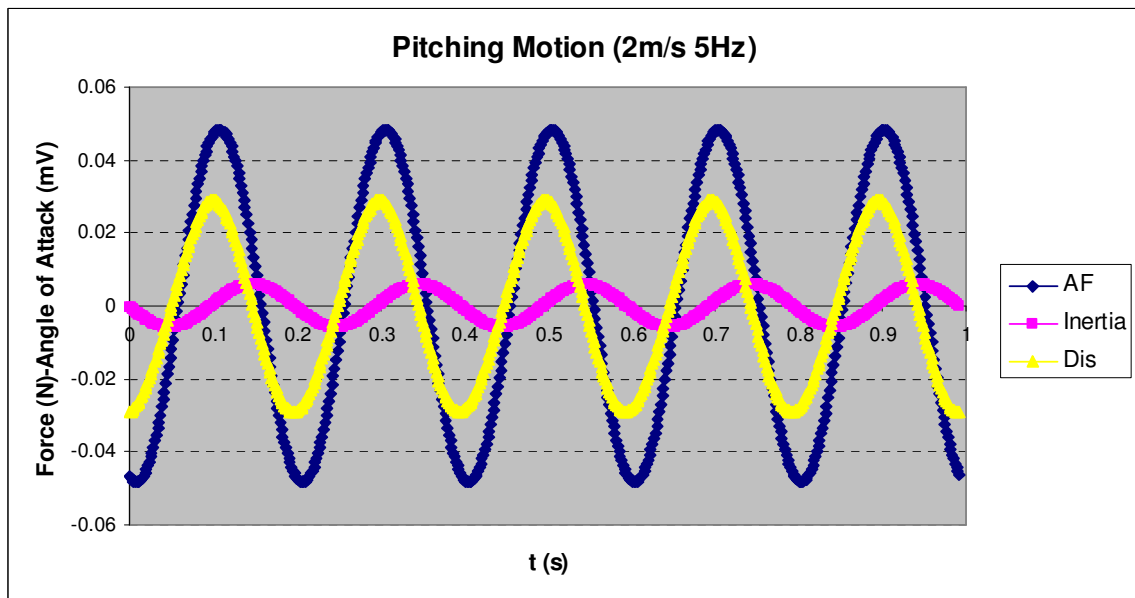


Figure A28 Test result of pitching motion at 2m/s, 5Hz

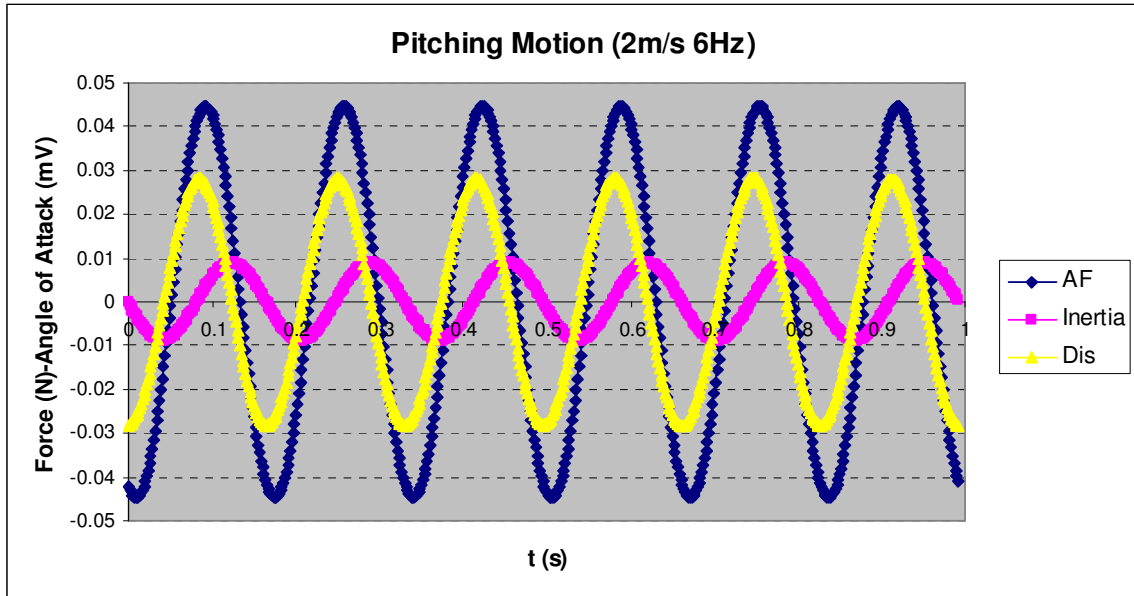


Figure A29 Test result of pitching motion at 2m/s, 6Hz

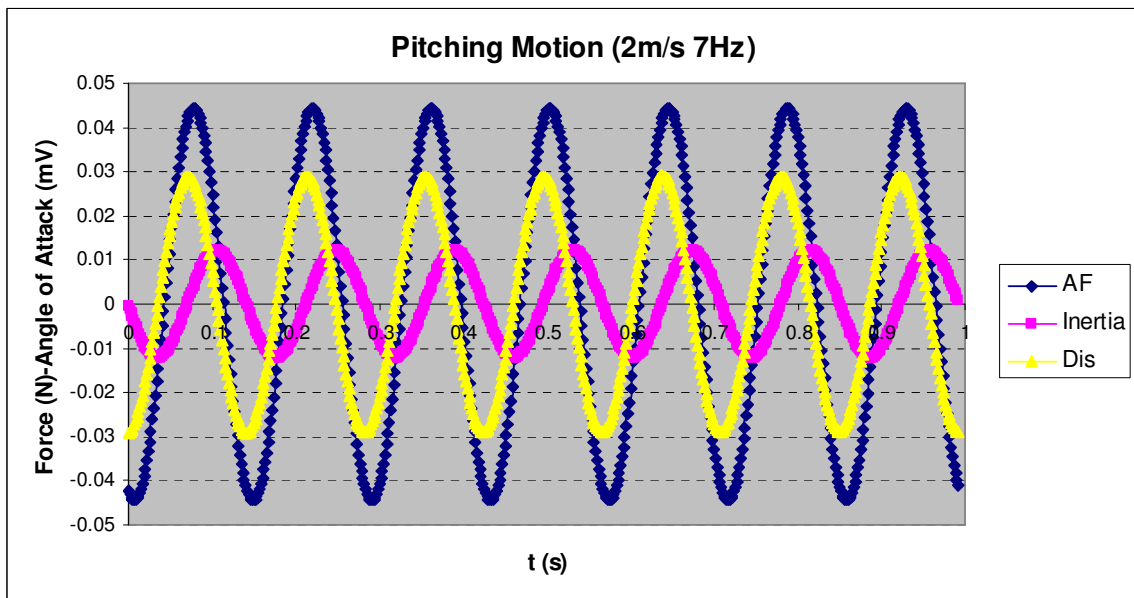


Figure A30 Test result of pitching motion at 2m/s, 7Hz

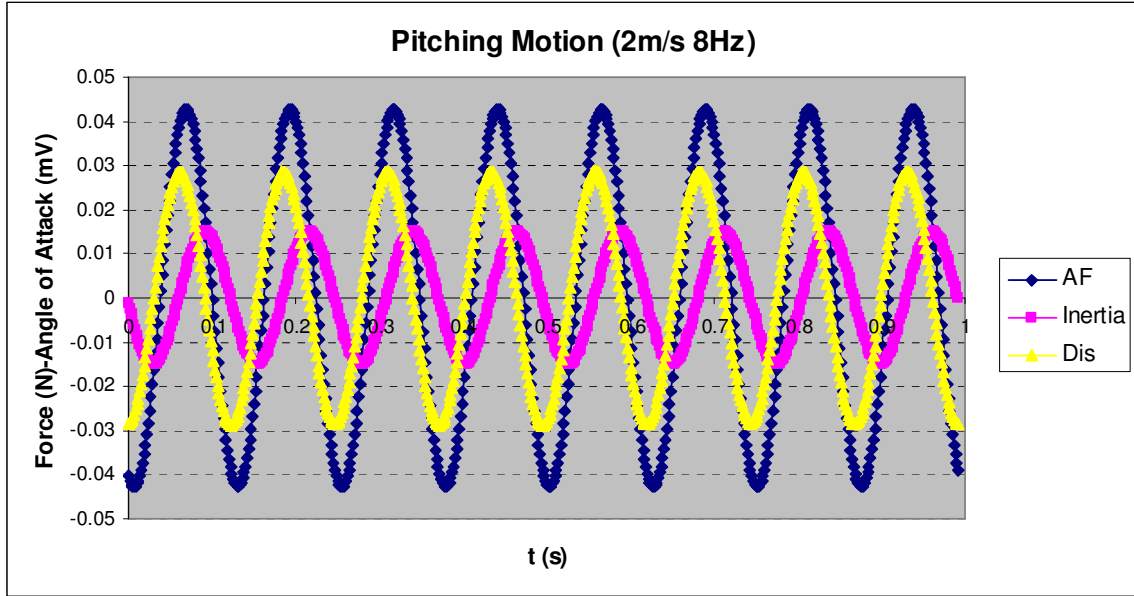


Figure A31 Test result of pitching motion at 2m/s, 8Hz

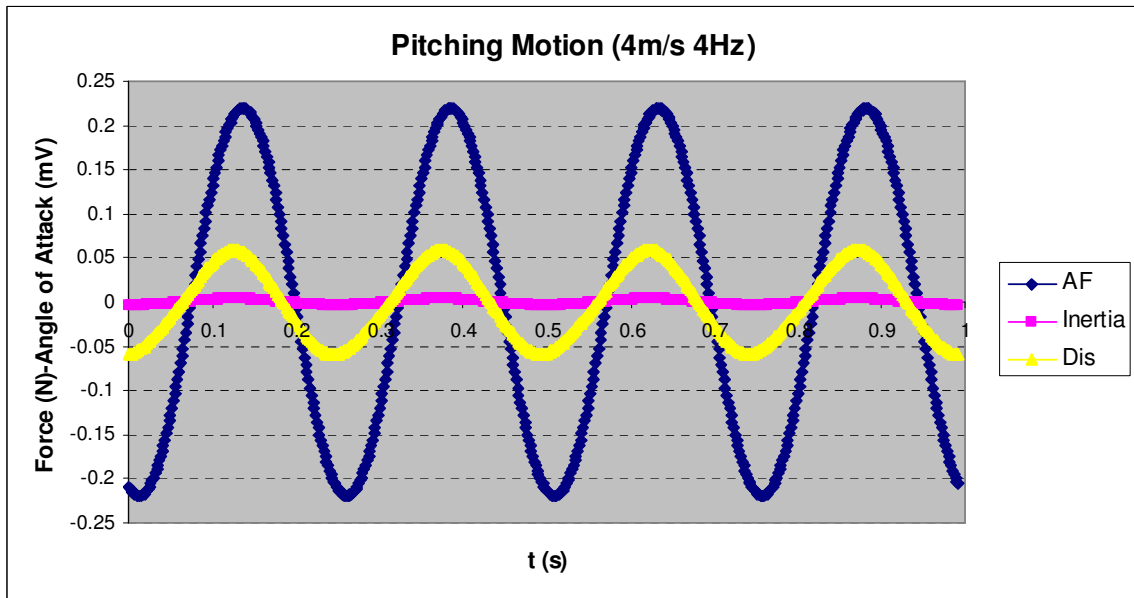


Figure A32 Test result of pitching motion at 4m/s, 4Hz



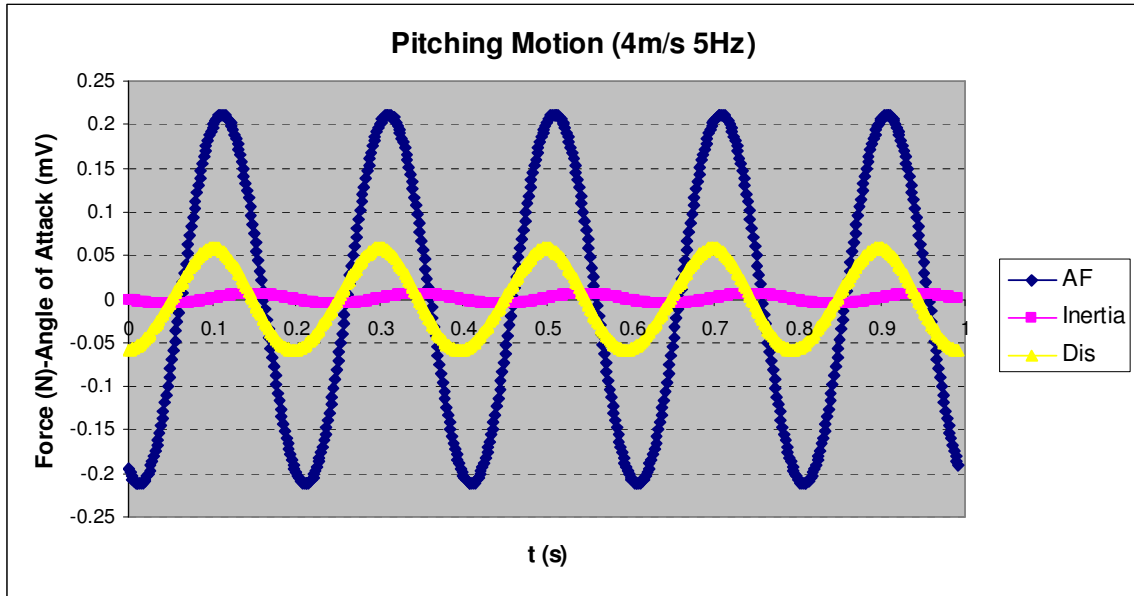


Figure A33 Test result of pitching motion at 4m/s, 5Hz

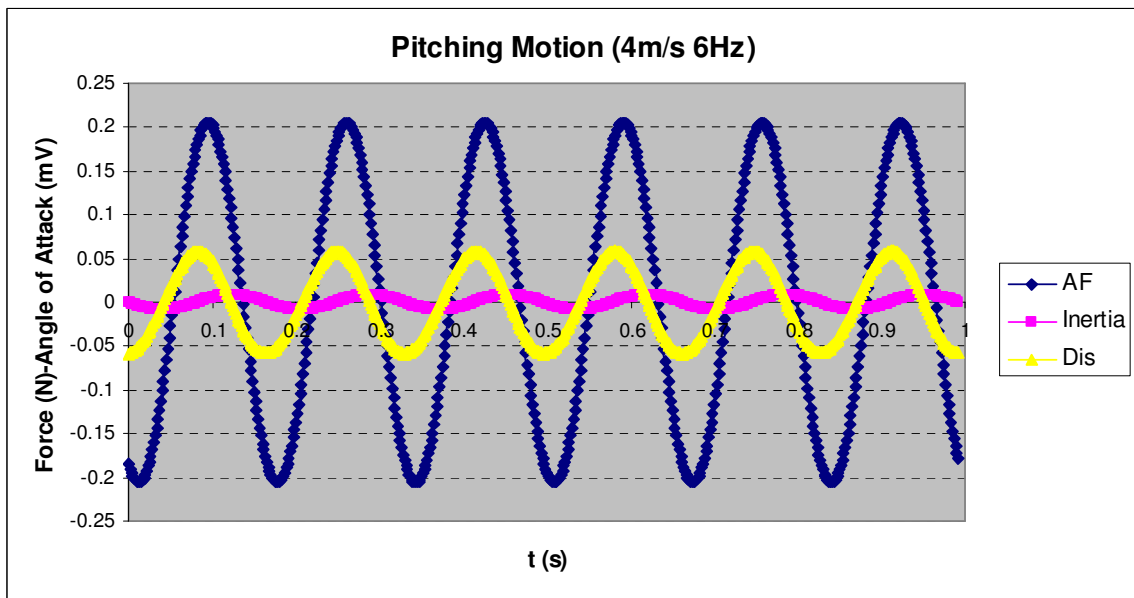


Figure A34 Test result of pitching motion at 4m/s, 6Hz

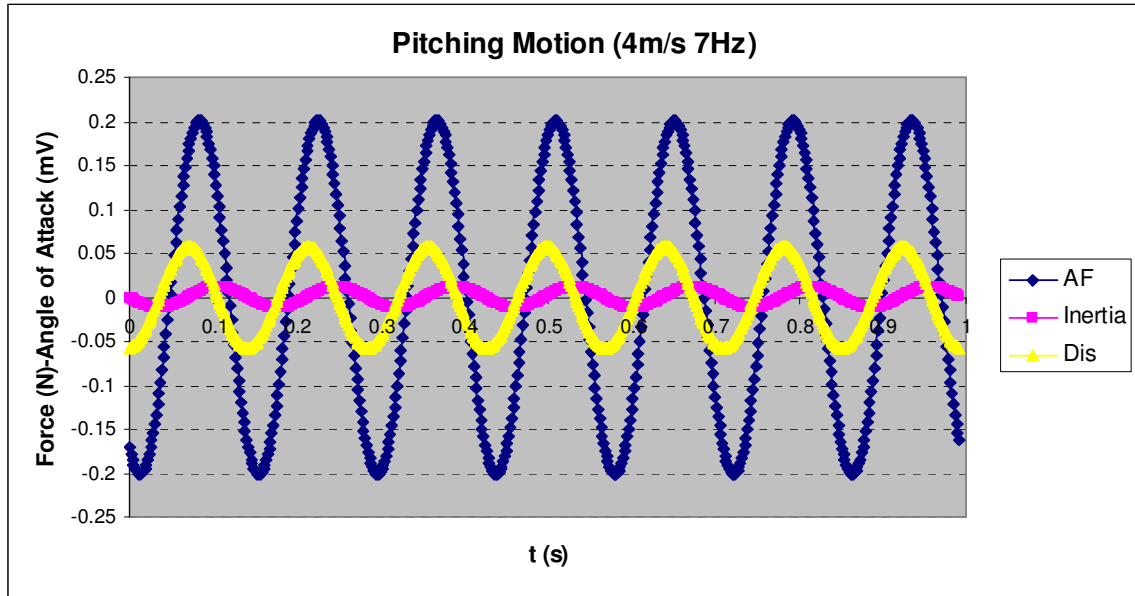


Figure A35 Test result of pitching motion at 4m/s, 7Hz

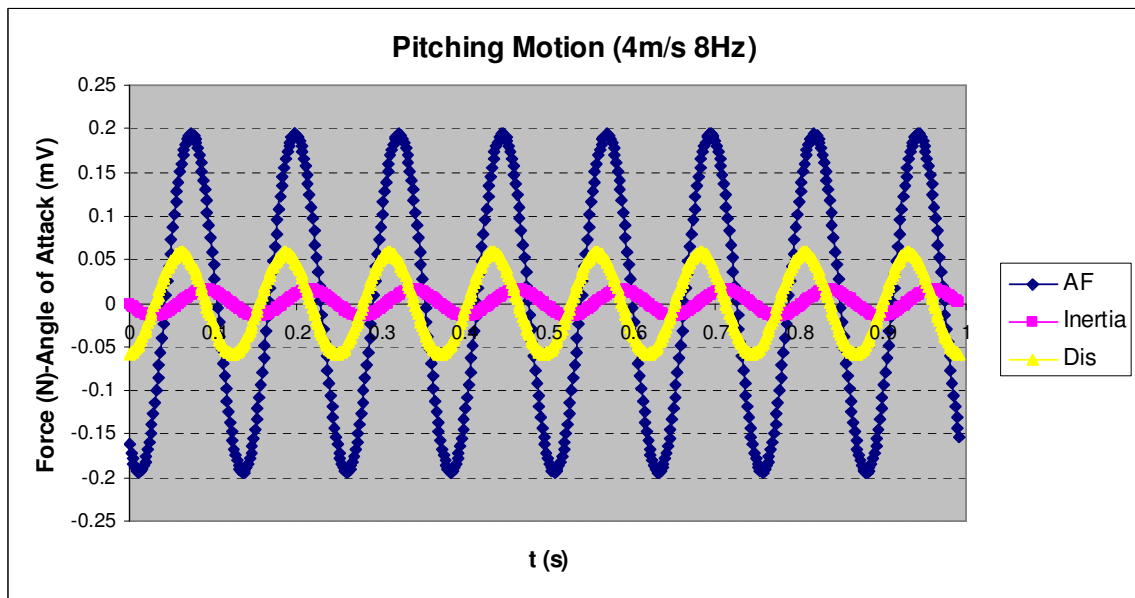


Figure A36 Test result of pitching motion at 4m/s, 8Hz

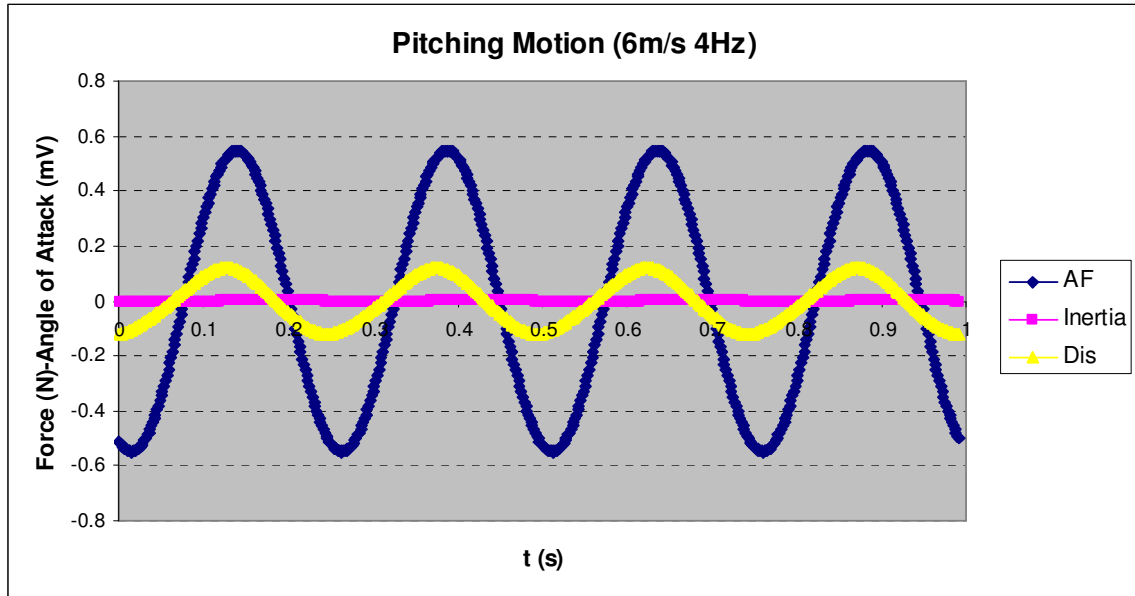


Figure A37 Test result of pitching motion at 6m/s, 4Hz

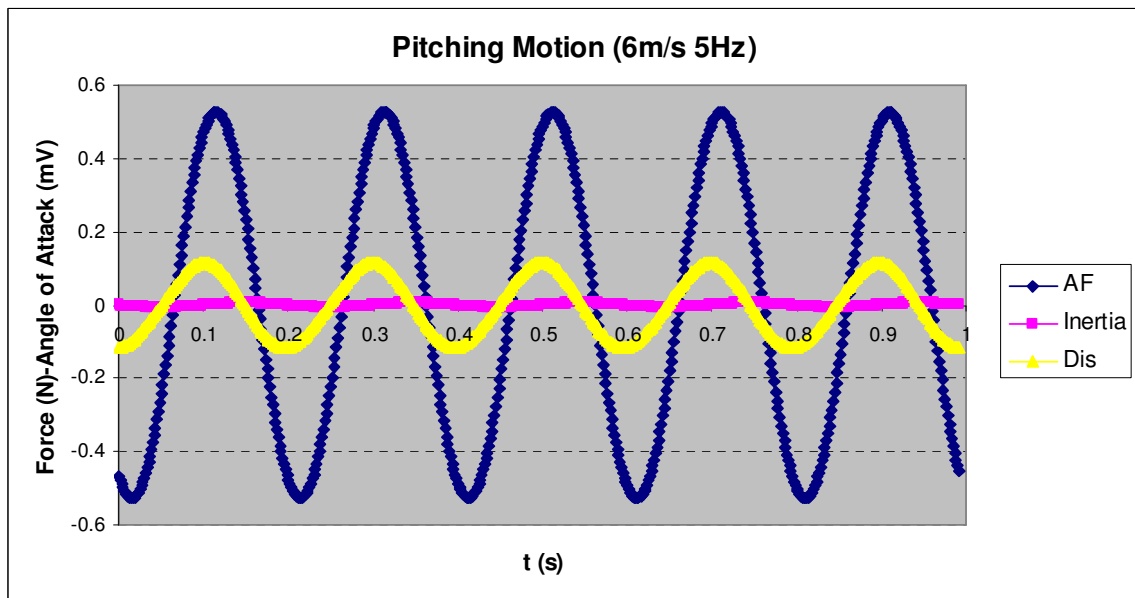


Figure A38 Test result of pitching motion at 6m/s, 5Hz

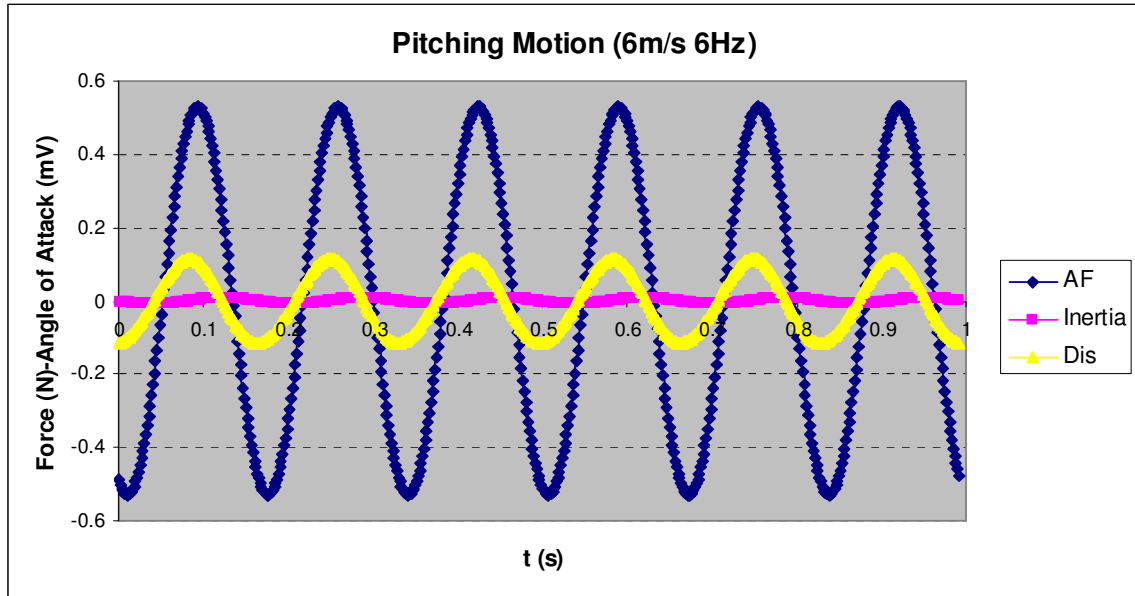


Figure A39 Test result of pitching motion at 6m/s, 6Hz

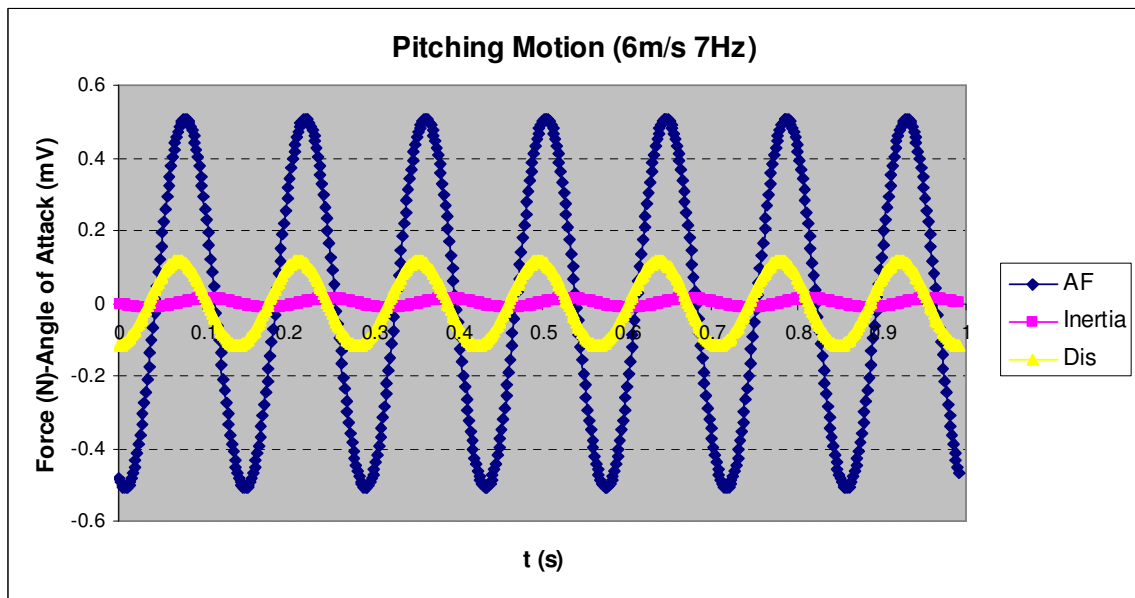


Figure A40 Test result of pitching motion at 6m/s, 7Hz

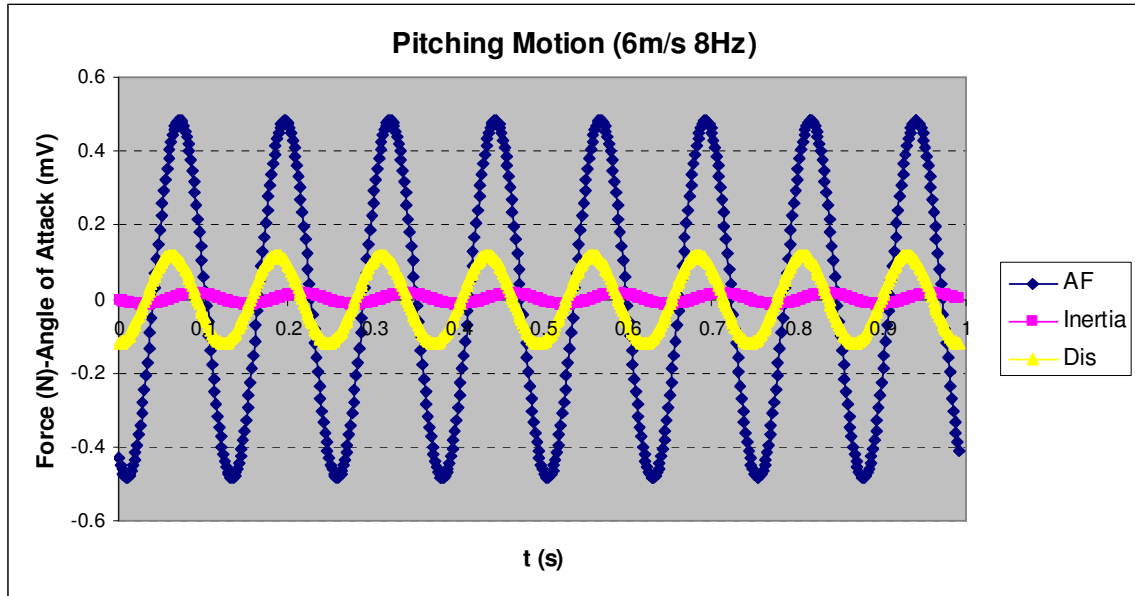


Figure A41 Test result of pitching motion at 6m/s, 8Hz

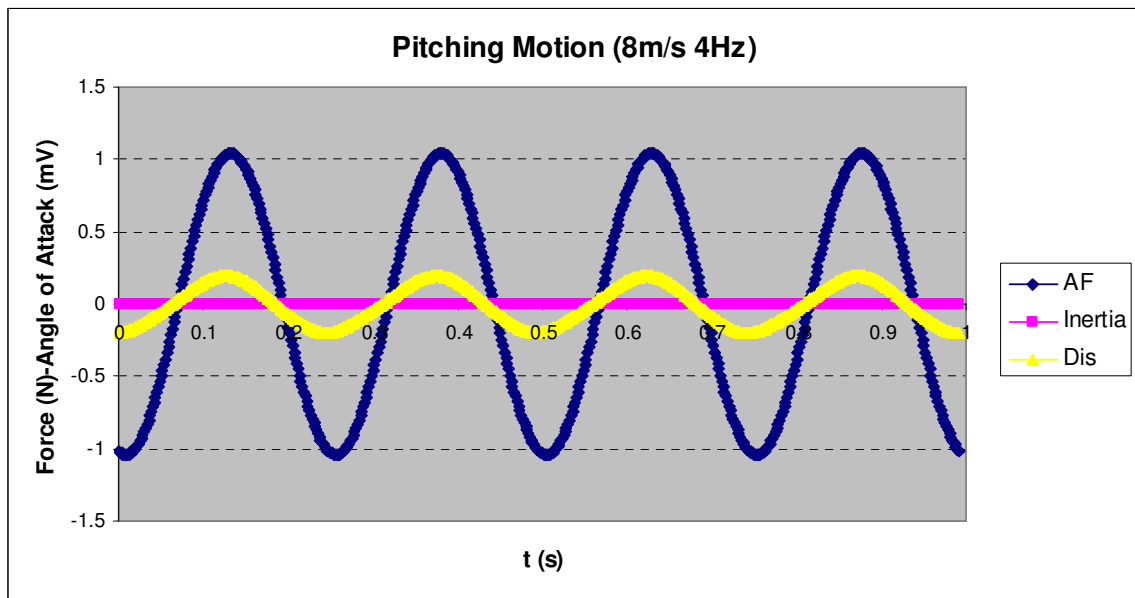


Figure A42 Test result of pitching motion at 8m/s, 4Hz

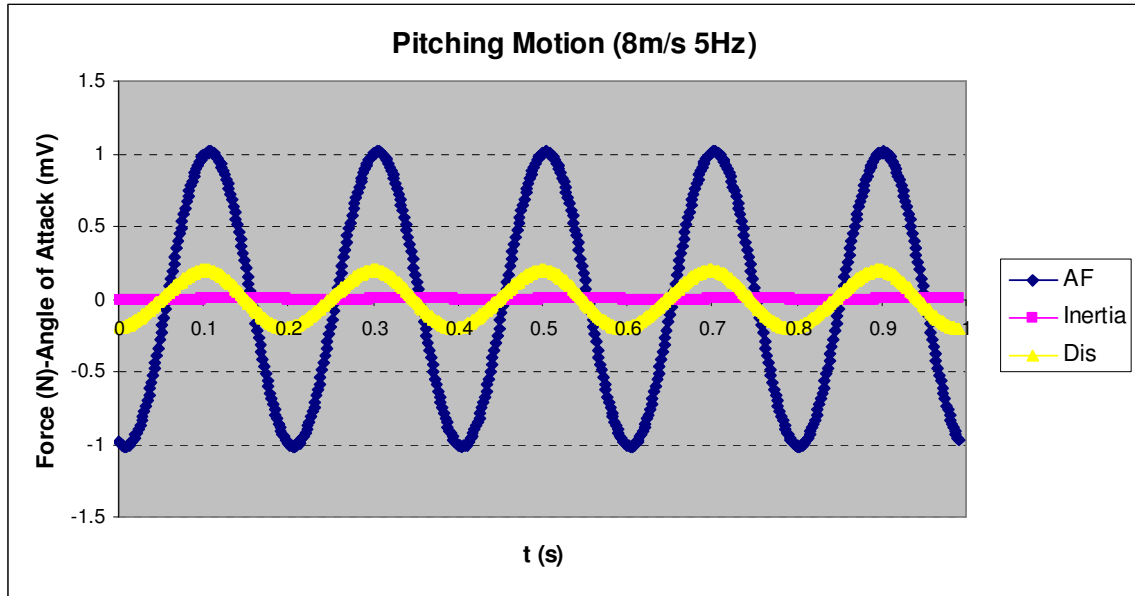


Figure A43 Test result of pitching motion at 8m/s, 5Hz

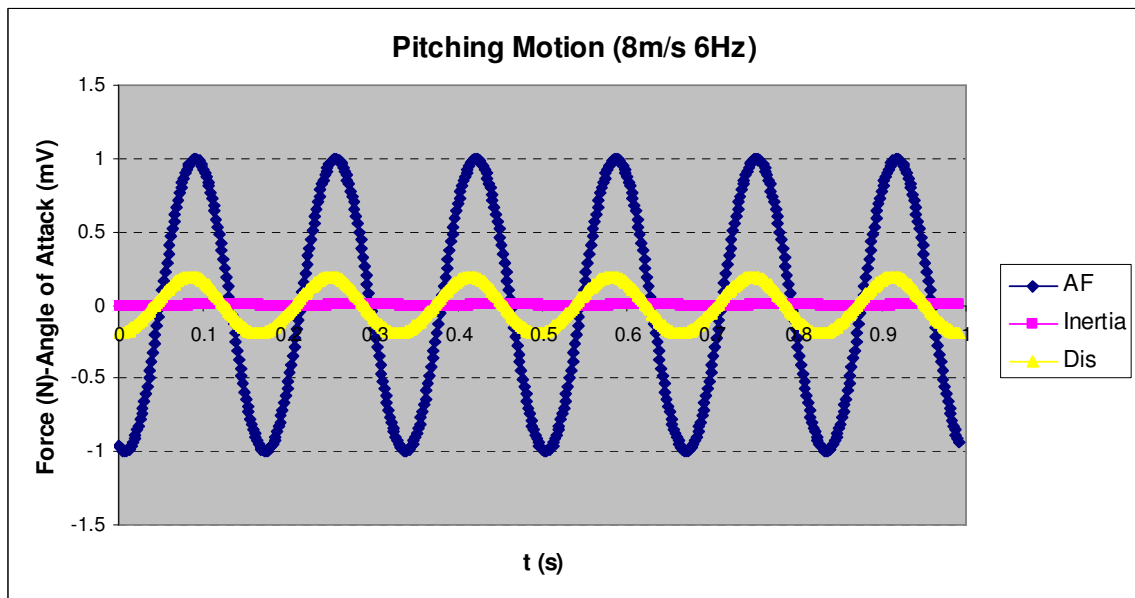


Figure A44 Test result of pitching motion at 8m/s, 6Hz

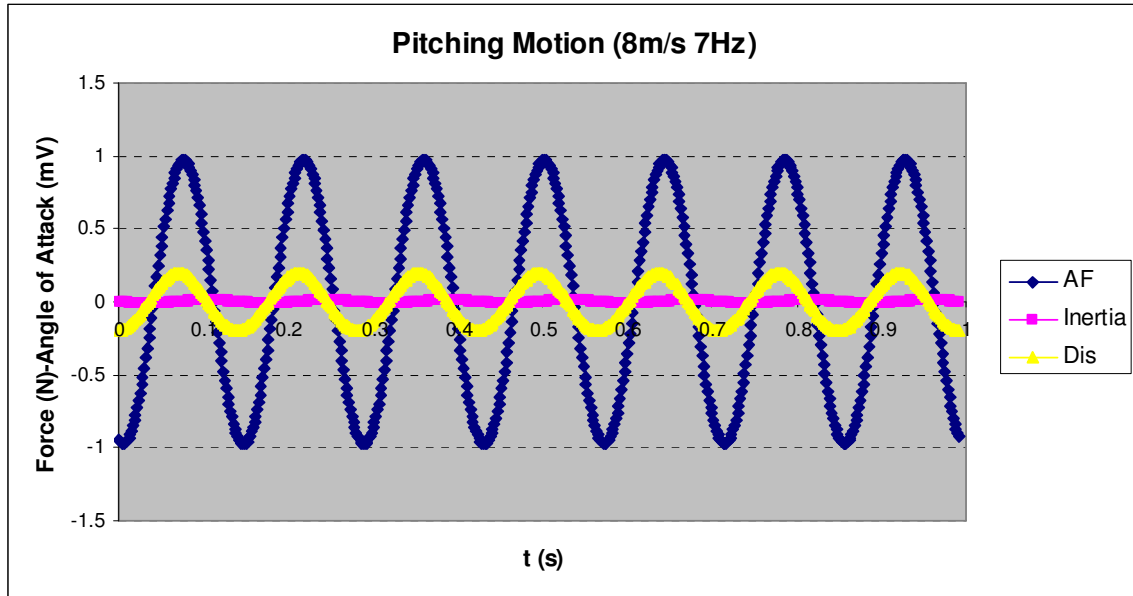


Figure A45 Test result of pitching motion at 8m/s, 7Hz

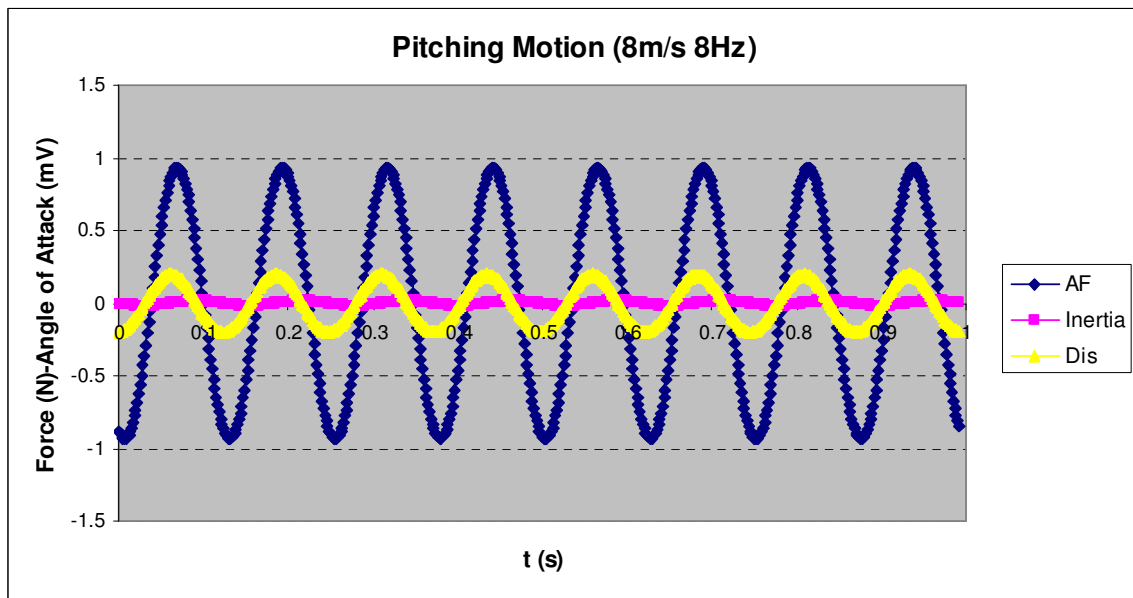


Figure A46 Test result of pitching motion at 8m/s, 8Hz

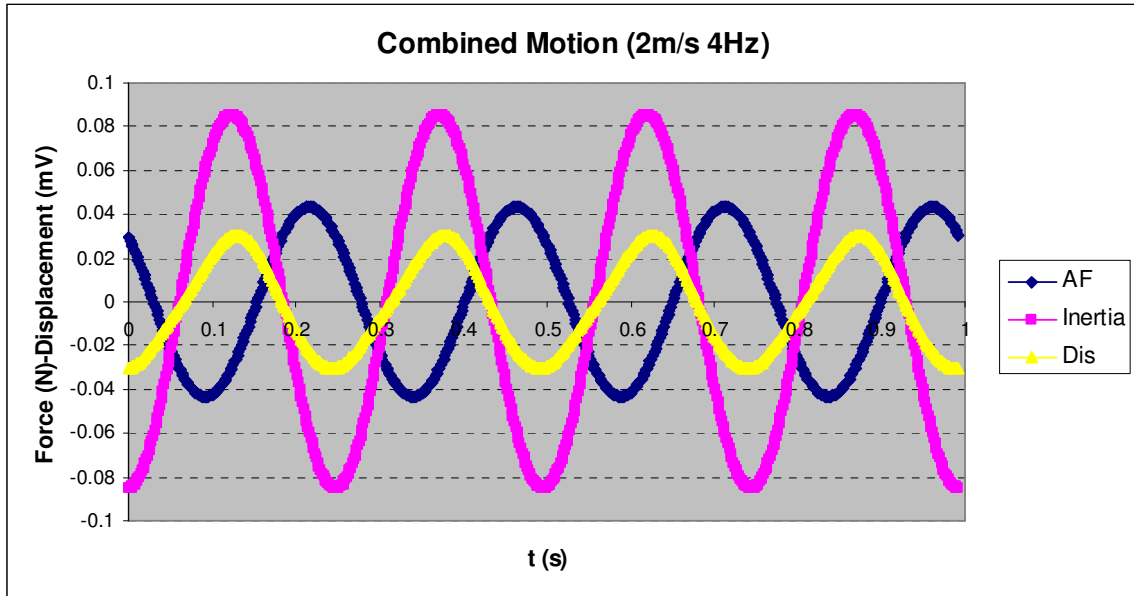


Figure A47 Test result of combined motion at 2m/s, 4Hz

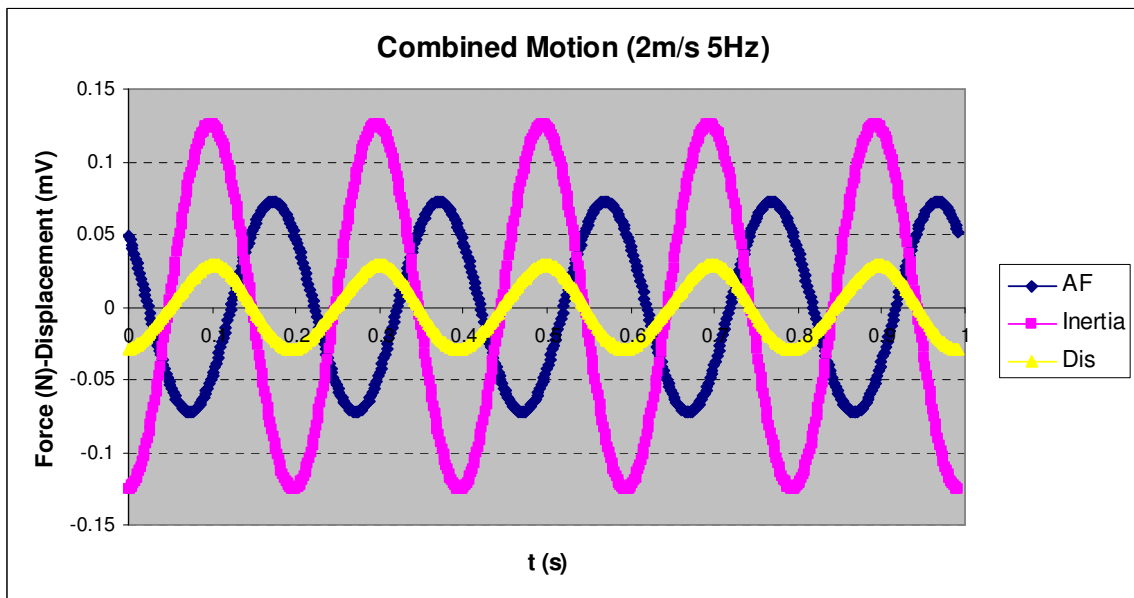


Figure A48 Test result of combined motion at 2m/s, 5Hz



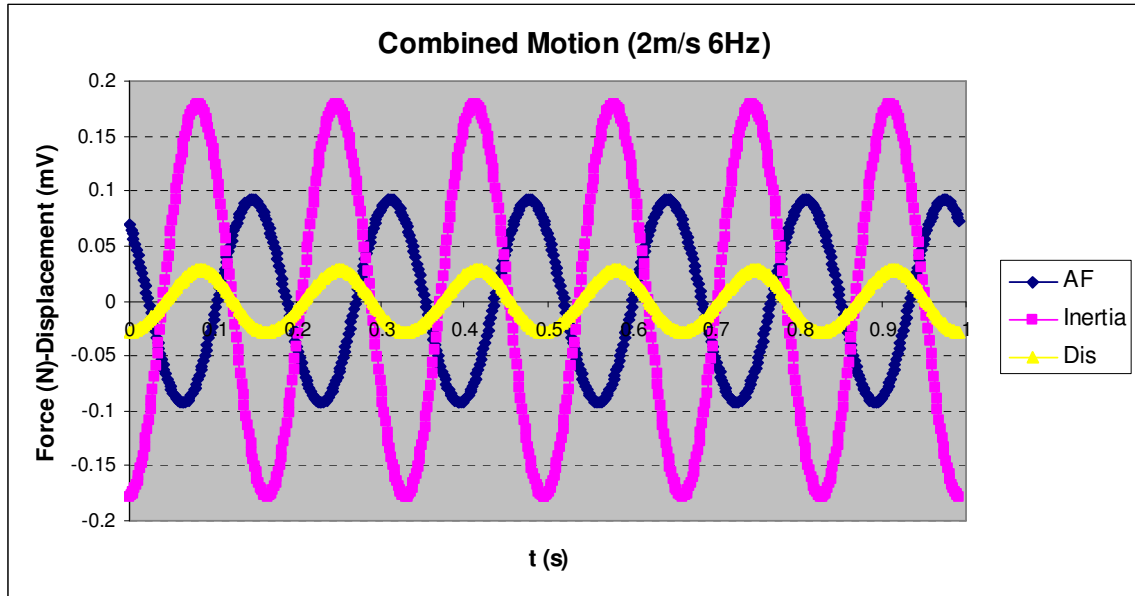


Figure A49 Test result of combined motion at 2m/s, 6Hz

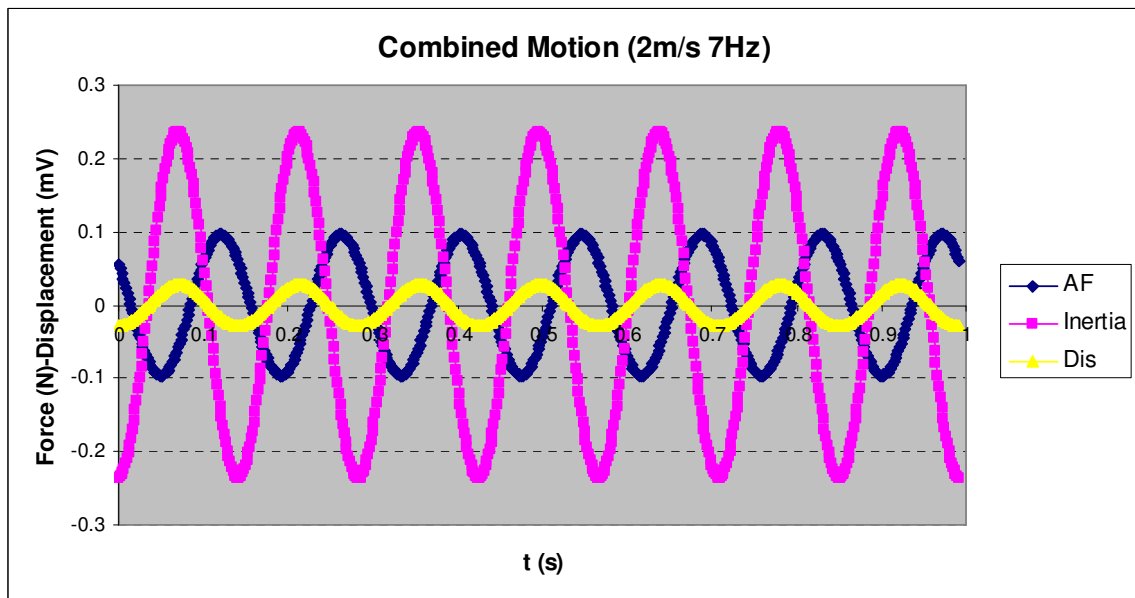


Figure A50 Test result of combined motion at 2m/s, 7Hz

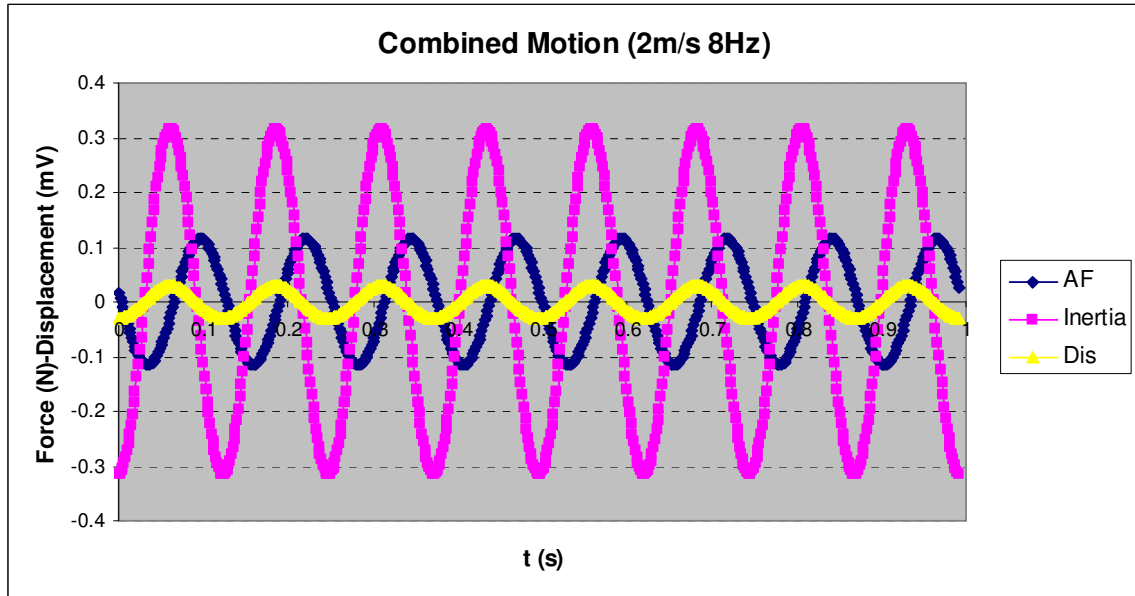


Figure A51 Test result of combined motion at 2m/s, 8Hz

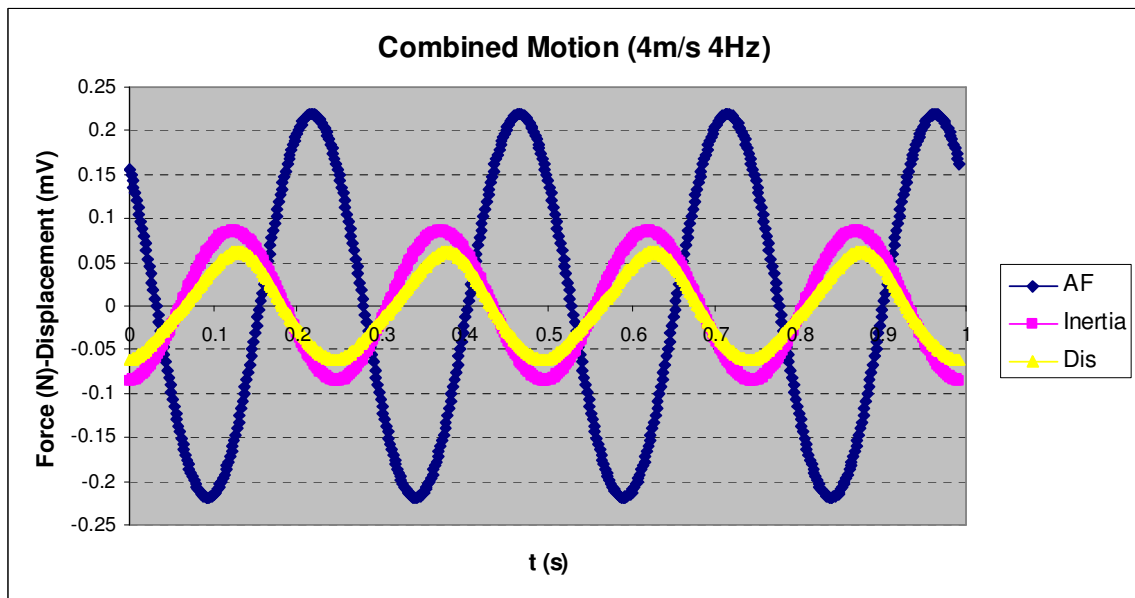


Figure A52 Test result of combined motion at 4m/s, 4Hz

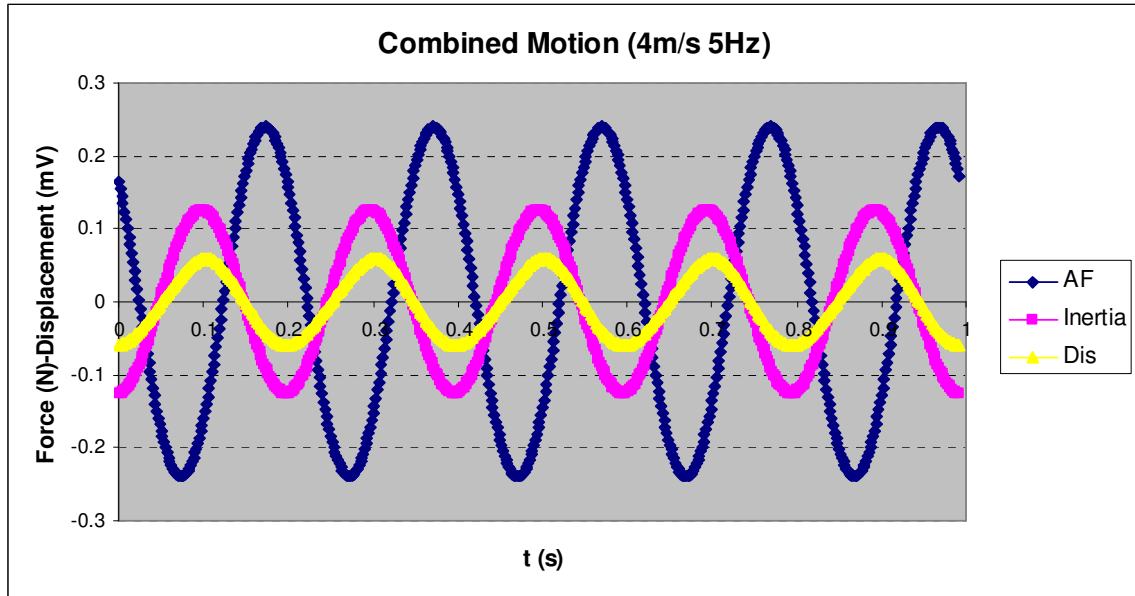


Figure A53 Test result of combined motion at 4m/s, 5Hz

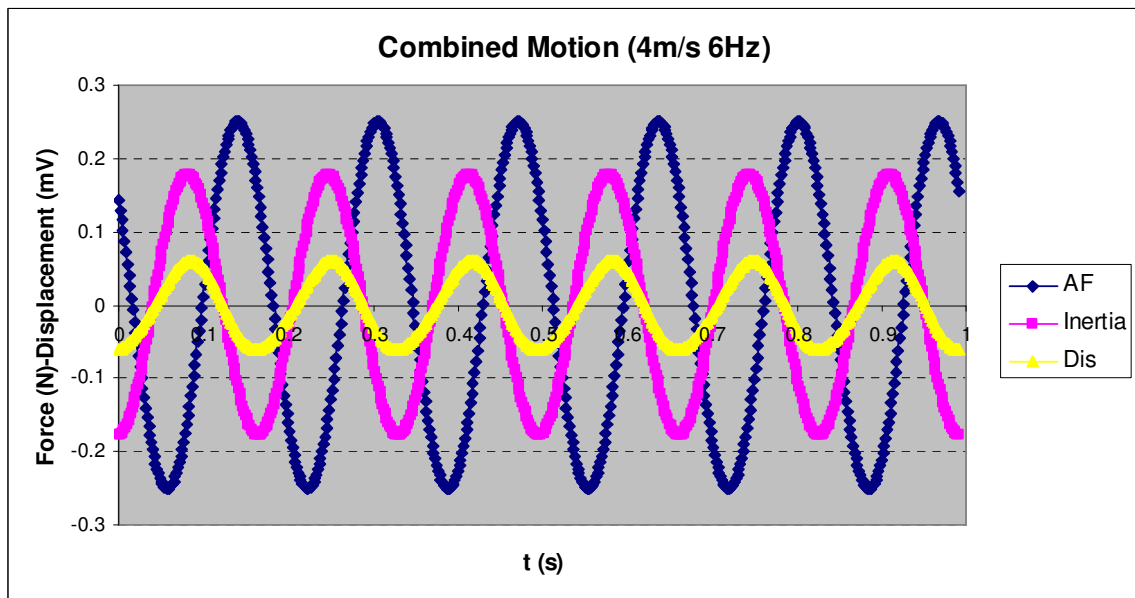


Figure A54 Test result of combined motion at 4m/s, 6Hz

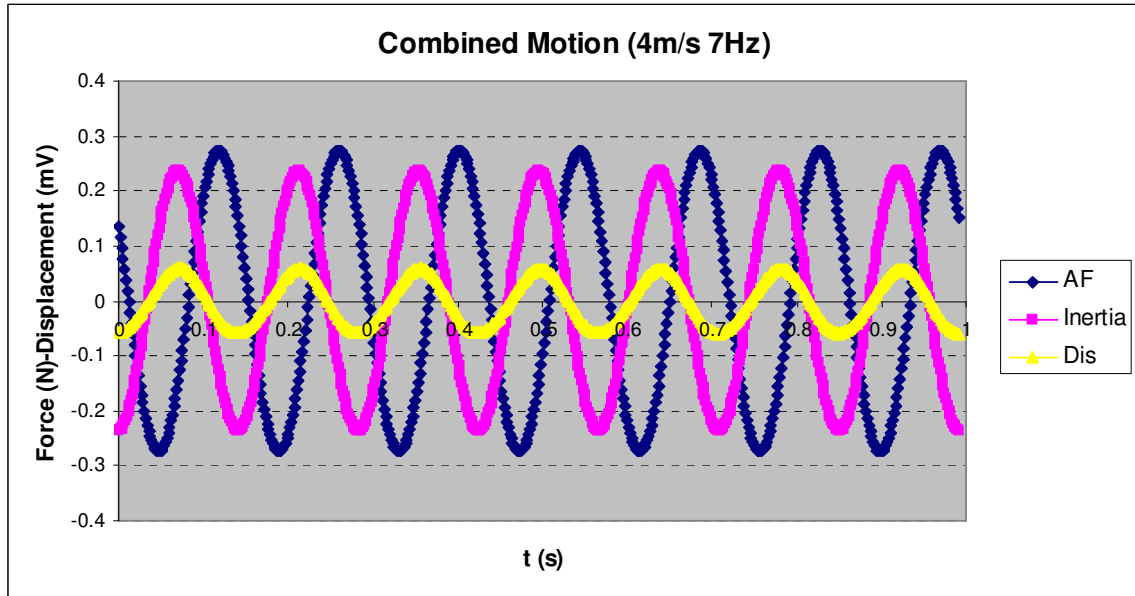


Figure A55 Test result of combined motion at 4m/s, 7Hz

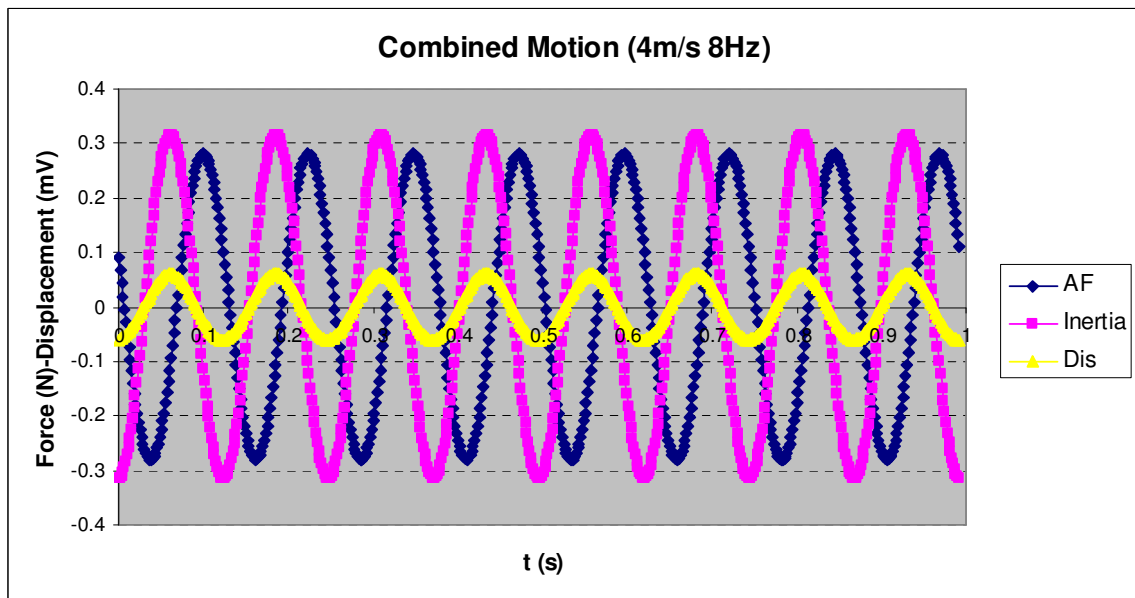


Figure A56 Test result of combined motion at 4m/s, 8Hz

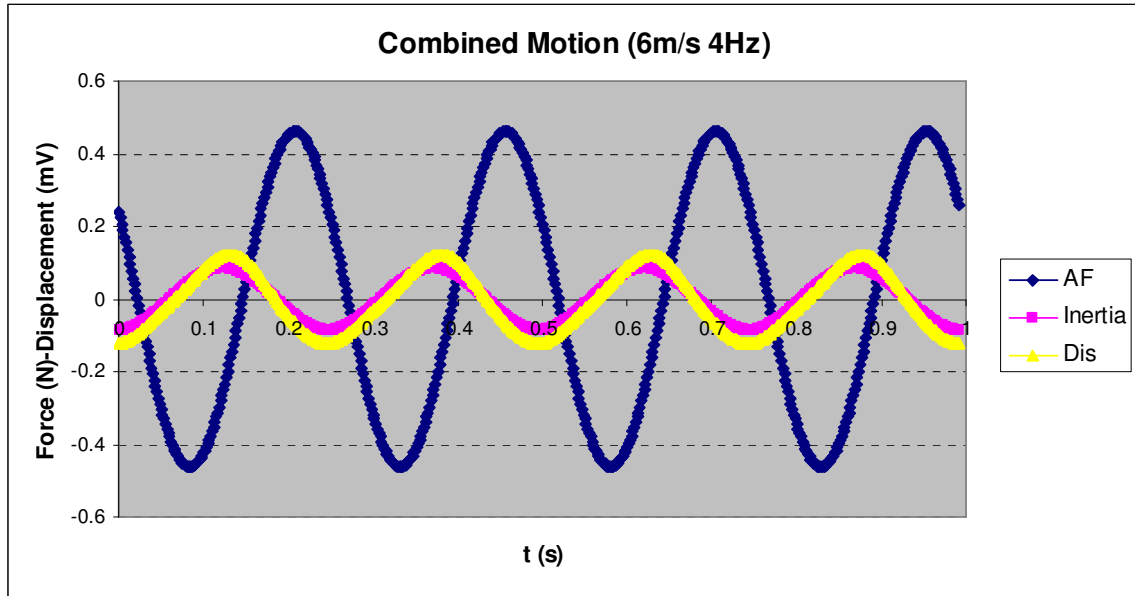


Figure A57 Test result of combined motion at 6m/s, 4Hz

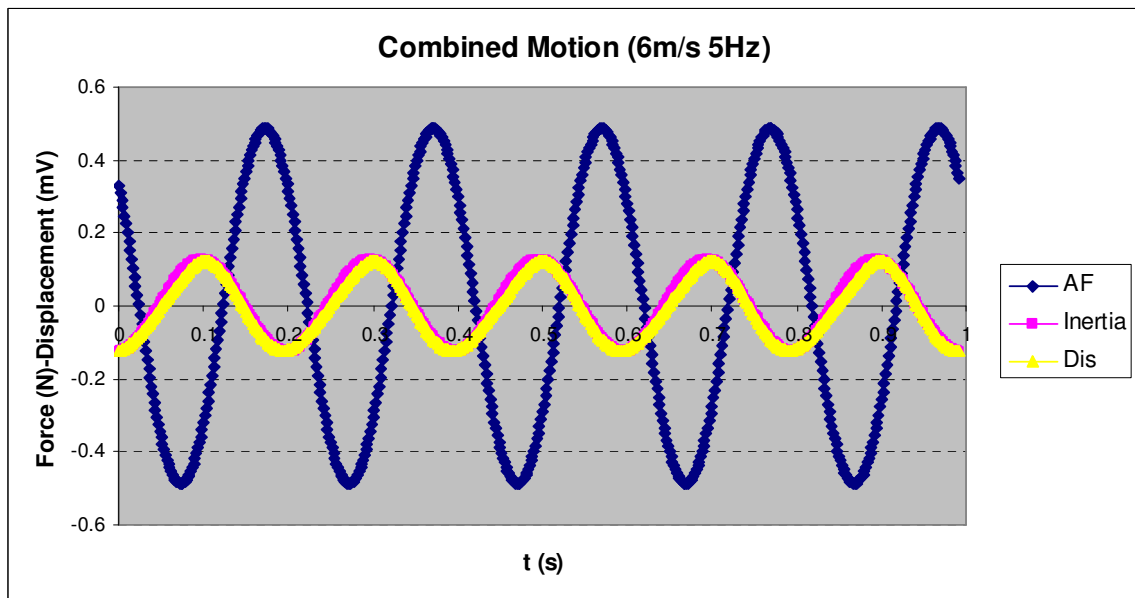


Figure A58 Test result of combined motion at 6m/s, 5Hz

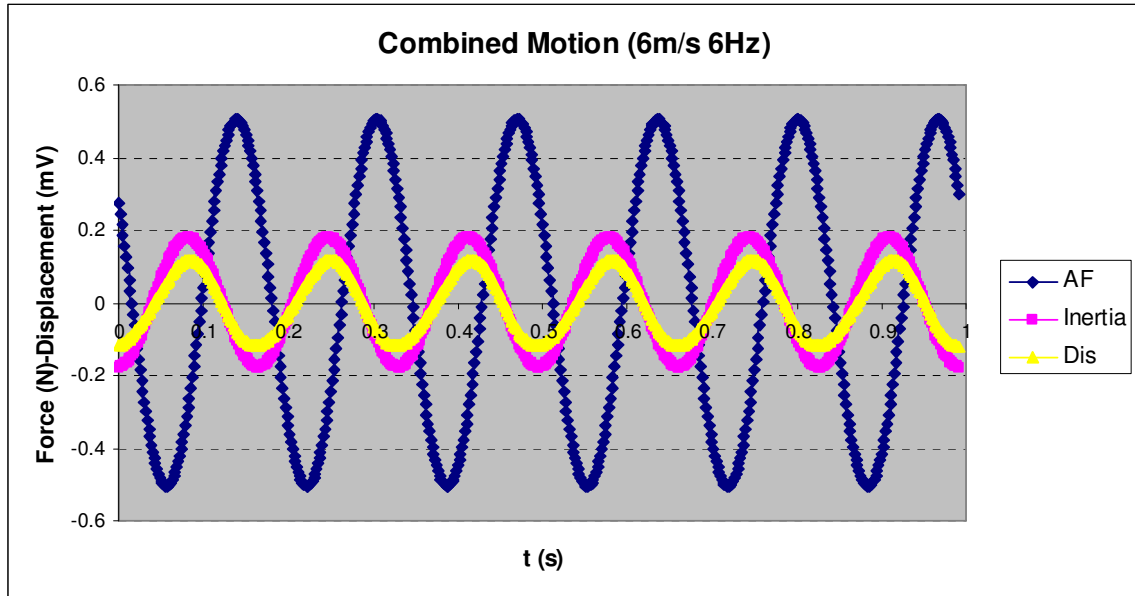


Figure A59 Test result of combined motion at 6m/s, 6Hz

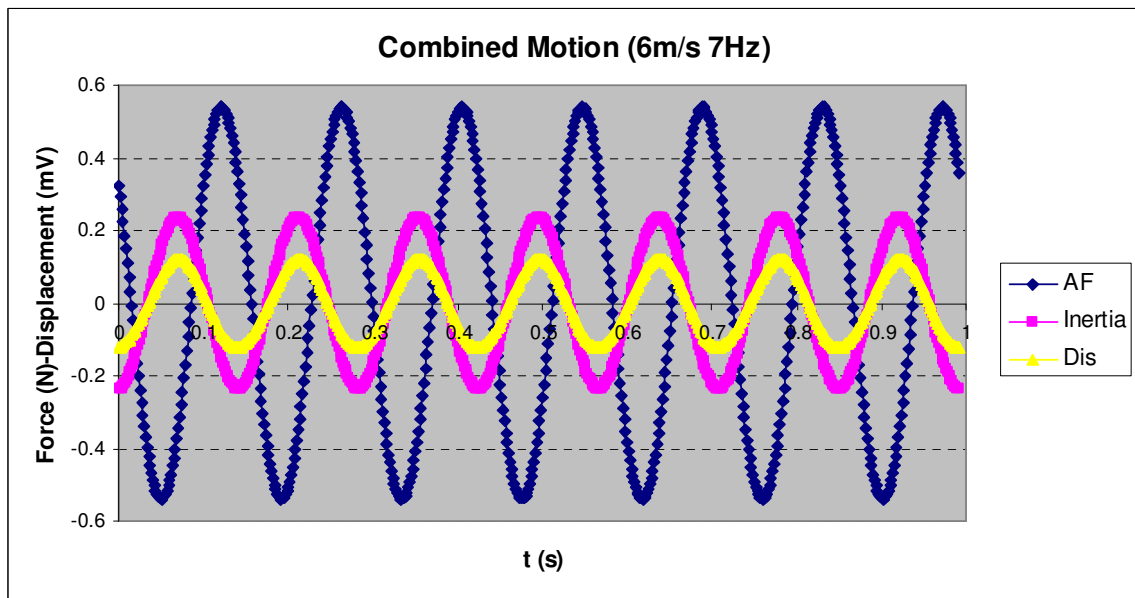


Figure A60 Test result of combined motion at 6m/s, 7Hz

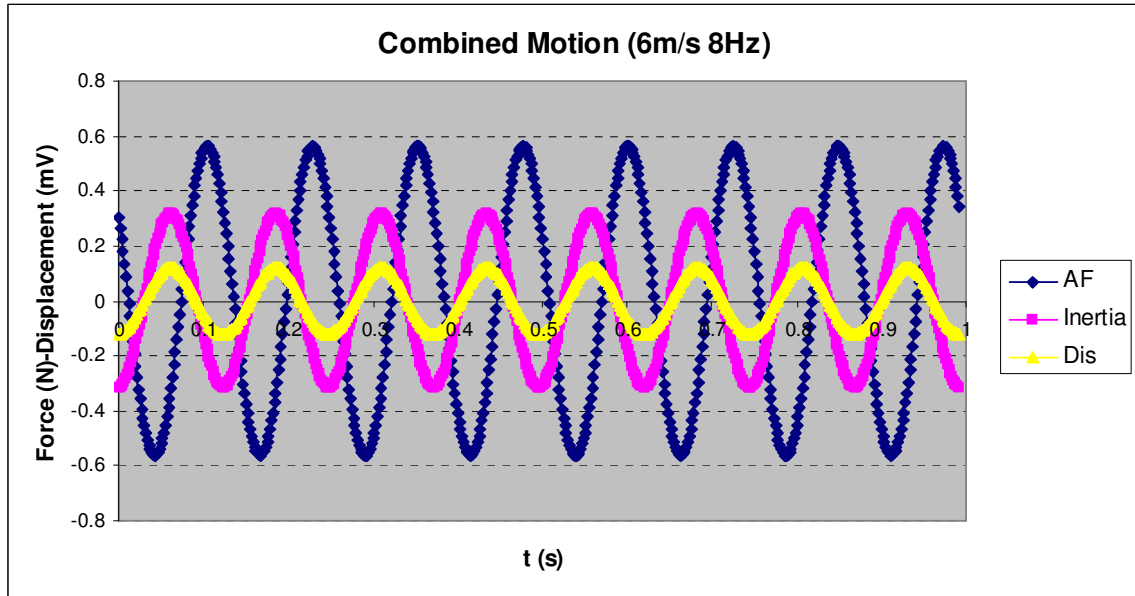


Figure A61 Test result of combined motion at 6m/s, 8Hz

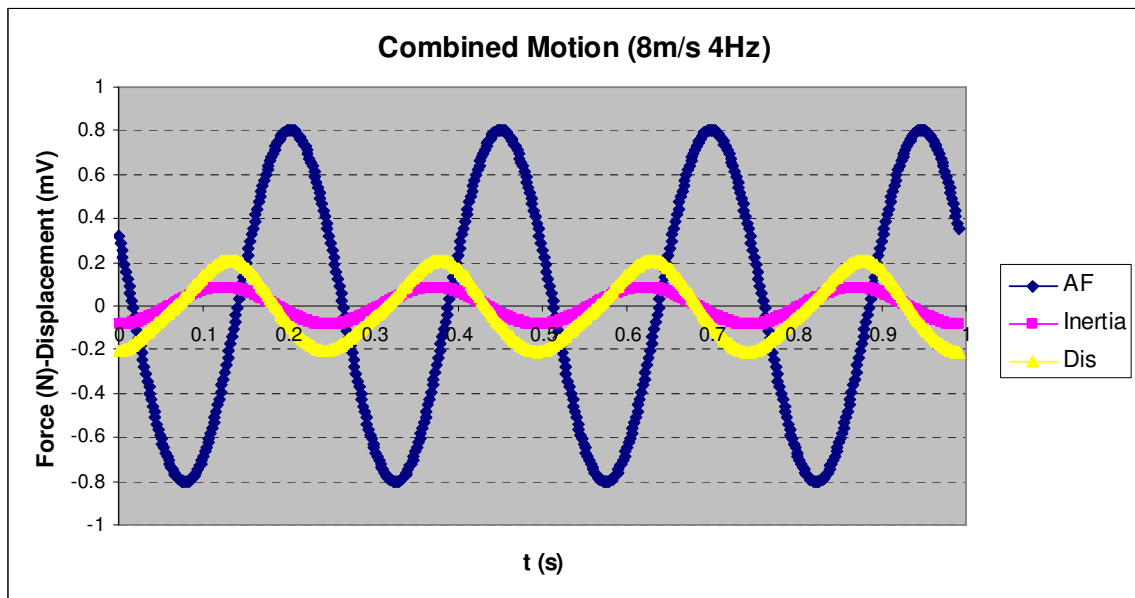


Figure A62 Test result of combined motion at 8m/s, 4Hz

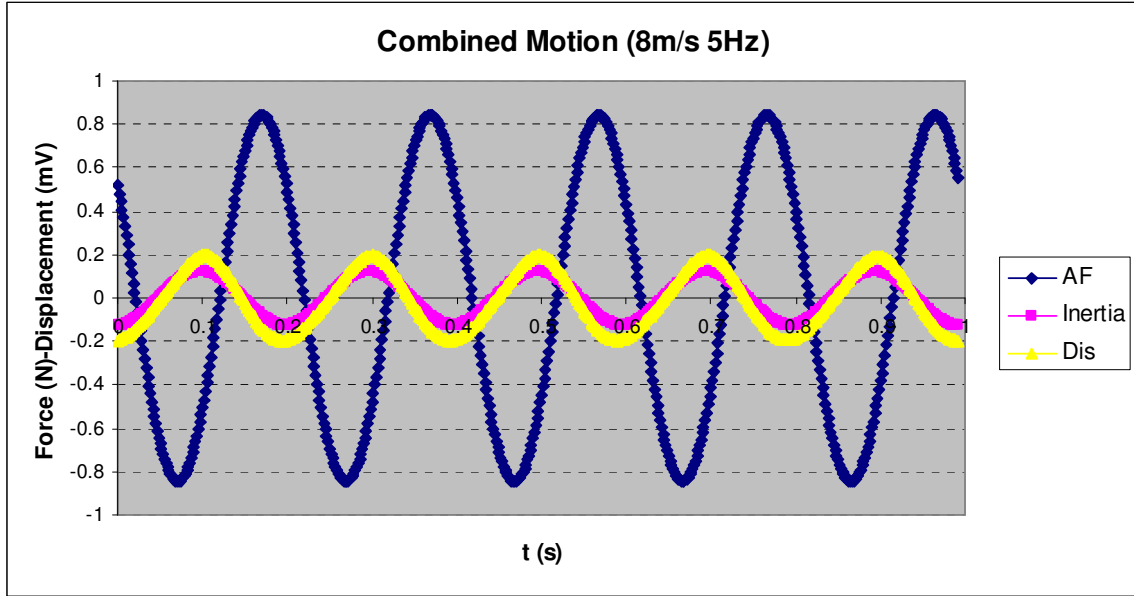


Figure A63 Test result of combined motion at 8m/s, 5Hz

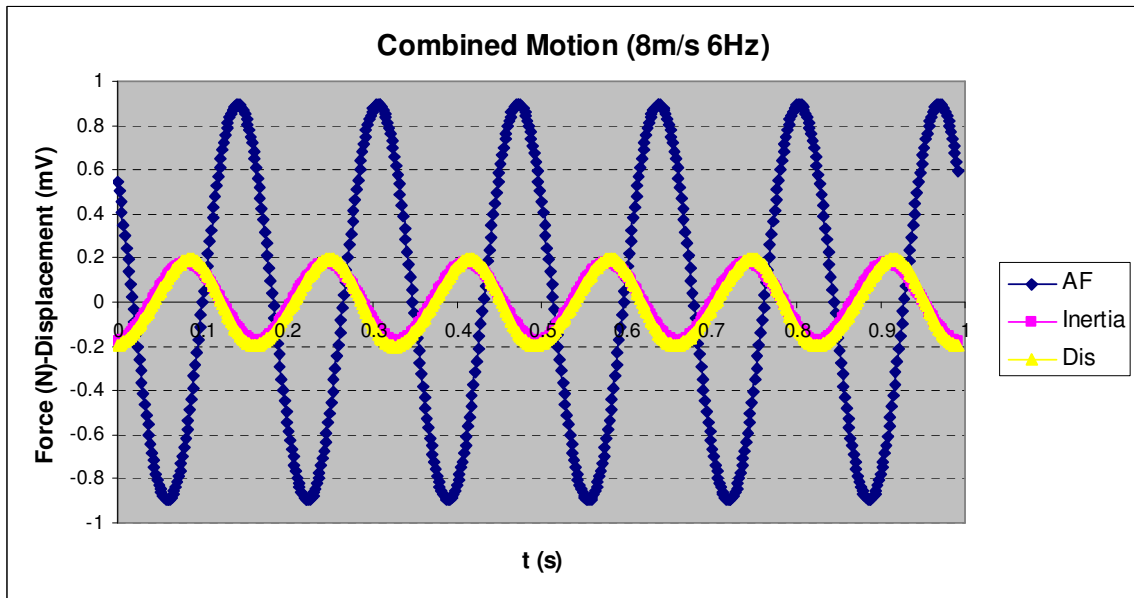


Figure A64 Test result of combined motion at 8m/s, 6Hz



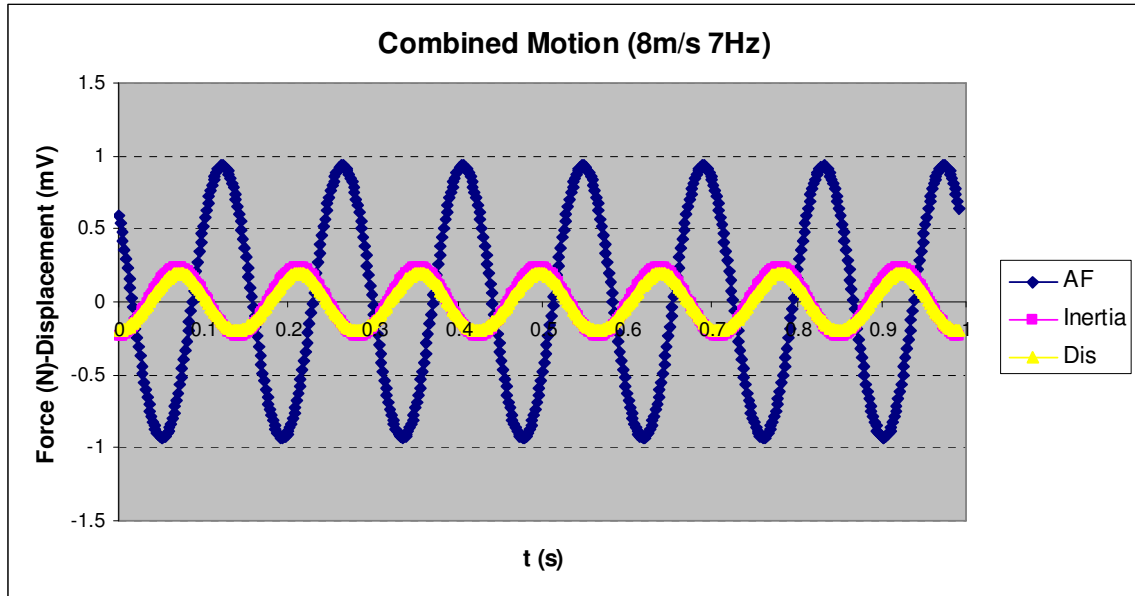


Figure A65 Test result of combined motion at 8m/s, 7Hz

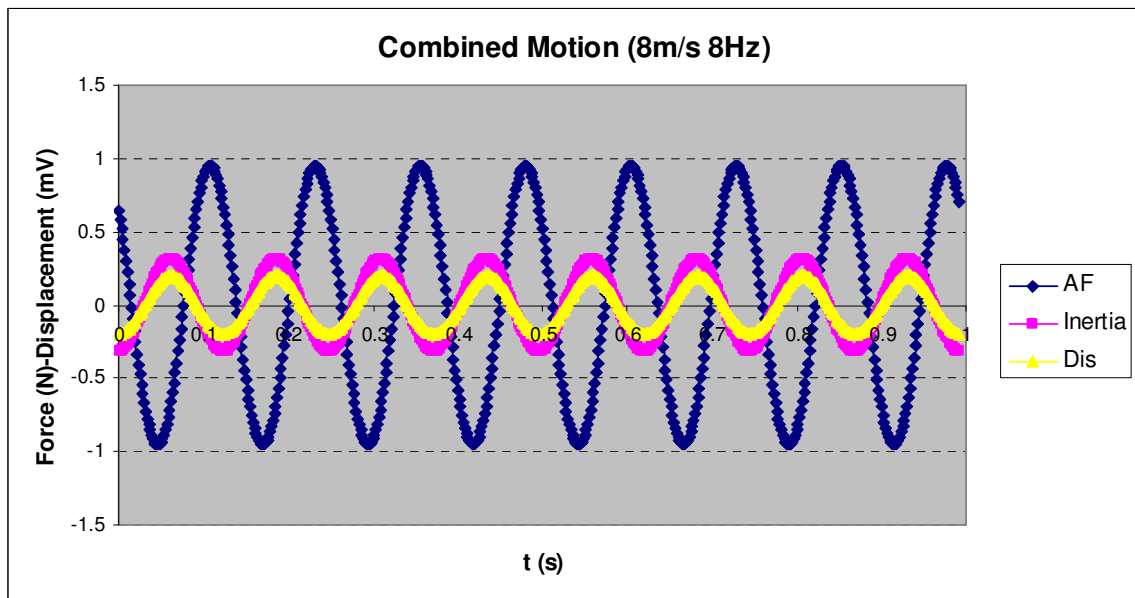


Figure A66 Test result of combined motion at 8m/s, 8Hz

**APPENDIX B**

Test Result of Wing 1			
V (m/s)	Lift (N)	Drag (N)	Power (W)
2	0.264	-0.031	3.177
4	0.347	-0.013	2.997
6	0.379	0.009	2.772
8	0.381	0.059	2.637

Table B1 Test result of wing 1

Test Result of Wing 1A			
V (m/s)	Lift (N)	Drag (N)	Power (W)
2	0.229	-0.037	2.367
4	0.228	-0.009	2.007
6	0.209	0.032	1.647
8	0.199	0.072	1.422

Table B2 Test result of wing 1A

Test Result of Wing 1B			
V (m/s)	Lift (N)	Drag (N)	Power (W)
2	0.322	-0.032	3.357
4	0.407	-0.014	3.222
6	0.435	0.011	3.087
8	0.448	0.052	2.862

Table B3 Test result of wing 1B

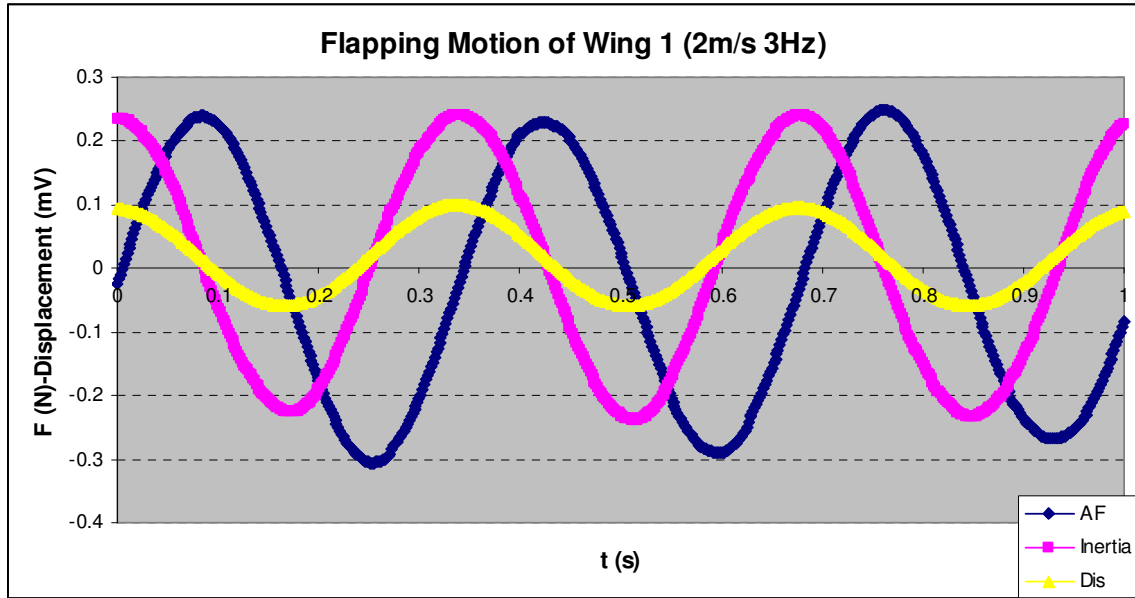


Figure B1 Test result of flapping motion of Wing 1 at 2m/s, 3Hz

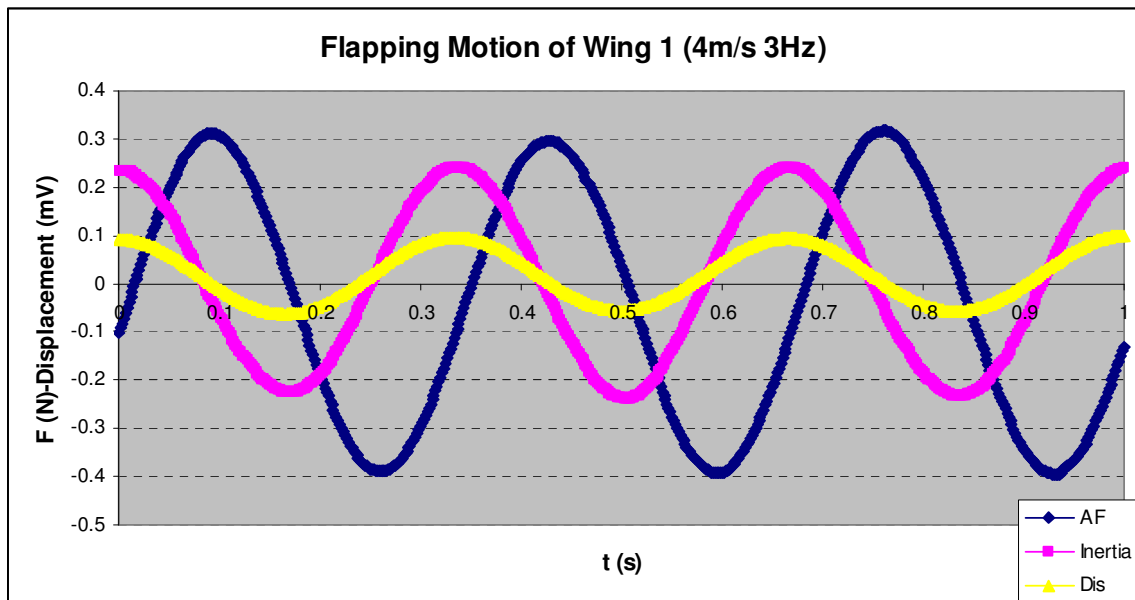


Figure B2 Test result of flapping motion of Wing 1 at 4m/s, 3Hz

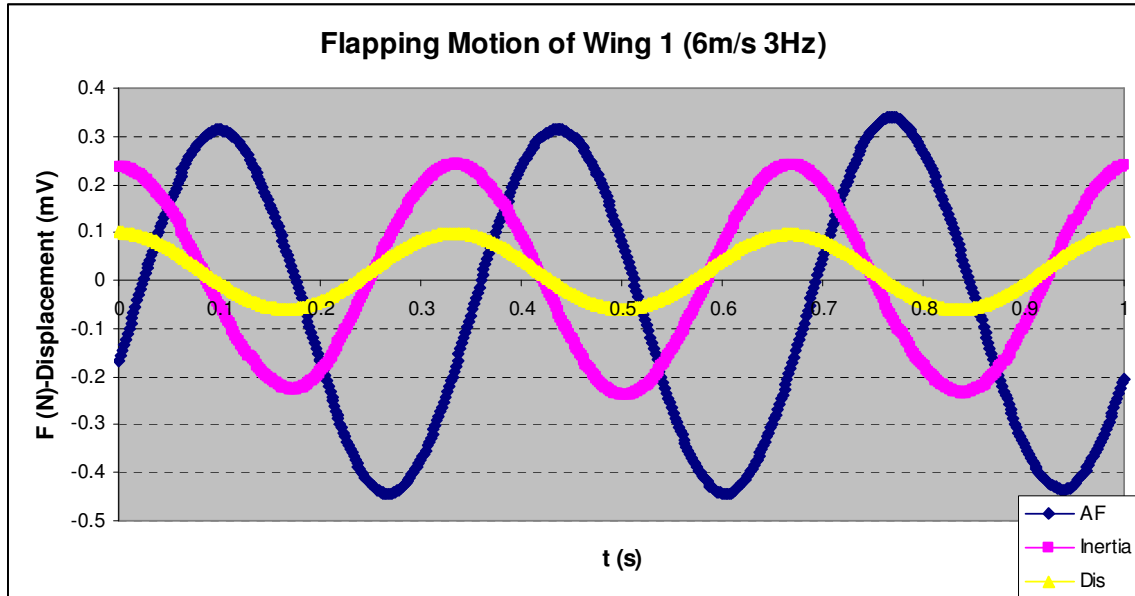


Figure B3 Test result of flapping motion of Wing 1 at 6m/s, 3Hz

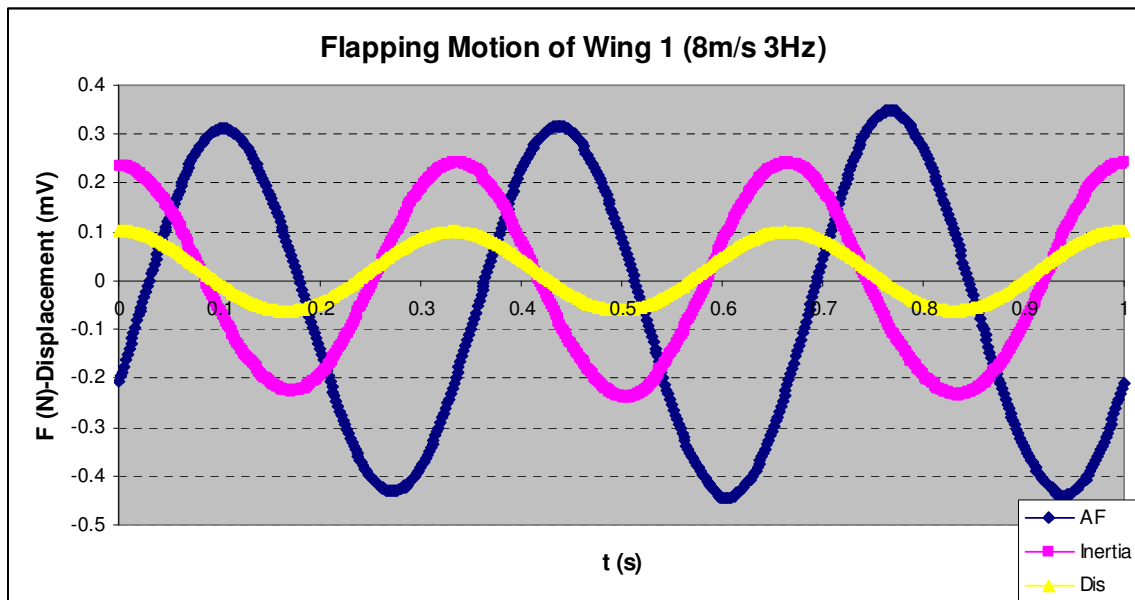


Figure B4 Test result of flapping motion of Wing 1 at 8m/s, 3Hz

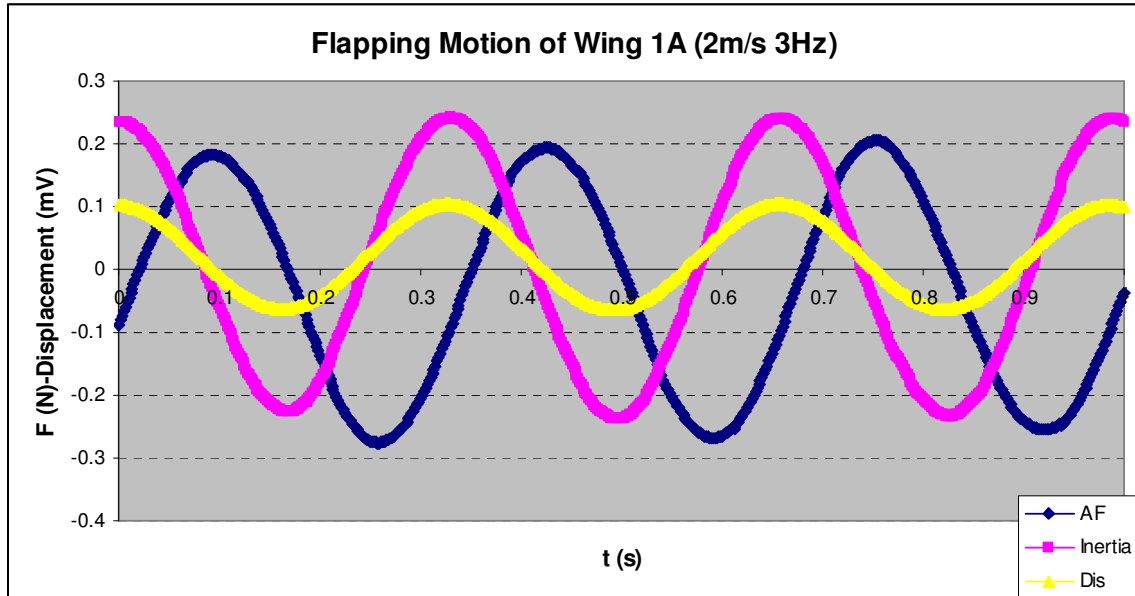


Figure B5 Test result of flapping motion of Wing 1A at 2m/s, 3Hz

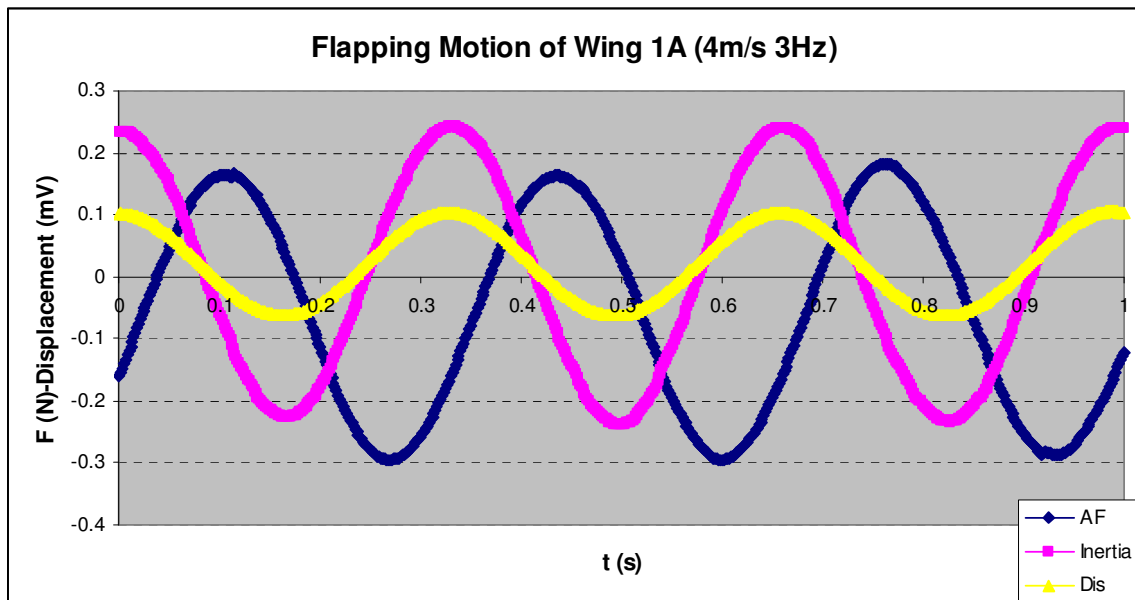


Figure B6 Test result of flapping motion of Wing 1A at 4m/s, 3Hz

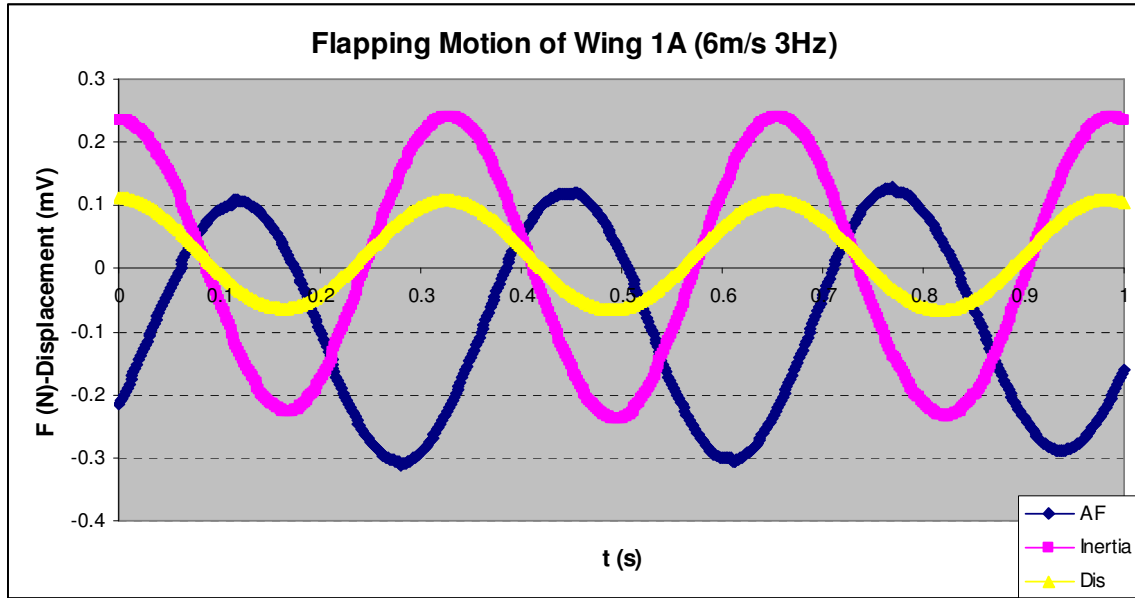


Figure B7 Test result of flapping motion of Wing 1A at 6m/s, 3Hz

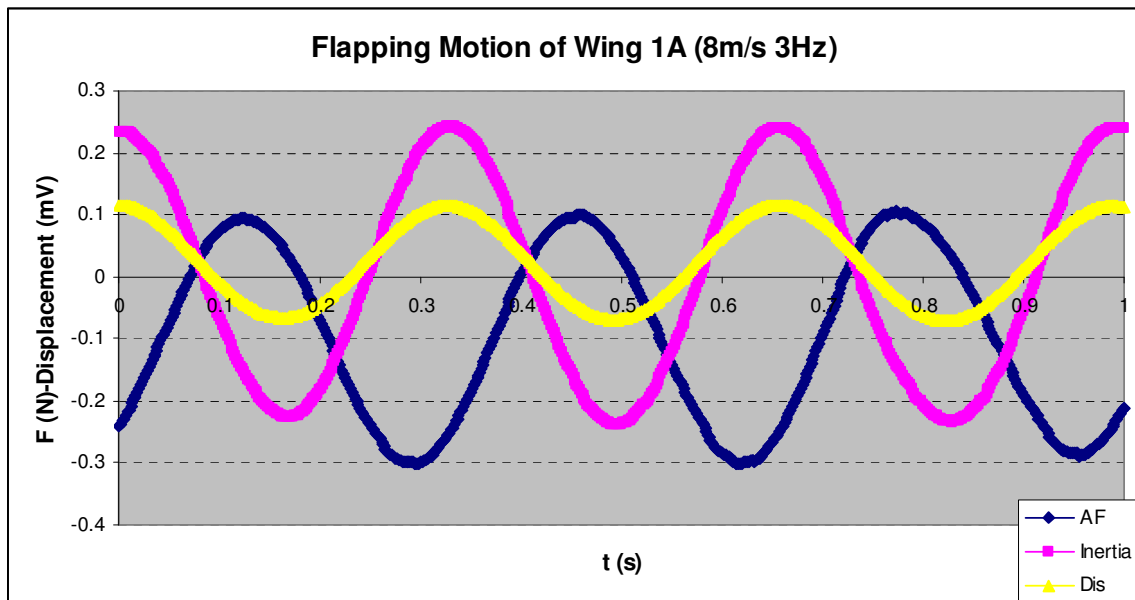


Figure B8 Test result of flapping motion of Wing 1A at 8m/s, 3Hz

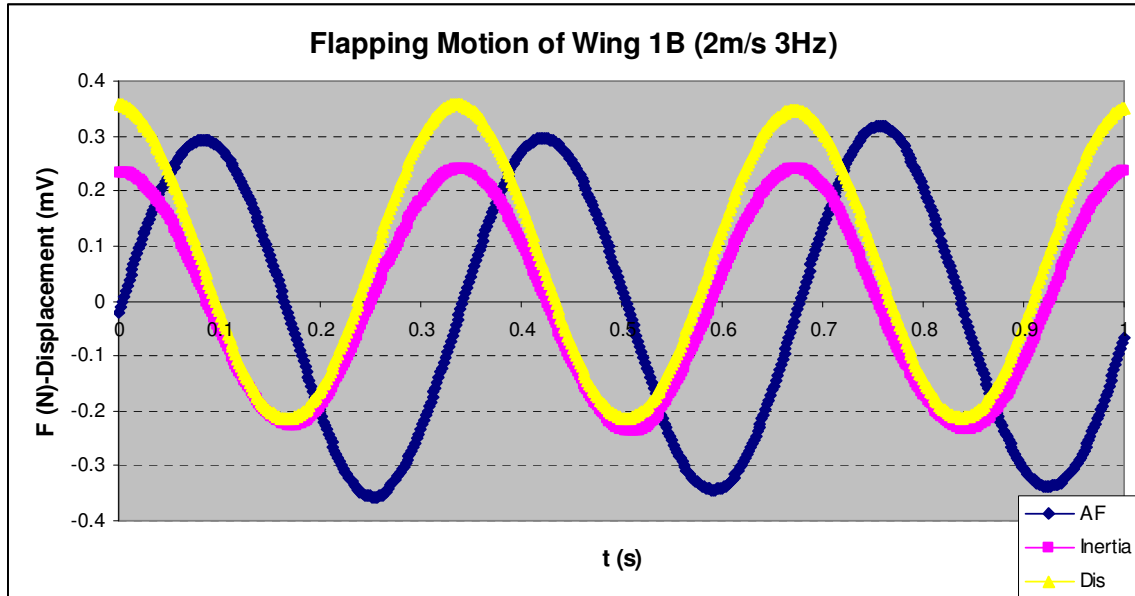


Figure B9 Test result of flapping motion of Wing 1B at 2m/s, 3Hz

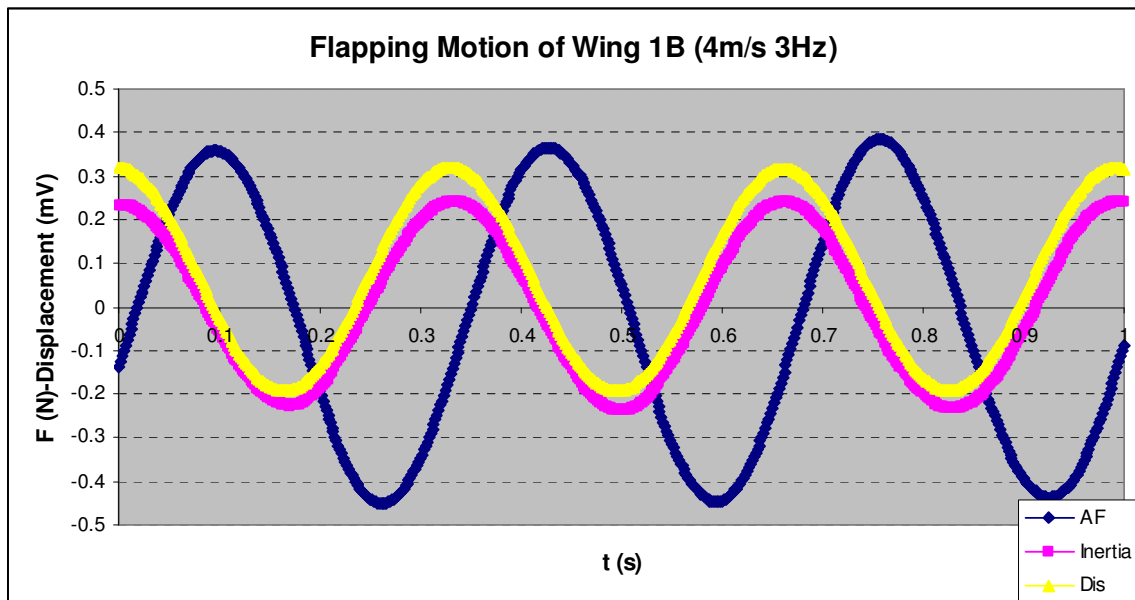


Figure B10 Test result of flapping motion of Wing 1B at 4m/s, 3Hz

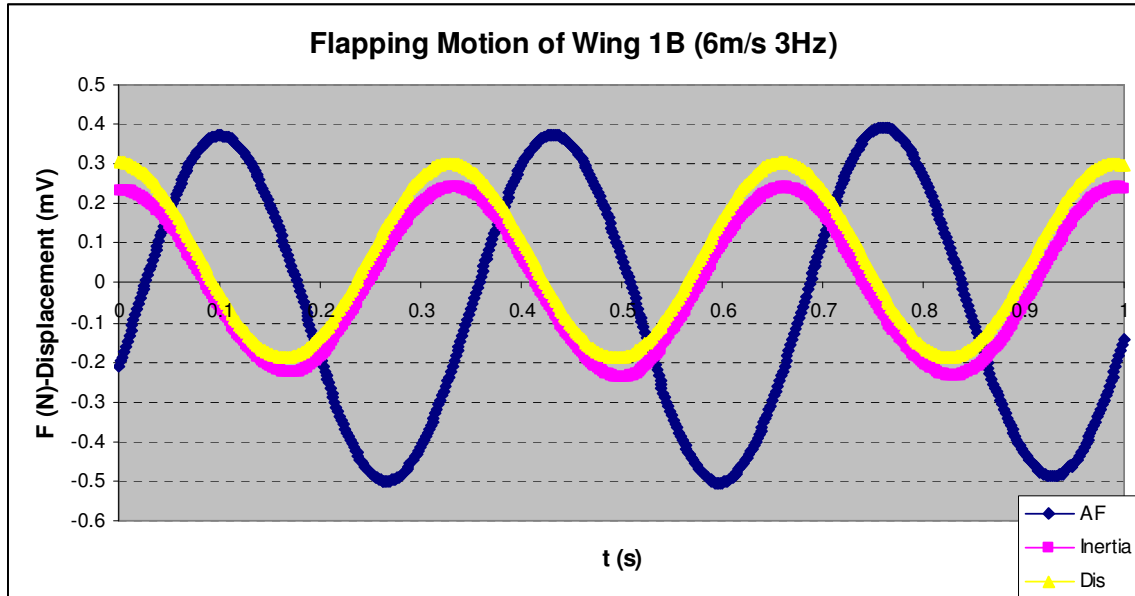


Figure B11 Test result of flapping motion of Wing 1B at 6m/s, 3Hz

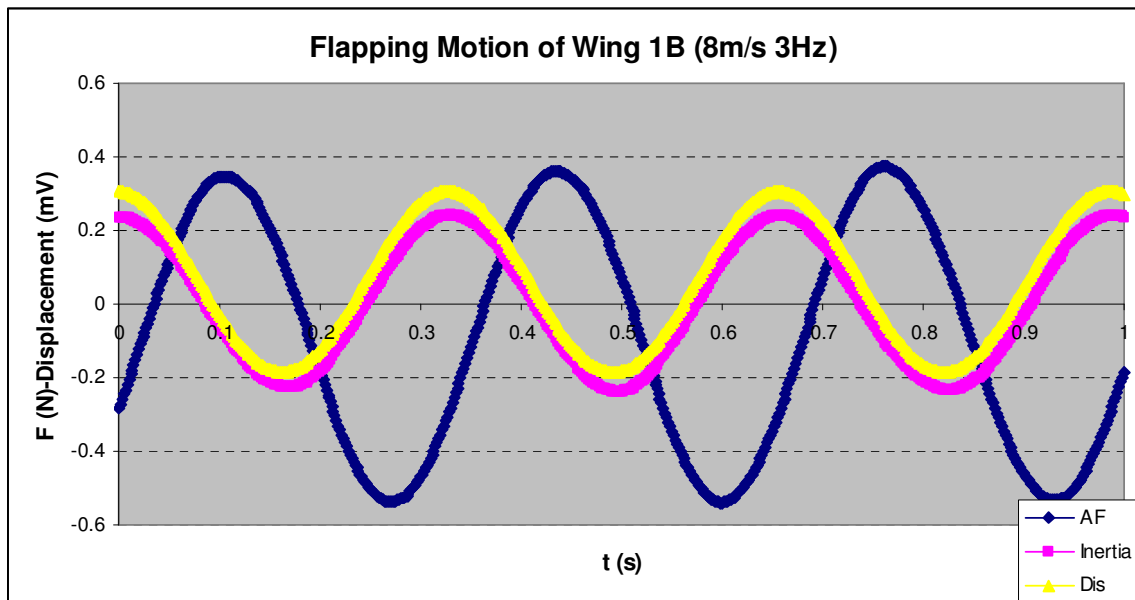


Figure B12 Test result of flapping motion of Wing 1B at 8m/s, 3Hz



## APPENDIX C

Test Result of Design Case 1				
V (m/s)	Lift (N)	Drag (N)	Lift (N) upstroke	Lift (N) downstroke
0	0.077	-0.011	-0.065	0.089
2	0.121	0.009	-0.112	0.130
4	0.232	0.051	-0.228	0.235
6	0.392	0.120	-0.414	0.369

Table C1 Test result of design case 1

Test Result of Design Case 2				
V (m/s)	Lift (N)	Drag (N)	Lift (N) upstroke	Lift (N) downstroke
0	0.075	-0.002	-0.070	0.080
2	0.118	0.013	-0.111	0.124
4	0.219	0.067	-0.186	0.252
6	0.378	0.146	-0.314	0.442

Table C2 Test result of design case 2

Test Result of Design Case 3				
V (m/s)	Lift (N)	Drag (N)	Lift (N) upstroke	Lift (N) downstroke
0	0.055	0.002	-0.042	0.067
2	0.107	0.019	-0.091	0.123
4	0.180	0.064	-0.149	0.210
6	0.297	0.136	-0.238	0.356

Table C3 Test result of design case 3

Test Result of Design Case 4				
V (m/s)	Lift (N)	Drag (N)	Lift (N) upstroke	Lift (N) downstroke
0	0.067	-0.002	-0.055	0.079
2	0.106	0.019	-0.070	0.142
4	0.204	0.058	-0.163	0.246
6	0.361	0.129	-0.327	0.394

Table C4 Test result of design case 4

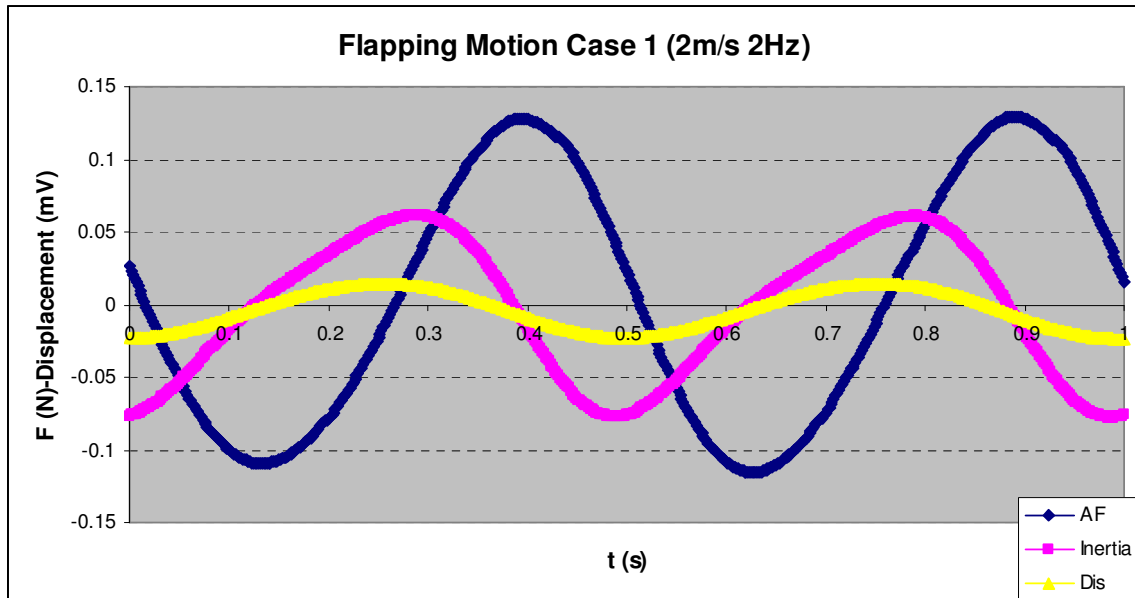


Figure C1 Test result of flapping motion of case 1 at 2m/s, 2Hz

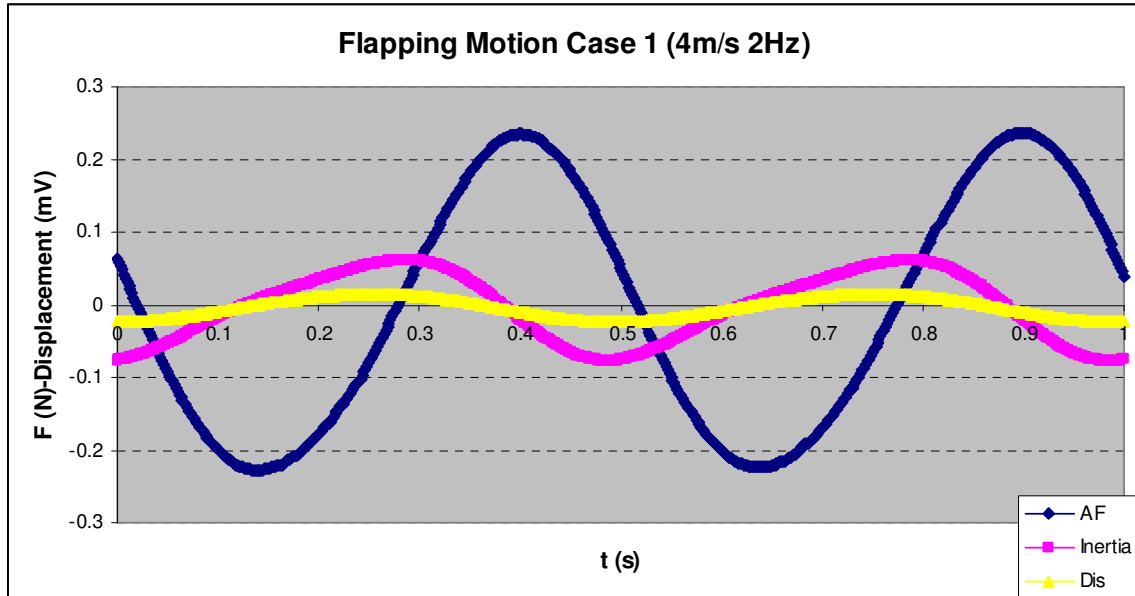


Figure C2 Test result of flapping motion of case 1 at 4m/s, 2Hz

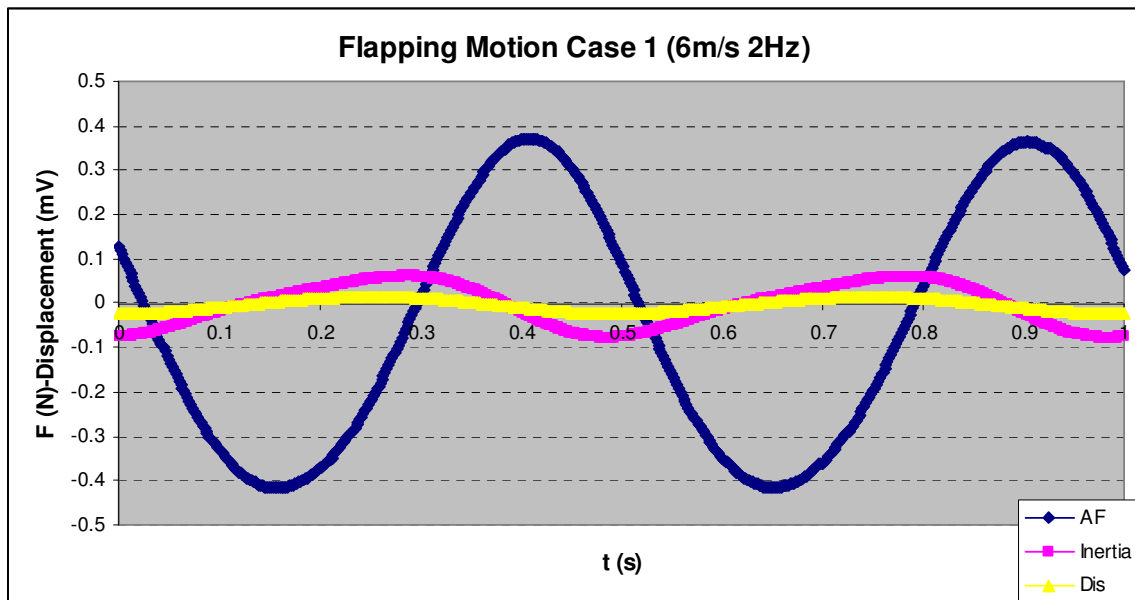


Figure C3 Test result of flapping motion of case 1 at 6m/s, 2Hz

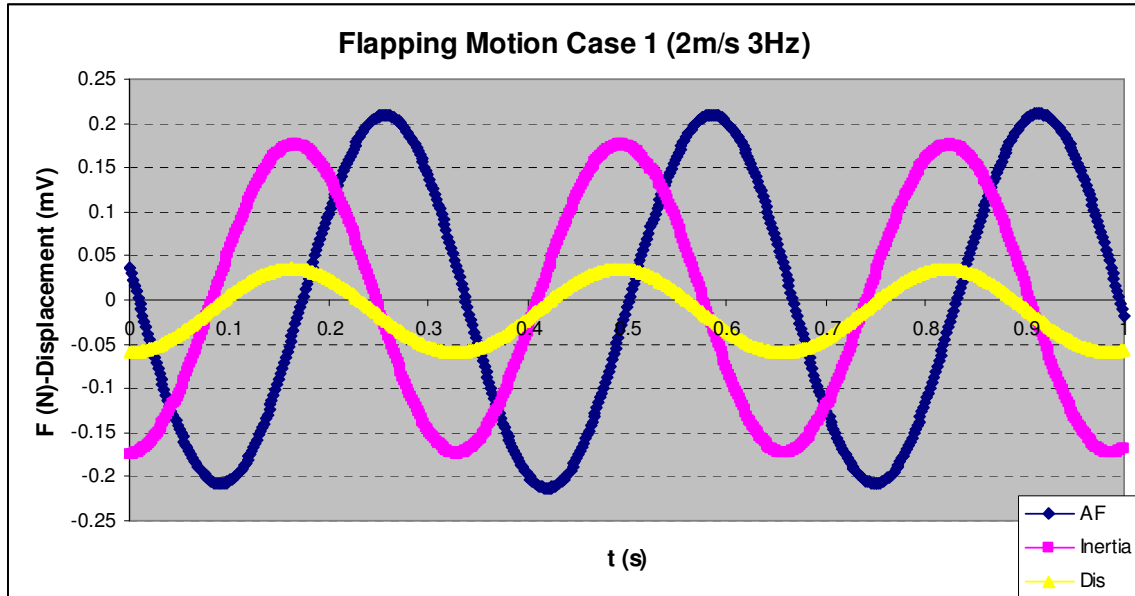


Figure C4 Test result of flapping motion of case 1 at 2m/s, 3Hz

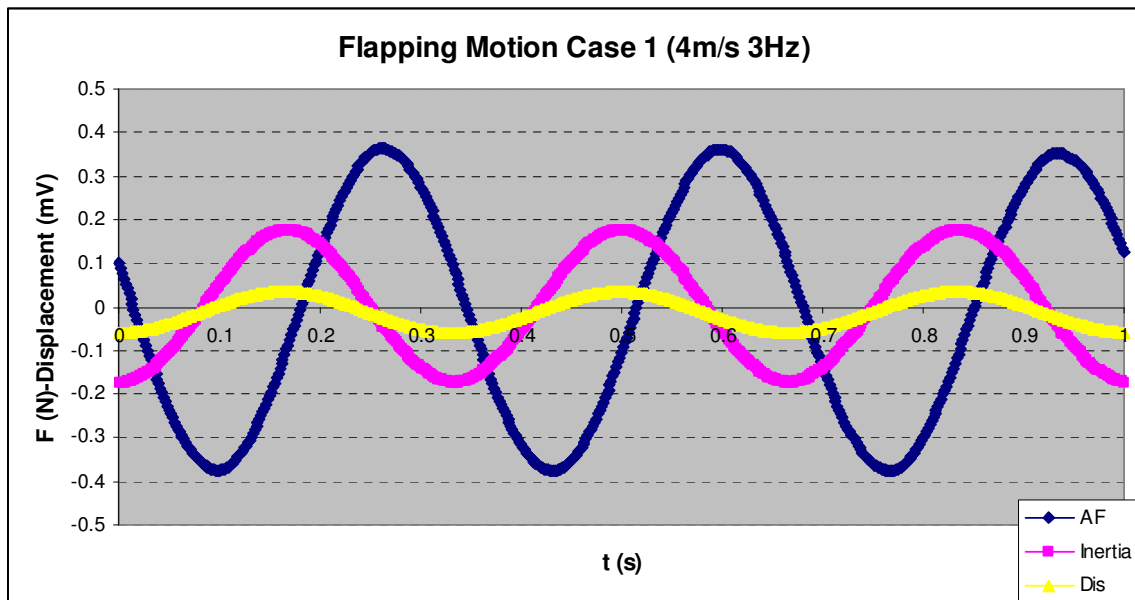


Figure C5 Test result of flapping motion of case 1 at 4m/s, 3Hz

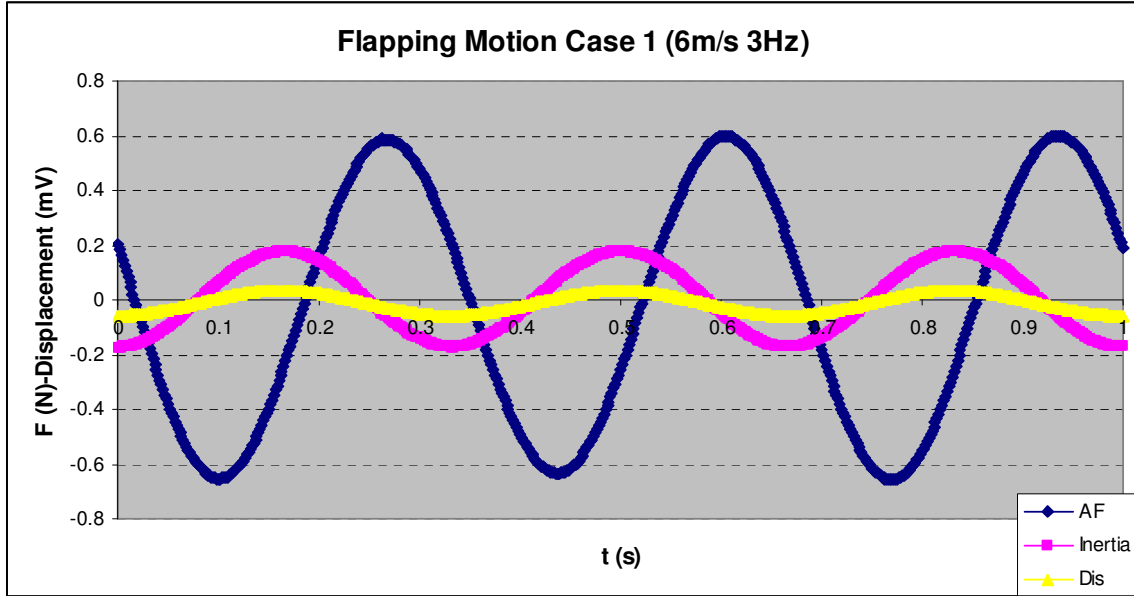


Figure C6 Test result of flapping motion of case 1 at 6m/s, 3Hz

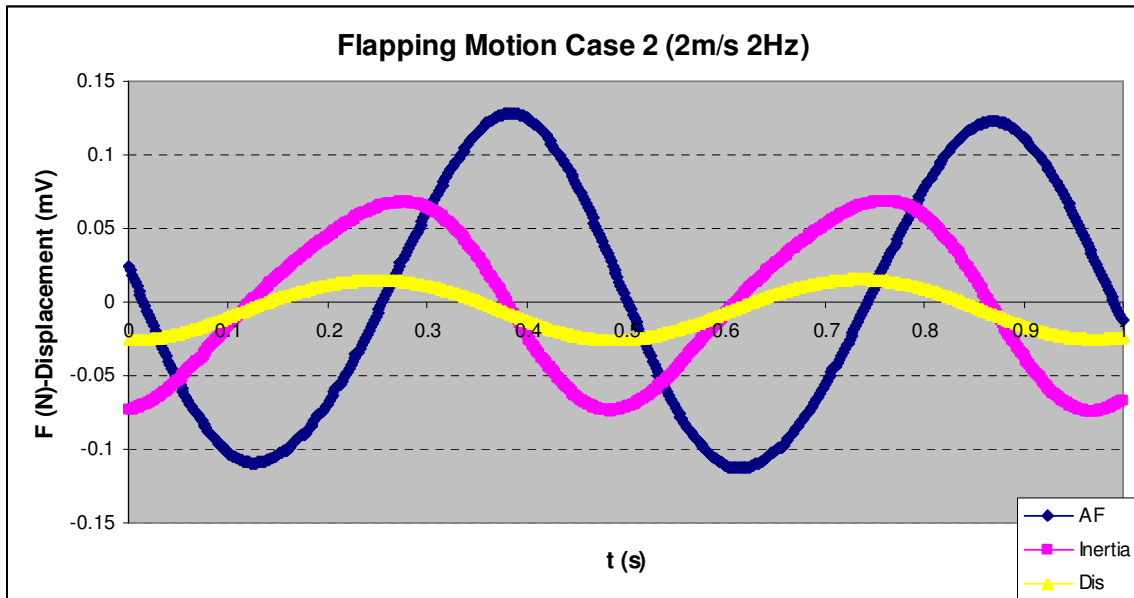


Figure C7 Test result of flapping motion of case 2 at 2m/s, 2Hz

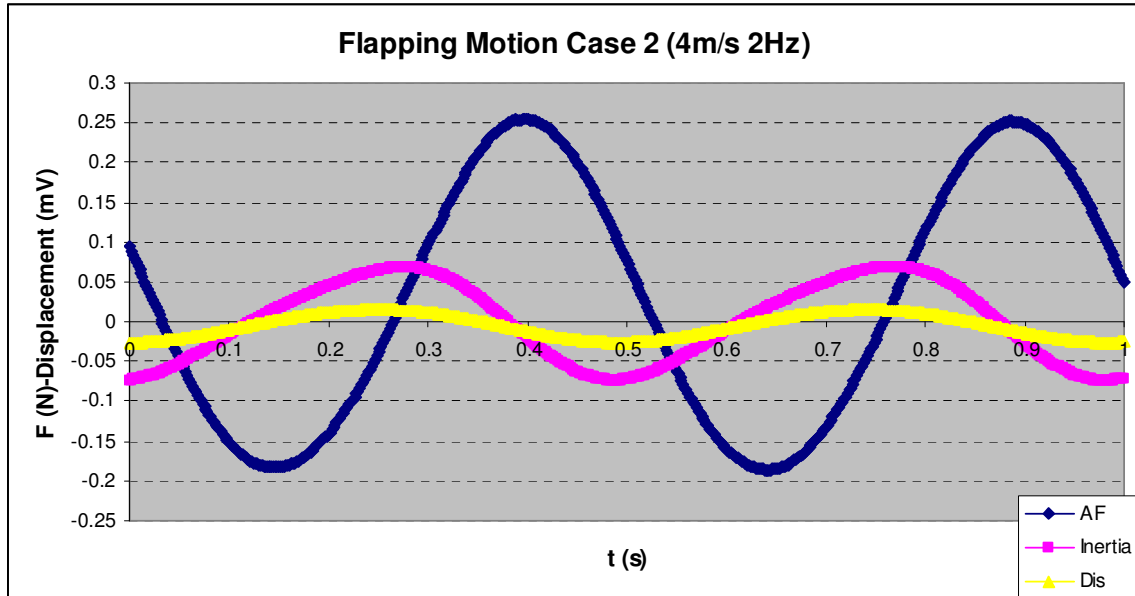


Figure C8 Test result of flapping motion of case 2 at 4m/s, 2Hz

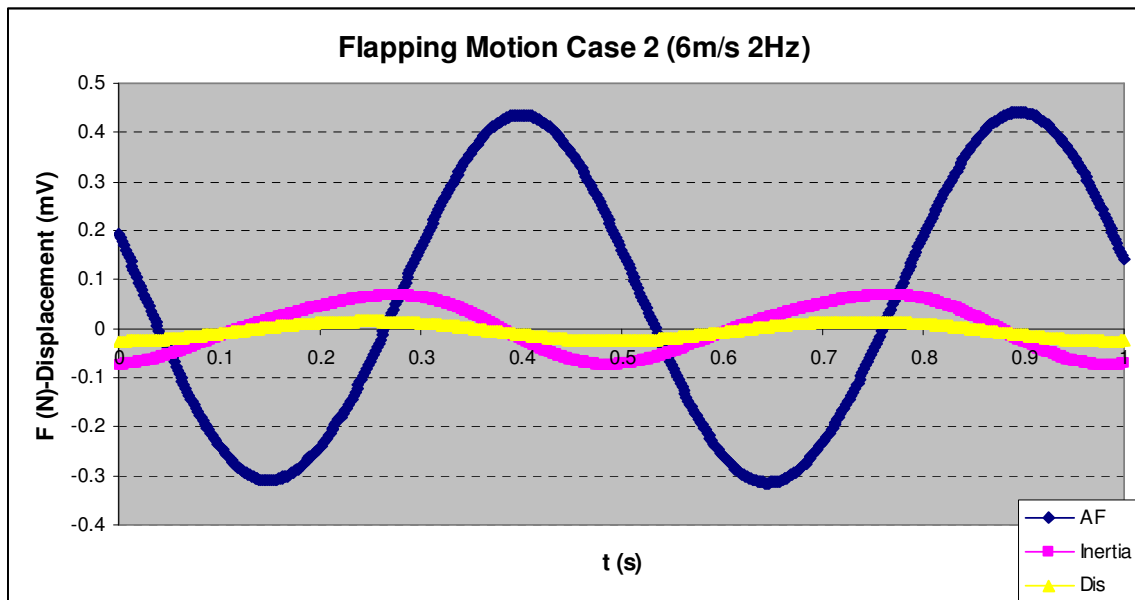


Figure C9 Test result of flapping motion of case 2 at 6m/s, 2Hz

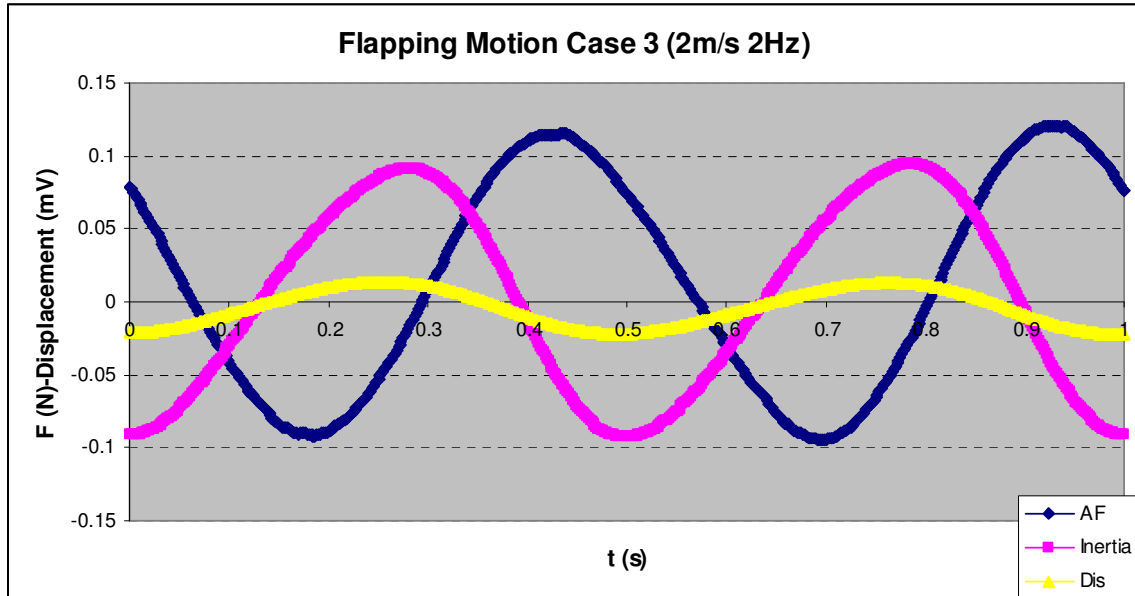


Figure C10 Test result of flapping motion of case 3 at 2m/s, 2Hz

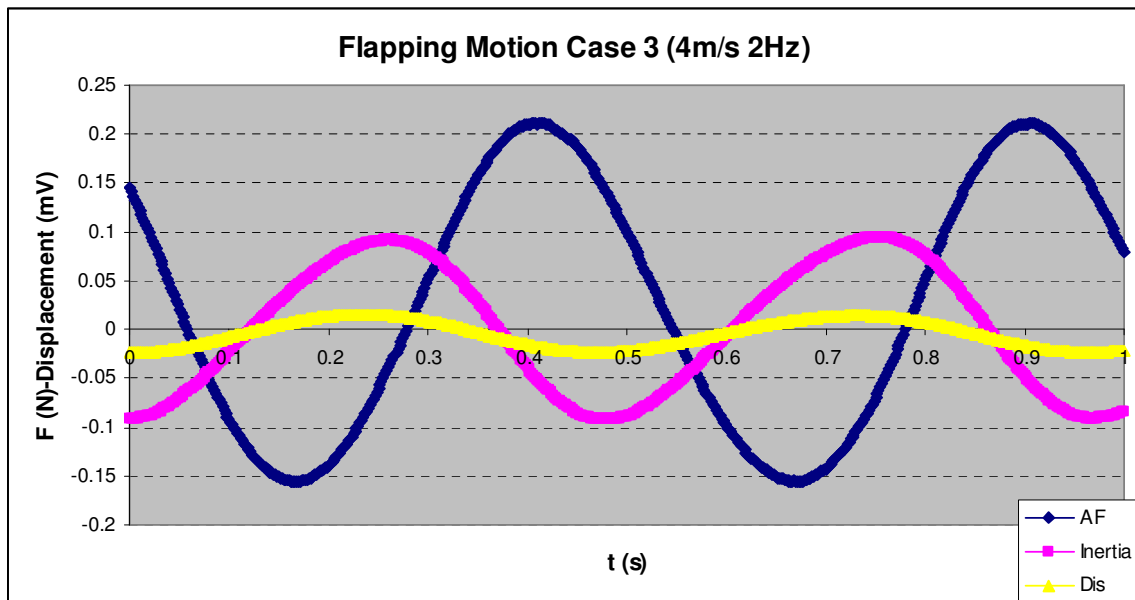


Figure C11 Test result of flapping motion of case 3 at 4m/s, 2Hz

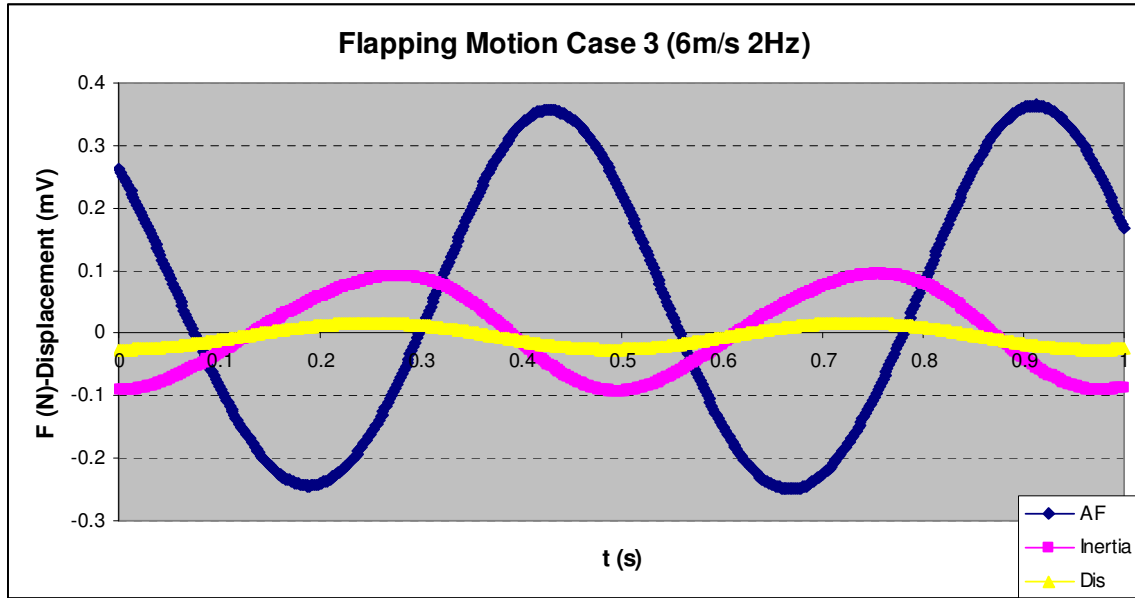


Figure C12 Test result of flapping motion of case 3 at 6m/s, 2Hz

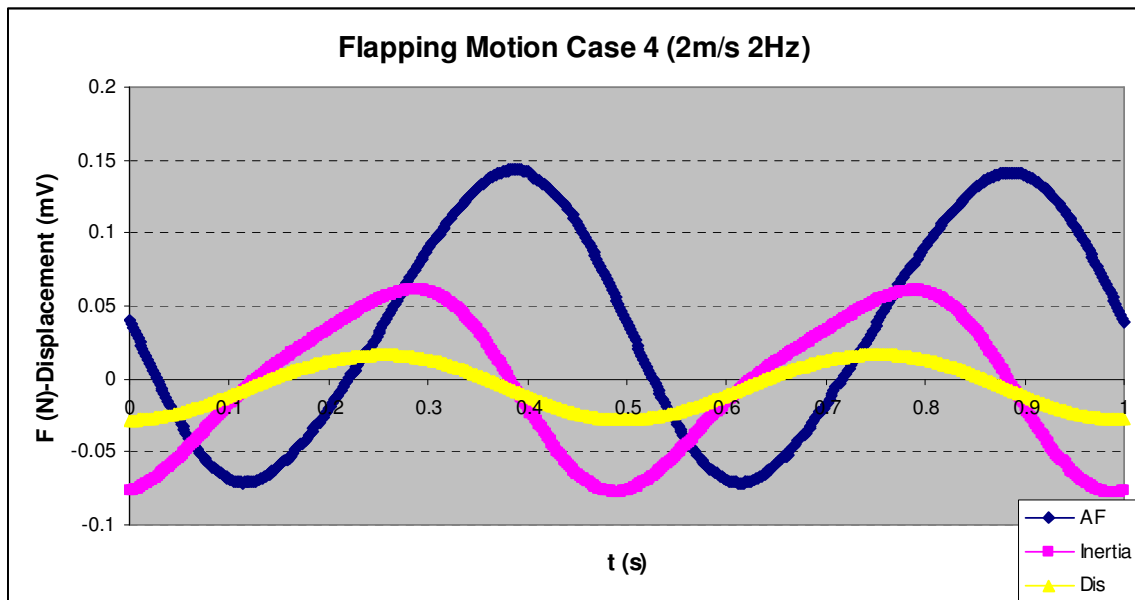


Figure C13 Test result of flapping motion of case 4 at 2m/s, 2Hz



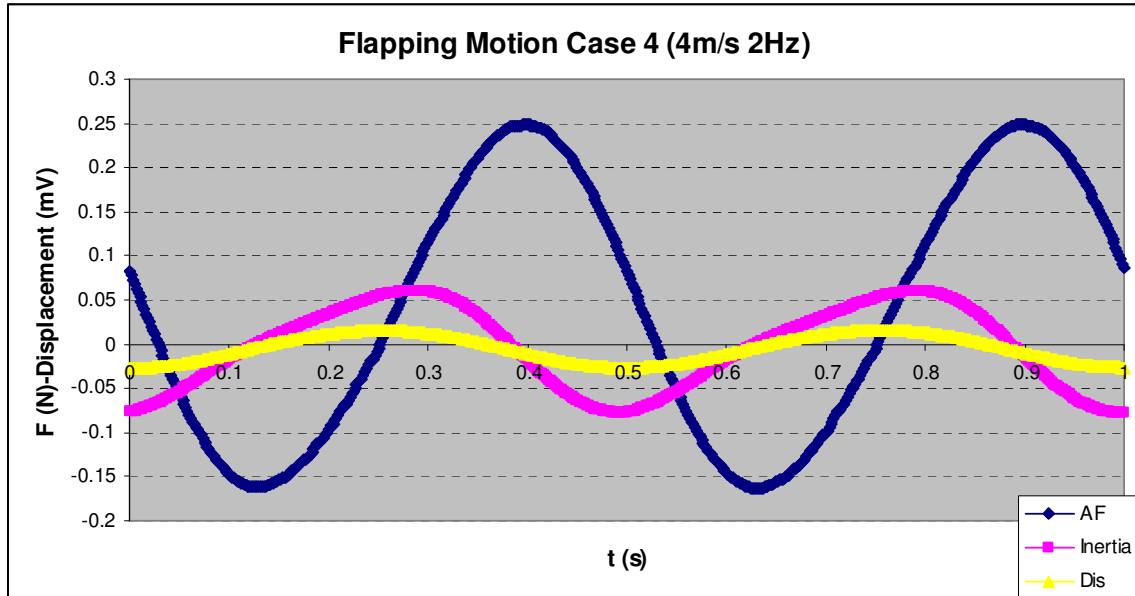


Figure C14 Test result of flapping motion of case 4 at 4m/s, 2Hz

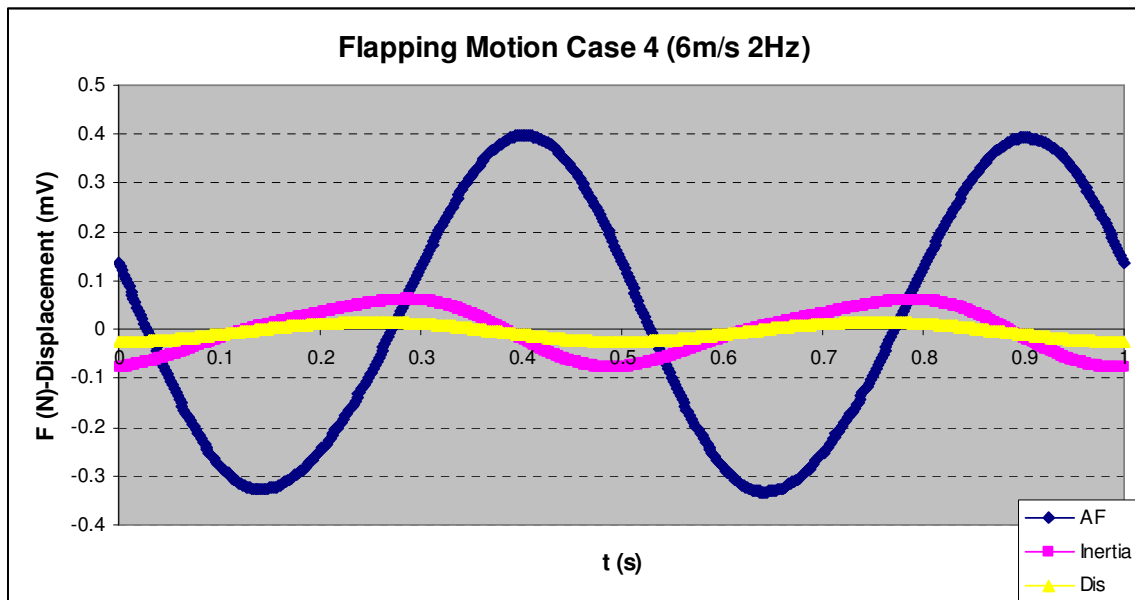


Figure C15 Test result of flapping motion of case 4 at 6m/s, 2Hz